Experimentation, Simulation and Modeling of Thermophysical Properties of asymmetric Mixtures

Abdoul Wahidou Saley Hamani

DOCTORAL THESIS

UNIVERSITE DE PAU ET DES PAYS DE L'ADOUR
École doctorale des sciences exactes et leurs applications

Experimentation, Simulation and Modeling of Thermophysical Properties of Asymmetric Mixtures.

Dissertation defended on November 4, 2019
By

Abdoul Wahidou SALEY HAMANI

In the fulfillment of the requirements for the degree of Doctor of Philosophy in

Chemical and Petroleum Engineering

Doctoral committee

Rapporteurs

• Bernard ROUSSEAU	DR-CNRS, Université Paris Sud
• Velisa VESOVIC	Pr, Imperial College London

Examiners

• Manuela ARTAL	Dr, Universidad Zaragoza
• Pierre CEZAC	Pr, Université de Pau et des Pays de l'Adour
• Julien COLLELL	Dr, Research Engineer TOTAL

PhD Advisors

• Guillaume GALLIERO	Pr, Université de Pau et des Pays de l'Adour
• Jean-Luc DARIDON	Pr, Université de Pau et des Pays de l'Adour

UNIVERSITÉ DE PAU ET DES PAYS DE L'ADOUR

THESE DE DOCTORAT DE L'UNIVERSITE DE PAU ET DES PAYS DE L'ADOUR

Ecole Doctorale n° 211 : Sciences Exactes et leurs Applications

Doctorat en Génie des Procédés

Spécialité : Génie Pétrolier

Par

Abdoul Wahidou SALEY HAMANI

Experimentation, Simulation et Modélisation des Properties Thermophysiques de Mélanges Asymétriques

Composition du jury

Bernard ROUSSEAU	DR-CNRS, Université Paris Sud	Rapporteur
Velisa VESOVIC	Pr, Imperial College London	Rapporteur
Manuela ARTAL	Dr, Universidad Zaragoza	Examinatrice
Pierre CEZAC	Pr, University de Pau et des Pays de l'Adour	Examinateur
Julien COLLELL	Dr, Ingénieur de recherche TOTAL SA	Examinateur
Jean-Luc DARIDON	Pr, Université de Pau et des Pays de l'Adour	Directeur
Guillaume GALLIERO	Pr, Université de Pau et des Pays de l'Adour	Co-Directeur

Laboratoire des Fluides Complexes et leurs Réservoirs,
UMR 5150 CNRS-TOTAL-UPPA

À mes parents

Acknowledgment (in French)

Ce travail de thèse a été réalisé dans l'équipe de recherche « Propriétés Thermophysiques » du Laboratoire des Fluides Complexes et leurs Réservoirs (LFCR) à l'Université de Pau et des Pays de l'Adour.

Je remercie dans un premier temps Bernard ROUSSEAU et Velisa VESOVIC qui m'ont fait l'honneur d'accepter d'être rapporteurs de cette thèse. Aussi, je remercie Manuela ARTAL, Julien COLLELL et Pierre CEZAC pour avoir accepté d'examiner ce travail et de faire partie du jury de soutenance.

Je tiens tout particulièrement à remercier mes Directeurs de thèse, Guillaume GALLIERO et Jean-Luc DARIDON, pour leur encadrement, leur disponibilité et les conseils, O combien enrichissant qu'ils m'ont apportés tout au long de ces années de thèse. Mes remerciements s'adressent également à Hai Hoang, pour nos très nombreux échanges et ce malgré le décalage horaire entre la France et le Vietnam.

C'est aussi l'occasion pour moi de remercier tous mes collègues et amis que j'ai côtoyés au cours de ces années de thèse : Fouad, Hafiz, Jun Cheng, Mohamed, Ezequiel, Deneb, Bich Ngoc, Dihya, Daoud, Samy, Nelson, Patrick, Romain, Amael, Catherine, Véronique, Blandine, Patricia, Sophie, Djamel, Jean-Patrick.

Enfin, mes plus sincères remerciements vont à l'endroit de toute ma famille et en particulier mes Parents, pour les sacrifices consentis et toutes les valeurs qu'ils m'ont inculquées : ***ce travail de thèse leur est spécialement dédié*** ! Je n'oublie pas Jade, pour son soutien avant et pendant cette thèse, mille mercis.

Abstract (in French)

Les mélanges asymétriques, constitués à la fois de composants légers (gaz) et lourds (liquides) sont impliqués dans de nombreux procédés industriels tels que les procédés de séquestration du CO_2 ou d'amélioration de la production pétrolière de champs matures. Cependant, il existe relativement peu de mesures de propriétés thermophysiques (équilibre de phase, propriétés PVT, viscosité, etc.) effectuées sur ces systèmes en conditions de réservoir. De plus, leur modélisation par des approches classiques reste problématique, précisément en raison de l'asymétrie entre les molécules et les conditions opératoires. Aujourd'hui, compte tenu des avancées considérables en matières de puissance de calcul, les techniques de simulation moléculaire se révèlent être des outils complémentaires prometteurs pour la prédiction des propriétés thermophysiques des mélanges de fluide. Néanmoins, peu d'études ont permis de déterminer si de telles techniques sont applicables de manière prédictive pour traiter des mélanges très asymétriques tels que les systèmes CO_2-huile. Ainsi, l'objectif de cette thèse est de combiner mesures expérimentales et simulations moléculaires, sur des mélanges asymétriques modèles liés à la problématique des géoressources, afin de fournir des données fiables et, in fine, de comprendre et d'améliorer la modélisation de ces systèmes. Pour cela, des mesures expérimentales, des simulations de Monte Carlo et de Dynamique Moléculaire de propriétés telles que la masse volumique, les compressibilités isothermes et isentropiques, la dilatation isobare, la capacité calorifique, la vitesse du son et la viscosité ont été réalisées. La première partie de ce travail a été consacrée à l'étude préliminaire d'un mélange asymétrique simple composé de paraffines. Il ressort de ces études que pour ce type de système, indépendamment du niveau de description moléculaire du champ de force (fin ou gros-grains), les techniques de simulation moléculaire sont capables de prédire quantitativement les propriétés thermodynamiques étudiées et les propriétés d'excès associées. Cependant, la transférabilité de ces mêmes champs de force à la prédiction de propriétés de transport telles que la viscosité est limitée, même pour un système aussi simple. Ensuite, nous avons concentré nos efforts sur l'étude de systèmes asymétriques plus complexes composés de dioxyde de carbone et de paraffines, au voisinage du point critique du dioxyde de carbone. Ces études ont permis d'une part, d'enrichir les bases de données existantes en fournissant des données expérimentales précises sur la masse volumique, la vitesse du son et leurs dérivés (compressibilités isotherme et isentropique), ainsi que les propriétés volumétriques et acoustiques d'excès. D'autre part, les résultats obtenus ont mis en exergue un comportement fortement non-idéal dans ce type de système. Cette forte non-idéalité résulte de la formation de « clusters » de molécules de solvant (CO_2) autour des molécules de soluté (paraffines) dans les conditions proches du point critique du CO_2. De plus, à l'aide des simulations moléculaires, des informations à l'échelle microscopique ont été apportées, permettant ainsi d'expliquer les observations macroscopiques et ouvrant la voie à de nouvelles approches pour la modélisation de ces systèmes.

Mots clés : Masse volumique, Compressibilité isotherme, Vitesse du son, Compressibilité isentropique, Viscosité, Hautes Pressions, Alcanes, Dioxyde de carbone, Monte Carlo, Dynamique moléculaire.

Introduction (in French)

1. Contexte général de la thèse

Depuis la première révolution industrielle (1850), on a assisté à une augmentation de la température terrestre moyenne (environ + 0,83 ° C). Ce réchauffement climatique, bien qu'apparemment faible, est connu pour être à l'origine d'événements météorologiques extrêmes. Aujourd'hui, il est largement admis que le CO_2 anthropique, c'est-à-dire celui issu de l'activité humaine, est l'un des principaux gaz à effet de serre à l'origine de cette augmentation de température. Ces émissions de CO_2, provenant principalement de la combustion de combustibles fossiles et de la production de ciment, ont augmenté en moyenne d'environ 4% au cours de la dernière décennie, atteignant ainsi 38 Gt en 2017, comme le montre la figure.1. Cette augmentation de température a conduit une majorité de pays à travers le monde à signer des accords tels que le Protocole de Kyoto ou plus récemment l'Accord de Paris (COP 21), afin d'atténuer ce réchauffement climatique en limitant, voire en réduisant les émissions de carbone. Pour atteindre cet objectif, le développement de solutions technologiques permettant de lutter contre les émissions de CO_2 est en plein essor.

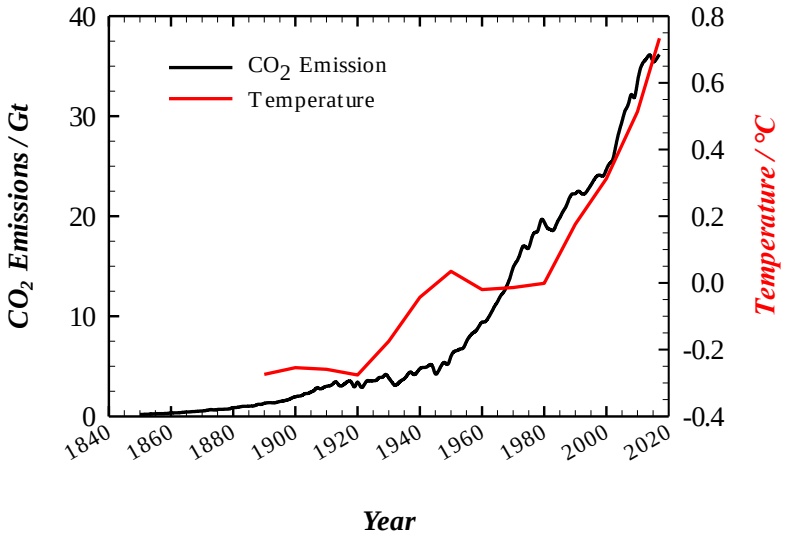

Figure.1 Historique de l'évolution de la température de la surface terrestre et des émissions de CO_2 anthropique. Données fournies par la NOAA (NASA).

Parmi ces solutions, la séquestration géologique et l'utilisation du dioxyde de carbone (en anglais, Carbon Capture Utilisation and Storage ou CCUS) est l'une des plus avancées. Il s'agit d'une suite intégrée de technologies consistant à capturer le CO_2 issus des processus industriels, puis à le transporter par pipelines, navires et camions citernes pour une utilisation et/ou un stockage en toute sécurité (séquestration), voir figure.2. Afin de rendre les projets de CCUS économiquement viables, la principale utilisation du CO_2 capturé est pour les procédés de récupération assistée de pétrole (CO_2 -EOR) provenant de champs pétroliers matures. En effet, en injectant du CO_2 dans des réservoirs géologiques épuisés de pétrole et de gaz, il permet l'augmentation de la production de pétrole. Cependant, la mise en œuvre des procédés de CCUS en général et en particulier de CO_2-EOR s'avère être un défi technique. Une des difficultés rencontrées demeure dans la caractérisation thermophysique des fluides impliqués, compte tenu de leur complexité et des conditions thermodynamiques correspondant aux conditions du réservoir.

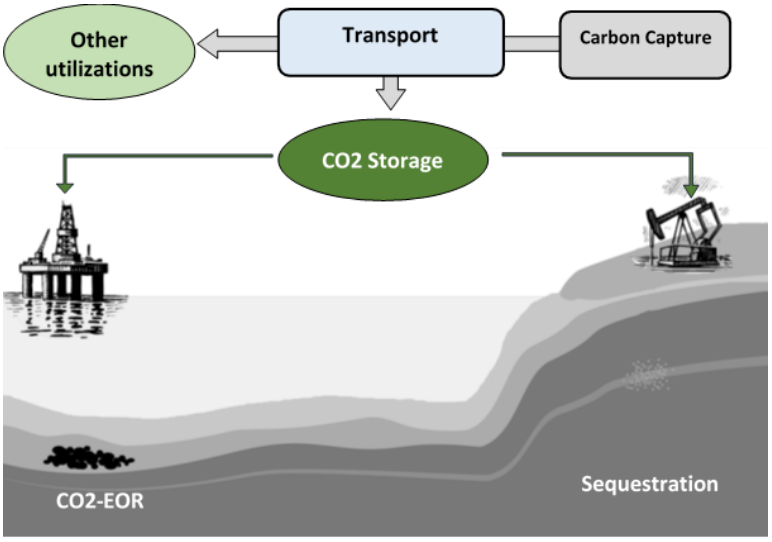

Figure.2 Schéma représentatif des étapes du CCUS.

2. Importance de la caractérisation thermophysique

Le développement des technologies de CCUS de manière sûre, efficace et économiquement viable, nécessite une connaissance précise des propriétés thermophysiques des fluides impliqués dans ces procédés. Ces propriétés thermophysiques sont généralement classées en deux familles : les propriétés thermodynamiques (provenant du système à l'équilibre) et celles de transport (provenant de fluides hors équilibre). Le tableau 1 présente les principales propriétés requises dans la mise en œuvre des procédés de CCUS.

Tableau.1 Propriétés thermophysiques importantes pour les procédés de CCUS

Propriétés	
Thermodynamique	Changement de phase
	Masse volumique
	Capacité calorifique
	Enthalpie et entropie
	Vitesse du son
Transport	Tension superficielle
	Viscosité
	Conductivité thermique
	Coefficient de Diffusion

Par exemple, le choix des matériaux ainsi que des différents éléments constituant le procédé tels que les compresseurs, les échangeurs de chaleur, les cuves de stockage ainsi que les pipelines de transport repose sur une connaissance précise des propriétés thermophysiques, telles que les propriétés de changement de phase, la masse volumique, la viscosité et la conductivité thermique. Une autre propriété importante est la vitesse du son qui joue un rôle clé pour déterminer la propagation des ondes de dépressurisation se produisant dans les pipelines

et qui est également utilisée dans la surveillance sismique des réservoirs pendant la phase de séquestration ou de récupération assistée de pétrole.

3. Estimation des propriétés thermophysiques des mélanges contenant du CO_2

Comme discuté dans la section précédente, les propriétés thermophysiques sont d'une importance capitale. L'estimation de ces propriétés se fait principalement par des mesures expérimentales ou des modèles empiriques/théoriques. Depuis des décennies, plusieurs mesures expérimentales de haute précision ont été réalisées sur du CO_2 pur ainsi que sur ses mélanges. Par conséquent, de nombreuses données sont disponibles dans la littérature pour les mélanges tels que CO_2-gaz (CO_2 /CH_4, CO_2 / H_2S, CO_2 / CH_4 /N_2) mais aussi CO_2-eau / saumure pour laquelle les équilibres de phase, les propriétés volumétriques et la viscosité sont fournis à différentes conditions. Cependant, la littérature est moins riche en ce qui concerne les systèmes CO_2-hydrocarbure, en particulier en ce qui concerne la viscosité. Cela peut s'expliquer par le fait que de tels mélanges « gaz-liquide » sont difficiles à étudier expérimentalement notamment dans les conditions de réservoir, qui sont souvent supercritiques du point de vue du CO_2.
Ainsi, malgré la croissance rapide des bases de données de propriétés thermophysiques des mélanges CO_2-hydrocarbures, les données rapportées dans la littérature ne couvrent toujours pas toutes les fenêtres opératoires des procédés de CO_2-EOR, ni tous les systèmes qui peuvent y être impliqués. Pour combler les lacunes des mesures expérimentales, divers modèles sont utilisés afin de prédire les propriétés thermophysiques de tels mélanges « gaz-liquide ». L'une des principales difficultés de la modélisation de ces mélanges, par rapport aux systèmes CO2-gaz, réside dans le fait que les mélanges CO2-hydrocarbures sont généralement asymétriques, c'est-à-dire que les mélanges sont composés d'espèces de tailles et/ou énergies et/ou masses très différentes.
Les propriétés thermodynamiques sont généralement calculées en utilisant des équations d'états (EOS). Ces modèles thermodynamiques sont applicables sur une large gamme de température et de pression. Pour les mélanges idéaux ou faiblement non-idéaux, les propriétés thermodynamiques des phases vapeur et liquide sont généralement prédites avec un minimum de données. Cependant, l'extension des EOS à des mélanges plus asymétriques nécessite généralement l'utilisation de règles de mélange complexes combinées à des paramètres d'interactions binaires, faisant ainsi perdre à ces modèles leur caractère totalement prédictif. Les EOS peuvent être regroupés en familles, parmi lesquelles les équations cubiques, les équations du Viriel et les équations de type SAFT sont les plus utilisées. La performance de ces équations dépend souvent de la propriété thermodynamique calculée et/ou des conditions thermodynamiques. Par exemple, les équations cubiques sont connues pour fournir de bons résultats en phase vapeur et en équilibre de phase, mais elles sont moins précises pour la prédiction des propriétés volumétriques en phase liquide et nécessitent des corrections de volume. Pour les EOS de type SAFT, ils fournissent une bonne prédiction des propriétés à la fois monophasiques et d'équilibre de phase, mais conduisent à de mauvaises prédictions dans la région autour du point critique. Il convient de noter que, en plus des « EOS généraux » évoquées ci-dessus, il existe des équations spécialisées telles que l’équation de Span et Wagner pour le CO2 pur. Cependant, ces équations spécialisées ne s'appliquent généralement qu'à des systèmes et conditions spécifiques.

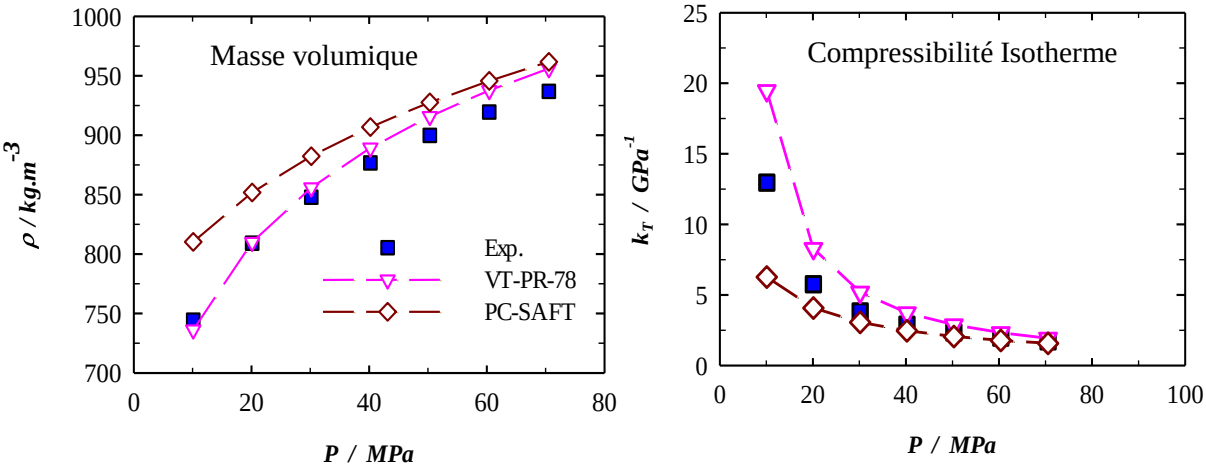

Figure.3 Illustration de la faible robustesse des différents modèles sur un binaire composé de dioxyde de carbone et de n-heptane. A gauche : comparaison de la masse volumique entre les mesures expérimentales et des EOS (VT-PR-78 et PC-SAFT). A droite : comparaison entre la compressibilité isotherme expérimentale et les résultats obtenus à partir d'EOS.

De la même manière que les propriétés thermodynamiques, plusieurs modèles ont été proposés pour la prédiction des propriétés de transport. Concernant la viscosité, le modèle le plus largement utilisé en génie pétrolier est la corrélation de Lohrenz-Bray-Clark (LBC), en raison de sa simplicité, de sa flexibilité et de sa cohérence. Ce modèle, basé sur le concept de viscosité résiduelle, consiste en une fonction polynomiale d'ordre 4 de la masse volumique réduite. Il fournit des résultats corrects, à condition que des valeurs précises de masse volumique soient disponibles, mais nécessitent souvent un ajustement des volumes critiques. Par ailleurs, la viscosité peut également être obtenue à partir de modèles prédictifs comme ceux basés sur la théorie des états correspondants, la théorie du volume libre, la théorie du frottement, la méthode de mise à l'échelle thermodynamique, la méthode de mise à l'échelle de l'entropie, etc.

Avec les avancées importantes en terme de capacités de calcul, les méthodes numériques telles que la relation quantitative structure (en anglais, Quantitative Structure-Property Relationship ou QSPR) ou les simulations moléculaires (en anglais, Molecular Simulation ou MS) se révèlent être des outils complémentaires prometteurs afin de prédire les propriétés thermophysiques des systèmes fluides. La méthode QSPR consiste à créer un modèle prédictif d'une propriété donnée à partir de descripteurs moléculaires. Les modèles sont obtenus au moyen de méthodes numériques telles que les réseaux de neurones artificiels. S'agissant de la simulation moléculaire, elle consiste à déterminer les propriétés macroscopiques à partir de simulations microscopiques de fluides à l'échelle atomique. Cependant, il n'y a pas ou peu d'études qui révèlent si de telles techniques de calcul sont applicables de manière prédictive pour traiter des mélanges très asymétriques tels que les systèmes CO_2-hydrocarbures.

4. Motivation et contexte local de la thèse

a. Problématique et Objectifs de la thèse

Dans la section précédente, il a été démontré que, malgré les études expérimentales réalisées dans la littérature, il existe encore relativement peu de données fiables sur les propriétés thermophysiques des mélanges asymétriques tels que ceux impliqués dans les procédés de CO_2-EOR, et leur modélisation à l'aide des approches classiques restent problématiques, précisément

en raison de l'asymétrie entre les molécules ainsi que les conditions opératoires observées. Par conséquent, les mesures expérimentales de ces propriétés restent la méthode la plus fiable pour fournir des données précises. Cependant, les mesures sur de tels systèmes sont toujours difficiles à réaliser de manière systématique, dans une large gamme de pression et de température, comme c'est le cas dans les conditions de réservoir.

Par conséquent, l'objectif de nos travaux est de combiner des mesures expérimentales et des simulations moléculaires, sur des systèmes asymétriques modèles liés aux problématiques des géoressources, afin de fournir des données fiables et, à terme, de comprendre et d'améliorer la modélisation de ces systèmes. Dans cet objectif, les activités réalisées au cours de cette thèse peuvent être regroupées sous les rubriques suivantes :

- La mise en place et la réalisation de mesures expérimentales de propriétés thermophysiques telles que la masse volumique, la compressibilité isotherme, la dilatation thermique isobare, la capacité calorifique, la vitesse du son et la viscosité, sur des mélanges binaires asymétriques, dans des conditions de réservoir. Le but est de fournir un ensemble de données cohérent et bien contrôlé pour la comparaison avec les simulations ainsi que pour enrichir les bases de données existantes.

- La mise en œuvre de simulations moléculaires de Monte Carlo (MC) et de Dynamique Moléculaire (MD), sur les systèmes étudiés expérimentalement. Dans ce travail, nous avons principalement utilisé le MCCG, un champ de force simple, à gros grains. Ce champ de force a été choisi car il semble être un bon compromis entre simplicité et précision et en plus, il existe une équation d'état qui permet de fournir ses propriétés thermodynamiques. Le but est à la fois d'évaluer les capacités de ces approches à traiter les propriétés d'équilibre et de transport et de mettre en lumière des phénomènes microscopiques qui ne sont pas accessibles expérimentalement.

Dans le corps du manuscrit, sont présentés en détail les résultats de l'étude de deux mélanges modèles. Le premier modèle est un mélange asymétrique simple composé de n-hexane et de n-dodécane pour lequel des mesures de masse volumique, de vitesse du son et de viscosité ainsi que des simulations moléculaires ont été effectuées. Le deuxième mélange étudié est un mélange plus asymétrique composé de dioxyde de carbone et de n-heptane. Pour ce système, des mesures de masse volumique et de vitesse du son ont été réalisées, mais en raison de difficultés techniques et de l'inadéquation de notre dispositif expérimental actuel, la mesure de viscosité sur ce système « gaz +liquide » n'a pas pu se faire. De plus, des résultats expérimentaux d'un troisième système composé de dioxyde de carbone et de n-dodécane sont fournis dans l'annexe A.

b. Contexte Local de la thèse

Cette thèse a été réalisée au sein de l'équipe « Propriétés Thermophysiques » du Laboratoire des Fluides Complexes et de leurs Réservoirs (LFCR UMR 5150), unité mixte de recherche rattachée à l'Université de Pau et Pays de l'Adour (UPPA), au Centre National de Recherche Scientifique (CNRS) et à la société Total SA. L'équipe Propriétés Thermophysiques est née de la fusion en 2016 entre deux équipes de recherche : « Hautes Pressions » et « Propriétés de Transport ». La première était spécialisée dans les mesures expérimentales et la modélisation des propriétés thermodynamiques tandis que la seconde était spécialisée dans les mesures et la simulation numérique des propriétés de transport. Ainsi, cette thèse, commencée en 2016 et associant mesures expérimentales et techniques de simulation moléculaire sur les propriétés thermodynamiques et de transport, s'inscrit dans la continuité de la fusion de ces deux équipes.

5. Organisation du manuscrit

Le plan du manuscrit est le suivant :

- Le chapitre 2 est consacré à la description des dispositifs expérimentaux ainsi qu'aux protocoles de mesure de la masse volumique, de la vitesse du son et de la viscosité. De plus, il comprend les méthodologies de calcul des propriétés dérivées telles que la compressibilité isotherme et la dilatation thermique isobare.
- Le chapitre 3 traite des techniques de simulation moléculaire utilisées pendant la thèse. La première partie est consacrée à une brève introduction à la physique statistique. Ensuite, les champs de force utilisés pour la modélisation moléculaire sont détaillés. Enfin, nous présentons dans la dernière partie, les méthodologies utilisées pour le calcul des propriétés thermophysiques.
- Le chapitre 4 présente les résultats d'une étude combinant des mesures expérimentales et des simulations moléculaires sur un mélange simple et faiblement asymétrique composé de n-hexane et de n-dodécane. À travers ce chapitre, le MCCG est comparé à un modèle de champs de force plus fin nommé TraPPE-ua et leurs performances pour la prédiction des propriétés thermodynamiques et de transport sont évaluées.
- Le chapitre 5 est consacré aux investigations expérimentales d'un mélange plus asymétrique composé de dioxyde de carbone et de n-heptane. Il fournit des propriétés volumétriques et acoustiques précises. En outre, plus d'informations sont fournies sur le comportement microscopique des fluides en analysant les volumes molaires partiels des composants des mélanges.
- Le chapitre 6 traite des simulations moléculaires du binaire composé de dioxyde de carbone et de n-heptane, dans les mêmes conditions que celles expérimentalement étudiées au chapitre 5. Tout d'abord, la prédiction des propriétés volumétriques et acoustiques avec des simulations moléculaires est évaluée, puis des investigations portant sur la structure microscopique du mélange sont effectuées.
- Le chapitre 7 résume les résultats de cette thèse et fournit quelques conclusions et perspectives.
- L'annexe A présente des investigations expérimentales supplémentaires effectuées sur un troisième mélange binaire composé de dioxyde de carbone et de n-dodecane.
- L'annexe B présente des données expérimentales et de simulation des propriétés thermophysiques du mélange binaire composé de n-hexane + n-dodécane, discutées au chapitre 4
- L'annexe C est consacrée aux tableaux de données des résultats de simulation sur le mélange binaire composé de dioxyde de carbone et de n-heptane, étudiés au chapitre 6.

Conclusions and Perspectives (in French)

Dans ce chapitre, nous présentons les conclusions générales sur les travaux développés dans ce manuscrit ainsi que des perspectives et recommandations pour de futurs travaux.

1. Conclusions

Il convient de rappeler que l'objectif de ces travaux, combinant mesures expérimentales et simulations moléculaires, est d'une part de fournir des données expérimentales fiables sur les mélanges asymétriques, en particulier sur ceux présentant un intérêt pour les procédés de CO_2-EOR , et d'autre part d'évaluer les performances des techniques de simulation moléculaire pour prédire quantitativement ces propriétés thermophysiques et de fournir un aperçu microscopique sur la structure des mélanges étudiés.

Dans le premier chapitre, nous avons réalisé des mesures expérimentales et des simulations moléculaires sur un simple mélange asymétrique liquide composé de n-hexane+n-dodécane. Cette étude a permis d'évaluer la capacité du modèle de champ de force gros grain (MCCG) par rapport à un champ de force grain fin (TraPPE- ua), de prédire simultanément les propriétés thermodynamiques (masse volumique et propriétés dérivées) et les propriétés de transport (viscosité). D'après nos résultats, il apparaît que les deux champs de force combinés avec des techniques de simulation moléculaire sont capables de prédire quantitativement les propriétés thermodynamiques étudiées et leurs propriétés d'excès associées pour ce mélange simple en utilisant les règles de combinaison classiques de Lorentz- Berthelot. Cependant, la transférabilité de ces champs de force à la prédiction de la viscosité et de ses valeurs d'excès n'est pas évidente, même pour un mélange aussi simple. On peut ainsi conclure de ces observations que la viscosité est une propriété intéressante non seulement pour évaluer la qualité des champs de force mais aussi la capacité des règles de combinaison à décrire les interactions croisées pour un modèle moléculaire donné.

Ensuite, dans le chapitre suivant, nous avons choisi d'étudier un système plus complexe, composé de CO_2 et de n-heptane pour deux températures (303 et 313 K) et des pressions allant de 10 à 70 MPa, soit autour du point critique du CO_2. Ce mélange a été choisi en raison de son intérêt en tant que modèle pour les systèmes de récupération assistée d'huile par injection de CO_2 et ces conditions thermodynamiques spécifiques ont été choisies de manière à analyser spécifiquement l'influence attendue de la proximité du point critique du CO_2 sur les non-idéalités du mélange étudié. Dans un premier temps, ce travail nous a permis d'enrichir les bases de données existantes en fournissant des données expérimentales précises sur la masse volumique, la vitesse du son et leurs dérivées (compressibilité isotherme et isentropique) mais également les propriétés volumétriques et acoustiques d'excès. Il convient de souligner que ce type de données est très rare dans la littérature ouverte sur les systèmes gaz + liquide. Dans les détails, nous avons observé que la masse volumique, à la plus basse pression (10 MPa), se comporte de façon non monotone en fonction de la concentration de CO_2, témoignant d'un important comportement non idéal de ces mélanges à proximité du pont critique. De plus, il a été observé, à T = 313 K et P = 10 MPa, un changement de signe, du positif au négatif, du volume molaire partiel du n-heptane en allant vers une dilution infinie. Un tel comportement, typique des mélanges dilués proches du point critique, peut être interprété comme le résultat de l'organisation des molécules de solvant (CO_2) autour de la molécule de soluté, conduisant à la formation d'agrégat (cluster) du solvant. De plus, en comparant les propriétés volumétriques des mélanges à celles des mélanges idéaux, il apparaît que ces propriétés volumétriques des mélanges, pour des teneurs en CO_2 faibles à modérées, pourraient être bien décrites par un

mélange binaire idéal où les propriétés réelles du CO_2 sont remplacées par leurs valeurs à dilution infinie.

Pour aller plus loin dans nos investigations sur les mélanges CO_2+ nC_7 étudiés, nous avons réalisé au chapitre 6 des simulations moléculaires en utilisant le champ de force MCCG. Il apparaît que grâce à une simple correction des règles de combinaison de Lorentz – Berthelot, au moyen d'un paramètre d'interaction binaire, les simulations moléculaires ont pu prédire les propriétés thermophysiques en très bonne adéquation avec les données expérimentales. Un point très intéressant est que les simulations moléculaires sont capables de prédire certaines propriétés thermodynamiques alors qu'elles ne peuvent pas être mesurées expérimentalement. Ce fut le cas, par exemple, pour la vitesse du son dans des mélanges riches en CO2. En outre, les simulations moléculaires ont été combinées à la théorie des solutions de Kirkwood-Buff afin d'obtenir les volumes molaires partiels des différents constituants des mélanges. Les valeurs obtenues se sont révélé cohérents avec celles déduites des données expérimentales. Enfin, le phénomène de clustering, mis en évidence expérimentalement, a été étudié par des simulation de dynamique moléculaire. Il a été constaté qu'en appliquant différentes définitions des clusters, les résultats donnent toutes un rayon des agrégats d'environ 30 Å. De plus, nos résultats montrent que les molécules de CO_2 restent en moyenne 28,5 ps dans les clusters autour de la molécule centrale nC_7 confirmant par conséquent la faible stabilité de ces agrégats. Ainsi, au fil du temps, le cluster perd son identité en échangeant des molécules avec le bulk, mais conserve son intégrité.

2. Perspectives et recommandations pour de futurs travaux

Les perspectives et recommandations pour les futurs travaux à court terme peuvent être regroupées sous les rubriques suivantes :

- **Mesures expérimentales.** Malgré la forte croissance des bases de données contenant les propriétés thermophysiques des mélanges asymétriques, il semble toujours nécessaire de continuer à produire des données expérimentales sur de tels systèmes, en particulier pour des conditions spécifiques où les modèles de prédictions doivent être améliorés. Dans ce contexte, des mesures supplémentaires sur les systèmes binaires constitués de CO_2 et de n-alcanes à longues chaines ainsi que de méthane et des n-alcanes à longues chaines, continuent à être réaliser dans notre laboratoire (voir annexe A). Ces études devraient également être étendues aux propriétés de transport telles que la viscosité, qui s'avère être une autre propriété très importante et pour laquelle la base de données est encore assez peu fournies.

- **Simulations moléculaires.** À court terme, il serait intéressant de continuer à investiguer sur le phénomène de clustering observé dans les chapitres 5 et 6. A cet effet, nous avons déjà effectué une série de simulations moléculaires sur des systèmes de CO_2+ nC_7 plus proches du point critique afin de déterminer l'effet de la distance au point critique de CO_2 sur la formation des clusters. De plus, une étude systématique de l'effet de la longueur des molécules de n-alcanes sur la taille des clusters devrait être menée, parallèlement aux mesures expérimentales. Tous ces résultats pourraient ensuite être utilisés pour évaluer les limites de l'équation d'état SAFT-Mie (Lafitte et ses collègues) qui est basée sur le modèle MCCG, afin de pouvoir décrire des comportements thermodynamiques subtiles tel que le clustering.

A moyen et long terme, un sujet de recherche intéressant pourrait être le développement de modèles moléculaires simples qui pourront prédire simultanément les propriétés

thermodynamiques et de transport. Pour cela, une approche gros grain, comme celle utilisée pour le champ de force MCCG utilisé dans ce travail, reste une bonne base car c'est un modèle assez simple, avec peu de paramètres. Cependant, il doit être enrichi en améliorant par exemple la manière dont la rigidité des molécules est décrite, tout en gardant sa simplicité. Le but ultime pourrait être sa déclinaison sous forme d'équation d'état (de type SAFT), nécessitant moins de ressources que les simulations moléculaires et donc plus compatible avec les exigences d'ingénierie. Un nouveau projet avec ce sujet comme un des principaux objectifs vient de démarrer dans notre laboratoire.

Abstract

Asymmetric mixtures, consisting of both light (gas) and heavy (liquid) components, are involved in many industrial processes such as CO_2 sequestration processes or improvement of oil production from mature fields. However, there are relatively few measurements of thermophysical properties (phase equilibrium, PVT properties, viscosity, etc.) carried out on these systems in reservoir conditions. Furthermore, their modeling using classical approaches remains problematic precisely due to the asymmetry between molecules and operating conditions achieved. With the great advance in computational capacities, Molecular Simulation turn out to be a promising complementary tool to deal with the thermophysical properties prediction of fluid systems. Nevertheless, there are not a lot of studies that elucidate whether such computational techniques are applicable in a predictive way to deal with very asymmetric mixtures such as CO_2-oil systems. Thus, the objective of our work is to combine experimental measurements and molecular simulations, on model asymmetric systems related to georesource problematics, in order to provide reliable data and, ultimately, to understand and improve the modeling of these systems. With this aim in mind, experimental measurements, Monte Carlo and Molecular Dynamic simulations of thermophysical properties such as density, isothermal and isentropic compressibilities, isobaric thermal expansion, heat capacity, speed of sound and viscosity have been carried out. The first part of the work has been dedicated to the preliminary study of a simple asymmetric binary mixture composed of paraffins. From these studies, it appears that for such a simple system, independently of the molecular description level of the force field (fine or coarse-grain), molecular simulation techniques are able to predict quantitatively the studied thermodynamic properties and their associated excess properties. However, the transferability of these force fields to the prediction of transport properties like viscosity is limited even for such a simple mixture. Then, we have focused our efforts on the study of a more complex asymmetric binary systems composed of carbon dioxide and paraffins in the vicinity of carbon dioxide critical point. First, our results allowed to enrich existing databases by providing accurate experimental data of density, speed of sound and their derivative (isothermal and isentropic compressibilities) but also the excess volumetric and acoustic properties. Second, these studies have identified a strong non-ideal behavior in such systems caused by the formation of “clusters” of solvent molecules (CO_2) around solute molecules (paraffins) for conditions close to the CO_2 critical point. Moreover, by using molecular simulations, microscopic details have been provided, thereby explaining macroscopic observations and paving the way for new approaches for the modeling of these systems.

Keywords: Density, Isothermal compressibility, Speed of sound, Isentropic compressibilities, Viscosity, High pressure, Carbon dioxide, normal alkane, Monte Carlo, Molecular Dynamics.

Contents

Contents iii

List of Figures xvii

List of Tables xxv

Chapter 1. Introduction 1

1.1. General Context of the Work 2
1.2. Importance of Thermophysical Characterization 3
1.3. Estimation of Thermophysical Properties of CO_2-mixtures 4
1.4. Motivation and Local Context of the Thesis 5
1.4.1 Problem Statement and Objectives of the Thesis 5
1.4.2 Local Context of the Work 6
1.5. Organization of the Manuscript 7
1.6. References 7

Chapter 2. Experimental Measurements 10

2.1. Density Measurement 11
2.1.1 Measurement Principle 11
2.1.2 Description of Experimental Setups 13
2.2. Speed of Sound Measurement 16
2.2.1 Measurement Principle 16
2.2.2 Description of Speed of Sound Experimental Setups 18
2.3. Viscosity Measurement 20
2.3.1 Atmospheric Pressure Viscosity Measurement 20
2.3.2 High Pressure Viscosity Measurement 20
2.4. Expanded Uncertainties of Experimental Measurements 22
2.5. Calculation of Volumetric Derivative Properties 23
2.5.1 Isothermal Compressibility 23
2.5.2 Isobaric Thermal Expansion 25
2.6. References 25

Chapter 3. Molecular Simulations 27

3.1. Statistical Mechanics 28
3.1.1 Phase Space 28
3.1.2 Averaging Methods 28
3.1.3 Ergodic Hypothesis 29
3.1.4 Statistical Ensembles 29
3.2. Molecular Simulations 33
3.2.1 Interaction Potential and Force Evaluation 33
3.2.2 Monte Carlo Simulations 38
3.2.3 Molecular Dynamics Simulations 40
3.3. Thermophysical Properties Estimation from Molecular Simulations 45
3.3.1 Thermodynamic Properties Calculation from MC Simulations 45
3.3.2 Calculation of a Transport Property: the Shear Viscosity 47

3.3.3 Calculation of Properties from Structural Information 48
3.4. References 51

Chapter 4. Experimental Measurements and Simulations of n-C_6 + n-C_{12} Mixtures 55

4.1. Experimental Measurements Details 56
4.2. Molecular Simulations Details 57
4.2.1 Thermodynamic Properties Simulations 57
4.2.2 Shear Viscosity Simulations 57
4.3. Thermodynamic Properties 59
4.3.1 Density and Excess Molar Volume 59
4.3.2 Isothermal Compressibility and Excess Isothermal Compressibility 62
4.3.3 Speed of Sound and Excess Speed of Sound 64
4.4. A Transport Property: the Shear viscosity 66
4.5. Conclusions 69
4.6. References 70

Chapter 5. Experimental Measurements of CO2+nC7 Mixtures 73

5.1. Mixtures Studied 74
5.2. Volumetric Properties 75
5.2.1 Density 75
5.2.2 Excess Volumes 81
5.3. Isothermal Compressibility and Excess Isothermal Compressibility 83
5.4. Acoustic Properties 88
5.4.1 Speed of Sound and Isentropic Compressibility 88
5.4.2 Excess Isentropic Compressibility and Excess Speed of Sound 93
5.5. Conclusions 98
5.6. References 99

Chapter 6. Molecular Simulations of CO_2+nC7 Mixtures 102

6.1. Preliminary Results 103
6.1.1 Prediction of Pure CO_2 Phase Behaviour by MCCG 103
6.1.2 Prediction of CO_2 + n-C_7 Mixtures Phase Behaviour by MCCG 104
6.2. Molecular Simulation Details 107
6.2.1 Thermodynamic Properties 107
6.2.2 Structural Properties 107
6.3. Thermodynamic Properties 108
6.3.1 Density and Derivative Properties 108
6.3.2 Excess Properties 111
6.4. Kirkwood Buff Integrals and Partial Molar Volumes 112
6.5. Microscopic Analysis of CO_2 Clusters 114
6.5.1 Definition of Clusters 115
6.5.2 Static Property of Cluster 119
6.5.3 Dynamic Properties of Cluster 120
6.6. Conclusions 121
6.7. References 122

Chapter 7. Conclusions and Perspectives 124

7.1. Conclusions 125
7.2. Perspectives and Recommendation for Future Works 126

Appendix A . Density, Speed of Sound, Compressibility and Excess Properties of Carbon Dioxide + n-Dodecane. 128

A .1 Chemicals 129
A .2 Speed of Sound and Density 129
A .3 Derivative Properties 137
A .4 Excess Properties 143
A .5 Partial Molar Volume 150
A .6 Conclusion 156
A .7 References 157

Appendix B . Experimental Measurements and Molecular Simulations Data of n-C_6 + n-C_{12} 159

B .1 Experimental Measurement Data 160
B .1 .1 Density Measurement Data 160
B .1 .2 Experimental Isothermal Compressibility Data 163
B .1 .3 Experimental Speed of Sound Data 163
B .1 .4 Experimental Viscosity Data 165
B .2 Molecular Simulation Results 170
B .2 .1 Molecular Simulation Density Results 170
B .2 .2 Isothermal Compressibility 172
B .2 .3 Molecular Simulation Results of Viscosity 174
B .3 References 175

Appendix C . Molecular Simulation Results of the Binary Mixtures of CO_2 + n-C_7. 177

C .1 Thermophysical Properties of MC Simulations of CO2 + n-C7 Mixtures. 178
C .2 Kirkwood Buff Integrals (KBIs) of CO2 + n-C7 Mixtures. 182

List of Figures

Figure 1.1 History of global surface temperature anomaly and anthropogenic CO_2 emissions. Data are provided from NOAA[1] (NASA). 2

Figure 1.2 Schematic representation of Carbon Capture Use and Storage processes 3

Figure 1.3 Illustration of the lack of robustness of different models on a binary mixture composed of carbon dioxide and n-heptane. On the left: comparison of density between experimental measurements and EOS (VT-PR-78 and PC-SAFT). On the right: comparison between experimental isothermal compressibility and results obtained from EOS. 5

Figure 2.1: Schematic representation[1] of a vibrating U-tube filled with he studied fluid (dark blue). 11

Figure 2.2: Percentage relative deviation between our experimental density of toluene and density data taken from Cibulka et al. [5] 13

Figure 2.3: Schematic diagram of the density experimental setup for liquid mixtures. (1) high pressure pump; (2) filling funnel; (3) pressure sensor; (4) Frequency meter; (5) density meter. 14

Figure 2.4: Schematic diagram of the density experimental setup. (1) high pressure discharge pump; (2) pressure sensor; (3) density meter (4) liquid tank; (5) liquid balance; (6) high pressure feeding pump; (7) gas balance; (8) gas tank; (9) tungsten ball inside the feeding pump. 15

Figure 2.5: Schematic diagram of the acoustic probe. (1) reflectors; (2) cylindrical support; (3) piezoelectric transducer; (4) Teflon ring. 16

Figure 2.6: Screen shot of the wave visualized on the oscilloscope used to calculate $\Delta t = \tau 2 - \tau 1$ 17

Figure 2.7: Percentage relative deviation between our experimental speed of sound values of toluene and speed of sound data taken from Meier and Kabelac [11]. 17

Figure 2.8: Schematic diagram of the speed of sound experimental setup for liquid mixtures. (1) high pressure piston pump; (2) filling funnel; (3) Pulser-Receiver; (4) oscilloscope; (5) autoclave; (6) acoustic wave sensor. 18

Figure 2.9: Schematic diagram of the speed of sound measurement setup. (1) High pressure vessel; (2) liquid tank; (3) liquid balance; (4) gas balance; (5) gas tank; (6) pressure sensor; (7) electrical feedthrough; (8) acoustic wave sensor; (9) piston with stirring system. 19

Figure 2.10: Synoptic table representing the operating principle of the high pressure viscosity measurement device. 21

Figure 2.11: Schematic representation of the falling time measurement system. (1): upper coil; (2): falling plug and (3): lower coil. 22

Figure 2.12 Input perturbed density distribution (—) and output isothermal compressibility distribution (•). This figure is taken from[14]. 23

Figure 2.13 Frequency histogram of the isothermal compressibility κT distributions obtained from the computation method retained and from the six equations considered in the procedure. •: Computed distribution obtained by using randomly six different equations; −·−: normal distribution; −♦−: Huddleston, −+−: Murnaghan, −○−⋮ Tait equation (), -△- quadratic tangent, --▲-- quadratic DER, -□- Ndiaye et al. This graph is taken from[14]. 24

Figure 3.1 Schematic representation of the canonical situation. 30

Figure 3.2 Schematic representation of the microcanonical (NVE) situation..... 31

Figure 3.3 Schematic representation of the isothermal-isobaric ensemble situation 32

Figure 3.4 Schematic representation of the grand canonical ensemble situation..... 32

Figure 3.5 Schematic representation of intramolecular interactions. Panel (a) represents stretching interactions , panel (b) represents the bending angle θijk , panel (c) represents the proper dihedral angle φijkl and panel (c) the improper dihedral angle φijkl Figures are taken from[10] 35

Figure 3.6 Schematic representation of a 2D periodic system. The central grey box is the primary box. Atoms can enter and leave each boxes across each of four boundaries. 35

Figure 3.7 Schematic representation of the cutoff and verlet neighbor list spheres around central purple atom..... 36

Figure 3.8 Schematic view of the momentum transfer process proposed by Müller-Plathe[50]. The dashed lines (---) represents the velocity profile created in the simulation box. 48

Figure 3.9 Effect of corrections on the calculation of KBI. Gkr and G0 are truncated KBI with and without weighting function wr. The plots represent GCO2-nC7 in a binary mixture of CO_2 + n-C_7 with 40 mol% of CO_2 at 303.35 K and 10.12 MPa. 50

Figure4.1 Shear viscosities for n-dodecane at T = 293.15 K and P = 100 MPa calculated via the RNEMD method at various shear rate. For comparison, simulation results were fit using a Carreau model[27] 58

Figure 4.2 First (✚) and second (▲) normal stress differences calculated with TraPPE-ua for n-dodecane at T = 293.15 K and P =100 MPa at various shear rate. 58

Figure 4.3 Molecular simulation data of density ρsim as a function of experimental density data ρexp for the mixture n-hexane + n-dodecane. Comparison between □: TraPPE-ua and ○: MCCG. Dashed line represents the reference, i.e. ρsim = ρexp..... 60

Figure 4.4 Density as a function of n-hexane concentration at different temperature and pressure conditions. Comparison between◆ : experimental data; □: TraPPE-ua and ○: MCCG. The error bars are too small to appear on the graphs. 61

Figure 4.5 Relative excess molar volume as a function of concentration of n-hexane at 333.15 K and 0.1 MPa. Comparison between data calculated from ◆: experimental density data; □: TraPPE-ua and ○: MCCG. 61

Figure 4.6 Molecular simulation data of isothermal compressibility κT-sim as a function of experimental data κT-exp for the mixture n-hexane + n-dodecane. Comparison between □: TraPPE-ua and ○: MCCG. 62

Figure 4.7 Isothermal compressibility as a function of n-hexane concentration at different temperature and pressure conditions. Comparison between ◆: experimental data; □: TraPPE-ua and ○: MCCG. 63

Figure 4.8 Relative excess isothermal compressibility as a function of concentration of n-hexane at 333.15 K and 0.1 MPa. Comparison between ◆: experimental data; □: TraPPE-ua and ○: MCCG..... 63

Figure 4.9 Calculated molecular simulation data of sound velocity wsim as a function of experimental data wexp for the mixture n-hexane + n-dodecane. Comparison between □: TraPPE-ua and ○: MCCG 64

Figure 4.10 Speed of sound as a function of n-hexane concentration at different temperature and pressure conditions. Comparison between ◆: experimental data; □: TraPPE-ua and ○: MCCG. 65

Figure 4.11 Relative excess sound velocity as a function of concentration of n-hexane at 333.15 K and 0.1MPa. Comparison between data calculated from ◆: experimental data; □: TraPPE-ua and ○: MCCG. For the sake of clarity, the large error bars are not represented. 66

Figure 4.12 Molecular simulation data of viscosity ηsim as a function of experimental data ηexp for the mixture n-hexane + n-dodecane. Comparison between □: TraPPE-ua and ○: MCCG. 67

Figure 4.13 Viscosity as a function of n-hexane concentration at different temperature and pressure conditions. Comparison between ◆: experimental data; □: TraPPE-ua and ○: MCCG. 68

Figure 4.14 Relative excess viscosity as a function of concentration of n-hexane at 293.15 K and 100 MPa. Comparison between data calculated from ◆: experimental data; □: TraPPE-ua and ○: MCCG . For the sake of clarity, the large error bars are not represented. 69

Figure 5.1 *P*, *T* projection of the carbon dioxide + n-heptane critical locus and experimental temperature and pressure conditions for the speed of sound and density measurements performed in this work. Δ: Kalra et al.[7]; ○: Chester and Haynes[8]; □: Choi an Yeo[9] ; ◆: CO_2 critical point; ◇: n-C_7 critical point; ●: critical conditions of the investigated mixtures estimated from interpolation of literature data; ×:experimental temperature and pressure conditions. 75

Figure 5.2 Deviations of the density data reported in Table 5.2 for CO_2 from correlation of Span and Wagner[11]: ○, 303.15 K; ■, 313.15 K; : expanded uncertainty. 77

Figure 5.3 Deviations of the density data reported in Table 5.2 for n-C_7 from correlation of Lemmon and Span[12]: ○, 303.15 K; ■, 313.15 K; : expanded uncertainty. 77

Figure 5.4 Density ρ as a function of pressure for different isopleths at 313 K. ■: pure n-C_7 ; ◇: 20 % CO_2 ; ▲: 40 % CO_2 ; □: 60 % CO_2 ; ◆: 83 % CO_2 ; ○: 88 % CO_2 ; - - - : pure CO_2. 78

Figure 5.5 Density ρ as a function of concentration for different isobars at 313 K. ●: 10 MPa ; □: 20 MPa ; ▲: 30 MPa ; ◇: 40 MPa ; ■ 50 MPa ; ○: 60 MPa ; ×: 70 MPa. 78

Figure 5.6 Density ρ as a function of concentration at 10 MPa and 303 K (panel a) and 313 K (panel b). Comparison between measurements (■) and ideal behavior (◆).- - - - : ideal solution with apparent density for CO_2 equal to MCO2/vCO2∞. 79

Figure 5.7 Partial molar volume of carbon dioxide and n-heptane as a function of CO_2 mol% at *P* = 10 MPa. ■: n-C_7 at 303 K; □: n-C_7 at 313 K; ●: CO_2 at 303 K; ○: CO_2 at 313 K. . 80

Figure 5.8 Ratio vC7∞/vC7 as a function of pressure. ○: 303 K; ■: 313 K. 81

Figure 5.9 Excess molar volume as a function of concentration for different isobars at 313 K. ●: 10 MPa ; □: 20 MPa ; ▲: 30 MPa ; ◇: 40 MPa ; ■ 50 MPa ; ○: 60 MPa ; ×: 70 MPa.83

Figure 5.10 Comparison between excess molar volume curve at 303 and 313 K. as a function of concentration for different isobars at. ●: 303 K and 10 MPa ; ○: 303 K and 70 MPa ; ■ 313 K and 10 MPa ; □: 313 K and 70 MPa. 83

Figure 5.11 Isothermal compressibility κT as a function of pressure for different isopleths at 313 K. ■: pure n-C_7 ; ◇: 20 % CO_2 ; ▲: 40 % CO_2 ; □: 60 % CO_2 ; ◆: 83 % CO_2 ; ○: 88 % CO_2 ; - - - : pure CO_2. 84

Figure 5.12 Isothermal compressibility κT as a function of volume fraction $\emptyset CO2$ for different isobars at 303 K. ●: 10 MPa ; □: 20 MPa ; ▲: 30 MPa ; ■ 50 MPa ; ×: 70 MPa. 86

Figure 5.13 Comparison between measurements (■) and ideal behavior (○) of the isothermal compressibility as a function of volume fraction $\emptyset CO2$ at 313 K and 10 MPa. - - - - : ideal solution with apparent compressibility $\kappa T, CO2\infty$ for CO_2 87

Figure 5.14 Excess Isothermal compressibility as a function of concentration for different isobars at 303 K. ●: 10 MPa ; □: 20 MPa ; ▲: 30 MPa ; ◇: 40 MPa ; ■ 50 MPa ; ○: 60 MPa ; ×: 70 MPa. 88

Figure 5.15 Speed of sound *w* as a function of pressure for different isopleths at 303 K. ■: pure n-C_7 ; ◇: 20 % CO_2 ; ▲: 40 % CO_2 ; □: 60 % CO_2 ; ◆: 83 % CO_2 ; ○: 88 % CO_2 ; - - - : pure CO_2. 90

Figure 5.16 Speed of sound *w* as a function of concentration for different isobars at 313 K. ●: 10 MPa ; □: 20 MPa ; ▲: 30 MPa ; ◇: 40 MPa ; ■ 50 MPa ; ○: 60 MPa ; ×: 70 MPa. 90

Figure 5.17 Speed of sound *w* as a function of as density for different isopleths at 303 K. ■: pure n-C_7 ; ◇: 20 % CO_2 ; ▲: 40 % CO_2 ; □: 60 % CO_2 ; ◆: 83 % CO_2 ; ○: 88 % CO_2 ; - - - : pure CO_2. 91

Figure 5.18 Comparison between isothermal and isentropic compressibility curves for extreme conditions. ●: κT at 303 K and 70 MPa ; ○: κs at 303 K and 70 MPa ; ■ : κT at 313 K and 10 MPa ; □: κs at 313 K and 10 MPa. 91

Figure 5.19 Comparison between measurements and ideal behavior of the isentropic compressibility as a function of CO_2 mol %. ■ : experimental at 313 K and 10 MPa ; ●: ideal behavior at 313 K and 10 MPa ; × : experimental at 313 K and 70 MPa ; - - - - : ideal behavior at 313 K and 70 MPa. 96

Figure 5.20 Comparison between measurements and ideal behavior of speed of sound as a function of CO_2 mol %. ■ : experimental at 313 K and 10 MPa ; ●: ideal behavior at 313 K and 10 MPa ; × : experimental at 313 K and 70 MPa ; - - - - : ideal behavior at 313 K and 70 MPa. 96

Figure 5.21 Excess isentropic compressibility as a function of concentration for different isobars at 303 K. ●: 10 MPa ; □: 20 MPa ; ▲: 30 MPa ; ◇: 40 MPa ; ■ 50 MPa ; ○: 60 MPa ; ×: 70 MPa. 97

Figure 5.22 Excess speed of sound as a function of concentration for different isobars at 313 K. ●: 10 MPa ; □: 20 MPa ; ▲: 30 MPa ; ◇: 40 MPa ; ■ 50 MPa ; ○: 60 MPa ; ×: 70 MPa. 97

Figure 5.23 Relative excess properties in % as a function of concentration at 313 K and 10 MPa. ■ : vE/v ; ●: κTE/κT ; ○: κSE/κS ; ×: wE/w. 98

Figure 6.1 Phase diagram of CO_2 . Comparison between GEMC simulations with MCCG and experimental data taken from the NIST database. 104

Figure 6.2 Equilibrium phase compositions for the CO_2+n-C_7 binary systems at different temperatures. Panel (a): 310.65 K, panel (b): 352.6 K and panel (c): 394.26 K. Comparison between experimental data provided by Kalra et al.[11]and GEMC simulation with and without kij..... 105

Figure 6.3 Henry's law constant calculated by molecular simulation as a function of experimental values taken from Kalra et al.[11] for carbon dioxide + n-heptane mixture. Comparison are made between simulation results with and without binary coefficient correction..... 106

Figure 6.4 Effect of the cut off radius rC value on the accuracy of simulation results of density near the CO_2 critical point for pure CO2 at 313.15 K and 10.11 MPa. The computed density decreases by increasing rC until it reaches a plateau around $rC = 7\sigma$ 108

Figure 6.5 Density ρ as a function of CO2 molar concentration at 313.25 K and 10.11 MPa. Comparison between ◆ **:** experimental measurement and ○: molecular MC simulation. 109

Figure 6.6 Isothermal compressibility kT as a function of CO2 volume concentration at 313.25 K and 10.11 MPa. Comparison between ◆ **:** experimental measurement and ○: molecular MC simulation. 110

Figure 6.7 Isentropic compressibility ks as a function of CO2 volume concentration at 313.25 K and 10.11 MPa. Comparison between ◆ : experimental measurement and ○: molecular MC simulation. 110

Figure 6.8 Speed of sound w as a function of CO2 molar concentration at 313.25 K and 10.11 MPa. Comparison between ◆ : experimental measurement and ○: molecular MC simulation. 111

Figure 6.9 Excess properties as a function of CO2 molar concentration at 313.25 K and 10 MPa. Comparison between ◆ : experimental measurement and ○: molecular MC simulation. For κSE and wE, wide expanded error bars have not been plotted for the sake of clarity of corresponding curves. 112

Figure 6.10 Comparison of molecular simulations results of isothermal compressibility of CO2 + n-C_7 mixtures at 313.25 K and 10.11 MPa. ○: molecular MC simulation and ▽: from KBIs. 113

Figure 6.11 Partial molar volume of CO_2 (blue) and n-heptane (red) as a function of CO2 molar fraction at 313.25 K and 10.11 MPa. Comparison between **- - -** : fit of experimental measurements and ○: calculation from KBIs. 114

Figure 6.12 A scheme to determine molecules belonging to the cluster. (Green color) Large circle corresponds to the solute molecule, i.e. central molecule. (Dark color) Small circles are the solvent molecules. The 1st to 10th solvent molecules are directly connected to the center molecule, so they are accounted for as belonging to the cluster. The 11th to 16th solvent molecules are indirectly connected to the center molecule, but only the 11th solvent molecule is considered to be in the cluster due to the added criterion of a limited region defined by RMax. 115

Figure 6.13 The radial distribution functions (RDF) of infinite dilute mixture of CO_2 + n-C_7 at T = 313.25 K and P = 10.11 MPa..... 116

Figure 6.14 Effect of RMax on the normalized autocorrelation functions of excess number of molecules in the cluster $CNt = CtCt = 0$. Panel (a): The cluster-type I in CO_2 + n-C_7. Panel (b): The cluster-type II in CO_2 + CO_2. 117

Figure 6.15 Time dependence of NRemaintNRemaint = 0 for various values of RMax for the cluster-type I, i.e. CO_2 + n-C_7. 118

Figure 6.16 Dependence of residence time on RMax for the cluster-types I and II, i.e. n-C_7+CO_2 and CO_2+CO_2 respectively. 118

Figure 6.17 A comparison between probability density (ρP) distributions of number of molecules Ncluster of the cluster-types I and II 119

Figure 6.18 A comparison between probability density (ρP) distributions of relative number of cluster NR of the cluster-types I and II. 120

Figure 6.19 Panel (a) : A comparison between the normalized autocorrelation functions of excess number of molecules in the clusters CNt = CtCt = 0 of cluster-types I and II. Panel (b): A comparison between normalizations of NRemaint, i.e. NRemaintNRemaint = 0, of cluster-types I and II. 120

Figure 6.20 Number of CO_2 molecules in cluster of type I as a function of time. 121

Figure.Appendix A.1 Deviation 100ρlit-ρ/ρ of the interpolated literature density value ρlit from density data reported in Table A.3 as function of a function of mole fraction xco2 at temperature *T* = 313.15 K and pressure *P* = 10 MPa. ✖, Zhang et al.[7]; ●, Zambrano et al. [8]. 133

Figure.Appendix A.2 Speed of sound *w* in the binary system carbon dioxide + n-dodecane as a function of mole fraction xco2 at temperature *T* = 303.15 K and at various pressures *p*: ●, 10 MPa;. □, 20 MPa; ▲, 30 MPa; ◇, 40 MPa; ■, 50 MPa; O, 60 MPa; ✖, 70 MPa. 133

Figure.Appendix A.3 Density ρ in the binary system carbon dioxide + n-dodecane as a function of mole fraction xco2 at temperature *T* = 303.15 K and at various pressures *p*: ●, 10 MPa;. □, 20 MPa; ▲, 30 MPa; ◇, 40 MPa; ■, 50 MPa; O, 60 MPa; ✖, 70 MPa 134

Figure.Appendix A.4 Speed of sound *w* in the binary system carbon dioxide + n-dodecane as a function of Density ρ at temperature *T* = 303.15 K and at various pressures *p*: ●, 10 MPa;. □, 20 MPa; ▲, 30 MPa; ◇, 40 MPa; ■, 50 MPa; O, 60 MPa; ✖, 70 MPa; - - - -, Pure CO_2; _____, Pure n-dodecane. 135

Figure.Appendix A.5 Comparison between ideal and real Density ρ in the binary system carbon dioxide + n-dodecane as a function of mole fraction xco2 at temperature *T* = 313.15 K and pressure *P* = 10 MPa. ■, measurements; ◆, ideal behavior; .- - - - : ideal solution with an apparent density for CO_2 equal to MCO2/vCO2∞. 136

Figure.Appendix A.6 Density ρ in the binary system carbon dioxide + n-dodecane as a function of pressure *p* at temperature *T* = 313.15 K and for various CO_2 contents: ■, 0%; ◇, 20%; ▲, 40%; □, 60%; ◆, 75 %; O, 85%; ●, 93%; ; △: 98 %; - - - , 100%. 136

Figure.Appendix A.7 Isothermal compressibility κT in the binary system carbon dioxide + n-dodecane as a function of volume fraction ØCO2 for different isobars at temperature *T* = 303.15 K. ●, 10 MPa ; □, 20 MPa ; ▲, 30 MPa ; ◇, 40 MPa ; ■, 50 MPa ; O, 60 MPa ; ✕, 70 MPa. 139

Figure.Appendix A.8 Comparison between ideal and real isothermal compressibility κT in the binary system carbon dioxide + n-dodecane as a function of volume fraction ØCO2 at pressure *P* = 10 MPa for different temperatures. ■, measurement at *T* = 303.15 K, ● ideal behavior at

T = 303.15 K; □, measurement at *T* = 313.15 K, ○ ideal behavior at *T* = 313.15 K; - - - - , ideal solution with apparent compressibility κT, CO2∞ for CO_2..... 140

Figure.Appendix A.9 Comparison between ideal and real isentropic compressibility κS as a function of mole fraction xco2 at temperature *T* = 303.15 K and pressure *P* = 70 MPa. ■, measurement , ● ideal behavior..... 141

Figure.Appendix A.10 Comparison between ideal and real isentropic compressibility κS as a function of mole fraction xco2 at temperature *T* = 313.15 K and pressure *P* = 10 MPa. □, measurement ; ○, ideal behavior. 143

Figure.Appendix A.11 Excess volume VmE as a function of mole fraction xco2 at pressure *P* = 10 MPa and at different temperatures. ●, 303.15 K; ○, 313 144

Figure.Appendix A.12 Excess isothermal compressibility κTE as a function of mole fraction xco2 at pressure *P* = 10 MPa and at different temperatures *T*. ●, 303.15 K; ○, 313.15 K... 146

Figure.Appendix A.13 Excess isentropic compressibility κSE as a function of mole fraction xco2 at pressure *P* = 10 MPa and at different temperatures *T*. ●, 303.15 K; ○, 313.15 K... 146

Figure.Appendix A.14 Excess speed of sound wE as a function of mole fraction xco2 at pressure *P* = 10 MPa and at different temperatures *T*. ●, 303.15 K; ○, 313.15 K..... 147

Figure.Appendix A.15 Excess volume VmE as a function of mole fraction xco2 at temperature *T* = 303.15 K and at various pressures *p*. □, 20 MPa ; ▲, 30 MPa ; ◇, 40 MPa ; ■, 50 MPa ; ○, 60 MPa ; ×, 70 MPa..... 147

Figure.Appendix A.16 Excess isothermal compressibility κTE as a function of mole fraction xco2 at temperature *T* = 303.15 K and at various pressures *p*. □, 20 MPa ; ▲, 30 MPa ; ◇, 40 MPa ; ■ 50 MPa ; ○, 60 MPa ; ×, 70 MPa..... 148

Figure.Appendix A.17 Excess isentropic compressibility κSE as a function of mole fraction xco2 at temperature *T* = 303.15 K and at various pressures *p*. □, 20 MPa ; ▲, 30 MPa ; ◇, 40 MPa ; ■ 50 MPa ; ○, 60 MPa ; ×, 70 MPa..... 148

Figure.Appendix A.18 Excess speed of sound wE as a function of mole fraction xco2 at temperature *T* = 303.15 K and at various pressures *p*. □, 20 MPa ; ▲, 30 MPa ; ◇, 40 MPa ; ■ 50 MPa ; ○, 60 MPa ; ×, 70 MPa 148

Figure.Appendix A.19 Relative excess properties in the binary system carbon dioxide + n-dodecane as a function of mole fraction xco2 at temperature *T* = 313.15 K and pressure *p*. ▲, 30 100 VmE/Vm ; ■ 50 100 wE/w; ×, 100 κTE/κT. ; ○, 100 κSE/κS..... 149

Figure.Appendix A.20 Partial molar volume of carbon dioxide VCO2 in the binary system Carbon Dioxide + n-Dodecane as a function of mole fraction xCO2 for different isobars at temperature *T* = 303.15 K. ●, 10 MPa ; □, 20 MPa ; ▲, 30 MPa ; ◇, 40 MPa ; ■, 50 MPa ; ○, 60 MPa ; ×, 70 MPa..... 151

Figure.Appendix A.21 Partial molar volume of n-dodecane VC12 in the binary system carbon dioxide + n-dodecane as a function of mole fraction xCO2 for different isobars at temperature *T* = 303.15 K. ●, 10 MPa ; □, 20 MPa ; ▲, 30 MPa ; ◇, 40 MPa ; ■, 50 MPa ; ○, 60 MPa ; ×, 70 MPa..... 152

Figure.Appendix A.22 Partial molar volume of n-dodecane VC12 in the binary system carbon dioxide + n-dodecane as a function of mole fraction xCO2 at pressure *P* = 10 MPa for different temperatures *T*. ●, 303.15 K ; □, 313.15 K. 153

Figure.Appendix A.23 Molar volume Vm, partial molar volumes of carbon dioxide VCO2 and n-dodecane VC12 in the binary system carbon dioxide + n-dodecane as a function of mole fraction xCO2 at temperature *T* = 313.15 K and pressure *P* = 10 MPa. ●, Vm ; □, VCO2; ○, VC12. 153

Figure.Appendix A.24 Cross-plot of partial molar volumes of n-dodecane at infinite dilution in carbon dioxide VC12∞ in the binary system carbon dioxide + n-dodecane and isothermal compressibility of pure carbon dioxide κT, CO2*as a function of pressure *p*. ●, VC12∞ ; ■, κT, CO2*. 154

Figure.Appendix A.25 Comparison between CO_2 + n-C_7 [1] and CO_2 + n-C_{12} excess properties. △, VmE of CO_2 + n-C_7; ▲, VmE of CO_2 + n-C_{12} ; ○, wE of CO_2 + n-C_7 ; ●, wE of CO_2 + n-C_{12} 155

Figure.Appendix A.26 Molar volume Vm in the binary system carbon dioxide + n-dodecane as a function of mole fraction xCO2 at temperature *T* = 313.15 K and different pressures *p*. ○, 10 MPa; ●, 20 MPa ; - - - -, slope calculated from data of Spicka et al. [33] at 10 MPa ; ————, slope calculated from data of Spicka et al. [33] at 20 MPa ; 155

Figure.Appendix A.27 Partial molar volumes of n-dodecane VC12 in the binary system carbon dioxide + n-dodecane as a function of fluid isothermal compressibilityκT for various condition of temperature T and pressure p. ●, T = 303.15 K and P = 10 MPa ; ○, T = 313.15 K and P = 10 MPa ; ■, T = 303.15 K and P = 20 MPa ; □, T = 313.15 K and P = 20 MPa ; ×, T = 303.15 K and p = 30 MPa ; △, T = 313.15 K and P = 30 MPa ;————, master curve. 156

Figure.Appendix B.1 Deviations of our experimental density data of n-hexane with those from ○: Cibulka et al. [2]; △: Assael et al.[3] and data from ×:REFPROP [4] 160

Figure.Appendix B.2 Deviations of our density data of n-dodecane with data from **○:** Cibulka et al.[2], **△:** Assael et al.[3]; **□:** Caudwell et al. [5]; **◇:** Bazile et al. [6] and **×:** REFPROP [4]..... 161

Figure.Appendix B.3 Deviations of our experimental speed of sound data of n-hexane with literature data of **×:** Kasanshin et Shchemelev [10]; ▽: Boelhouwer [7]; △: Kagramanyan and Badalyan [12] ; ▼: Kiriakov and Panin [13]; **◇:** Takagi et al. [14]; □: Ball and Trusler [9]; ○: Daridon et al. [8]..... 164

Figure.Appendix B.4 Deviations of our experimental speed of sound data of n-dodecane with literature data of **× :** Kasanshin and Shchemelev [10]; **▽:** Boelhouwer [7]; ✚: Dzida and Cempa. [15] ; - : Bazile et al. [6]; and ◆ : Plantier et al. [11]..... 164

Figure.Appendix B.5 Deviations between n-hexane viscosity correlation of this work and literature data of ○: Assael et al.[17]; **□:** Oliveira and Wakeham [18]; **▽:** Dymond and Awan [19]; **×:** Michailidou et al.[27] and **◇ :** Kiran and Sen [20]..... 166

Figure.Appendix B.6 Deviations between n-dodecane viscosity correlation of this work and literature data from △: Ducoulombier et al. [16] ;**▽:** Dymond and Awan [19] ; ⬣ : Tanaka et al. [21] ; ✚ : Knapstad et al. [22] ; and ◆ : Caudwell et al.[5]..... 167

List of Tables

Table 1.1 Important thermophysical properties for CCUS 3

Table 2.1 : List of the six equation of states used to calculate the isothermal compressibility 24

Table 3.1 Summary of statistical classical ensembles with thermodynamic functions and the corresponding thermodynamic identities 33

Table 3.2 Mie Chain Coarse Grained (MCCG) parameters of n-hexane, n-heptane, n-dodecane and carbon dioxide. 37

Table 5.1 Composition in mol % of the different carbon dioxide + n-heptane binary mixtures investigated 75

Table 5.2 Density ρ and its expended uncertainty Uρ in carbon dioxide + n-heptane binary mixtures as a function of temperature *T*, pressure *P* and composition xco2 76

Table 5.3 Excess molar volume vE and its expended uncertainty UvE in carbon dioxide + n-heptane binary mixtures as a function composition xco2 for different temperatures *T* and pressures *p*. 82

Table 5.4 Isothermal compressibility κT and its expended uncertainty UκT in carbon dioxide + n-heptane binary mixtures as a function of temperature *T*, pressure *P* and composition xco2. 85

Table 5.5 Excess isothermal compressibility κTE and its expended uncertainty UκTE in carbon dioxide + n-heptane binary mixtures as a function composition xco2 for different temperatures *T* and pressures *P*. 87

Table 5.6 Speed of sound *w* and its expended uncertainty Uw in liquid CO_2+ n-heptane binary mixtures as a function of temperature *T*, pressure *P* and composition xco2. 89

Table 5.7 Isentropic compressibility κS and its expended uncertainty UκS in carbon dioxide + n-heptane binary mixtures as a function of temperature *T*, pressure *P* and composition xco2. 92

Table 5.8 Isobaric expansion αP and its expended uncertainty UαP in pure carbon dioxide and pure n-heptane as a function of pressure at *p* at 303.35 K and 313.25 K 94

Table 5.9 Excess isentropic compressibility κSE and its expended uncertainty UκSE in carbon dioxide + n-heptane binary mixtures as a function composition xco2 for different temperatures *T* and pressures *P*. 95

Table 5.10 Excess speed of sound wE and its expended uncertainty UwE in carbon dioxide + n-heptane binary mixtures as a function of temperature *T*, pressure *P* and composition xco2. 95

Table.Appendix A.1 Sample Description 130

Table.Appendix A.2 Mole fraction xco2 and its expanded uncertainty Uxco2 (level of confidence = 0.95, k = 2) of the different sample mixtures investigated of the binary system (Carbon Dioxide + n-dodecane). 130

Table.Appendix A.3 Values of speed of sound w and its expanded uncertainty *U(w)* (level of confidence = 0.95, k = 2) at Temperatures T, and Pressures p, and Mole Fraction x_co2 for (Carbon Dioxide + n-Dodecane) 131

Table.Appendix A.4 Values of density ρ and its expanded uncertainty Uρ (level of confidence = 0.95, k = 2) at Temperatures T, and Pressures p, and Mole Fraction xco2 for (Carbon Dioxide + n-Dodecane)[a] 132

Table.Appendix A.5 Values of density ρ and its expanded uncertainty Uρ (level of confidence = 0.95, *k* = 2) at Temperatures *T*, and Pressures *P*, and Mole Fraction xco2 for the high CO_2 content mixtures of the binary (Carbon Dioxide + n-Dodecane)[a] 134

Table.Appendix A.6 Values of isothermal compressibility κT and its expanded uncertainty UκT (level of confidence = 0.95, *k* = 2) at Temperatures *T*, and Pressures *p*, and Mole Fraction xco2 for (Carbon Dioxide + n-Dodecane) 137

Table.Appendix A.7 Values of isothermal compressibility κT and its expanded uncertainty UκT (level of confidence = 0.95, *k* = 2) at Temperatures *T*, and Pressures *p*, and Mole Fraction xco2 for the high CO_2 content mixtures of the binary (Carbon Dioxide + n-Dodecane) 138

Table.Appendix A.8 Values of isentropic compressibility κS and its expanded uncertainty UκS (level of confidence = 0.95, *k* = 2) at Temperatures *T*, and Pressures *p*, and Mole Fraction xco2 for (Carbon Dioxide + n-Dodecane)[a] 142

Table.Appendix A.9 Values of isobaric expansion αP* and its expanded uncertainty UαP* (level of confidence = 0.95, *k* = 2) at Temperatures *T*, and Pressures *p*, for pure Carbon Dioxide and n-Dodecane. 143

Table.Appendix A.10 Excess molar volume VmE, excess isothermal compressibility κTE, excess isentropic compressibility κSE, excess speed of sound wE and their expanded uncertainty (level of confidence = 0.95, *k* = 2) at Temperatures *T*, and Pressures *p*, and Mole Fraction xco2 for (Carbon Dioxide + n-Dodecane) 145

Table.Appendix A.11 Excess molar volume VmE, excess isothermal compressibility κTE and their expanded uncertainty (level of confidence = 0.95, *k* = 2) at Temperatures *T*, and Pressures *p* for the high CO_2 content mixtures of the binary (Carbon Dioxide + n-Dodecane) 149

Table.Appendix A.12 Coefficients of 2/3 Padé Approximant (Eq. A.12) for Correlating Molar Volume Vm as a Function of Mole Fraction xco2 at Fixed temperature *T* and Pressure *p*. .. 150

Table.Appendix B.1 Experimental density data for the binary mixtures n-hexane + n-dodecane 162

Table.Appendix B.2 Experimental isothermal compressibility of the binary mixtures n-hexane + n-dodecane 163

Table.Appendix B.3 Experimental sound velocity data of the binary mixtures of n-hexane+n-dodecane 165

Table.Appendix B.4 Parameters of Eq. B.1, B.2 and B.4 from 293.15 to 353.15 K and from pressure range 0.1 MPa-100 MPa and relative deviations (Bias%), absolute average deviation (AAD%) and maximum deviation (Max AD%) from experimental values 168

Table.Appendix B.5 . Experimental viscosity data of n-hexane + n-dodecane binary mixture 169

Table.Appendix B.6 . Molecular Simulation isothermal compressibility and standard deviation data with TraPPE-ua for the binary mixtures n-hexane + n-dodecane 170

Table.Appendix B.7 Molecular Simulation isothermal compressibility and standard deviation data with MCCG for the binary mixtures n-hexane + n-dodecane 171

Table.Appendix B.8 Molecular Simulation isothermal compressibility and standard deviation data with TraPPE-ua for the binary mixtures n-hexane + n-dodecane 172

Table.Appendix B.9 Molecular Simulation isothermal compressibility and standard deviation data with MCCG for the binary mixtures n-hexane + n-dodecane. 173

Table.Appendix B.10 Molecular Simulation viscosity and standard deviation data with TraPPE-ua for the binary mixtures n-hexane + n-dodecane 174

Table.Appendix B.11 Molecular Simulation viscosity and standard deviation data with MCCG for the binary mixtures n-hexane + n-dodecane 174

Table.Appendix C.1 Density data of CO_2 + n-C_7 obtained from MC simulations 178

Table.Appendix C.2 Isothermal compressibility data of CO_2 + n-C_7 obtained from MC simulations 179

Table.Appendix C.3 Isentropic compressibility data of CO_2 + n-C_7 obtained from MC simulations 180

Table.Appendix C.4 Speed of sound data of CO_2 + n-C_7 calculated from MC simulations 181

Table.Appendix C.5 KBIs between CO_2 molecules 182

Table.Appendix C.6 KBIs between CO_2 and n-C_7 molecules 183

Table.Appendix C.7 KBIs between n-C_7 molecules 184

Chapter 1. Introduction

Contents

1.1. General Context of the Work 2
1.2. Importance of Thermophysical Characterization 3
1.3. Estimation of Thermophysical Properties of CO_2-mixtures 4
1.4. Motivation and Local Context of the Thesis 5
1.4.1 Problem Statement and Objectives of the Thesis 5
1.4.2 Local Context of the Work 6
1.5. Organization of the Manuscript 7
1.6. References 7

1.1. General Context of the Work

Since the first industrial revolution (1850), there has been an increase (around +0.83°C) [1] of the average global temperature. This global warming, even though apparently low, is known to be the cause of extreme weather events[2]. Today, it is widely accepted that anthropogenic CO_2, that is CO_2 arising from human activity, is one of the main greenhouse gases at the origin of this temperature increase[3]. These CO_2 emissions, mainly coming from the combustion of fossil fuels and cement production, have increased on average by around 4% in the last decade, reaching 38 Gt in 2017[1] as shown in Figure 1.1. This increase has led a majority of countries worldwide to sign agreements such as the Kyoto Protocol[4] or most recently the Paris Agreement (COP 21)[5] to mitigate global warming by limiting and even reducing carbon emissions. To achieve this goal, development of solutions preventing the CO_2 emissions from entering the atmosphere are in full swing.

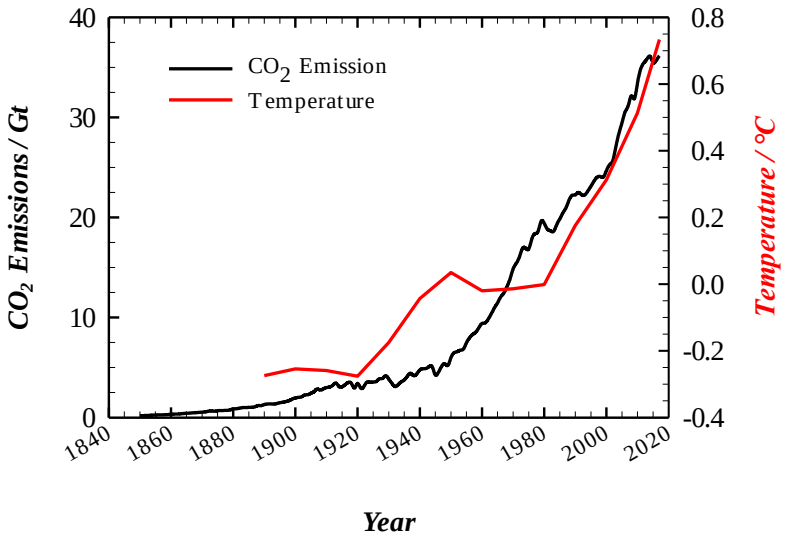

Figure 1.1 History of global surface temperature anomaly and anthropogenic CO_2 emissions. Data are provided from NOAA[1] (NASA).

Among these solutions, carbon capture, use and storage (CCUS) is one of the most advanced one[6]. It is an integrated suite of technologies consisting in capturing CO_2 produced by industrial processes, then transporting it by pipeline, ships and road tanker for its safe use and/or storage (sequestration), see Figure 1.2. To create a revenue stream for CCUS projects, the main utilization of the captured CO_2 is for Enhancing Oil Recovery (CO_2-EOR)[7] from mature oilfields. Indeed, by injecting CO_2 in depleted geological oil & gas reservoirs, it allows the increase of the oil production. However, the implementation of CCUS processes in general and particularly CO_2-EOR turns out to be technically challenging. One of the difficulties encountered remains in the thermophysical characterization of the fluids involved, given their complexity and the thermodynamic conditions corresponding to reservoir conditions.

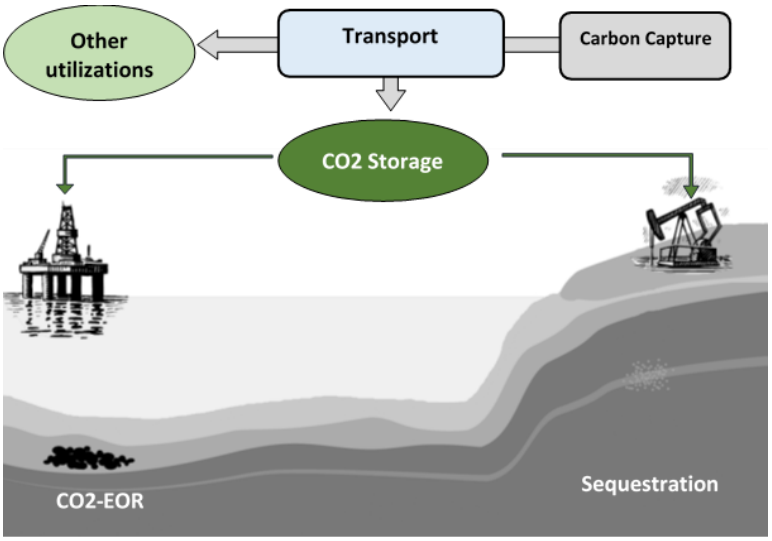

Figure 1.2 Schematic representation of Carbon Capture Use and Storage processes

1.2. Importance of Thermophysical Characterization

The development of CCUS technologies in a safe, efficient and economically viable way, requires precise knowledge of thermophysical properties of the fluids involved in these processes[8,9]. These thermophysical properties are generally classified in two families: thermodynamic properties (coming from system at equilibrium) and transport ones (coming from fluids away from equilibrium). Table 1.1 presents the main properties required in the implementation of CCUS processes.

Table 1.1 Important thermophysical properties for CCUS

Properties	
Thermodynamic	Phase Change
	Density
	Heat capacity
	Enthalpy and entropy
	Speed of sound
	Surface tension
Transport	Viscosity
	Thermal conductivity
	Diffusion coefficient

For example, the selection of materials and process components such as compressors, heat exchangers, storage tanks, and transport pipelines rely on accurate data of thermophysical properties, such as phase-change behavior, density, viscosity, and heat conductivity[9]. Another important property is the speed of sound which plays a key role to resolve depressurization

waves propagation occurring in pipelines and is also used in reservoir seismic monitoring during the sequestration or oil production enhancement.

1.3. Estimation of Thermophysical Properties of CO_2-mixtures

As discussed in the previous section, thermophysical properties are of paramount importance. The estimation of such properties is mainly achieved via experimental measurements or empirical/theoretical models. For decades, several high precision experimental measurements have been carried out on pure CO_2 as well as its mixtures. Consequently, several data are available in the literature for mixtures[10,11] such as CO_2-gas (CO_2/CH_4, CO_2/H_2S, $CO_2/CH_4/N_2$) but also CO_2-water/brine for which phase equilibria, volumetric properties and viscosities are provided for many conditions . However, the literature is less rich when dealing with CO_2-oil systems, in particular regarding viscosities [12]. This may be explained by the fact that such "gas-liquid" mixtures are difficult to study experimentally especially in reservoir conditions which are often supercritical from the CO_2 point of view.

Thus, despite the rapid growth of database of CO_2-oil thermophysical properties, the reported data still do not cover all CO_2-EOR operating windows, neither all systems that may be involved. To fill the gaps of experimental measurements, various models are used for predicting thermophysical properties of such "gas-liquid" mixtures. One of the main difficulties in modeling such mixtures, compared to CO_2-gas systems, lies in the fact that CO_2-oil mixtures are usually asymmetric, i.e. the mixtures are composed of species of very different sizes and/or energies and/or masses.

Thermodynamic properties are usually computed by using equations of states (EOS). Such thermodynamic models are applicable over a wide range of temperature and pressure. For ideal or weakly non-ideal mixtures, the thermodynamic properties of vapor and liquid phases are usually predicted with a minimal amount of data. However, the extension of EOS to more asymmetric mixtures generally requires the use of complex mixing rules[13] combined to binary interaction parameters, thus making these models lose their fully predictive character. EOS can be grouped in families, among which cubic equations[13–15], virial equations[16]and SAFT-like equations[17–19] are the most widely employed. The performance of these equations often depends on the calculated thermodynamic property and/or thermodynamic conditions. For example, cubic equations are known to provide good vapor phase and phase equilibrium results, however they are less accurate for the prediction of liquid phase volumetric properties and requires volume corrections[20,21]. For SAFT-like EOS, they provide good prediction of both monophasic and phase equilibrium properties, however lead to poor predictions in region around the critical point[22]. It is worth noting that, in additions to "general EOS" discussed above, there are specialized ones such as Span and Wagner[23] equation for pure CO_2. However, such specialized equations generally apply only to specific systems and conditions.

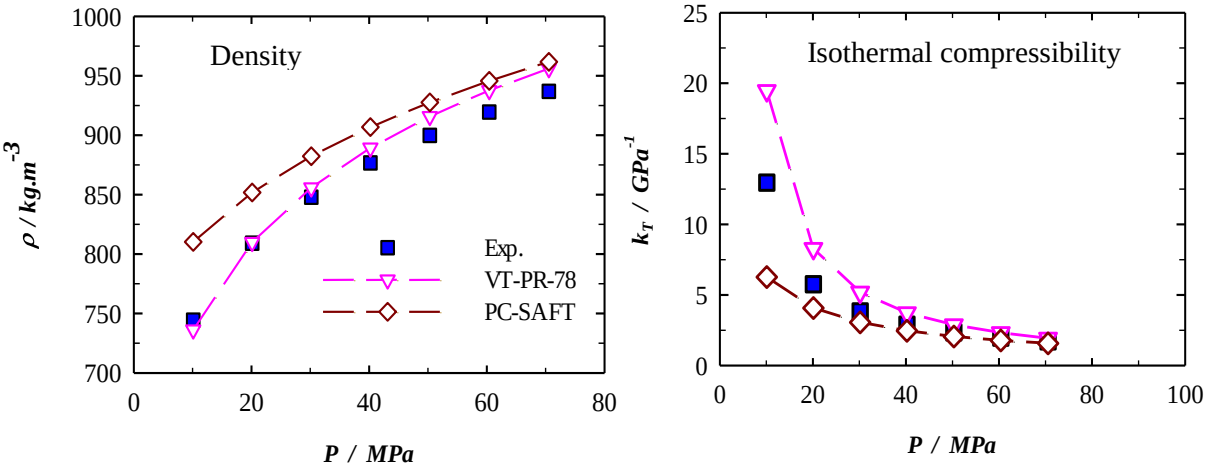

Figure 1.3 Illustration of the lack of robustness of different models on a binary mixture composed of carbon dioxide and n-heptane. On the left: comparison of density between experimental measurements and EOS (VT-PR-78 and PC-SAFT). On the right: comparison between experimental isothermal compressibility and results obtained from EOS.

As for thermodynamic properties, several models have been proposed for the prediction of transport properties. Considering viscosity, the most widely used model in petroleum engineering is the Lohrenz-Bray-Clark (LBC)[24] correlation, due to its simplicity, flexibility and consistency. This model, based on the concept of residual viscosity, consists of a fourth-degree polynomial function of reduced density. It provides acceptable results, provided accurate density values are available, but often require an adjustment of critical volumes. Otherwise, viscosity can also be obtained from predictive models[25] as that based on corresponding states theory, free volume theory, friction theory, thermodynamic scaling, entropy scaling.

With the great advance in computational capacities, numerical methods such as Quantitative Structure-Property Relationship (QSPR) or Molecular Simulations (MS) turns out to be some promising complementary tools to deal with the thermophysical properties prediction of fluid systems. The QSPR method consists of creating predictive model of a given property based on molecular descriptors[26,27]. The models are achieved by the mean of numerical methods such as Artificial Neural Network. Concerning molecular simulation, it consists in determining macroscopic properties from microscopic simulations of fluids at the atomic scale [28]. However, there are not a lot of studies that elucidate whether such computational techniques are applicable in a predictive way to deal with very asymmetric mixtures such as CO_2-oil systems[27,29,30] .

1.4. Motivation and Local Context of the Thesis

1.4.1 Problem Statement and Objectives of the Thesis

In the previous section it has been enlightened that, despite the experimental studies performed in the literature, there are still relatively few reliable data on the thermophysical properties of asymmetric mixtures such as those involved in the CO_2-EOR processes, and their modeling using classical approaches remains problematic precisely due to the asymmetry between molecules and operating conditions achieved. Consequently, experimental measurements of these properties remain the most reliable method to provide accurate data. However,

measurements of such systems are still difficult to achieve routinely under an extended pressure and temperature range as found under reservoir conditions.

Therefore, the objective of our work is to combine experimental measurements and molecular simulations, on model asymmetric systems related to georesources problematic, in order to provide reliable data and, ultimately, to understand and improve the modeling of these systems. With this aim in mind, activities realized during this thesis can be broadly grouped under the following headings:

- Setting up of experimental measurements of thermophysical properties such as density, isothermal compressibility, isobaric thermal expansion, heat capacity, speed of sound and viscosity of asymmetric binary mixtures under reservoir conditions. The purpose is to provide consistent and well controlled set of data for the comparison with simulations as well as enriching existing databases.
- Implementation of molecular simulations consisting of Monte Carlo (MC) and Molecular Dynamics (MD), of the systems studied experimentally. In this work, we mainly used the Mie Chain Coarse Grained (MCCG), a simple coarse grained force field. This force field was chosen since it seems to be a good compromise between simplicity and accuracy[31] and there exists an equation of state which is able to provide its thermodynamic properties [19]. The purpose is both to evaluate the capabilities of such approaches to deal with equilibrium and transport properties and to shed light on microscopic phenomena which are not accessible experimentally.

In the body of the manuscript, are presented in details the results of the study of two models mixtures. The first model is a simple asymmetric mixture composed of n-hexane and n-dodecane for which density, speed of sound and viscosity measurements and molecular simulations have been performed. The second mixture studied is a more asymmetric one composed of carbon dioxide and n-heptane. For this system density and speed of sound measurements have been performed, however due technical difficulties and unsuitability of our current device, viscosity measurement on such “liquid + gas” system has not been achieved. In addition, experimental results on a third system composed of carbon dioxide and n-dodecane are provided in appendix A.

1.4.2 Local Context of the Work

This thesis was carried out within the “Thermophysical Properties” team of the Laboratory of Complex Fluids and their Reservoirs (LFCR UMR 5150), a joint research unit attached to the University of Pau and Pays de l'Adour (UPPA), the French National Center of Scientific Research (CNRS) and Total S.A. The Thermophysical Properties team was born from the merger in 2016 between two teams: “High Pressure” and “Transport Properties”. The former was specialized in experimental measurements and modelling of thermodynamic properties whereas the latter was specialized in measurement and numerical simulation of transport properties. Therefore, this thesis, started in 2016 and combining experimental measurements and molecular simulations techniques on both thermodynamic and transport properties, is in the continuity of the merger of these two teams.

1.5. Organization of the Manuscript

The manuscript plan is as follows:

- Chapter 2 is dedicated to the description of experimental devices as well as measurement protocols for density, sound velocity and viscosity. In addition, it includes calculation methodologies of derivative properties such as isothermal compressibility and isobaric thermal expansion.
- Chapter 3 deals with the description of molecular simulations techniques used during the thesis. The first part is dedicated to a brief introduction to statistical physics. Then, the force fields used for the molecular modeling are detailed. Finally, we present in the last part, the methodologies used for the calculations of thermophysical properties.
- Chapter 4 presents the results of a study combining experimental measurements and molecular simulations on a simple, weakly asymmetric mixture composed of n-hexane and n-dodecane. Through this chapter, MCCG is compared to a finer grain model named TraPPE-ua and their performance to predict both thermodynamic and transport properties are evaluated.
- Chapter 5 is devoted to experimental investigations of a more asymmetric mixture composed of carbon dioxide and n-heptane. It provides accurate volumetric and acoustic properties. In addition, more information is provided about the fluid microscopic behavior by analyzing partial molar volumes of mixtures components.
- Chapter 6 deals with molecular simulations on the binary mixture composed of carbon dioxide and n-heptane, in the same conditions as experimentally investigated in Chapter 5. First, prediction of volumetric and acoustic properties with molecular simulations are evaluated, then investigations on microscopic structure of the mixture are performed.
- Chapter 7 summarizes the findings of this thesis, give some conclusions and perspectives.
- Appendix A presents additional experimental investigations performed on a third binary mixture composed of carbon dioxide and n-dodecane.
- Appendix B presents experimental and simulation data of thermophysical properties of the binary mixture composed of n-hexane + n-dodecane, discussed in chapter 4
- Appendix C is devoted to data tables of simulation results on the binary mixture composed of carbon dioxide and n-heptane, investigated in chapter 6.

1.6. References

(1) National Centers for Environmental Information, Climate at a glance: Global Time Series https://www.ncdc.noaa.gov/cag/global/time-series/globe/land_ocean/12/12/1880-2019

(2) Rosenzweig, C.; Iglesias, A.; Yang, X. B.; Epstein, P. R.; Chivian, E. Climate Change and Extreme Weather Events; Implications for Food Production, Plant Diseases, and Pests. Glob. Change Hum. Health 2001, 2 (2), 90–104.

(3) NASA GISS: Science Briefs: Greenhouse Gases: Refining the Role of Carbon Dioxide https://www.giss.nasa.gov/research/briefs/ma_01/

(4) KYOTO PROTOCOL https://unfccc.int/resource/docs/convkp/kpeng.html

(5) The Paris Agreement | UNFCCC https://unfccc.int/process-and-meetings/the-paris-agreement/the-paris-agreement

(6) Boot-Handford, M. E.; Abanades, J. C.; Anthony, E. J.; Blunt, M. J.; Brandani, S.; Dowell, N. M.; Fernández, J. R.; Ferrari, M.-C.; Gross, R.; Hallett, J. P.; et al. Carbon Capture and Storage Update. Energy Environ. Sci. 2013, 7 (1), 130–189.

(7) Alcorn, Z. P.; Fredriksen, S. B.; Sharma, M.; Rognmo, A. U.; Føyen, T. L.; Fernø, M. A.; Graue, A. An Integrated Carbon-Dioxide-Foam Enhanced-Oil-Recovery Pilot Program With Combined Carbon Capture, Utilization, and Storage in an Onshore Texas Heterogeneous Carbonate Field. SPE Reserv. Eval. Eng. 2019.

(8) Tan, Y.; Nookuea, W.; Li, H.; Thorin, E.; Yan, J. Property Impacts on Carbon Capture and Storage (CCS) Processes: A Review. Energy Convers. Manag. 2016, 118, 204–222.

(9) Li, H.; Wilhelmsen, Ø.; Yan, J. Properties of CO 2 Mixtures and Impacts on Carbon Capture and Storage. In Handbook of Clean Energy Systems; American Cancer Society, 2014; pp 1–17.

(10) Li, H.; Wilhelmsen, Ø.; Lv, Y.; Wang, W.; Yan, J. Viscosities, Thermal Conductivities and Diffusion Coefficients of CO2 Mixtures: Review of Experimental Data and Theoretical Models. Int. J. Greenh. Gas Control 2011, 5 (5), 1119–1139.

(11) Li, H.; Jakobsen, J. P.; Wilhelmsen, Ø.; Yan, J. PVTxy Properties of CO2 Mixtures Relevant for CO2 Capture, Transport and Storage: Review of Available Experimental Data and Theoretical Models. Appl. Energy 2011, 88 (11), 3567–3579.

(12) Mohammed, M.; Ciotta, F.; Trusler, J. P. M. Viscosities and Densities of Binary Mixtures of Hexadecane with Dissolved Methane or Carbon Dioxide at Temperatures from (298 to 473) K and at Pressures up to 120 MPa. J. Chem. Eng. Data 2017, 62 (1), 422–439.

(13) Poling, B. E.; Prausnitz, J. M.; O'Connell, J. P. Properties of Gases and Liquids, Fifth Edition; McGraw-Hill Education: New York, Chicago, San Francisco, Athens, London, Madrid, Mexico City, Milan, New Delhi, Singapore, Sydney, Toronto, 2001.

(14) Peng, D.-Y.; Robinson, D. B. A New Two-Constant Equation of State. Ind. Eng. Chem. Fundam. 1976, 15 (1), 59–64.

(15) Redlich, O.; Kwong, J. N. S. On the Thermodynamics of Solutions; an Equation of State; Fugacities of Gaseous Solutions. Chem. Rev. 1949, 44 (1), 233–244.

(16) Benedict, M.; Webb, G. B.; Rubin, L. C. An Empirical Equation for Thermodynamic Properties of Light Hydrocarbons and Their Mixtures I. Methane, Ethane, Propane and n-Butane. J. Chem. Phys. 1940, 8, 334–345.

(17) Chapman, W. G.; Gubbins, K. E.; Jackson, G.; Radosz, M. SAFT: Equation-of-State Solution Model for Associating Fluids. Fluid Phase Equilibria 1989, 52, 31–38.

(18) Gross, J.; Sadowski, G. Perturbed-Chain SAFT: An Equation of State Based on a Perturbation Theory for Chain Molecules. Ind. Eng. Chem. Res. 2001, 40 (4), 1244–1260.

(19) Lafitte, T.; Apostolakou, A.; Avendaño, C.; Galindo, A.; Adjiman, C. S.; Müller, E. A.; Jackson, G. Accurate Statistical Associating Fluid Theory for Chain Molecules Formed from Mie Segments. J. Chem. Phys. 2013, 139 (15), 154504.

(20) Péneloux, A.; Rauzy, E.; Fréze, R. A Consistent Correction for Redlich-Kwong-Soave Volumes. Fluid Phase Equilibria 1982, 8 (1), 7–23.

(21) Ungerer, P.; Batut, C. Prédiction des propriétés volumétriques des hydrocarbures par une translation de volume améliorée. Rev. Inst. Fr. Pétrole 1997, 52 (6), 609–623.

(22) Diamantonis, N. I.; Economou, I. G. Evaluation of Statistical Associating Fluid Theory (SAFT) and Perturbed Chain-SAFT Equations of State for the Calculation of Thermodynamic Derivative Properties of Fluids Related to Carbon Capture and Sequestration. Energy Fuels 2011, 25 (7), 3334–3343.

(23) Span, R.; Wagner, W. A New Equation of State for Carbon Dioxide Covering the Fluid Region from the Triple-Point Temperature to 1100 K at Pressures up to 800 MPa. J. Phys. Chem. Ref. Data 1996, 25 (6), 1509–1596.

(24) Lohrenz, J.; Bray, B. G.; Clark, C. R. Calculating Viscosities of Reservoir Fluids From Their Compositions. J. Pet. Technol. 1964, 16 (10), 1171–1176.

(25) Monnery, W. D.; Svrcek, W. Y.; Mehrotra, A. K. Viscosity: A Critical Review of Practical Predictive and Correlative Methods. Can. J. Chem. Eng. 1995, 73 (1), 3–40.

(26) Todeschini, R.; Consonni, V. Handbook of Molecular Descriptors; Wiley-VCH: Weinheim, 2000.

(27) Nieto-Draghi, C.; Fayet, G.; Creton, B.; Rozanska, X.; Rotureau, P.; de Hemptinne, J.-C.; Ungerer, P.; Rousseau, B.; Adamo, C. A General Guidebook for the Theoretical Prediction of Physicochemical Properties of Chemicals for Regulatory Purposes. Chem. Rev. 2015, 115 (24), 13093–13164.

(28) D.Frenkel; B. Smit. Understanding Molecular Simulation: From Algorithms to Applications,Second Edition; Academic Press, 2001.

(29) Ungerer, P.; Tavitian, B.; Boutin, A.; Montel, F. Applications of Molecular Simulation in the Oil and Gas Industry; Editions Technip: Paris, 2005.

(30) Dysthe, D. K.; Fuchs, A. H.; Rousseau, B.; Durandeau, M. ;Fluid Transport Properties by Equilibrium Molecular Dynamics. II. Multicomponent Systems. J. Chem. PhysEng. Chem. Res. 2017, 56 (32), 9213–9226.

(31) Hoang, H.; Delage-Santacreu, S.; Galliero, G. Simultaneous Description of Equilibrium, Interfacial, and Transport Properties of Fluids Using a Mie Chain Coarse-Grained Force Field. Ind. Eng. Chem. Res. 2017, 56 (32), 9213–9226.

Chapter 2. Experimental Measurements

Contents

2.1. Density Measurement 11
2.1.1 Measurement Principle 11
2.1.2 Description of Experimental Setups 13
2.2. Speed of Sound Measurement 16
2.2.1 Measurement Principle 16
2.2.2 Description of Speed of Sound Experimental Setups 18
2.3. Viscosity Measurement 20
2.3.1 Atmospheric Pressure Viscosity Measurement 20
2.3.2 High Pressure Viscosity Measurement 20
2.4. Expanded Uncertainties of Experimental Measurements 22
2.5. Calculation of Volumetric Derivative Properties 23
2.5.1 Isothermal Compressibility 23
2.5.2 Isobaric Thermal Expansion 25
2.6. References 25

Introduction

This chapter is dedicated to the description of experimental devices as well as measurement protocols used in this work. It is organized as follow:

- Section 2.1 presents the scientific principle of the U-tube density meter as well as experimental setups employed for both liquid mixtures and liquid+CO2 mixtures.
- Section 2.2 is devoted to the sound velocity measurements. The measurement probe and its principle are briefly presented followed by the experimental setups.
- Section 2.3 depicted the experimental devices for both atmospheric and high pressure viscosity measurements
- Section 2.4 introduces the uncertainty estimation formulae for all properties measured in this work.
- Section 2.5 is devoted to the description of a calculation procedure used to compute isothermal compressibility and isobaric thermal expansion from experimental density data.

2.1. Density Measurement

2.1.1 Measurement Principle

Density measurements were carried out using a vibrating U-tube density meter. The operating principle of this kind of density meter consists in linking the density of the studied fluid to the oscillation period of the the U-tube filled with the latter.

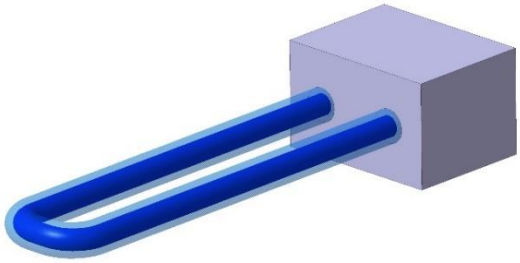

Figure 2.1: Schematic representation[1] of a vibrating U-tube filled with he studied fluid (dark blue).

The system composed of the tube and the studied fluid, is excited in a non-damped manner. So it can be modeled as a one dregree of freedom oscillator formed with a body of mass *m* that oscillates without friction at the end of a spring with a stiffness coefficient C. The natural frequency for this type of oscillator is defined by:

$$f = \frac{1}{\tau} = \frac{1}{2\pi}\sqrt{\frac{C}{m}} = \frac{1}{2\pi}\sqrt{\frac{C}{m_0+\rho V_0}} \tag{2.1}$$

where τ is the period of the oscillator, m_0 and V_0 are the unknown mass and internal volume of the empty vibrating cell, respectivly.

Equation (2.1) can be rewritten as :

$$\tau^2 = \frac{4\pi^2}{C}(m_0 + \rho V_0) \tag{2.2}$$

The density is then expressed as a function of the oscillator periode, at a given temperature *T* and pressure *P*, as follow:

$$\rho(T,P) = A(T,P)\tau^2 + B(P,T) \tag{2.3}$$

With

$$A(P,T) = \frac{C(P,T)}{4\pi^2 V_0(P,T)} \tag{2.4}$$

$$B(P,T) = \frac{-m_0}{V_0(P,T)} \tag{2.5}$$

Since *C*, m_0 and V_0 are unknown, *A* and *B* cannot be determined directly. Consequently, they appear as apparatus constants that must be determined by applying a calibration protocol that consists in determining the vibrating periods τ_1 and τ_2 of two reference fluids which densities are well known in the operating temperature and pressure range.

In this work, we chose the calibration protocol proposed by Lagourette et al. [2], which consists in assuming that C and V_0 depend on P in the same way so that A appears as pressure independent. Consequently, it can be estimated for each temperature by the calibration with vacuum and water under atmospheric pressure. Choosing in addition density data of water under pressure as reference for determining B parameter, the working equation becomes:

$$\rho(T,P) = \rho_w(T,P) + \rho_w(T,0.1MPa)\left[\frac{\tau^2(T,P) - \tau_w^2(T,P)}{\tau_w^2(T,0.1\ MPa) - \tau_{vac}^2(T)}\right] \tag{2.6}$$

Where τ , τ_w and τ_{vac} are the vibration periods of the U-tube filled with the studied sample, deionized water and vacuum respectively, and ρ_w is the density of water given by Wagner and Pruß[3].

The combined standard uncertainty in the density measurements is calculated by combining in a quadratic sum the different sources of uncertainty appearing in equation (2.6) , according to the GUM of NIST[4] as follows:

$$u_M^2(\rho) = \left[\left(\tau^2 - \tau_w^2\right)u_c(A)\right]^2 + [2A\tau u_c(\tau)]^2 + [2A\tau_w u_c(\tau_w)]^2 + [u(\rho_w)]^2 \tag{2.7}$$

With

$$u_c^2(A) = \left[\frac{A}{\rho_{w0}}u(\rho_{w0})\right]^2 + \left[\frac{2A^2\tau_{w0}}{\rho_{w0}}u_c(\tau_{w0})\right]^2 + \left[\frac{2A^2\tau_{vac}}{\rho_{w0}}u_c(\tau_{vac})\right]^2 \tag{2.8}$$

And

$$u_c^2(\tau_i) = [u(\tau_i)]^2 + \left[\left(\frac{\partial \tau_i}{\partial T}\right)_p u(T)\right]^2 + \left[\left(\frac{\partial \tau_i}{\partial p}\right)_T u(P)\right]^2 \quad (2.9)$$

Where subscript i refers to either the studied sample or water or vacuum .

To validate the calibration, the density of toluene has been measured and compared to experimental data provided by Cibulka et al. [5]. As observed on the graph of Figure 2.2, our results are in very good agreement with the literature data with average deviation not greater than 0.2%.

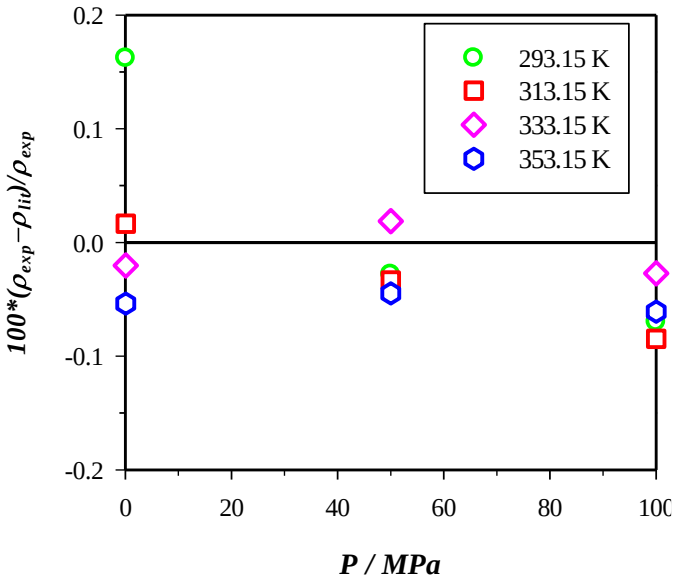

Figure 2.2: Percentage relative deviation between our experimental density of toluene and density data taken from Cibulka et al. [5].

2.1.2 Description of Experimental Setups

2.1.2.1 Experimental Setup for Simple Liquid Mixtures

For the liquid mixtures investigated, density measurements were carried out using an Anton-Paar vibrating U-tube density meter equipped with a high pressure cell (DMA HPM) that can operate up to 100 MPa. The full experimental setup is depicted in Figure 2.3. The core of the setup is the measurement cell connected to a frequency meter mPDS 2000V3 which displays the vibration period of the tube with 7 significant digits. The pressure of the system is generated using a volumetric pump and is measured by means of a Presens manometer with a standard uncertainty of $\pm$0.02%. The thermal regulation of the system is carried out using a thermostatic bath and the temperature is measured with a Pt100 thermometer with a standard uncertainty of 0.03 K. The liquid mixture, prepared ex situ by mass weighing, is injected in the U-tube by vacuum suck up through a funnel placed on the upper part of the piston pump.

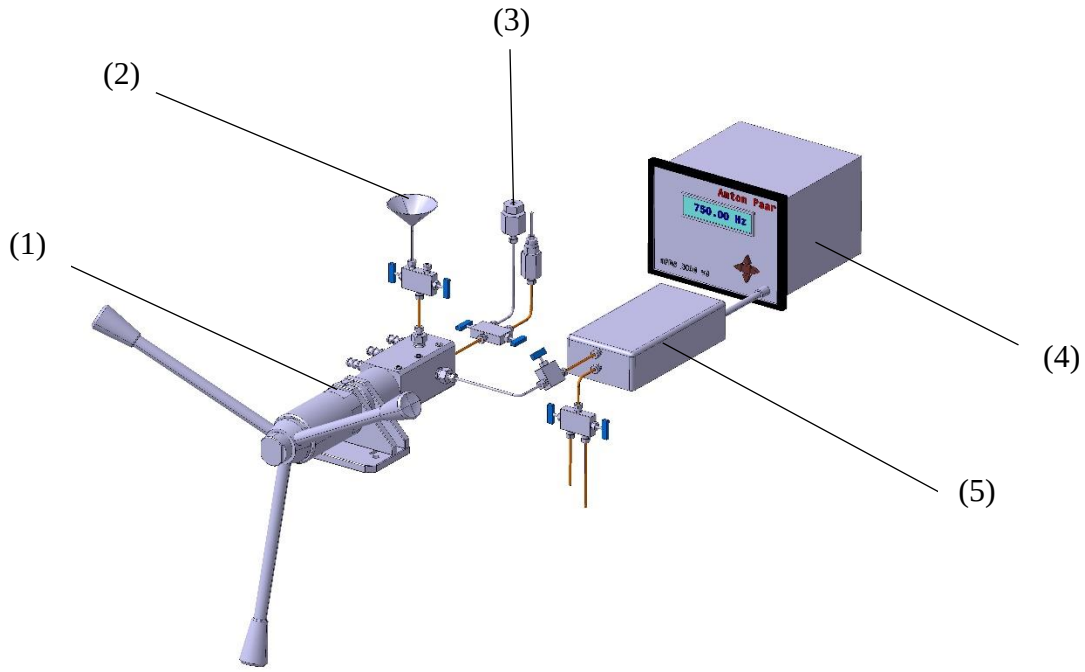

Figure 2.3: Schematic diagram of the density experimental setup for liquid mixtures. (1) high pressure pump; (2) filling funnel; (3) pressure sensor; (4) Frequency meter; (5) density meter.

2.1.2.2 Experimental Setup for Liquid + CO2 Mixtures

In addition to the high pressure density meter, the experimental setup for liquid + gas mixtures (depicted in Figure 2.4) includes two volumetric pumps required to both imposing pressure and injecting the light gas + hydrocarbon liquid mixture in homogeneous liquid state within the measurement cell. One (the feeding pump) is used to prepare and homogenize the liquid + gas mixture since there is no mixing mechanism in the density measuring cell. The other (discharge pump) serves to maintain the pressure above the bubble pressure during the transfer of the sample mixture from the feeding pump to the measurement cell. The mixtures were prepared by weighing both the liquid and gas injected in the feeding pump. For this operation the piston of the pump is retracted so as to offer the maximum volume for injection of the required amount of liquid and gas. The liquid is first loaded into the cell by vacuum suck up. During this process, the mass of liquid charged is determined by means of a precision balance having an uncertainty of 10^{-3} g. The carbon dioxide is then added under pressure. So as to determine the amount of gas injected, the CO_2 is initially charged in liquid-vapor two phases equilibrium condition in an aluminum tank with a high capacity (1 L) fixed on a high weight / high precision balance that achieves weighing with an uncertainty of 10^{-3} g. In order to avoid perturbation of the balance during gas weighing, the CO_2 tank is connected to the measuring cell through a flexible tubing in PEEK with an internal diameter of 1/16”. Because of the high capacity of the reservoir in comparison to the amount of CO_2 transferred, the pressure stays constant at the saturation pressure of CO_2 (5.7 MPa at room temperature) in the reservoir tank as well as into the connecting tube during gas injection. Consequently, the mass of gas injected into the measuring cell is directly determined by weighting the reservoir tank during the filling.

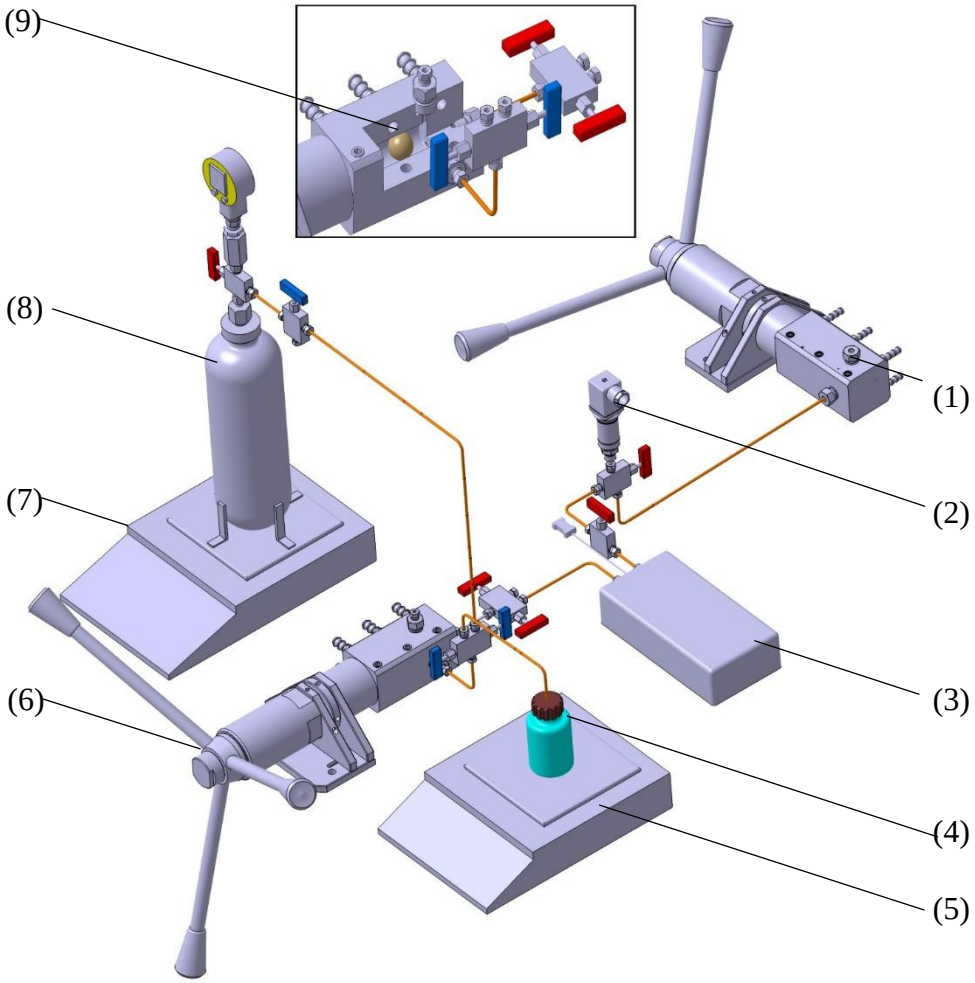

Figure 2.4: Schematic diagram of the density experimental setup. (1) high pressure discharge pump; (2) pressure sensor; (3) density meter (4) liquid tank; (5) liquid balance; (6) high pressure feeding pump; (7) gas balance; (8) gas tank; (9) tungsten ball inside the feeding pump.

After injection of the targeted quantity of liquid and gas components, the mixture is pressurized inside the feeding pump at the pressure of 70 MPa and the pump is shaken so as to generate a to-and-fro movement of a tungsten ball placed inside the pump with a small annular gap between it and the internal wall of the pump. The alternative shift of the tungsten ball in the mixture under high pressure enables to achieve a rapid and efficient homogenization of the mixture. An initial volume of 20 cm^3 of the liquid mixture is first prepared inside the feeding pump. After homogenization under high pressure, a sample volume of 3 cm^3 of the mixture is charged in the measurement cell by generating a positive displacement of the feeding pump while the output pump, in withdrawal position, maintains the pressure constant. To avoid any pressure drop below the bubble point of the mixture during this operation, the full transfer line is initially charged with a buffer fluid corresponding to the same system. This buffer is then expelled to the output pump by actually transferring more than three times the volume of the measuring cell from the feeding pump to the output pump. Finally, when the transfer is achieved, the valve of the output pump is closed and only the feeding pump is used to change the pressure in the system.

2.2. Speed of Sound Measurement

2.2.1 Measurement Principle

The speed of sound measurements were performed using a pulse-echo technique working in the reflection mode at 3 MH_Z. This frequency represents a satisfactory compromise between lower frequencies which give clear signals in fluids but reduce accuracy in measurement and higher frequencies that improve accuracy but with a greater wave damping, especially in CO_2 rich systems. The acoustic sensor (depicted in Figure 2.5) made of stainless steel, is composed of a piezoelectric disk mounted between two hollow cylindrical supports of different lengths (L_1 and L_2) so as to form a long and a short path length for the acoustic waves. Two reflectors are fixed at the ends of the cylindrical supports. Four small holes and two longitudinal cuts are made in the cylindrical support so that the volumes inside the sensor can be filled by the studied fluid.

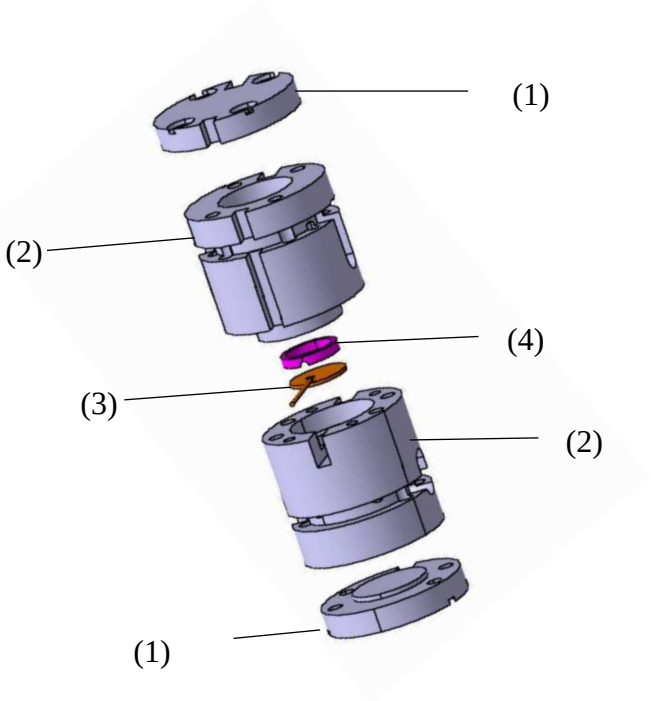

Figure 2.5: Schematic diagram of the acoustic probe. (1) reflectors; (2) cylindrical support; (3) piezoelectric transducer; (4) Teflon ring.

The speed of sound w in the studied liquid was determined by measuring the time delay Δt between echoes reflected back to the piezoelectric disk from the different reflectors by a digital overlap method [6] as shown in Figure 2.6. The speed of sound is then calculated considering the difference in path length Δl according to the following relation:

$$w = \frac{2\Delta l}{\Delta t} \tag{2.10}$$

with

$$\Delta l(P,T) = L_2 - L_1 = \Delta L_0[1 + a(T - T_0)] \cdot [1 + b(P - P_{\text{atm}})] \tag{2.11}$$

Where ΔL_0, the path difference at the reference temperature ($T_0 = 293.15\ K$) and pressure (P_{atm} =0.1013MPa) as well as a and b parameters, are estimated by calibration with water [7–10].

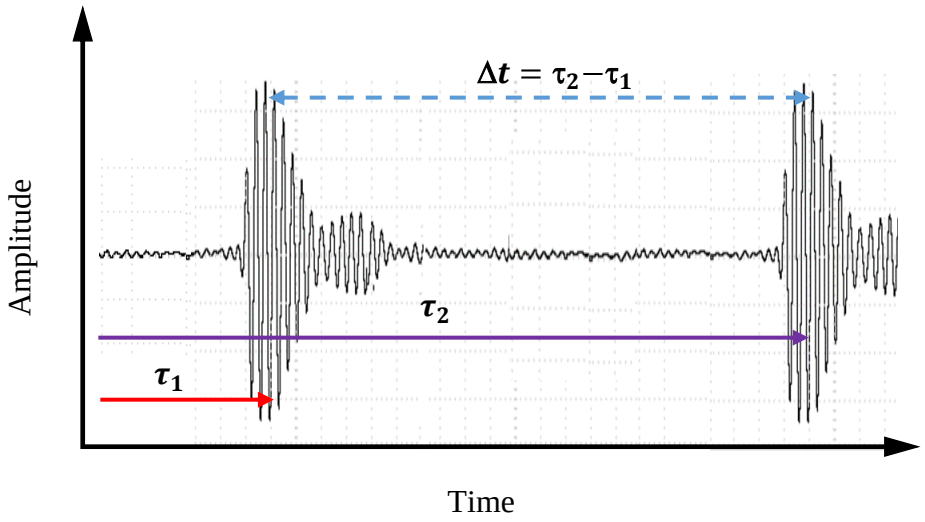

Figure 2.6: Screen shot of the wave visualized on the oscilloscope used to calculate $\Delta t = \tau_2 - \tau_1$.

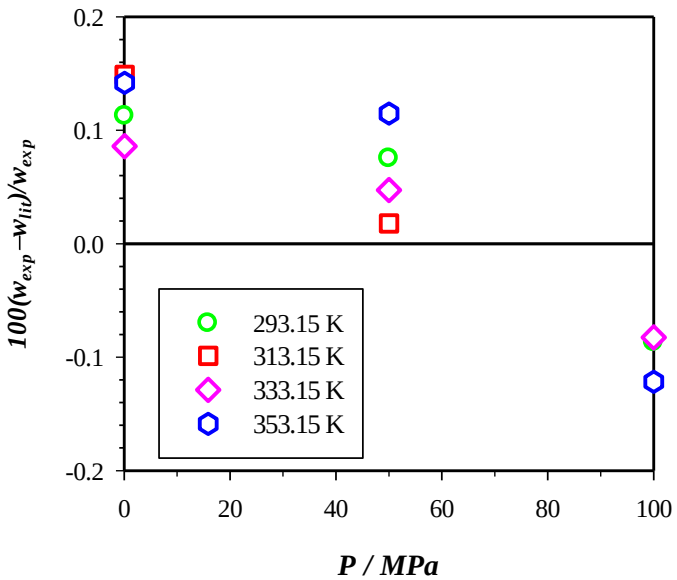

Figure 2.7: Percentage relative deviation between our experimental speed of sound values of toluene and speed of sound data taken from Meier and Kabelac [11].

The combined standard uncertainty of speed of sound measurements was estimated by propagating the input uncertainties $u(\triangle t)$ and $u(\triangle l)$ but also the effects of temperature and pressure uncertainties:

$$u_M^2(w) = \left[w\frac{u(\Delta t)}{\Delta t}\right]^2 + \left[w\frac{u(\Delta l)}{\Delta l}\right]^2 + \left[\left(\frac{\partial w}{\partial T}\right)u(T)\right]^2 + \left[\left(\frac{\partial w}{\partial P}\right)u(P)\right]^2 \qquad (2.12)$$

To validate the calibration method, the speed of sound in toluene is measured and compared to data provided in the literature by Meier and Kabelac [11]. As shown, in Figure 2.7, our experimental measurements are in very good agreement with the reported data, with deviation not greater than 0.15%.

2.2.2 Description of Speed of Sound Experimental Setups

2.2.2.1 Experimental Setup for Liquid Mixtures

The experimental setup for liquid mixtures is described in Figure 2.8. The acoustic sensor is enclosed in an autoclave cell filled with the studied liquid (prepared ex situ) and connected to a volumetric high pressure piston pump. The pressure measurement is performed using a pressure transducer with an uncertainty of 0.01 MPa, mounted between the pump and the high pressure vessel. The thermal regulation is insured by immerging the high pressure cell within a thermostatic bath of stability 0.02 K. The temperature measurement was made using a Pt 100 probe, placed inside the cell. With this probe, the temperature of the studied fluid is measured with an uncertainty less than 0.1 K. The ultrasonic sensor is connected to an electronic circuit composed of a Pulser-Receiver and a digital oscilloscope.

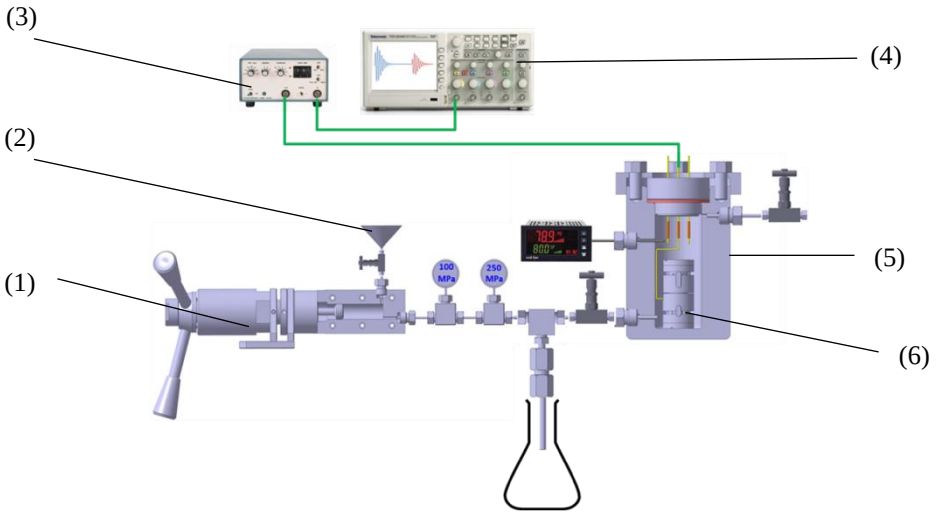

Figure 2.8: Schematic diagram of the speed of sound experimental setup for liquid mixtures. (1) high pressure piston pump; (2) filling funnel; (3) Pulser-Receiver; (4) oscilloscope; (5) autoclave; (6) acoustic wave sensor.

2.2.2.2 Experimental Setup for Liquid + CO_2 Mixtures

For the liquid + CO_2 mixtures, the apparatus is essentially made up of a variable volume cell with an internal volume of about 300 ml as illustrated in Figure 2.9. It consists of horizontal cylinder, closed at one end by a stainless steel plug with two HP electrical feedthroughs used to hold and connect the speed of sound sensor. The sensor occupies a significant portion (60 ml) of the internal volume of the cell and generates a large dead volume (20 ml). The external parts of the electrical feedthroughs are connected to the electronic circuit composed of a Pulser-Receiver and a digital oscilloscope. The second end of the cell is closed by a moveable piston equipped with a magnetically coupled stirrer that rotates at variable speeds in order to provide an efficient fluid mixing and ensures a rapid homogenization of liquid + gas mixtures despite

the complex geometry of the sensor. The temperature of the fluid inside the cell is regulated by heating cartridges embedded in a jacket that surround the full cell body. A temperature sensor (Pt 100) is place inside the jacket between the cell surface and the heating cartridges in order to control the heating power. A second temperature sensor is inserted in the cell so as to measure the temperature of the fluid with an uncertainty of 0.1 K. The pressure is measured by using a pressure gauge in direct contact with the fluid inside the measurement cell so as to avoid isolating a part of the fluid from the sensing area and thus avoid modification of the feed composition. The pressure sensor is calibrated as a function of temperature against a primary standard pressure sensor with an uncertainty better than 0.02 % on the full scale.

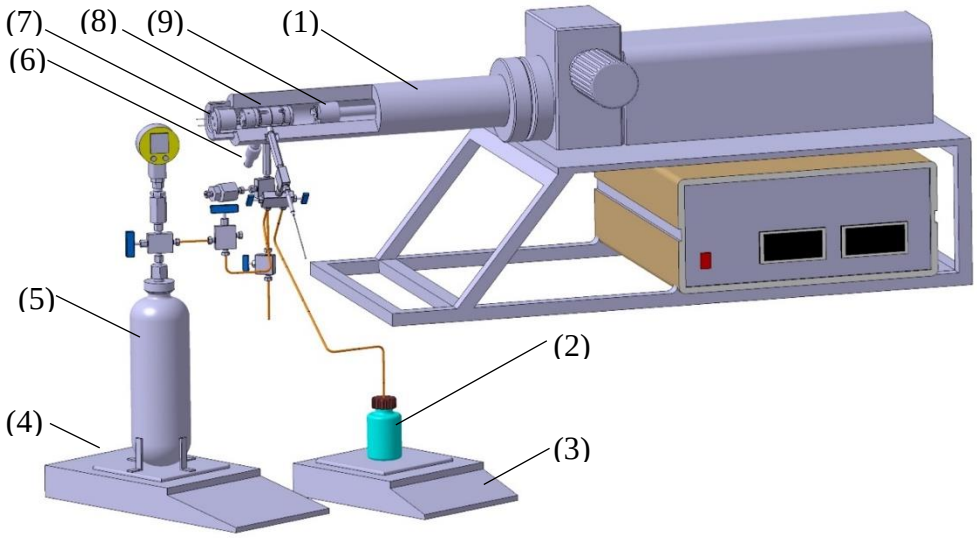

Figure 2.9: Schematic diagram of the speed of sound measurement setup. (1) High pressure vessel; (2) liquid tank; (3) liquid balance; (4) gas balance; (5) gas tank; (6) pressure sensor; (7) electrical feedthrough; (8) acoustic wave sensor; (9) piston with stirring system.

For these experiments, the mixtures were prepared in situ by injecting directly both the liquid and gas in the measurement cell. As for density, the amount of gas and liquid injected were determined by weighing. Once both components have been injected into the cell, its pressure is increased to force the components to mix in a single fluid phase. For that purpose, the binary mixture is vigorously stirred for a sufficient period to achieve the homogenization of the fluid throughout the cell. During this equilibration time, speed of sound is continuously recorded to check the progress of the homogenization.

2.3. Viscosity Measurement

2.3.1 Atmospheric Pressure Viscosity Measurement

Viscosity measurements at atmospheric pressure were performed using a commercial Ubbellohde type capillary viscometer. It consists in measuring the falling time of a fluid, due to gravity effect, inside a vertical capillary previously calibrated. The capillary tube is connected to an automatic analyzer AVS 350 Schott Geräte with an uncertainty of 0.01% on the falling time measurement. The measuring capillary is immersed in a transparent thermostatic bath Schott CT53 with an uncertainty of ±0.1K. The Kinematic viscosity $\mu(T,P)$ was then obtained by absolute measurements using the following expression :

$$\mu(T,P) = K\,(\Delta t - y) \tag{2.13}$$

Where K is the constant of the capillary tube, Δt is the average falling time of the sample fluid and y is the correction of Hagenbach corresponding to the difference between the measured and theoretical flow time. The dynamic viscosity values $\eta(T,P_0)$ are then deduced by multiplying the kinematic viscosity values by the density of the studied sample .

2.3.2 High Pressure Viscosity Measurement

2.3.2.1 Measurement Principle

High Pressure viscosities of liquid mixtures were measured using a vertical falling plug viscometer. It consists of recording the falling time of a cylindrical plug under the effect of gravity in the fluid of interest. The configuration is such that the fluid is subject to a laminar flow in an annular space limited by the vertical plug and the internal cylindrical walls of the tube. The falling time Δt of the plug on a height h is correlated to the viscosity of the fluid by:

$$\eta = \Delta t \frac{(1-\rho_l/\rho_s)}{A} \tag{2.14}$$

With

$$A = \frac{2\pi h_s h}{mg\left[\ln\left(r_2/r_1\right) - \left(r_2^2 - r_1^2\right)/\left(r_2^2 - r_1^2\right)\right]} \tag{2.15}$$

Where g is the gravity constant, ρ_l is the density of the studied liquid, ρ_s is the density of the falling plug, h_s is the height of the falling cylinder, m the mass of the falling cylinder, r_1 is the radius of the falling cylinder and r_2 is the inner radius of the cylindrical tube.

In theory, knowing all the parameters of the viscometer mentioned above, it is possible to use it in an absolute manner, i.e. without any calibration. But, in practice, it is almost never the case. Indeed, the flow around the falling body is never perfectly axial. In addition, the falling body is never completely cylindrical. Therefore, the viscometer is used in a relative manner, that is, the viscometer constants are deduced from measurements made on a reference fluid, for which viscosity is well known in the pressure domain of investigation. With this aim in mind, the working equation for the falling cylinder viscometer, deduced from equations (2.14) and (2.15) is rewritten as follow:

$$\eta(T,P) = K(\rho_s - \rho_l)\Delta t \tag{2.16}$$

Where $K = K(T,P)$ is the apparatus constant that must be calibrated for each falling body in the operating pressure and temperature range.

In this work, we used as reference toluene, for which reliable data of viscosity are provided by Assael et al.[12].

The combined standard uncertainty in the viscosity measurement is calculated by combining the quadratic sum of the different sources of uncertainty appearing in equation (2.16) but also the effects of temperature and pressure uncertainties:

$$u_M^2(\eta) = [\Delta t(\rho_s - \rho_l)u(K)]^2 + [\Delta t K u(\rho_s)]^2 + [\Delta t K u(\rho_l)]^2 + [K(\rho_s - \rho_l)u(\Delta t)]^2 + \left[\left(\frac{\partial \eta}{\partial T}\right)u(T)\right]^2 + \left[\left(\frac{\partial \eta}{\partial P}\right)u(P)\right]^2 \tag{2.17}$$

2.3.2.2 Experimental Setup

The experimental setup of the high pressure viscometer is summarized in Figure 2.10. It has been developped in our laboratory by Daugé et al.[13]. The measurement cell is connected to an auxiliary device consisting of an air compressor and a hydraulic cylinder which keeps the fluid at the desired pressure. The pressure is measured using a metal gauge sensor connected to a digital display whose accuracy is of ± 0.01 MPa at atmospheric pressure and ± 0.1 MPa for pressure up to 100 MPa.

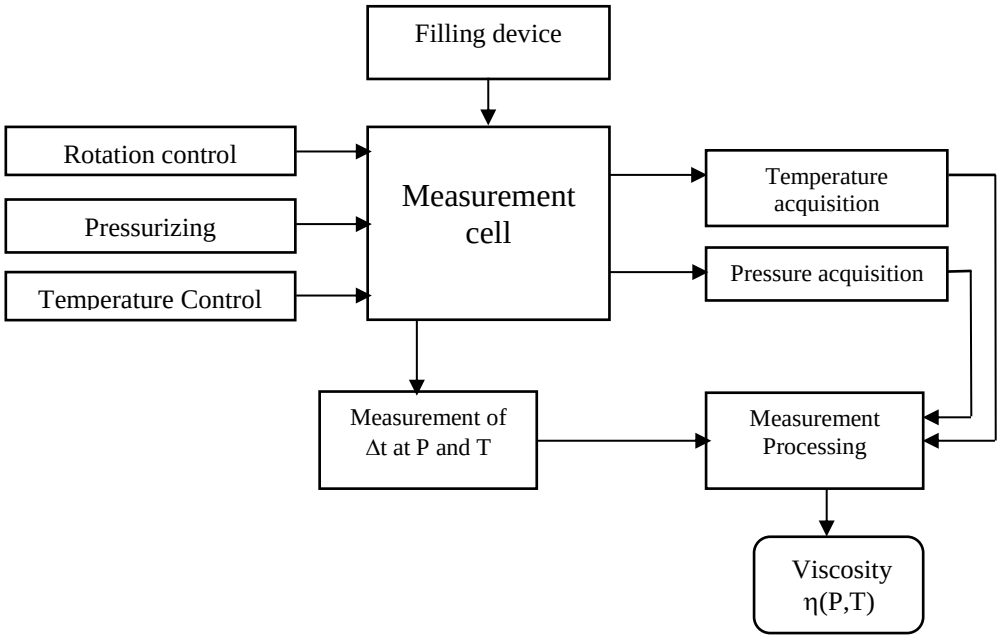

Figure 2.10: Synoptic table representing the operating principle of the high pressure viscosity measurement device.

The thermal control of the system is carried out using a thermostatic bath Huber Unistat CC. In addition, the whole measurement cell is placed in an oven to avoid temperature fluctuations during measurements. The temperature acquisition was made using a platinum probe 100 Ω, placed inside the measurement cell and connected to a display AOIP PN5207 with an uncertainty of ± 0.1 K. The falling time is measured by a stopwatch whose switching on and

off are caused by the passage of the metallic cylindrical plug through two coils placed respectively on the upper and lower parts of the measuring cell as depicted in Figure 2.11 and explained in details by Daugé et al [13].

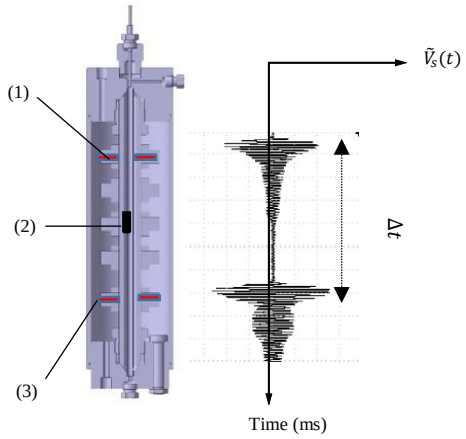

Figure 2.11: Schematic representation of the falling time measurement system. (1): upper coil; (2): falling plug and (3): lower coil.

2.4. Expanded Uncertainties of Experimental Measurements

In addition to the standard uncertainties in measurements u_M, the uncertainty u_x caused by mixture preparation and sample purities x_{sp} was also taken in consideration. Assuming a rectangular distribution for the sample impurities reported by the supplier and fractional density difference ξ between the pure compounds and their impurities arbitrary set to 20 % for both components, the uncertainty u_x is expressed as follow:

$$u_x^2(y) = \left[\left(\frac{\partial y}{\partial x_\alpha}\right) u_c(x_\alpha)\right]^2 + \left[x_\alpha \frac{1-x_{sp,\alpha}}{\sqrt{3}} \xi y_\alpha\right]^2 + \left[(1-x_\alpha) \frac{1-x_{sp,\beta}}{\sqrt{3}} \xi y_\beta\right]^2 \quad (2.18)$$

Where y denotes either the density ρ, the speed of sound w or the viscosity η and the subscripts α and β represent the two components of the considered binary mixtures.

For liquid + CO_2 mixtures, the standard uncertainty in the mole faction x of CO_2 is estimated from the uncertainty in liquid (m_l) and gas (m_{co2}) weights when preparing the mixtures:

$$u_c(x_{co2}) = x_{co2}(1-x_{co2}) \left(\frac{u^2(m_{co2})}{m_{co2}^2} + \frac{u^2(m_{liq})}{m_{liq}^2}\right)^{1/2} \quad (2.19)$$

Concerning simple liquid mixtures, the uncertainties in the mole fraction are negligible given the large quantities of mixture prepared and the low uncertainties on liquid components weighing.

Finally, the expanded uncertainty with a conventional coverage factor k_P = 2 (*Probability* = 95 %) was determined by considering both sources of uncertainty:

$$U(y) = 2\sqrt{u_M^2(y) + u_x^2(y)} \quad (2.20)$$

2.5. Calculation of Volumetric Derivative Properties

2.5.1 Isothermal Compressibility

Isothermal compressibility κ_T was determined from density measurements by fitting and analytically deriving the isothermal density data, according to its definition :

$$\kappa_T = \frac{1}{\rho}\left(\frac{\partial \rho}{\partial P}\right)_T \tag{2.21}$$

To estimate the corresponding derivative property and the combined standard uncertainty associated, we used an in-house computational procedure proposed by Daridon et al. [14].This procedure, based on a Monte Carlo statistical method, uses the experimental density values as input. Each input datum is randomly perturbed by a Gaussian distribution of a large number of at least 5000 pseudo-random trials. For each experimental condition, ρ_{exp} is set to the mean of the distribution and $U_M(\rho_{exp})$ to its standard deviation. Then, each set of data point randomly generated is used for fitting and deriving isothermal compressibility. Likewise, the generated output shows a Gaussian distribution (Figure 2.12) which mean and standard deviation are respectively the calculated derivative property κ_T and the corresponding standard uncertainty in compressibility computation $u_{comp}(\kappa_T)$.

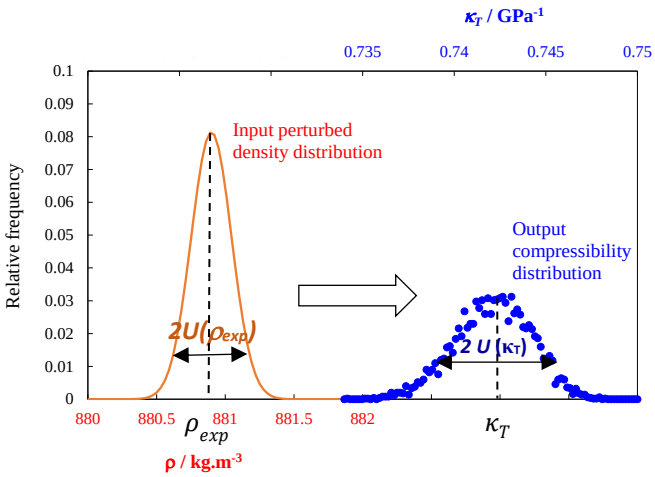

Figure 2.12 Input perturbed density distribution (—) and output isothermal compressibility distribution (•). This figure is taken from[14].

As this procedure depends on the analytical form of the equation of state used for fitting data, both the compressility value and the standard uncertainty in compressibility computation are function of the equation actually chosen. Nowaday most of works consider the so-called Tait equation developed by Tammann[15] but several comparative studies[14,16–18] have shown that many empirical equations of state are able to represent the effect of pressure on volumetric properties in a pressure range of 100 MPa. Among these equations we have considered 6 different empirical equations of state[19–21] for fitting perturbed density data. These equations, presented in Table 2.1, have been chosen because they were shown to be suitable for deriving density data in the investigated pressure range [14] with a limited (3 or 4) number of parameters.

Table 2.1 : List of the six equation of states used to calculate the isothermal compressibility

Equation name	Form[a]	Number of parameters
Hudleston[19]	$\widetilde{P} = \frac{A-l}{l^2} exp\left(B + C(A-l)\right)$ with $l = v^{1/3}$	3
Murnaghan[20]	$\rho = A\left(1 + B\widetilde{P}\right)^C$	3
Tait Equation[15]	$\rho = \left(A - Cln\left(\frac{\widetilde{P} + B}{B}\right)\right)^{-1}$	3
Quadratic Tangent BM	$\rho = A\left(\frac{1 + B\widetilde{P}}{1 + D\widetilde{P}}\right)^C$	4
Quadratic DER	$\rho = \left(A - Cln\left(\frac{\widetilde{P} + B}{D\widetilde{P} + B}\right)\right)^{-1}$	4
Ndiaye et al.[21]	$\rho = \left(A - Cln\left(\frac{\widetilde{P} + B}{B}\right) - D\widetilde{P}\right)^{-1}$	4

[a] where $\widetilde{P} = P - P_{atm}$ is the relative pressure.

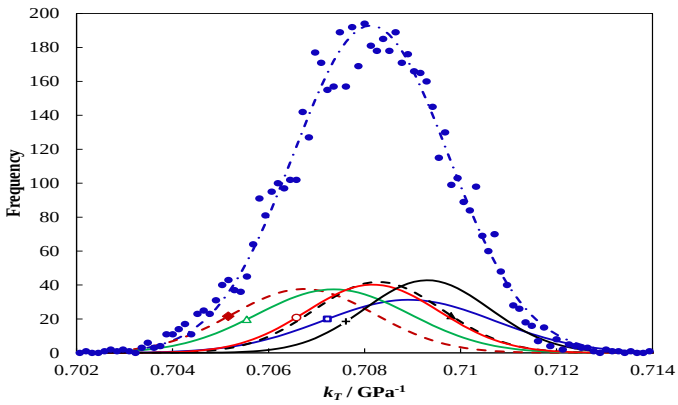

Figure 2.13 Frequency histogram of the isothermal compressibility κ_T distributions obtained from the computation method retained and from the six equations considered in the procedure. •: Computed distribution obtained by using randomly six different equations; –·–: normal distribution; –♦–: Huddleston, –+–: Murnaghan, –○–: Tait equation (), -△- quadratic tangent, --▲-- quadratic DER, -□- Ndiaye et al. This graph is taken from[14].

Moreover, these equations appear as the most efficient for deriving compressibility when uncertainty in density data becomes significant. So as to combine the uncertainty caused from the form $u_{form}(\kappa_T)$ of the equation of state chosen with the uncertainty arising from fitting and derivation $u_{der}(\kappa_T)$, the six selected equations were randomly used at each trial of the Monte Carlo method developed. As can be observed in Figure 2.13 the resulting compressibility distribution has a Gaussian shape yet. It allows estimating simultaneously the compressibility and the combined standard uncertainty in compressibility computation $u_{comp}(\kappa_T)$ from the mean and the standard deviation of the distribution respectively.

2.5.2 Isobaric Thermal Expansion

The isobaric thermal expansion data were determined from derivation of density measurements with respect to temperature at constant pressure according to its definition:

$$\alpha_P = -\frac{1}{\rho}\left(\frac{\partial \rho}{\partial T}\right)_P \tag{2.22}$$

As for compressibility, such derivation was carried out by a Monte Carlo method that consists first in generating a 5000 data sets with density values randomly perturbed around the experimental measurements by using a normal probability distribution function centered on the experimental density values. Each density data set where then fitted to an analytical equation so as to carry out the derivation of density with respect to temperature. As no theoretical equation was proposed in the literature for representing temperature influence on density at constant pressure, a polynomial function was simply considered for that operation:

$$\rho = \sum_{i=0}^{n} a_i T^i \tag{2.23}$$

Where a_i are the coefficients of the polynomial. The order *n* of the polynomial was fixed for each experiment according to the temperature interval as well as the number of experimental data available on each isobar. Finally, the averages and standard deviations of the resulting distributions were calculated in order to obtain the isobaric expansion α_P and its standard uncertainty computation $u_{comp}(\alpha_P)$for each experimental condition.

2.6. References

(1) The Very Basics Of Density Measurement Methods - Anton Paar Blog https://blog.anton-paar.com/the-very-basics-of-density-measurement/

(2) Lagache, M.; Ungerer, P.; and A. H. Fuchs, A. Boutin Prediction of Thermodynamic Derivative Properties of Fluids by Monte Carlo Simulation,. Phys Chem Chem Phys 2001, 3.

(3) Wagner, W.; Pruß, A. The IAPWS Formulation 1995 for the Thermodynamic Properties of Ordinary Water Substance for General and Scientific Use. J. Phys. Chem. Ref. Data 2002, 31 (2), 387–535.

(4) C. E. Kuyatt; B.N.Taylo. "Guidelines for Evaluating and Expressing the Uncertainty of NIST Measurement Results,," NIST Technical Note 1297; 1994.

(5) Cibulka, I.; Takagi, T. P−ρ−T Data of Liquids: Summarization and Evaluation. 5. Aromatic Hydrocarbons. J. Chem. Eng. Data 1999, 44 (3), 411–429.

(6) Bazile, J.-P.; Nasri, D.; Daridon, J.-L. Speed of Sound, Density, and Derivative Properties of Tris(2-Ethylhexyl) Trimellitate under High Pressure. J. Chem. Eng. Data 2017, 62 (5), 1708–1715.

(7) Del Grosso, V. A.; Mader, C. W. Speed of Sound in Pure Water. J. Acoust. Soc. Am. 1972, 52 (5B), 1442–1446.

(8) Marczak, W. Water as a Standard in the Measurements of Speed of Sound in Liquids. J. Acoust. Soc. Am. 1997, 102 (5), 2776–2779.

(9) Wilson, W. D. Speed of Sound in Distilled Water as a Function of Temperature and Pressure. J. Acoust. Soc. Am. 1959, 31 (8), 1067–1072.

(10) Vance, S.; Brown, J. M. Sound Velocities and Thermodynamic Properties of Water to 700 MPa and −10 to 100 °C. J. Acoust. Soc. Am. 2010, 127 (1), 174–180.

(11) Meier, K.; Kabelac, S. Measurements of the Speed of Sound in Liquid Toluene. J. Chem. Eng. Data 2013, 58 (5), 1398–1406.

(12) Assael, M. J.; Dalaouti, N. K.; Dymond, J. H. The Viscosity of Toluene in the Temperature Range 210 to 370 K1. Int. J. Thermophys. 2000, 21 (2), 291–299.

(13) Daugé, Pierre; Baylaucq, A.; Marlin, L.; Boned, C. Development of an Isobaric Transfer Viscometer Operating up to 140 MPa. Application to a Methane + Decane System. J. Chem. Eng. Data 2001, 46 (4), 823–830.

(14) Daridon, J.-L.; Bazile, J.-P. Computation of Liquid Isothermal Compressibility from Density Measurements: An Application to Toluene. J. Chem. Eng. Data 2018, 63 (6), 2162–2178.

(15) Tammann, G. Ueber Die Abhängigkeit Der Volumina von Lösungen Vom Druck. Z. Für Phys. Chem. 1895, 17U (1), 620–636.

(16) Hayward, A. T. J. Compressibility Equations for Liquids: A Comparative Study. Br. J. Appl. Phys. 1967, 18, 965–977.

(17) MACDONALD, J. R. Review of Some Experimental and Analytical Equations of State. Rev. Mod. Phys. 1969, 41 (2), 316–349.

(18) Sun, T. F.; Schouten, J. A.; Kortbeek, P. J.; Biswas, S. N. Experimental Equations of State for Some Organic Liquids Between 273 and 333 K and Up to 280 MPa. Phys. Chem. Liq. 1990, 21 (4), 231–237.

(19) Hudleston, L. J. Intermolecular Forces of Normal Liquids. Trans. Faraday Soc. 1937, 33 (0), 97–103.

(20) Murnaghan, F. D. The Compressibility of Media under Extreme Pressures. Proc. Natl. Acad. Sci. 1944, 30 (9), 244–247.

(21) Ndiaye, E. H. I.; Habrioux, M.; Coutinho, J. A. P.; and J. L. Daridon, M. L. L. P. Speed of Sound, Density, and Derivative Properties of Ethyl Myristate, Methyl Myristate, and Methyl Palmitate under High Pressure. J Chem Eng Data 2013, 58, 1371–1377.

Chapter 3. Molecular Simulations

Contents

3.1. Statistical Mechanics 28
3.1.1 Phase Space 28
3.1.2 Averaging Methods 28
3.1.3 Ergodic Hypothesis 29
3.1.4 Statistical Ensembles 29
3.2. Molecular Simulations 33
3.2.1 Interaction Potential and Force Evaluation 33
3.2.2 Monte Carlo Simulations 38
3.2.3 Molecular Dynamics Simulations 40
3.3. Thermophysical Properties Estimation from Molecular Simulations 45
3.3.1 Thermodynamic Properties Calculation from MC Simulations 45
3.3.2 Calculation of a Transport Property: the Shear Viscosity 47
3.3.3 Calculation of properties from Structural Information 48
3.4. References 51

Introduction

This chapter is dedicated to a brief description of molecular simulations techniques used during this work. It is organized as follow:

- Section 3.1 is presents a brief introduction to statistical physics.
- Section 3.2 introduces the two molecular simulation methods as well as the force fields employed in this work.
- Section 3.3 is devoted to the determination of thermophysical properties using both Monte Carlo and Molecular Dynamics.

3.1. Statistical Mechanics

The macroscopic state of a system is defined by a limited number of observable properties such as temperature, pressure, volume or internal energy. Statistical mechanics offers a theoretical framework to deduce such macroscopic observables from the large amount of properties defining the system at the microscopic level[1].

In the following sections, we will summarize the statistical mechanics aspects of interest for the scope of this work.

3.1.1 Phase Space

At the microscopic level, the instantaneous state of a system of *N* particles (atoms or molecules) is described by particles coordinates $\vec{r}$ and their momenta $\vec{p}$. Therefore, such particles evolve in a multidimensional 6N-dimensions space defined as phase space. Each point of this phase space describes a given microstate (Γ) of the system, whereas a macroscopic state is described by a set of Ω microstates. The positions described by a particular point of the phase space over time constitutes its trajectory in the phase space. The conversion of microscopic information to macroscopic observables such as temperature or pressure, requires the use of statistical tools (averaging, deviations, probabilities) [1,2].

3.1.2 Averaging Methods

As discussed in the previous section, macroscopic observables can be deduced from averages on microscopic properties. There are mainly two averaging techniques, as presented below.

- The first technique, proposed by Ludwig Boltzmann (1868), consists in averaging trajectories in phase space. Thus, considering an instantaneous microscopic property $\mathcal{A}(\Gamma(t))$, the corresponding macroscopic observable property $\mathcal{A}_{obs}$ is obtained by time averaging on $\mathcal{A}(\Gamma(t))$ as follows :

$$\mathcal{A}_{obs} = \langle \mathcal{A}(\Gamma) \rangle_{time} = \lim_{t_{obs} \to \infty} \frac{1}{t_{obs}} \int_0^{t_{obs}} \mathcal{A}\big(\Gamma(t)\big) dt \qquad (3.1)$$

  Where t_{obs} is the observation time and $\langle \quad \rangle_{time}$ denotes the time average.

- The second method, proposed by Josiah Willard Gibbs (1902), consists in calculating the observable $\mathcal{A}_{obs}$ by performing, at a given time τ, an ensemble averaging on

$\mathcal{A}(\Gamma)$ weighted by the probability denoted $f(\vec{r}^N, \vec{p}^N)d\vec{r}^N d\vec{p}^N$, that at this time τ the system is in a microstate ($\Gamma(\tau)$) represented by a point of the element $d\vec{r}^N d\vec{p}^N$ of the phase space:

$$\mathcal{A}_{obs} = \langle \mathcal{A}(\Gamma) \rangle_{ensemble} = \int \mathcal{A}(\vec{r}^N, \vec{p}^N) f(\vec{r}^N, \vec{p}^N) d\vec{r}^N d\vec{p}^N \quad (3.2)$$

Where $\langle \quad \rangle_{ensemble}$ is the ensemble average and $f(\vec{r}^N, \vec{\mathrm{p}}^N)$ is the probability density written as:

$$f(\vec{r}^N, \vec{\mathrm{p}}^N) = \frac{\exp(-\beta E(\vec{r}^N, \vec{\mathrm{p}}^N))}{Q(\vec{r}^N, \vec{\mathrm{p}}^N)} \quad (3.3)$$

In which E is the Hamiltonian of the system corresponding to the sum of the kinetic energy *K* and the potential energy U ($E = U + K$). β is the inverse of the temperature Boltzmann constant product $\beta = 1/K_b T$. Finally $Q(\vec{r}^N, \vec{\mathrm{p}}^N)$ represents the partition function depending on the statistic ensemble in which the simulation is performed. The concept of ensemble and associated partition function will be discussed in detail, in the section 3.1.4.

Throughout the rest of the manuscript, the notation $\langle \quad \rangle$ is used to designate either a time average ($\langle \quad \rangle_{time}$) or an ensemble average ($\langle \quad \rangle_{ensemble}$), depending on the type of simulation.

3.1.3 Ergodic Hypothesis

The ergodic hypothesis was formulated for the first time by Ludwig Boltzmann in the context of his kinetic theory of gases [3]. This hypothesis states that at equilibrium, the time average (as measured experimentally) of a property is equivalent to its ensemble average. This hypothesis, although not yet theoretically demonstrable, is therefore essential for comparing experimental measurements with results obtained from statistical physics. Concerning the analysis of molecular simulation results, this assumption implies an equivalence between the results obtained by two different simulation techniques namely molecular dynamics (based on time averaging) and Monte Carlo simulations (based on statistical averaging)[2]

3.1.4 Statistical Ensembles

In statistical physics, an ensemble is the collection of all microstates, with the associated probabilities, for which the same macroscopic thermodynamic restrictions are imposed [1,2]. A statistical ensemble is defined by its partition function Q (depending only on macroscopic constrained properties) and the associated thermodynamic potential Ψ [4]. The notion of thermodynamic potential is of primary importance since it makes the connection between statistical mechanics and classical thermodynamics. It is linked to the partition function by [1]:

$$\Psi = -k_B T ln(Q) \quad (3.4)$$

Average macroscopic properties can then be directly derived from the partition function with the help of thermodynamic identities[4]. Hereafter, we presented the main ensembles used in the cope of this thesis. For more details about other statistical ensembles, the reader is referred to reference books[1,2,5,6]

[1] *excepted in NVE, due to unfortunate historical definition of statistical entropy by Boltzmann*[2]

3.1.4.1 Canonical Ensemble (NVT)

The canonical ensemble (NVT) corresponds to a macroscopic system containing N particles in a fixed volume V that can exchange energy E with a larger system to keep its temperature T constant. In such an ensemble, a microstate i with a total energy E_i can occur with a probability P_i^{NVT} defined as follow:

$$P_i^{NVT} = \frac{\exp(-\beta E_i)}{Q_{NVT}} \tag{3.5}$$

Where Q_{NVT} is the canonical ensemble partition function. The normalization of P_i^{NVT} on all Ω microstates (i.e. $\sum_i^{\Omega} P_i^{NVT} = 1$), allows to deduce the expression of Q_{NVT}, written as:

$$Q_{NVT} = \sum_i^{\Omega} exp(-\beta E_i) \tag{3.6}$$

In classical statistical mechanics, the variable $\vec{r}$ and $\vec{p}$ can vary continuously, so that the number of microstates is actually uncountable. In this case the discrete sum of equation (3.6) over all Ω microstates must be replaced by an integral over configurations. The canonical partition function in its continuous form is then written as:

$$Q_{NVT} = \frac{1}{h^{3N}N!} \int_{\vec{r}^N} \int_{\vec{p}^N} d\vec{r}^N d\vec{p}^N exp(-\beta E(\vec{r}^N, \vec{p}^N)) \tag{3.7}$$

Where h is the Plank constant, h^3 is a normalization factor that can be considered as the volume of a microstate**.** The factor $1/N!$ is used to take into account the indistinguishability in case of identical particles.

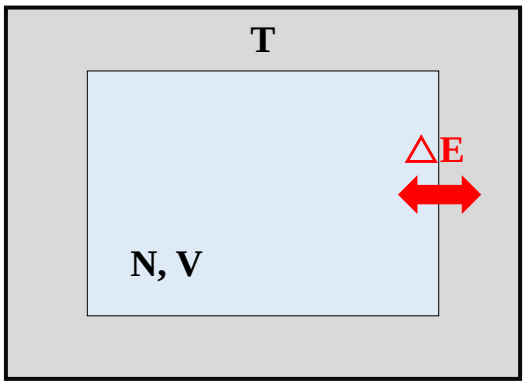

Figure 3.1 Schematic representation of the canonical situation.

The thermodynamic potential of the canonical ensemble is the Helmholtz free energy F defined as follow:

$$F = -k_B T ln(Q_{NVT}) \tag{3.8}$$

In the NVT ensemble, macroscopic conjugate variables (chemical potential μ, pressure P and entropy S) are deduced from the partition function Q_{NVT} as follows:

$$\mu = \left(\frac{\partial F}{\partial N}\right)_{V,T} = -k_B \left(\frac{\partial Q_{NVT}}{\partial N}\right)_{V,T} \tag{3.9}$$

$$S = -(\frac{\partial F}{\partial T})_{N,V} = k_B ln Q_{NVT} + k_B T(\frac{\partial Q_{NVT}}{\partial T})_{N,V} \quad (3.10)$$

$$P = -(\frac{\partial F}{\partial V})_{N,T} = k_B T(\frac{\partial Q_{NVT}}{\partial V})_{N,T} \quad (3.11)$$

3.1.4.2 Microcanonical Ensemble (NVE)

This statistical ensemble is composed of different micro-states corresponding to a system macroscopically considered as isolated, i.e. the particle number N, the volume V and the total energy E are kept constant. The NVE ensemble corresponds to thermodynamic conditions where the system does not exchange matter and energy with its surrounding. At macroscopic equilibrium, the Ω_{NVE} microstates have the same probability P_i^{NVE} of occurrence defined as :

$$P_i^{NVE} = \frac{1}{\Omega_{NVE}} \quad (3.12)$$

Where Ω_{NVE} is the partition function in the microcanonical ensemble. It is expressed in its classical continuous form as

$$\Omega_{NVE} = \frac{1}{h^{3N} N!} \int_{\vec{r}^N} \int_{\vec{p}^N} d\vec{r}^N d\vec{p}^N \quad (3.13)$$

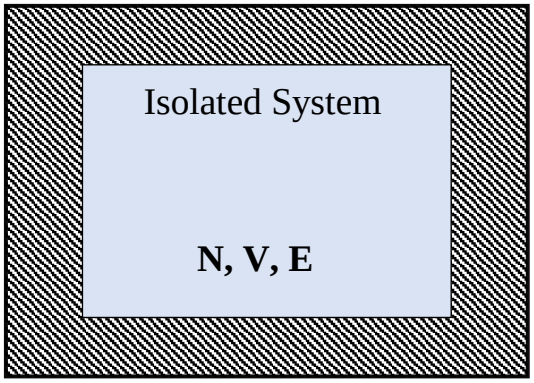

Figure 3.2 Schematic representation of the microcanonical (NVE) situation

The thermodynamic potential of the NVE ensemble is the thermodynamic entropy S of the system defined as:

$$S = k_B \ln(\Omega_{NVE}) \quad (3.14)$$

3.1.4.3 Isothermal-Isobaric Ensemble (NPT)

The isothermal-isobaric ensemble is one of the most widely used since it corresponds to the conditions for which most experiments are carried out. NPT ensemble corresponds to a closed macroscopic system for which the pressure P and the temperature T are kept constant by exchanging with the surroundings heat (thermostat) and work (barostat). The partition function in NPT ensemble is given in its classical continuous form as follows:

$$\Delta_{NPT} = \frac{1}{h^{3N} N! V_0} \int_v \, dv \int_{\vec{r}^N} \int_{\vec{p}^N} d\vec{r}^N d\vec{p}^N exp(-\beta E(\vec{r}^N, \vec{p}^N)) \quad (3.15)$$

Where Δ_{NPT} is the isothermal-isobaric ensemble partition function and the factor V_0 is a normalization factor.

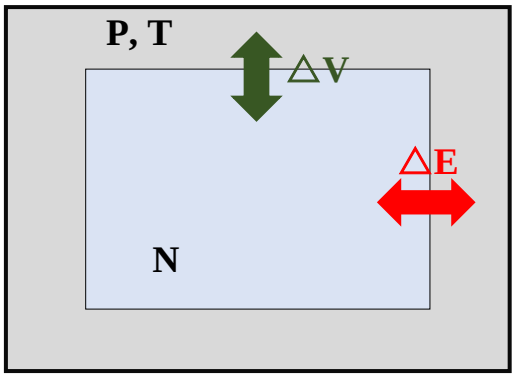

Figure 3.3 Schematic representation of the isothermal-isobaric ensemble situation

The thermodynamic potential associated to Δ_{NPT} is the Gibbs free enthalpy, defined as:

$$G = -k_B T ln(\Delta_{NPT}) \tag{3.16}$$

3.1.4.4 Grand Canonical Ensemble (μVT)

The grand canonical ensemble (μVT) represents the collection of microstates corresponding to a macroscopic system for which the volume V, the chemical potential μ and the temperature T are constrained. μ and T are kept constant by exchanging particles and energy respectively, with an external reservoir. Therefore, μVT ensemble is useful to represent open thermodynamic systems.

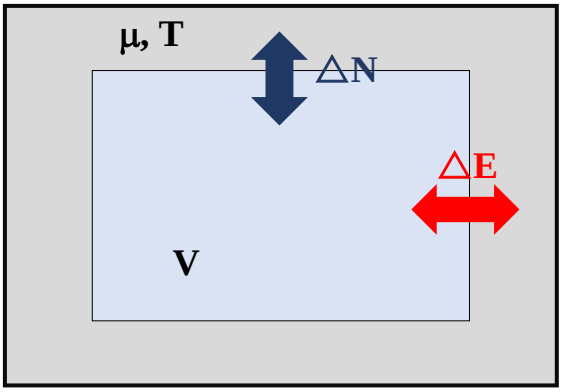

Figure 3.4 Schematic representation of the grand canonical ensemble situation.

The partition function in the μVT ensemble $\Xi_{\mu VT}$ is given in its classical continuous form as:

$$\Xi_{\mu VT} = \sum_{N=0}^{\infty} \frac{exp(\beta \mu N)}{h^{3N} N!} \int d\vec{r}^N d\vec{p}^N exp(-\beta U(\vec{r}^N, \vec{p}^N)) \tag{3.17}$$

The thermodynamic potential associated to $\Xi_{\mu VT}$ is the Landau free energy J, also called grand potential, defined as:

$$J = -k_B T ln(\Xi_{\mu VT}) \tag{3.18}$$

Table 3.1 Summary of statistical classical ensembles with thermodynamic functions and the corresponding thermodynamic identities

Statistical ensemble	Thermodynamic potential	Thermodynamic identity
Microcanonical NVE	Entropy S $S = k_B \ln(\Omega_{NVE})$	$dS = \frac{1}{T}dE + \frac{P}{T}dV - \frac{\mu}{T}dN$
Canonical NVT	Helmholtz free energy F $F = -k_B T ln(Q_{NVT})$	$dF = -SdT - PdV + \mu dN$
Isothermal-isobaric NPT	Gibbs energy G $G = -k_B T ln(\Delta_{NPT})$	$dG = -SdT + VdP + \mu dN$
Grand canonical μVT	Grand potential J $J = -k_B T ln(\Xi_{\mu VT})$	$dJ = SdT + PdV + Nd\mu$

3.2. Molecular Simulations

In the following sections, we present the two classical molecular simulation techniques used in this thesis: Molecular Dynamics (MD) and Monte Carlo (MC). Before we detail these simulation methods, we introduce the notion of force fields essential to both MC and MD simulations.

3.2.1 Interaction Potential and Force Evaluation

In this section we present a general description of force fields followed by the details of the two force fields used in this work: the Mie Chain Coarse Grained model (MCCG)[7] and the Transferable Potential for Phase Equilibria united atom (TraPPE-ua)[8].

3.2.1.1 Generality on Force Fields

An important step in molecular simulations is the description of the different interactions between particles by the mean of a total energy potential. The choice of this energy potential is crucial for the accuracy and the reality of simulation results [1,2,9]. With regard to molecular (polyatomic) systems, the potential between the atoms of the system is divided into intramolecular energy (U_{intra}) between the atoms which are connected by one, two or three covalent bonds, and intermolecular energy (U_{inter}), between the other atoms (separated by

more than 3 covalent bonds or unbounded). The total energy potential (U_{total}) can then be written as:

$$U_{total} = U_{intra} + U_{inter} \tag{3.19}$$

A. Intermolecular Interactions

Intermolecular unbounded interactions are usually divided in two terms and expressed as a sum of the form:

$$U_{inter} = U_{elec} + U_{vdw} \tag{3.20}$$

where U_{elec} is the electrostatic energy, resulting from the coulombic interaction between permanent point charges and U_{vwd} is the Van der Waals energy, including dispersive interactions arising from electronic field fluctuations, polar momentum and repulsive interactions due to steric exclusion. Generally, intermolecular interactions are modeled using pairwise interaction potential between two interacting particles i and j. The corresponding pair (two body) potentials used in this work are detailed thereafter in each force field presentation section.

B. Intramolecular Interactions

For flexible molecules, the intramolecular energy potential can be written as the sum of four terms[9]:

$$U_{intra} = U_{strech} + U_{bend} + U_{torsion} + U_{dn} \tag{3.21}$$

Where U_{strech} is the stretching energy, arising from the bond length variation between two atoms, U_{bend} is the bending energy, resulting from the variations of the angle formed by two successive chemical bonds, $U_{torsion}$ is the torsion energy, induced by the variations of either the proper dihedral angle formed by four successive atoms in a chain or the improper dihedral angle formed by three atoms centered around a fourth atom. U_{dn}, is the distant neighbor energy arising from interactions between atoms belonging to the same molecule but separated by more than three chemical bonds. U_{dn} is generally modeled by a pair potential. Schematic representations of these potentials are provided by Figure 3.5.

3.2.1.2 Efficient Evaluation of Forces

A. Periodic Boundary Conditions

One of the main limitations in molecular simulations comes from the finite size of the simulation box. Evaluating the interactions on an isolated simulation box, would lead to an inaccurate estimation of the forces due to surface effects [11]**.** Indeed, the particles on the boundaries of the simulation box interact with less neighbors than the particles in the center of the box. To avoid this problem, one could consider a simulation box of very large size, however it would induce very important computing time. Alternatively to this, we use periodic boundary conditions (PBC)[1,2,5,6]. This technique consists of performing simulations in an "infinite" system, by repeating the simulation box in all the directions of the space as presented in Figure 3.6. Thus, a particle on the boundary of a given box, interacts with that on the boundary of the

opposite box, resulting in a significant reduction in surface effects. The distance between particles is evaluated using a modified procedure known as the minimum image convention [1,2]**.** This method considers only the interactions of a given particle with its closest images.

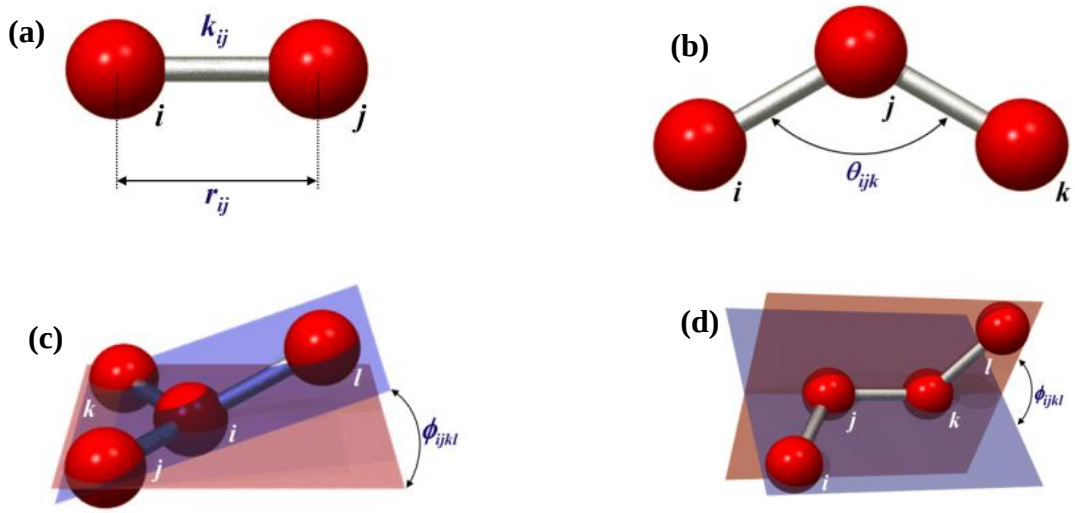

Figure 3.5 Schematic representation of intramolecular interactions. Panel (a) represents stretching interactions , panel (b) represents the bending angle θ_{ijk} , panel (c) represents the proper dihedral angle φ_{ijkl} and panel (c) the improper dihedral angle φ_{ijkl} Figures are taken from[10]

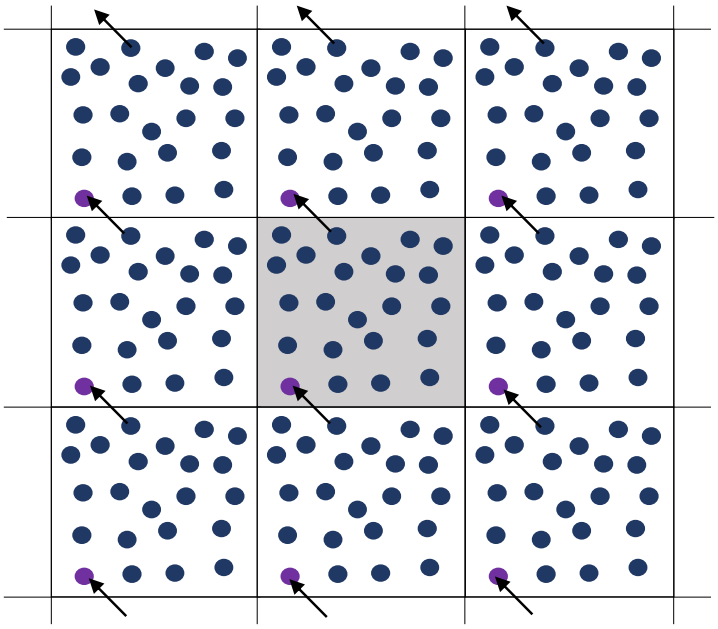

Figure 3.6 Schematic representation of a 2D periodic system. The central grey box is the primary box. Atoms can enter and leave each boxes across each of four boundaries.

B. Truncation of Intermolecular Interactions

Considering intermolecular potential energy, the Van der Waals interactions decay quite rapidly compared to the electrostatic interactions[1,2,9]**.** To save computational resources, it is possible to limit the number of particles interacting with a given particle by ignoring ones that are beyond

some distance r_c referred as cutoff radius. This method is known as truncation of pair potential**.** However, using this artifact can negatively impact the simulation results**.** Indeed, the truncation can induce a strong discontinuity of the potential and the derived forces at a distance $r_{ij} = r_c$. To overcome this problem, long range tail corrections are applied during our simulations. These corrections are applied to the truncated energy and derived properties such as pressure etc. More details about long range contributions can be found in reference books[1,2,5]

It is worth recalling that the aforementioned truncation method is only applicable to Van der Waals interactions. For electrostatic interactions, that have longer range, more advanced methods such as Ewald sum[12] or Particle Mesh Ewald[13] must be used.

C. Verlet Neighbor List

The use of a cutoff radius makes it possible to limit the number of forces to be calculated, but the number of tests of intermolecular distances between a given particle i and the $N_{rc} - 1$ particles at a distance $r < r_c$ remains the same as without a cutoff radius. To reduce this number of tests, Verlet[14] proposed a method consisting in listing the particles located at a distance $r_l > r_c$ of the particle i . The same list is used in the evaluation of the forces acting on this given particle and the $N_{rc} - 1$ atoms for several successive time steps. This list is updated once one of the N_{rc} atoms has traveled the distance $(r_l - r_c)$**.** r_l is referred as list radius. In our work, this method has been used for Molecular dynamic simulations, however it can also be implemented for Monte Carlo simulations[2].

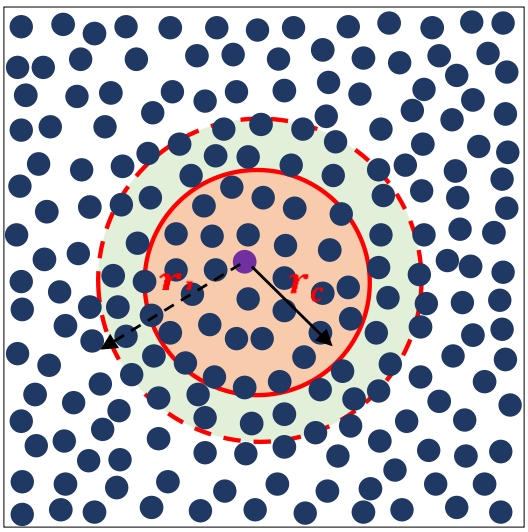

Figure 3.7 Schematic representation of the cutoff and verlet neighbor list spheres around central purple atom.

3.2.1.3 The Mie Chain Coarse Grained Force Field

The Mie Chain Coarse Grained (MCCG) model was proposed by Hoang et al. [7]**.** The molecular representation with this force field consists in homo-nuclear chains composed of *N* freely jointed spheres. Interaction between two non-bonded spheres *i* and *j* is described by the Mie λ-6 pair potential [15]:

$$U_{inter}(r_{ij}) = \left(\frac{\lambda_{ij}}{\lambda_{ij}-6}\right)\left(\frac{\lambda_{ij}}{6}\right)^{6/(\lambda_{ij}-6)} \varepsilon_{ij}\left[\left(\frac{\sigma_{ij}}{r_{ij}}\right)^{\lambda_{ij}} - \left(\frac{\sigma_{ij}}{r_{ij}}\right)^{6}\right] \quad (3.22)$$

where ε_{ij}, σ_{ij}, λ_{ij} and $r_{ij} = |r_i - r_j|$, are respectively the potential well depth, the collision diameter, the exponent characterizing the repulsive interactions and the distance between two unbounded spheres i and j.

The calculation of MCCG parameters relies on an extended corresponding state strategy [16,17]. For each molecule, its parameters ε and σ are determined respectively from the critical temperature T_c and the saturated liquid density $\rho_{sat,l}$ at a reduced temperature $T_r = T_c/T = 0.7$, while N and λ are determined from the acentric factor [18] and a reference liquid viscosity data.

In the scope of this work, MCCG has been used to model n-hexane, n-heptane, n-dodecane and carbon dioxide. The parameters corresponding to these molecules are listed in Table 3.2.

Table 3.2 Mie Chain Coarse Grained (MCCG) parameters of n-hexane, n-heptane, n-dodecane and carbon dioxide.

Molecules	N	σ_{ii} (Å)	ε_{ii}/k_B [K]	λ_{ii}
n-hexane	3	3.8620	267.8800	13.380
n-heptane	3	4.0490	294.2929	14.034
n-dodecane	5	4.0250	336.3300	15.840
co_2	2	2.8610	211.5395	16.930

When dealing with mixtures, σ_{ij} and ε_{ij} are calculated using the classical Lorentz-Berthelot combining rules[19,20] defined as follow:

$$\sigma_{ij} = \frac{(\sigma_{ii}+\sigma_{jj})}{2} \quad (3.23)$$

$$\varepsilon_{ij} = \sqrt{\varepsilon_{ii}\varepsilon_{jj}} \quad (3.24)$$

The repulsion exponent of the cross-interactions, λ_{ij}, is evaluated using the following arithmetic average :

$$\lambda_{ij} = \frac{\lambda_{ii}+\lambda_{jj}}{2} \quad (3.25)$$

3.2.1.4 The Transferable Potential for Phase Equilibria Force Field

The Transferable Potential for Phase Equilibria united atom (TraPPE-ua) was proposed by Siepmann et al.[8]**.** The parametrization of this force field is mainly based on a fitting procedure to reproduce experimental phase equilibrium data [21]. In the scope of this work, we used TraPPE-ua to model linear n-alkanes **(**cf. Chapter 4.). The description of n-alkane molecules with the TraPPE-ua model relies on united-atom groups, i.e. the hydrogen atoms are not explicitly described. The intermolecular non-bonded interactions are described by the Lennard-Jones (LJ) 12-6 pair potential[22,23]:

$$U_{inter}(r_{ij}) = 4\varepsilon_{ij}\left[\left(\frac{\sigma_{ij}}{r_{ij}}\right)^{12} - \left(\frac{\sigma_{ij}}{r_{ij}}\right)^{6}\right] \quad (3.26)$$

where, r_{ij} is the distance between particles *i* and *j*, ε_{ij} and σ_{ij} are the LJ interaction parameters representing the depth of LJ potential well and the size of particles, respectively.

For unlike non-bonded united-atoms, the LJ parameters are determined using the standard Lorentz-Berthelot combining rules as defined in equations (3.23) and (3.24).

The bond interaction is described in two different ways, depending on the type of simulation as recommended by Kelkar et al.[24]. For Monte Carlo simulations, the bond length is considered fixed since this method has been shown to be more efficient for MC simulations [25]**.** Concerning molecular dynamic simulations, the use of a harmonic bond stretching has been adopted. The harmonic potential is defined as follows:

$$U_{stretch} = \frac{K_r}{2}\left(r - r_{eq}\right)^2 \quad (3.27)$$

where, r is the distance between adjacent particles, r_{eq} and K_r are parameters of the harmonic bond stretching potential to represent equilibrium bond length and the force constant, respectively. Since TraPPE-ua force field was not provided with bond stretching parameters, we used the ones from Mundy et al.[25]**.** This modification of the force field is known to have a negligible effect on the performance of the force field[24].

The bending potential is described by a harmonic potential:

$$U_{bend} = \frac{K_\theta}{2}(\theta - \theta_{eq})^2 \quad (3.28)$$

Where θ_{eq} and K_θ, are the equilibrium bending angle and the force constant, respectively.

The torsional potential interactions for sites separated by three bonds is described by a cosines series as follows:

$$U_{torsion} = c_0 + c_1(1 + \cos(\emptyset)) + c_2(1 - \cos(2\emptyset)\ ) + c_3(1 + \cos(3\emptyset)) \quad (3.29)$$

where $\emptyset$ is the proper dihedral angle and $c_{\mathrm{i=0;3}}$ are the Fourier coefficients.

All the TraPPE-ua parameters used in this work can be found elsewhere[21,25].

3.2.2 Monte Carlo Simulations

Historically, the Monte Carlo method is the first of the classical molecular simulation techniques. It was developed in 1953 with the work of Metropolis et al.[11]**.** This purely statistical method randomly generates a large number of configurations of a particles system, in order to explore its potential energy surface[1,2]. By its construction, this method is intimately related to statistical mechanics and is well suited to the study of equilibrium thermodynamic properties such as density and its derivative properties as well as fluid phase equilibrium properties [9,26].

The macroscopic observables are determined by statistical ensemble averaging (cf. section 3.1.2) of microscopic properties on the different configurations of the system. However, a purely random generation of configurations generates with the same probability the configurations of high potential energies, having little physical meaning and that of low potential energies, physically more realistic. To solve this problem, Metropolis et al.[11] proposed a method that introduces a bias to preferentially generate low energy configurations [1].

In the scope of this thesis, Monte Carlo simulations have been performed using an in-house code[7] for the MCCG force field and the free Monte Carlo simulation software Towhee MCCS[27] for simulations with TraPPE-ua.

3.2.2.1 Metropolis Algorithm Principle

The metropolis algorithm is based on the generation of configurations following a Markov Chain, i.e. the different configurations are generated randomly so that the transition probability from one state to another only depends on these two states[1,2,9,11].

Starting from an initial configuration of the system with a given probability density ρ_{old}, the probability of acceptance of a new configuration with a probability density ρ_{new}, referred as $P_{acc}(old \rightarrow new)$, follows the following criterion:

$$P_{acc}(old \rightarrow new) = \min(1, \frac{\rho_{new}}{\rho_{old}}) \tag{3.30}$$

The implementation of this criterion in the Metropolis algorithm is as follow:

- If $\rho_{new} > \rho_{old}$, the new configuration is accepted
- If $\rho_{new} < \rho_{old}$, a random number γ is chosen between 0 and 1 and compared to ρ_{new}/ρ_{old}. If $\rho_{new}/\rho_{old} > \gamma$, the new configuration is accepted, otherwise it is rejected and the system stays in its initial configuration.

At equilibrium, the metropolis scheme is shown to respect the microscopic reversibility (or detailed balance) principle[9], which basically states that at equilibrium the transition probability from a configuration old to a configuration new equals the transition probability from new to old. This principle is shown to be a sufficient condition to achieve a Markov chain. For more details, the reader is referred to [1,2,9].

3.2.2.2 Elementary Monte Carlo Trial Moves

As previously discussed, the aim of the Metropolis algorithm is to sample the microscopic system in the most probable configurations. To do so, the new configurations are generated by the mean of Monte Carlo moves (MC moves). In this section, are presented the main elementary MC moves used in the scope of this thesis.

A. Translation Move

This MC move is the most basic one. It consists in randomly choosing a particle and displacing it from one position to another, according to a translation vector $d\vec{r}$. In order to satisfy the microreversibility principle[2] briefly mentioned above, $d\vec{r}$ has to be a random vector, uniformly selected in an interval $[-r_{max}, r_{max}]$, where r_{max} is the maximum amplitude of $d\vec{r}$. This restriction on the amplitude of $d\vec{r}$ also makes it possible to control the average acceptance rate of this MC move.

B. Rotation Move

Another basic MC move is the rotation one. It consists of applying, to a randomly selected molecule, a rotation in a random direction. In a similar way to the translation move, the rotation

angle $d\alpha$, is chosen in an interval $[-\alpha_{max}, \alpha_{max}]$ so as to satisfy the microreversibility principle and to control the acceptance rate of such a trial move.

C. Volume Change Move

The aforementioned translation and rotation MC moves applies in any ensemble, however, when performing simulations in a case where volume fluctuates, for example in NPT or other isobaric ensembles, a volume change move is required. This move consists in expanding/shrinking the simulation box by a randomly selected amount of volume dV. This volume variation dV is chosen in an interval $[-\Delta V_{max}, \Delta V_{max}]$. The volume move is applied in a way that the dimensionless positions of the particles as well as dimensionless distances between particles are not changed by the move[1,9].

D. Insertion/ Destruction Moves

This move is specific to MC simulations performed in the grand canonical ensemble (GCMC). It consists of choosing a random particle i and to perform random insertions and deletions of this particle to and from the simulation box. Thus, such a move implies the fluctuation of particles number in the simulation box. However, it worth noting that for very dense system or large molecules, the acceptance rate of this MC move, especially insertion moves, can be dramatically low due to overlapping of molecules[9].

In addition to the elementary trial moves presented in this section, there are several more sophisticated moves[9] such as reptation, pivot, regrowth which are required to change the internal conformation of flexible molecules. Furthermore, for systems consisting of very long linear molecules, or molecules with ramifications, a biased method known as configurational bias[28,29] has been proposed.

3.2.3 Molecular Dynamics Simulations

In this work, we used Molecular Dynamic simulations to compute transport and structural properties in addition to thermodynamic quantities. Depending on the force field, two simulations tools were used. For MCCG we used an in-house code[7], while for TraPPE-ua, simulations were performed with the free MD simulation tool LAMMPS[30].

3.2.3.1 Molecular Dynamics Principle

The classical molecular dynamics technique consists in studying the evolution over time of a set of particles to deduce its macroscopic properties using space-time averages[1,2,5]. These averages are representative of the studied system provided that the particles explore a significant part of the phase space. The displacement of each particle i with a position $\vec{r}_i$ and a momentum $\vec{p}_i$ is governed by Newton's second law of motion defined as:

$$\begin{cases} m_i \frac{d\vec{r}_i}{dt} = \vec{p}_i \\ \frac{d\vec{p}_i}{dt} = \vec{F}_i \end{cases} \tag{3.31}$$

Where m_i is the mass of particle i and $\vec{F}_i$ the sum of forces exerted on particle i. The resulting differential equation system is solved using an algorithm which main steps are as summarized below:

- The system initialization:

It consists in defining the initial positions, velocities and accelerations of the particles constituting the system. The particles are positioned either randomly in the simulation box or in a defined crystal structure. Regarding the initialization of the velocities, it must be done with much more precaution. Indeed, the velocities directions must be randomly chosen and the total momentum must be zero on each direction. Concerning the amplitude of these velocities, it is chosen according to Maxwell-Boltzmann distribution [31,32]. Initial accelerations are set to zero.

- Calculation of forces

The system being conservative, the forces are then directly derived from the total potential energy as follows:

$$\vec{F}_i = -\vec{\nabla}\mathrm{U_i} \tag{3.32}$$

Where U_i is the total potential energy presented in section 3.2.1.

- Solving of the equations of motion

Integration of newton's equations of motion is done by a numerical algorithm. There are several integration methods[33] among which the Euler method **,** the Runge-Kutta methods, the leapfrog method**,** the predictor-corrector methods or the Verlet-velocity method. In the case of MD simulations performed during this work, we used the Verlet-velocity[34] method. The advantage of this method is that it is fast, relatively simple to implement, reversible over time and allows good energy and momentum conservation in the long term[1,2]. The algorithm is based on a Taylor expansion of position $\vec{r}_i$ of a given particle i at a time t. The particle's position at $t + \delta t$ is given as follows:

$$\vec{r}_i(t+\delta t) = \vec{r}_i(t) + \delta t \cdot v_i(t) + \frac{1}{2}\delta t^2 a_i(t) + O(\Delta t^3) \tag{3.33}$$

Where $\vec{v}_i(t)$ and $\vec{a}_i(t)$ are respectively the velocity and acceleration of the particle i at t.

The next step consists in calculating the particle's velocity at $t + \frac{1}{2}\delta t$ and its acceleration at $t + \delta t$ from the calculation of forces.

$$\vec{v}_i(t+\tfrac{1}{2}\delta t) = \vec{v}_i(t) + \frac{1}{2}\delta t \cdot \vec{a}_i(t) \tag{3.34}$$

$$\vec{a}_i(t+\delta t) = -\frac{1}{m_i}\vec{\nabla}(U_i(t+\delta t)) \tag{3.35}$$

Finally, we deduced the particle's velocity at $t + \delta t$:

$$\vec{v}_i(t+\delta t) = \vec{v}_i\left(t+\tfrac{1}{2}\delta t\right) + \frac{1}{2}\delta t \cdot \vec{a}_i(t+\delta t) + O(\Delta t^3) \tag{3.36}$$

The truncation error of the Verlet-velocity method is of order 3 in time, i.e. $O(\Delta t^3)$.

- Calculation of macroscopic properties by time averaging

At this step, the macroscopic properties accessible in a given statistical ensemble are deduced from the microscopic properties using time averaging.

3.2.3.2 Molecular Dynamics at Constant Temperature and /or Pressure

The natural ensemble in which molecular dynamic simulations are performed is the NVE ensemble. Indeed, we study the time evolution of a system of *N* particles, in a volume *V* and with a total energy *E* which is a constant of motion [2]. However, it is sometimes necessary to perform the simulations in other ensembles. This is the case for example when one wants to compare results of molecular simulations with experimental results at fixed temperature and pressure. For such situation, simulation in NPT ensemble seems more adequate[1]. To maintain the temperature of a system one need a thermostat, while the pressure is kept constant using a barostat. In the followings, we described some barostat and thermostat used in the scope of this work.

A. Molecular Dynamics at Constant Temperature

At thermodynamic equilibrium, according to the equipartition theorem[1], the temperature T of a system is linked to the average kinetic energy as follow:

$$T = \frac{1}{k_B N_f} \langle \sum_{i=1}^{N} \frac{|\vec{p}_i|^2}{m_i} \rangle \tag{3.37}$$

Where N_f is the degree of freedom of the system.

From equation (3.37), it is convenient to define an instantaneous kinetic temperature $\mathcal{T}$[1,2] such as:

$$\mathcal{T} = \frac{1}{k_B N_f} \sum_{i=1}^{N} \frac{|\vec{p}_i|^2}{m_i} \tag{3.38}$$

At equilibrium, the average of the instantaneous temperature $\langle \mathcal{T} \rangle$ is equivalent to the macroscopic temperature *T*. Since the instantaneous temperature $\mathcal{T}$ of the system is directly linked to the particles momenta, one can obviously alter the temperature of the system to a target temperature T_0 by modifying particles velocity. Conceptually, this is done by coupling the system to a heat bath which constant temperature correspond to T_0[35]. For MD simulations at constant temperature performed in this work, we used Berendsen and Nosé-Hoover thermostats that are briefly presented thereafter.

- Berendsen Thermostat

For the Berendsen[36] thermostat, also known as the weak coupling thermostating method, the system is coupled to an external heat source T_0 to maintain its temperature constant. At each timestep δt, the particle's momenta are directly rescaled as follow:

$$\vec{p}_i^{\,new} = \vec{p}_i^{\,old} \sqrt{1 + \frac{\delta t}{\tau_T} \left(\frac{T_0}{\mathcal{T}} - 1\right)} \tag{3.39}$$

Where τ_T is the thermostat coupling parameter. In practice, the choice of τ_T is crucial for the thermostat efficiency[1]. A typical value is $\tau_T \approx 0.1\ ps$.

The Newton's equations of motion are then rewritten as follow:

$$\begin{cases} \mathrm{m_i}\frac{\mathrm{d}\vec{r_i}}{\mathrm{dt}} = \vec{p}_i \\ \frac{\mathrm{d}\vec{p}_i}{\mathrm{dt}} = -\vec{\nabla}U_i - \frac{1}{2\tau_T}\left(\frac{T_0}{\mathcal{T}} - 1\right)\vec{p}_i \end{cases} \tag{3.40}$$

However, as pointed out by different authors[37,38], the ensemble generated when using the Berendsen thermostat is not canonical.

- Nosé-Hoover Thermostat

This thermostat, firstly proposed by Nosé [39]and modified by Hoover [40] consists of considering the heat bath as an integral part of the system, which adds an additional degree of freedom to the extended system. Thus, a new coordinate s is defined, with an effective mass Q_s and an associated momentum p_s . The Newton's equations of motion then become:

$$\begin{cases} m_i\frac{d\vec{r}_i}{dt} = \vec{p}_i \\ \frac{d\vec{p}_i}{dt^2} = -\vec{\nabla}U_i - \xi\vec{p}_i \\ \frac{d\ \xi(t)}{dt} = \frac{1}{Q_s}\left(\sum_{i=1}^{N}\frac{\vec{p}_i^2}{m_i} - N_f k_b T_0\right) \\ with \xi(t) = \frac{p_s}{Q_s} \end{cases} \tag{3.41}$$

Physically, ξ(t) acts like a fictitious friction coefficient, introduced to reduce or increase the particle's velocity and consequently the kinetic energy until the target temperature T_0 is reached. Q_s determines the relaxation of the dynamics of the friction. In practice, it controls the coupling with heat bath and therefore its choice is of primary importance for the thermostat efficiency. Contrary to Berendsen thermostat, Nosé-Hoover thermostat yield a canonical probability density distribution[1,2].

B. Molecular Dynamics at Constant Pressure

According to the virial theorem[41], the macroscopic pressure P of the system can be derived from the temperature T and the interaction between particles as follow:

$$P = \frac{N_f k_B T}{V} N_f k_B T + \frac{\langle W \rangle}{V} \tag{3.42}$$

Where W is the internal virial defined as:

$$\langle W \rangle = \langle \frac{1}{3}\sum_{i=1}^{N-1}\sum_{j>i}^{N}\vec{r}_{ij}\cdot\vec{\mathrm{F}}_{ij} \rangle \tag{3.43}$$

Where $\vec{\mathrm{r}}_{ij} = \vec{\mathrm{r}}_j - \vec{\mathrm{r}}_i$ is the distance between particles j and i and $\vec{\mathrm{F}}_{ij} = \vec{\mathrm{F}}_j - \vec{\mathrm{F}}_i$ is the force exerted by j on i.

The instantaneous pressure[42] $\mathcal{P}$ is then defined from equations (3.42) and (3.43) as:

$$\mathcal{P} = \frac{1}{V}\left[N_f k_B \mathcal{T} + \frac{1}{3}\sum_{i=1}^{N-1}\sum_{j>i}^{N} \vec{r}_{ij} \cdot \vec{\mathrm{F}}_{ij}\right] \tag{3.44}$$

where V is the system volume on which the pressure is evaluated.

As for thermostat, it appears that if the number of particles is constant, one can control the instantaneous pressure of the fluid by a variation of the volume V and consequently inter-particles distances. In this work, two barostatting methods have been used: the Berendsen barostat for MCCG and Hoover barostat for TraPPE-ua. Such barostats are briefly presented below.

- Berendsen Barostat

This barostat, proposed by Berendsen et al.[36] consist of coupling the fluid to a piston subject to an external constant pressure P_0. At each time step, the volume V is rescaled as follow:

$$V^{new} = V^{old}\left[1 - \frac{k_T \delta t}{3\tau_p}(P_0 - \mathcal{P})\right] \tag{3.45}$$

where k_T is the isothermal compressibility and τ_p is the barostat coupling parameter. This leads to the following modified Newton's equations of motion:

$$\begin{cases} \frac{d\vec{r}_i}{dt} = \frac{\vec{p}_i}{m_i} - k_T m_i \left(\frac{P_0 - \mathcal{P}}{3\tau_p}\right)\vec{r}_i \\ \frac{d\vec{p}_i}{dt} = -\vec{\nabla} U_i \end{cases} \tag{3.46}$$

As for Berendsen thermostat, this barostat does not provide a correct distribution of configurations [38].

- Hoover Barostat

In a similar way to Nosé-Hoover thermostat, the method consists in considering an extended-system composed of the system and an external piston subject to a constant pressure P_0. It was firstly proposed by Hoover[43]. However, when coupled to a thermostat to perform a simulation in the NPT ensemble, this method was shown to fail to generate an accurate NPT ensemble. In this work, we used the modified version proposed by Martyna[44] which is referred in the literature as Hoover barostat **.** The newton's equations of motion are then rewritten as follow:

$$\begin{cases} \frac{d\vec{r}_i}{dt} = \frac{\vec{p}_i}{m_i} - \frac{p_\chi}{Q_\chi}\vec{r}_i \\ \frac{d\vec{p}_i}{dt} = -\vec{\nabla} U_i - \left(1 + \frac{3}{N_f}\right)\frac{p_\chi}{Q_\chi}\vec{p}_i \\ \frac{dp_\chi}{dt} = 3V(\mathcal{P} - P_0) - \frac{3}{N_f}\sum_{i=1}^{N}\frac{p_i^2}{m_i} \end{cases} \tag{3.47}$$

Where Q_χ is a parameter behaving as the mass of the piston, p_χ the momentum associated to the piston .

3.3. Thermophysical Properties Estimation from Molecular Simulations

In this section, we present the methods used to compute thermophysical equilibrium and transport properties.

3.3.1 Thermodynamic Properties Calculation from MC Simulations

As previously mentioned in section 3.2.2, Monte Carlo simulation techniques are very well suited to the estimation of thermodynamic properties. In the scope of this work, MC simulations have been performed to estimate density, vapor liquid coexistence curves and derivative properties such as isobaric thermal expansion, isothermal compressibility, isobaric heat capacity and speed of sound. The calculation methodologies of the aforementioned properties are detailed bellow.

3.3.1.1 Density and Derivative Properties

Density and derivative properties are simultaneously computed by MC simulations in the NPT ensemble[45].

Density ρ is directly calculated by averaging its instantaneous values over MC moves as:

$$\rho = \langle \frac{\sum_i N_i \times M_i}{V} \rangle \tag{3.48}$$

where, N_i and M_i are number of molecules and molecular mass of compound i^{th}, respectively, V is the box volume, and $\langle ... \rangle$ denotes an average over MC moves.

Concerning derivative properties, they are computed from the analysis of fluctuations in the NPT ensemble[1,9,46]. According to the fluctuation theory, the partial derivative of a given property X, with respect to an intensive state variable Y, can be obtained by the analysis of the covariance[45,46] between X and Z , $\sigma(X,Z)$ expressed as:

$$\sigma(X,Y) = \langle XZ \rangle - \langle X \rangle \langle Z \rangle \tag{3.49}$$

Where Z is the extensive conjugate variable of Y.

By deriving the isothermal-isobaric partition function and applying equation (3.49), Lagache et al.[45] obtained formulae for the isobaric thermal expansion and the isothermal compressibility expressed as:

$$\alpha_P = \frac{1}{\langle V \rangle} \left(\frac{\partial \langle V \rangle}{\partial T} \right)_P = \frac{1}{\langle V \rangle k_B T^2} \left(\langle V \widehat{H} \rangle - \langle V \rangle \langle \widehat{H} \rangle \right) \tag{3.50}$$

$$\kappa_T = -\frac{1}{\langle V \rangle} \left(\frac{\partial \langle V \rangle}{\partial P} \right)_T = \frac{1}{\langle V \rangle k_B T} \left(\langle V^2 \rangle - \langle V \rangle^2 \right) \tag{3.51}$$

Where $\widehat{H}$ is the configurational enthalpy: $\widehat{H} = U^{ext} + U^{int} + PV$, where U^{ext} and U^{int} are the intermolecular and intramolecular potential energy, respectively.

Regarding the molar isobaric heat capacity c_P , since the kinetic energy is not considered in MC simulation[45,47], it is decomposed in an ideal and residual isobaric heat capacities as follows:

$$c_P = c_P^{id} + c_P^{res} \tag{3.52}$$

Where c_P^{id} is the ideal molar heat capacity obtained from the NIST database and c_P^{res} is the residual heat capacity estimated from the simulations thanks to the fluctuation theory as:

$$c_P^{res} = \left(\frac{N_a}{k_B N T^2} \left(\langle U^{ext} \widehat{H} \rangle - \langle U^{ext} \rangle \langle \widehat{H} \rangle \right) + \frac{N_a P}{k_B N T^2} \left(\langle V \widehat{H} \rangle - \langle V \rangle \langle \widehat{H} \rangle \right) - N_a k_B \right. \tag{3.53}$$

where N_a is the Avogadro number.

Finally, the isentropic compressibility κ_s and the speed of sound w was deduced from the other thermodynamic properties via a classical thermodynamic relations as:

$$k_s = \kappa_T - \frac{TM\alpha_P^2}{\rho c_p} \tag{3.54}$$

$$w = \frac{1}{\sqrt{\rho(\kappa_T - \frac{TM\alpha_P^2}{\rho c_p})}} \tag{3.55}$$

3.3.1.2 Phase Equilibrium calculations

In the preliminary results section of Chapter 6, we will present Phase equilibria simulations of the studied mixtures (CO_2 + nC7). The simulations have been performed using the Gibbs Ensemble Monte Carlo (GEMC) method[48,49].

The basic idea of GEMC simulation method is to determine the phase coexistence properties of a system in equilibrium at a temperature T. Two separated simulation boxes are used for each phase. Considering simulation box I for the liquid phase with a volume V^I and N^I particles and box II for the gas phase, with a volume V^{II} and N^{II} particles, the two boxes taken together form a system which is representative of the canonical ensemble at constant NVT, with $N = N^I + N^{II}$ and $V = V^I + V^{II}$. The two phases are at equilibrium when the following three conditions are achieved:

$$T^I = T^{II} = T \tag{3.56}$$

$$P^I = P^{II} = P \tag{3.57}$$

$$\mu^I = \mu^{II} \tag{3.58}$$

The equilibrations between phases are achieved by the mean of three distinct Monte Carlo moves: (a) a particle displacement to achieve the temperature equilibrium, (b) a volume rearrangement move leading to the pressure equilibrium, and (c) a particle interchange based on insertion/destruction MC moves, leading to the chemical potential equilibrium condition. For a multicomponent system[26], the methodology described above remain valid.

3.3.1.3 Evaluation of Chemical Potential

As mentioned in the section above, the computation of chemical potential is essential for Monte Carlo simulations in the grand canonical ensemble (GCMC) and in the Gibbs ensemble (GEMC). In this work, the chemical potential is estimated by using the Widom method[1,2]. Widom proposed a method to evaluate the chemical potential of a system based on a fictitious insertion of a test particle. This move consists in the same MC insertion move than simulation in the grand canonical ensemble, except that the insertion is not effective. For example, in the NVT ensemble, according to equation 3.9 deduced from thermodynamic identities, the chemical potential μ_i by inserting a test particle i is given by:

$$\mu_i = \left(\frac{\partial F}{\partial N_i}\right)_{V,T,N_{j\neq i}} = -k_B T ln \left\langle \frac{V}{(N_i+1)\Lambda_i^3} \exp(-\beta \Delta U_{test}) \right\rangle \tag{3.59}$$

Where F is the partition function of the NVT ensemble, U_{test} is the variation of the total potential energy by inserting the test particle, $\langle \quad \rangle$ refers to the NVT ensemble average over all test insertions

and $\Lambda = \sqrt{h^2/2\pi m k_B T}$ is the De Broglie wavelength. The total chemical potential can be rewritten as the sum of an ideal gas (μ^{ideal}) and excess contributions (μ^{excess}) with:

$$\mu^{ideal} = k_B T ln(\frac{V}{(N_i+1)\Lambda_i^3}) \tag{3.60}$$

$$\mu^{excess} = k_B T ln\langle \exp(-\beta U_{test}) \rangle \tag{3.61}$$

3.3.2 Calculation of a Transport Property: the Shear Viscosity

An advantage among others of molecular dynamics is its ability to predict transport (time-dependent) properties such as diffusion coefficient, heat transfer coefficient, or viscosity. Generally, transport coefficients are defined in terms of the response to a perturbation. Thus, the transport coefficient is determined by analyzing the linear response of the system to the perturbation and comparing it to macroscopic constitutive equations[1,2]. Depending on the perturbations' origin, there are two main groups of methods:

- Equilibrium Molecular Dynamics (EMD), for which the considered perturbations arise from the natural fluctuation of the system at equilibrium.
- Non-equilibrium Molecular Dynamics (NEMD), for which the system is artificially maintained out of equilibrium by an external perturbation.

In this work, we are particularly interested in the calculation of shear viscosity. The computation of this property was performed using the Reverse Non-Equilibrium Molecular Dynamic (RNEMD) method proposed by F. Müller Plathe[50]. The choice of this non-equilibrium method is justified by the fact that, the equilibrium methods are subject to greater statistical errors due to the small amplitude of the natural fluctuations, especially at long times[1].

3.3.2.1 Shear Viscosity Calculation by RNEMD

The reverse non-equilibrium molecular dynamics consist of dividing the simulation box into n_{slab} (even number) slabs along one direction, say *z*, then a bi-periodic linear momentum flux is imposed by exchanging momentum of atoms along the *x* direction every N_{swap} time steps as illustrated by Figure 3.8. More precisely, at the exchange time step, an atom in the 1st slab with the most negative x velocity component (v_x) exchanges this component with the one of an atom in the $(n_{slab}/2)^{th}$ slab that has the most positive x velocity component. To keep the periodic boundary condition in the *z* direction, a similar exchange is also applied between $(n_{slab})^{th}$ slab and $(n_{slab}/2 +1)^{th}$ slab. This momentum transfer implies a velocity gradient in the simulation box. The linear momentum flux, i.e. the shear stress, induced by this exchange is determined as:

$$j_z(p_x) = \frac{\Delta P_x}{2tL_xL_y} \tag{3.62}$$

where, ΔP_x is the total exchanged momentum during the time t, L_x and L_y are the lengths of the simulation box in the *x* and *y* directions, respectively.

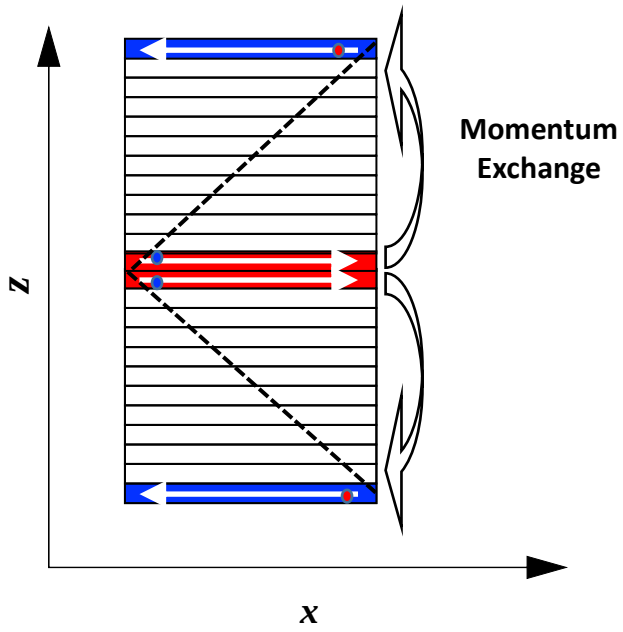

Figure 3.8 Schematic view of the momentum transfer process proposed by Müller-Plathe[50]. The dashed lines (---) represents the velocity profile created in the simulation box.

When the system reaches the steady state, the shear viscosity is estimated thanks to the Newton constitutive law as:

$$\eta = -\frac{j_z}{(\partial v_x/\partial z)} \tag{3.63}$$

where, $\partial v_x/\partial z$ is the shear rate which is computed from the velocity profile. It is worth noting that if the momentum flux j_z is large, i.e. N_{swap} is small, the velocity profile could be non-linear, i.e. the system is in non-linear response regime (shear thinning regime for instance). We will discuss this aspect in Chapter 4.

3.3.3 Calculation of Properties from Structural Information

3.3.3.1 Radial Distribution Function

The radial distribution function (RDF) $g(r)$, also known as pair correlation function, provides important information on fluid organization at the microscopic scale[5]. It gives the probability to find a pair of particles at distance r apart, relative to the probability for a completely random distribution at the same density[1]. For a homogeneous fluid, the pair correlation function is defined as:

$$g_{ij}(r) = \frac{2V}{N^2}\langle \sum_i \sum_{i<j} \delta(r - r_{ij})\rangle \tag{3.64}$$

Where δ is the Dirac distribution function.

In the scope of our work, in addition to the study of the microscopic structure of the fluids, the RDF has been used to link microscopic information of the fluid to macroscopic properties by using the Kirkwood-Buff solution theory[51]. This theory is based on the calculation of Kirkwood Buff Integrals, detailed in the following section.

3.3.3.2 Kirkwood and Buff Integral

Kirkwood and Buff[51] (KB) developed a general statistical mechanical theory of solutions in the grand canonical μVT ensemble which relates the microscopic structure of a system to its macroscopic thermodynamic quantities. The theory defined Kirkwood-Buff integral (KBIs) as:

$$G_{\alpha\beta} = 4\pi \int_0^\infty \left[g_{\alpha\beta}^{\mu VT}(r) - 1\right] r^2 dr \tag{3.65}$$

Where $g_{\alpha\beta}^{\mu VT}(r)$ is the radial distribution function between component α and β in the μVT ensemble. Furthermore, Kirkwood and Buff used the theory of fluctuations to propose an alternative way to compute the KBIs as:

$$G_{\alpha\beta}^{\infty} = \lim_{V\to\infty} \left[V \frac{\langle N_\alpha N_\beta\rangle - \langle N_\alpha\rangle\langle N_\beta\rangle}{\langle N_\alpha\rangle\langle N_\beta\rangle} - \frac{\delta_{\alpha\beta}}{c_\alpha}\right] \tag{3.66}$$

Where N_α and N_β are the number of molecules of type α and β, V the volume, $\langle ... \rangle$ denotes the μVT ensemble average, c_α is the bulk molecular concentration of species α and $\delta_{\alpha\beta}$ is the Kronecker delta (equal 1 if $\alpha = \beta$ and is zero otherwise).

In principle, KBIs could be computed by both MD and MC simulations. Indeed, molecular simulations allow to compute either the RDFs or the molecules number fluctuations. However, in this work, it has been chosen to compute the KBIs from the integral of RDFs. Indeed, as we study dense systems, the use of the second method based on equation (3.66) is not convenient, especially because MC insertion move is difficult to achieve correctly for such dense systems[1]. Moreover, when dealing with highly dilute mixture as studied in this work, the method based on the fluctuation may lead to simulation results with a poor statistics and so to very large error bars.

It is worth to point out that estimating KBIs by using equation with RDFs obtained from the molecular simulations is not straightforward. This is because of two main reasons. First, the molecular simulations are carried out on finite systems, so the integral cannot be computed over an infinite volume. Second, the molecular simulations in the grand canonical ensemble are not easy to implement for dense and molecular systems, i.e. the RDFs in μVT ensemble are sometimes not correctly estimated by molecular simulations.

To tackle the first problem, many approaches have been proposed in the literature. Among them, the theory for KBI of finite volumes developed by Krüger and co-workers [52] seems efficient to accurately compute $G_{\alpha\beta}^{\infty}$. In this theory, a sub volume *V* embedded in the simulation box is considered, in which the latter acts as a reservoir. For a spherical sub volume *V* of radius *R*, a finite-size KBI is defined as follow:

$$G_{\alpha\beta}^{V} = 4\pi \iint^{V} \left[g_{\alpha\beta}(r) - 1\right] r^2 dr_1 dr_2 \tag{3.67}$$

This double integral is then rewritten and is reduced to a single one using a weighting function[52,53] $w(r)$:

$$G_{\alpha\beta}^{V} = G_{\alpha\beta}^{R} = \int_0^{2R} w(r)\left[g_{\alpha\beta}(r) - 1\right] dr \tag{3.68}$$

with

$$w(r) = \frac{1}{V}\int \quad dr_1 \int \quad \delta(r - r_{12})dr_2 \tag{3.69}$$

Where $\delta(r - r_{12})$ is the Dirac delta function and $r_{12} = |r_1 - r_2|$ is the pair distance. $w(r)$ is a geometrical function[54], proportional to the probability that two points inside the sub volume V are at distance r. For a spherical volume, it is defined as:

$$w(r) = 4\pi r^2(1 - 3r/4R + r^3/4R) \tag{3.70}$$

$G_{\alpha\beta}^R$ is shown to vary asymptotically with 1/R for any system having a finite correlation length[52]. Interestingly, by extrapolating equation (3.68) to the thermodynamic limit (i.e. $1/R \to 0$), such formulation reduces to the Kirkwood Buff Integral of equation (3.65) which so provides an efficient way to take into account finite-size effects on the KBI.

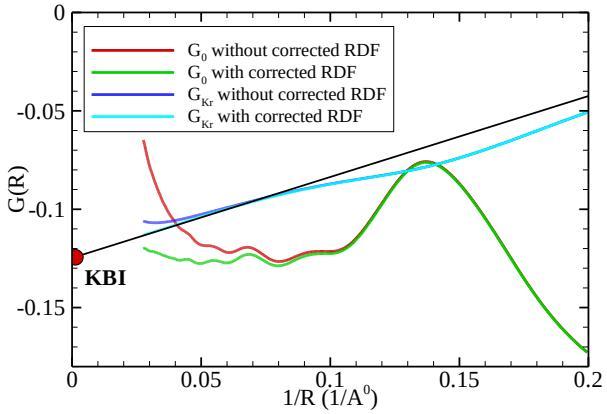

Figure 3.9 Effect of corrections on the calculation of KBI. G_{kr} and G_0 are truncated KBI with and without weighting function $w(r)$. The plots represent $G_{CO2-nC7}$ in a binary mixture of CO_2 + n-C_7 with 40 mol% of CO_2 at 303.35 K and 10.12 MPa.

For the second problem, it is proposed to use the RDFs of systems in the NVT or NPT ensemble combined with corrections as proposed in the literature. To do so, Ganguly and Van der Vegt[55] proposed an efficient approach to correct the RDF as:

$$g_{\alpha\beta}^{correct} = g_{\alpha\beta}(r)\frac{N_\alpha\left(1-\frac{(4/3)\pi r^3}{V}\right)}{N_\alpha\left(1-\frac{(4/3)\pi r^3}{V}\right)-\Delta N_{\alpha\beta}(r)-\delta_{\alpha\beta}} \tag{3.71}$$

with

$$\Delta N_{\alpha\beta}(r) = 4\pi\int_0^r \rho_\beta\left[g_{\alpha\beta}(r') - 1\right]r'^2 dr' \tag{3.72}$$

Where $\Delta N_{\alpha\beta}(r)$ is the excess or depletion number of particles of type α within a sphere of radius r around particles of type β and ρ_β the number density of particle of type β.

In this work, we have used equation (3.71) and (3.68) to compute KBIs. As shown in Figure 3.9, it is worth noting that using only one of the two equations (3.71) or (3.68) cannot provide accurate estimate of KBI.

One of the main advantages of the KB theory is that the thermodynamics derivative properties of mixtures can be computed directly from KBIs. Thus, in this work, we have employed the KB theory to compute the isothermal compressibility κ_T and the partial molar volume $\bar{v}_\alpha$ from :

$$\kappa_T = \frac{1+c_\alpha G_{\alpha\alpha}+c_\beta G_{\beta\beta}+c_\alpha c_\alpha (G_{\alpha\alpha}G_{\beta\beta}-G_{\alpha\beta})^2}{k_B T(c_\alpha+c_\beta+c_\alpha c_\beta(G_{\alpha\alpha}+G_{\beta\beta}-2G_{\alpha\beta}))} \tag{3.73}$$

$$\bar{v}_\alpha = \frac{1+(G_{\beta\beta}-G_{\alpha\beta})c_\beta}{c_\alpha+c_\beta+c_\alpha c_\beta(G_{\alpha\alpha}+G_{\beta\beta}-2G_{\alpha\beta})} \tag{3.74}$$

Having a direct way of computing the partial molar volumes is of great interest, as these properties are often obtained indirectly from a fitting procedure[56] , which may induce important errors.

3.4. References

(1) Allen, M. P.; Tildesley, D. J. Computer Simulation of Liquids: Second Edition, 2nd ed.; OUP Oxford: Oxford, United Kingdom, 2017.

(2) Frenkel, D.; Smit, B. Understanding Molecular Simulation; Elsevier, 2002.

(3) Boltzmann, L. K Akad. Wiss. 1871, 63, 679.

(4) Callen, H. B.; Callen, H. B. Thermodynamics and an Introduction to Thermostatistics; Wiley, 1985.

(5) Rapaport, D. C. The Art of Molecular Dynamics Simulation; Cambridge University Press: New York, NY, USA, 1995.

(6) Haile, J. M. Molecular Dynamics Simulation: Elementary Methods, 1st ed.; John Wiley & Sons, Inc.: New York, NY, USA, 1992.

(7) Hoang, H.; Delage-Santacreu, S.; Galliero, G. Simultaneous Description of Equilibrium, Interfacial, and Transport Properties of Fluids Using a Mie Chain Coarse-Grained Force Field. Ind. Eng. Chem. Res. 2017, 56 (32), 9213–9226.

(8) J. I. Siepmann; M.G.Martin. Transferable Potentials for Phase Equilibria. 1. United-Atom Description of n-Alkanes,. J Phys Chem 1998.

(9) Ungerer P., Tavitian B.; Boutin A. In Applications of molecular simulations in the oil and gas industry, Monte Carlo methods; Editions TECHNIP, 2005.

(10) PumMa » Theory » Potentials http://cbio.bmt.tue.nl/pumma/index.php/Theory/Potentials.

(11) Metropolis, N.; Rosenbluth, A. W.; Rosenbluth, M. N.; Teller, A. H.; Teller, E. Equation of State Calculations by Fast Computing Machines. J. Chem. Phys. 1953, 21 (6), 1087–1092.

(12) Ewald, P. P. Die Berechnung Optischer Und Elektrostatischer Gitterpotentiale. Ann. Phys. 1921, 369 (3), 253–287.

(13) Darden, T.; York, D.; Pedersen, L. Particle Mesh Ewald: An N·log(N) Method for Ewald Sums in Large Systems. J. Chem. Phys. 1993, 98 (12), 10089–10092.

(14) Verlet, L. Computer “Experiments” on Classical Fluids. I. Thermodynamical Properties of Lennard-Jones Molecules. Phys. Rev. 1967, 159 (1), 98–103.

(15) Mie, G. “Zur kinetischen Theorie der einatomige,” Annu; 1903.

(16) Xiang, H. W. The Corresponding-States Principle and Its Practice: Thermodynamic, Transport and Surface Properties of Fluids; Elsevier, 2005.

(17) Mejía, A.; Herdes, C.; Müller, E. A. Force Fields for Coarse-Grained Molecular Simulations from a Corresponding States Correlation. Ind. Eng. Chem. Res. 2014, 53 (10), 4131–4141.

(18) Pitzer, K. S.; Lippmann, D. Z.; Curl, R. F.; Huggins, C. M.; Petersen, D. E. The Volumetric and Thermodynamic Properties of Fluids. II. Compressibility Factor, Vapor Pressure and Entropy of Vaporization1. J. Am. Chem. Soc. 1955, 77 (13), 3433–3440.

(19) Lorentz, H. A. Ueber die Anwendung des Satzes vom Virial in der kinetischen Theorie der Gase,. Ann. Phys. 1881, 248.

(20) Berthelot, D. "Sur le mélange des gaz," Comptes rendus hebdomadaires des séances de l'Académie des. Sciences 1898, 126.

(21) TraPPE: Transferable Potentials for Phase Equilibria Force Field http://chem-siepmann.oit.umn.edu/siepmann/trappe/index.html

(22) Lennard-Jones, J. E. On the Determination of Molecular Fields,. Proc R Soc Lond 1924.

(23) LENNARD-JONES, J. E. "Cohesion," Proc. Phys. Soc 1931, 43 (240).

(24) Kelkar, M. S.; Rafferty, J. L.; Maginn, E. J.; Ilja Siepmann, J. Prediction of Viscosities and Vapor–Liquid Equilibria for Five Polyhydric Alcohols by Molecular Simulation. Fluid Phase Equilibria 2007, 260 (2), 218–231.

(25) Mundy, C. J.; Balasubramanian, S.; Bagchi, K.; Siepmann, J. I.; Klein, M. L. Equilibrium and Non-Equilibrium Simulation Studies of Fluid Alkanes in Bulk and at Interfaces. Faraday Discuss. 1996, 104, 17.

(26) Panagiotopoulos, A. Z. Monte Carlo Methods for Phase Equilibria of Fluids. J. Phys. Condens. Matter 1999, 12 (3), R25–R52.

(27) Martin, M. G. MCCCS Towhee: A Tool for Monte Carlo Molecular Simulation. Mol. Simul. 2013, 39 (14–15), 1212–1222.

(28) de Pablo, J. J.; Laso, M.; Suter, U. W. Estimation of the Chemical Potential of Chain Molecules by Simulation. J. Chem. Phys. 1992, 96 (8), 6157–6162.

(29) Smit, B.; Karaborni, S.; Siepmann, J. I. Computer Simulations of Vapor–Liquid Phase Equilibria of N-alkanes. J. Chem. Phys. 1995, 102 (5), 2126–2140.

(30) Plimpton, S. Fast Parallel Algorithms for Short-Range Molecular Dynamics. J. Comput. Phys. 1995, 117 (1), 1–19.

(31) M.A, J. C. M. V. Illustrations of the Dynamical Theory of Gases.—Part I. On the Motions and Collisions of Perfectly Elastic Spheres. Lond. Edinb. Dublin Philos. Mag. J. Sci. 1860, 19 (124), 19–32.

(32) Boltzmann, L. Weitere Studien Über Das Wärmegleichgewicht Unter Gasmolekülen. Sitzungsberichte Kais. Akad. Wiss. Wien Math.-Naturwissenschaftliche Cl. 1872, 66, 275–370.

(33) Press, W. H.; Teukolsky, S. A.; Vetterling, W. T.; Flannery, B. P. Numerical Recipes 3rd Edition: The Art of Scientific Computing, 3 edition.; Cambridge University Press: Cambridge, UK ; New York, 2007.

(34) Swope, W. C.; Andersen, H. C.; Berens, P. H.; Wilson, K. R. A Computer Simulation Method for the Calculation of Equilibrium Constants for the Formation of Physical Clusters of Molecules: Application to Small Water Clusters. J. Chem. Phys. 1982, 76, 637–649.

(35) Basconi, J. E.; Shirts, M. R. Effects of Temperature Control Algorithms on Transport Properties and Kinetics in Molecular Dynamics Simulations. J. Chem. Theory Comput. 2013, 9 (7), 2887–2899.

(36) Berendsen, H. J. C.; Postma, J. P. M.; van Gunsteren, W. F.; DiNola, A.; Haak, J. R. Molecular Dynamics with Coupling to an External Bath. J. Chem. Phys. 1984, 81 (8), 3684–3690.

(37) Morishita, T. Fluctuation Formulas in Molecular-Dynamics Simulations with the Weak Coupling Heat Bath. J. Chem. Phys. 2000, 113 (8), 2976–2982.

(38) Hünenberger, P. H. Thermostat Algorithms for Molecular Dynamics Simulations. In Advanced Computer Simulation: Approaches for Soft Matter Sciences I; Dr. Holm, C., Prof. Dr. Kremer, K., Eds.; Advances in Polymer Science; Springer Berlin Heidelberg: Berlin, Heidelberg, 2005; pp 105–149.

(39) Nosé, S. A Unified Formulation of the Constant Temperature Molecular Dynamics Methods. J. Chem. Phys. 1984, 81 (1), 511–519.

(40) Hoover, W. G. Canonical Dynamics: Equilibrium Phase-Space Distributions. Phys. Rev. A 1985, 31 (3), 1695–1697.

(41) Clausius, R. XVI. On a Mechanical Theorem Applicable to Heat. Lond. Edinb. Dublin Philos. Mag. J. Sci. 1870, 40 (265), 122–127.

(42) Cheung, P. S. Y. On the Calculation of Specific Heats, Thermal Pressure Coefficients and Compressibilities in Molecular Dynamics Simulations. Mol. Phys. 1977, 33 (2), 519–526.

(43) Hoover, W. G. Constant-Pressure Equations of Motion. Phys. Rev. A 1986, 34 (3), 2499–2500.

(44) Martyna, G. J.; Tobias, D. J.; Klein, M. L. Constant Pressure Molecular Dynamics Algorithms. J. Chem. Phys. 1994, 101 (5), 4177–4189..

(45) Lagache, M.; Ungerer, P.; and A. H. Fuchs, A. B. Prediction of Thermodynamic Derivative Properties of Fluids by Monte Carlo Simulation,. Phys Chem Chem Phys 2001, 3.

(46) Y. Mishin. Thermodynamic Theory of Equilibrium Fluctuations,. Ann. Phys. 2015, 363.

(47) Jorgensen, W. L. Optimized Intermolecular Potential Functions for Liquid Alcohols. J. Phys. Chem. 1986, 90 (7), 1276–1284.

(48) Panagiotopoulos, A. Z.; Quirke, N.; Stapleton, M.; Tildesley, D. J. Phase Equilibria by Simulation in the Gibbs Ensemble. Mol. Phys. 1988, 63 (4), 527–545.

(49) Panagiotopoulos, A. Z. Direct Determination of Phase Coexistence Properties of Fluids by Monte Carlo Simulation in a New Ensemble. Mol. Phys. 1987, 61 (4), 813–826.

(50) Müller-Plathe, F. Reversing the Perturbation in Nonequilibrium Molecular Dynamics: An Easy Way to Calculate the Shear Viscosity of Fluids. Phys. Rev. E 1999, 59 (5), 4894–4898.

(51) Kirkwood, J. G.; Buff, F. P. The Statistical Mechanical Theory of Solutions. I. J. Chem. Phys. 1951, 19 (6), 774–777.

(52) Krüger, P.; Schnell, S. K.; Bedeaux, D.; Kjelstrup, S.; Vlugt, T. J. H.; Simon, J.-M. Kirkwood–Buff Integrals for Finite Volumes. J. Phys. Chem. Lett. 2013, 4 (2), 235–238.

(53) Giorgini, S.; Pitaevskii, L. P.; Stringari, S. Anomalous Fluctuations of the Condensate in Interacting Bose Gases. Phys. Rev. Lett. 1998, 80 (23), 5040–5043.

(54) Dawass, N.; Krüger, P.; Schnell, S. K.; Simon, J.-M.; Vlugt, T. J. H. Kirkwood-Buff Integrals from Molecular Simulation. Fluid Phase Equilibria 2019, 486, 21–36.

(55) Ganguly, P.; van der Vegt, N. F. A. Convergence of Sampling Kirkwood–Buff Integrals of Aqueous Solutions with Molecular Dynamics Simulations. J. Chem. Theory Comput. 2013, 9 (3), 1347–1355.

(56) Stubbs, J. M.; Drake-Wilhelm, D. D.; Siepmann, J. I. Partial Molar Volume and Solvation Structure of Naphthalene in Supercritical Carbon Dioxide: A Monte Carlo Simulation Study. J. Phys. Chem. B 2005, 109 (42), 19885–19892.

Chapter 4. Experimental Measurements and Simulations of n-C_6 + n-C_{12} Mixtures.

Contents

4.1. Experimental Measurements Details 56
4.2. Molecular Simulations Details 57
4.2.1 Thermodynamic Properties Simulations 57
4.2.2 Shear Viscosity Simulations 57
4.3. Thermodynamic Properties 59
4.3.1 Density and Excess Molar Volume 59
4.3.2 Isothermal compressibility and Excess Isothermal Compressibility 62
4.3.3 Speed of Sound and Excess Speed of Sound 64
4.4. A Transport Property: the Shear viscosity 66
4.5. Conclusions 69
4.6. References 70

Introduction

Mixtures of hydrocarbons, are widely present in the industry, particularly in petroleum engineering. Therefore, the thermophysical characterization of these mixtures is of primary importance to optimize the related processes. Despite the great interest for this question, it remains a topical issue considering that the predictive approaches (equations of states, mixing rules, correlations) are not always able to provide satisfactory results in particular when dealing with derivative thermophysical properties [1–3] or transport properties such as viscosity[4,5] under high pressures as found in the oil and gas industry.

Molecular simulation is a complementary tool[6] to deal with the thermophysical properties of such molecular systems over a wide range of thermodynamic conditions. Previous works [1,6–12] showed that it is possible to predict with a good accuracy the thermodynamic properties of hydrocarbon molecules and their mixtures, even when using the molecular simulation techniques combined with force fields based on a coarse grained representation. However, it seems less clear whether such approaches are able to provide simultaneously derivative properties like speed of sound, excess properties in mixtures, and transport properties like viscosity even for simple molecular systems such as hydrocarbons mixtures[10,13,14].

Thus, in this work, which deals with liquid binary mixtures of n-hexane and n-dodecane, we have evaluated the ability of two force fields to provide equilibrium properties (density, isothermal compressibility, speed of sound), the corresponding excess properties, and transport (viscosity) properties over a wide range of thermodynamic conditions (from 293.15 to 353.15K and pressure up to 100 MPa). With this aim in mind, we have chosen a recently developed coarse grained force field the Mie Chain Coarse Grained (MCCG)[9,11] for which an accurate equation of state has been developed[12] and a widely used united atom force field, the Transferable Potential for Phase Equilibria (TraPPE-ua)[8].To perform the comparisons on a consistent and controlled set of experimental data, we have measured accurately density, speed of sound and shear viscosity of these mixtures.

The chapter is organized as follows. In section 4.1, a brief description of the experimental measurements conditions is presented. Additional details are provided in Appendix B. Then, the molecular simulations and computations are detailed in section 4.2. In sections 4.3 and 4.4, the simulations results are systematically compared to the experimental data obtained for each studied property. Finally, the main outcomes of this study are summarized in the last section.

4.1. Experimental Measurements Details

To achieve a consistent and controlled comparison of molecular simulations results with experimental data, some dedicated experiments were performed. Experimental measurements of density, speed of sound and viscosity were carried out on pure n-hexane and n-dodecane and on four binary mixtures of these components at mole fractions of 20, 40, 60 and 80 % of n-hexane, along four isotherms spaced at 20 K intervals in the temperature range of 293.15-353.15 K and for pressures ranging from 0.1 to 100 MPa by 10 MPa steps, except for the isotherm at 353.15 K where the minimum pressure was 10 MPa for the n-hexane and the four binary mixtures. For this isotherm, atmospheric measurements were not carried out in order to avoid

possible evaporation of the n-hexane. All data are provided in Appendix B, see Table B.1 to B.5. The quality of the measurements was validated by comparing data obtained for pure component to reference correlations available in the literature for both components. The comparison plots, provided along with experimental data in Appendix B, indicate that our experimental measurements data are consistent with those provided in the literature.

4.2. Molecular Simulations Details

4.2.1 Thermodynamic Properties Simulations

To estimate the thermodynamic properties such as density, isothermal compressibility and speed of sound, Monte-Carlo (MC) molecular simulations in the isothermal-isobaric ensemble (NPT) were implemented. The simulation boxes, containing 200 molecules, were cubic with classical periodic boundary[15,16] conditions applied in all directions. The pair potentials were truncated at a cut-off radius (r_C) value of 3σ and long range corrections were included. In these simulations, four MC moves[15–17] were implemented: (1) volume change , (2) molecular translation , (3) molecular rotation and (4) configurational-bias MC partial regrowth [18–20]. All MC simulations consist of two steps. First, the systems were equilibrated during a run of more than 5×10^6 MC moves. During equilibration step, maximum amplitudes of the first three MC moves were adjusted so that the acceptance rates of these moves were approximately of 50 %. Then, the samplings were performed during at least 3×10^7 MC moves to compute the thermodynamic properties.

4.2.2 Shear Viscosity Simulations

Shear viscosity were computed in the canonical ensemble (NVT), by using the Reverse Non-Equilibrium Molecular Dynamics (RNEMD) method (cf. section 3.3.2). All MD simulations consisted of three steps. In a first step, the systems were equilibrated during a run of more than 10^6 time steps. Then, in a second step, the RNEMD method was applied to shear the fluid during at least 10^6 time steps. In a last step, the system the steady state, a run of more than 6×10^6 time steps was used to perform samplings. Simulation boxes, containing at least 300 molecules for the TraPPE-ua force field and at least 600 molecules for the MCCG force field, were designed in such a way that $L_z = 2L_x = 2L_y$. This box shape was used in order to reduce shear boundary effect relative to the comparable cubic box[21]. Classical periodic boundary conditions were applied in all directions. Newton's equations of motion were integrated using the velocity Verlet algorithm. To keep the temperature constant at each step, thermostat algorithms (Nose-Hoover[22–24] for TraPPE-ua force field and Berendsen[10] for MCCG force field) were applied to all three velocity components (*x*, *y*, and *z*) during the equilibrium MD simulations, whereas they were applied only to *y* and *z* velocity components during RNEMD simulations, in order not to introduce a bias in the flow direction, *z*. To constrain the bond length in the MCCG force field, the classical RATTLE algorithm[26] was employed.

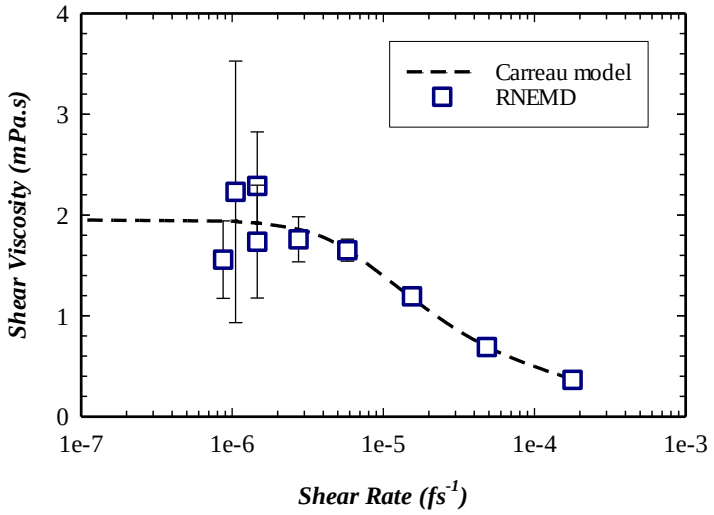

Figure4.1 Shear viscosities for n-dodecane at T = 293.15 K and ρ= 823.62 kg.m^2 (i.e at P =100 Mpa)calculated via the RNEMD method at various shear rate. For comparison, simulation results were fit using a Carreau model[27] .

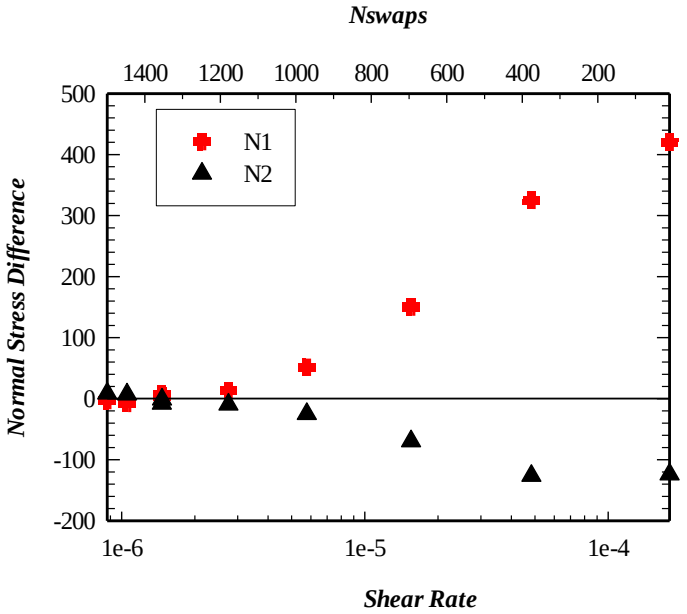

Figure 4.2 First (✚) and second (▲) normal stress differences calculated with TraPPE-ua for n-dodecane at T = 293.15 K and ρ= 823.62 kg.m^2 (i.e at P =100 MPa) at various shear rate.

When computing the shear viscosity by the RNEMD method, there is risk to impose a very high shear rate to the system, leading to simulation systems out of a linear response regime (newtonian). To avoid being in a non-newtonian regime, a preliminary study was carried out for selecting the momentum exchange frequency denoted as Nswaps. Figure 4.1 shows the different regimes obtained with TraPPE-ua for a system of pure n-dodecane at T = 293.15 K and ρ= 823.62 kg.m^2 . The adequate Nswaps value was chosen so as to generate a shear rate

corresponding to the newtonian regime.The system studied being the most viscous case, the value of Nswaps chosen for this case led to a linear response for all other compositions investigated in this work.

For the purpose of evaluating the rheological behavior of the system for each particle swapping frequency, we systematically computed the first and second stress differences of the system denoted as N_1 and N_2 respectively and defined as:

$$N_1 = \mathcal{P}_{zz} - \mathcal{P}_{xx} \tag{4.1}$$

$$N_2 = \mathcal{P}_{xx} - \mathcal{P}_{yy} \tag{4.2}$$

where $\mathcal{P}_{ii}$ is the i^{th} diagonal element of the stress tensor, calculated from virial theorem (see equation 3.42).

In Figure 4.2, the normal stress differences are plotted as a function of shear rate (bottom axe) and Nswaps (top axe). It appears in this graph that for low shear rate, corresponding to the newtonian regime (see Figure 4.1), the normal differences are zero within error bars. Subsequently, these criteria were systematically checked to validate all our RNEMD simulations.

4.3. Thermodynamic Properties

4.3.1 Density and Excess Molar Volume

Monte Carlo simulations of densities were performed at the same conditions (P, T, x) than the experimental measurements so as to allow comparisons. The simulation results and the corresponding standard errors are listed in Tables B.6 and B.7 of Appendix B for TraPPE-ua and MCCG, respectively. For both force fields, we observe a reasonable agreement of the computed density with experimental results but with a systematic overestimation, see the parity plot in Figure 4.3. The observed deviations become larger as the system is denser whatever the force field. Consequently, decreasing the amount of n-hexane, the temperature or increasing the pressure negatively affects the accuracy of the simulation results as depicted in the different panels of Figure 4.4. Quantitatively, the MCCG force field provides results that are slightly better than those of the TraPPE-ua. More precisely, for TraPPE-ua, the overall Absolute Average Deviation (AAD) over the full pressure and temperature range is 1.5%, the overall relative deviation (Bias) is -1.5 % and the Maximum Absolute Deviation (Max AD) is 3.0 %. Whereas for MCCG, we observed an AAD of 1.2 %, a Max AD of 2.2 % and a Bias of -0.5 %.

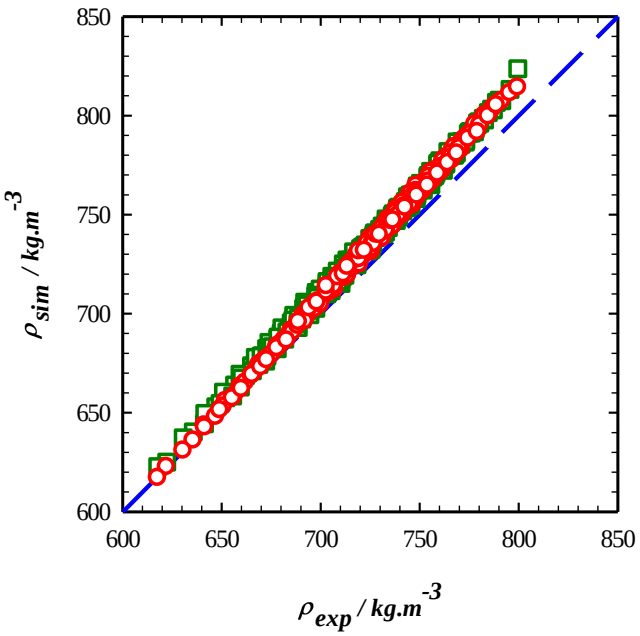

Figure 4.3 Molecular simulation data of density $\boldsymbol{\rho_{sim}}$ as a function of experimental density data $\boldsymbol{\rho_{exp}}$ for the mixture n-hexane + n-dodecane. Comparison between □: TraPPE-ua and ○: MCCG. Dashed line represents the reference, i.e. $\boldsymbol{\rho_{sim} = \rho_{exp}}$.

To highlight the mixing behavior of the system, the excess molar volume of the binary mixture was calculated from densities by using the following equation:

$$v^E = \frac{x_{nC6}M_{nC6}+(1-x_{nC6})M_{nC12}}{\rho} - \left(\frac{x_{nC6}M_{nC6}}{\rho_{nC6}} + \frac{(1-x_{nC6})M_{nC12}}{\rho_{nC12}}\right) \quad (4.3)$$

Where x_{nC6} is the mole fraction of n-hexane, M_{nC6} and M_{nC12} the molecular weights of n-hexane and n-dodecane respectively, and ρ, $\rho_{nC6}$and ρ_{nC12} the density values of the binary mixture, the n-hexane and the n-dodecane, respectively.

We observed that v^E increases by increasing the temperature at fixed pressure and decreases by increasing the pressure at a given temperature. As expected for such a simple mixture, the excess molar volumes are small (i.e. below 1% of the total molar volume) and are globally negative. This trend is related to the lodgment of n-hexane molecule[28] in the interstices formed by the larger n-dodecane molecules, thus decreasing the free volume of the real mixture, an effect which is here slightly larger than the positive one due to weak dipole-induced dipole-induced interactions between the two constituents.

Figure 4.5 compares the experimental relative excess molar volume to that obtained from simulation densities for a given thermodynamic state. It is shown that simulation values are consistent with experimental data despite a systematic underestimation of the absolute values.

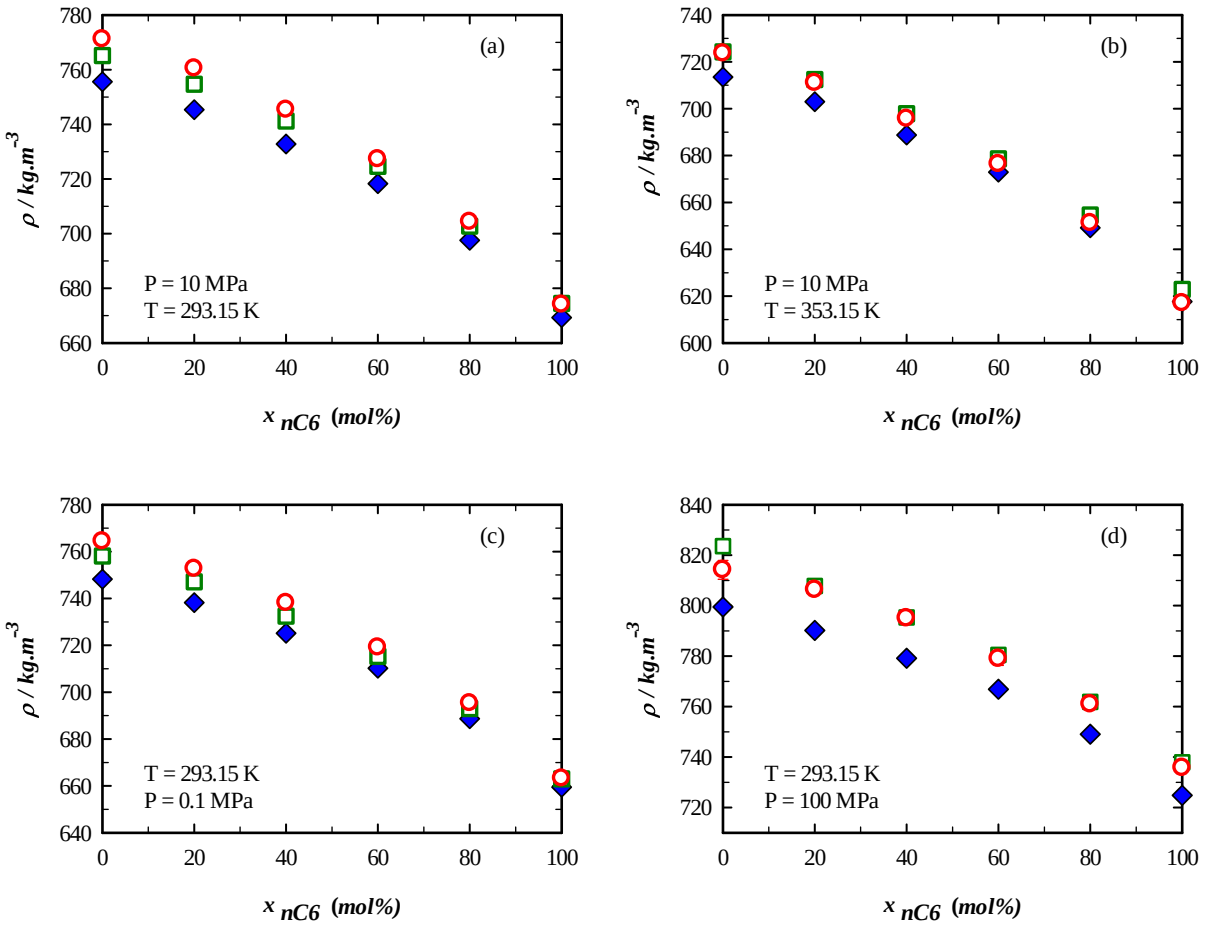

Figure 4.4 Density as a function of n-hexane concentration at different temperature and pressure conditions. Comparison between◆ : experimental data; □: TraPPE-ua and ○: MCCG. The error bars are too small to appear on the graphs.

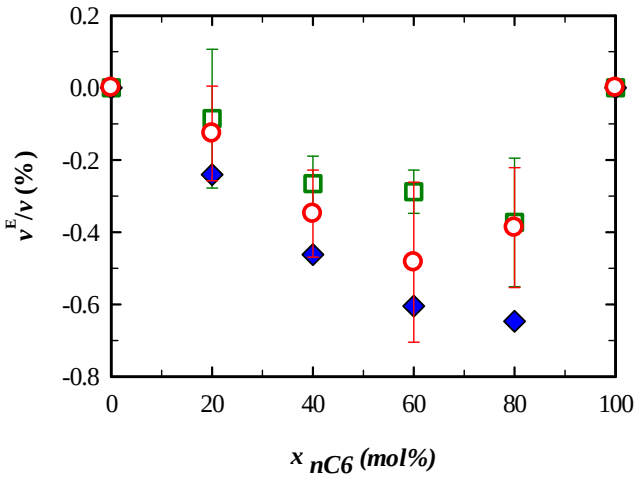

Figure 4.5 Relative excess molar volume as a function of concentration of n-hexane at 333.15 K and 0.1 MPa. Comparison between data calculated from ◆: experimental density data; □: TraPPE-ua and ○: MCCG.

Thus, the weak non-ideality of the studied binary mixture, from the excess molar volume point of view, is reasonably well captured by the simulations, i.e. the simple Lorentz-Berthelot rule combined with the tested force fields seems sufficient for such mixtures and properties, even if not perfect. This result confirms that the misevaluation of the density by molecular simulations, shown in Figures 4.3 and 4.4, is not due to the combining rules but to the limitations of the tested force fields to model very finely the pure components densities, in particular the n-dodecane ones.

4.3.2 Isothermal Compressibility and Excess Isothermal Compressibility

The compressibility data obtained from derivation of density measurements (cf. section 2.5.1) are reported in Table B.2 of Appendix B. From a qualitative point of view, see Figures 4.6 and 4.7, we can notice a systematic overestimation of κ_T by the TraPPE-ua force field while for MCCG the simulation results fluctuate around experimental data. More precisely, we have computed an AAD of 11.1 %, a Bias of -11.1 % and a Max AD of 28.3 % for TraPPE-ua and an AAD of 5.9 %, a Bias of -3.2 % and a Max AD of 22.7 % for MCCG. This indicates, as found on densities, that the MCCG performs better than the TraPPE-ua to describe isothermal compressibilities.

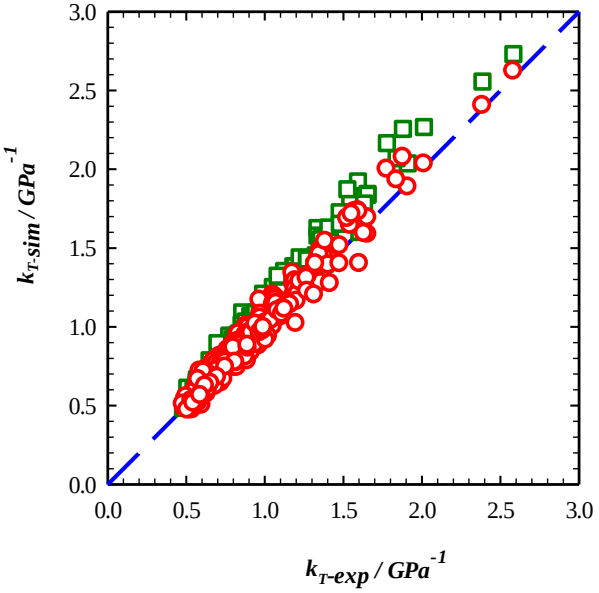

Figure 4.6 Molecular simulation data of isothermal compressibility κ_{T-sim} as a function of experimental data κ_{T-exp} for the mixture n-hexane + n-dodecane. Comparison between □: TraPPE-ua and ○: MCCG.

To highlight the mixing effect of the studied mixture in terms of κ_T, we calculated the excess isothermal compressibility from the following relation[29]:

$$\kappa_T^E = \kappa_T - \emptyset_{nC6}\kappa_{T,nC6} - (1 - \emptyset_{nC6})\kappa_{T,nC12} \quad (4.4)$$

Where $\emptyset_{nC6}$ is the volume fraction of n-hexane in the binary mixture.

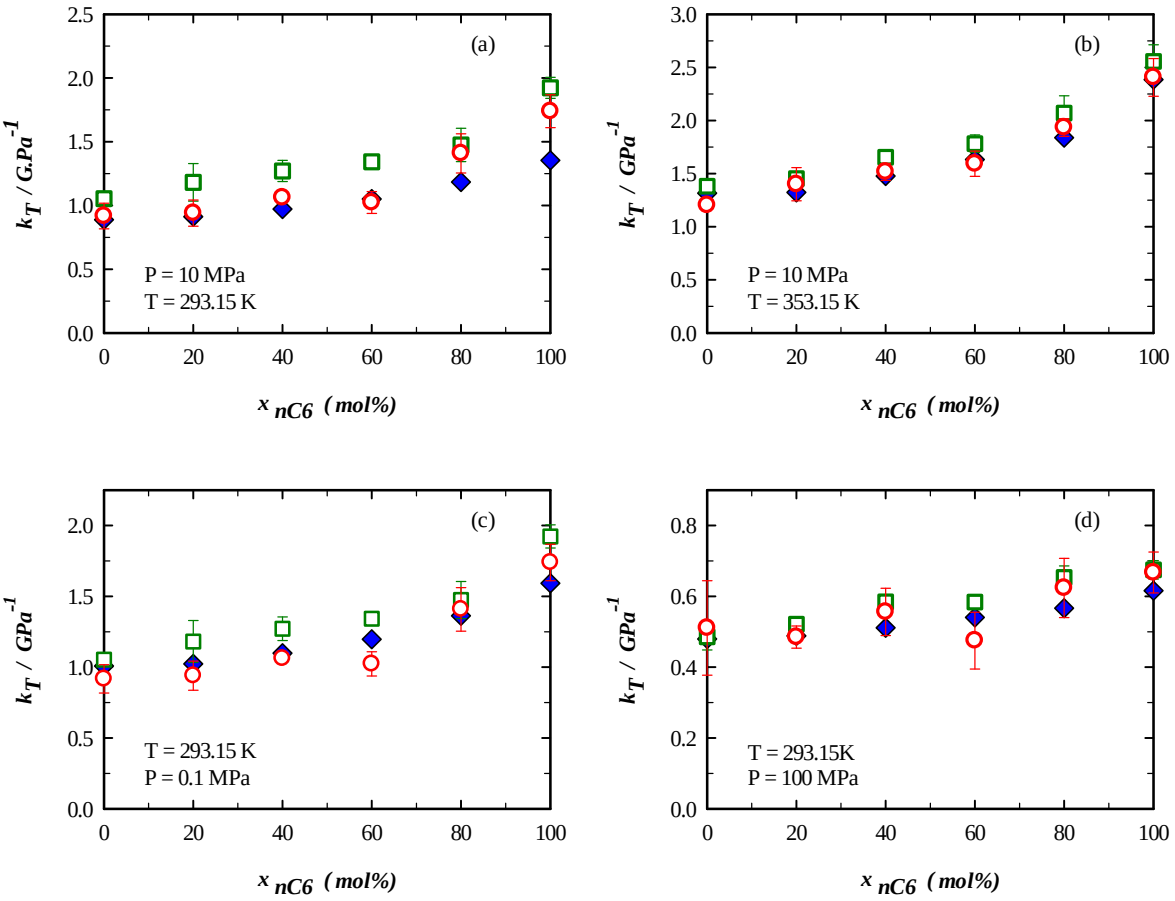

Figure 4.7 Isothermal compressibility as a function of n-hexane concentration at different temperature and pressure conditions. Comparison between ◆: experimental data; □: TraPPE-ua and ○: MCCG.

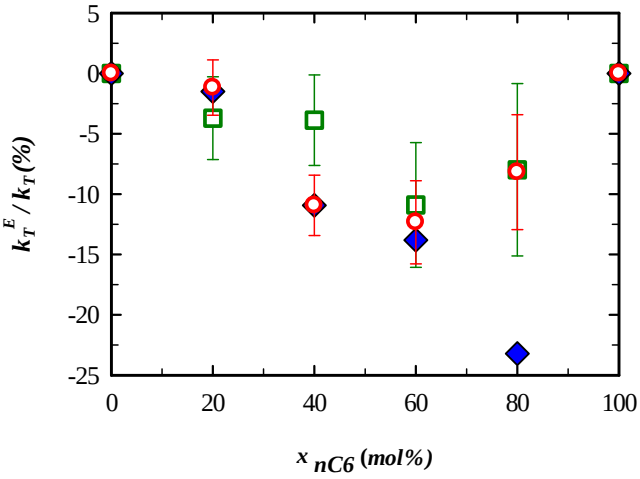

Figure 4.8 Relative excess isothermal compressibility as a function of concentration of n-hexane at 333.15 K and 0.1 MPa. Comparison between ◆: experimental data; □: TraPPE-ua and ○: MCCG.

In our experimental pressure and temperature range, κ_T^E values are negative and tend to zero by increasing the pressure. Interestingly, although κ_T^E values are often very small, they can be

sometimes significant relatively to the real mixture values of κ_T, reaching up to 25% at T=313.15 K; P=0.1MPa, see Figure 4.8. For these conditions, we evaluated the capability of molecular simulations to describe the non-ideal behaviour of the mixture in terms of κ_T, see Figure 4.6. This figure shows that the simulation results, for both force fields, depict the same trend as the experimental values, except at 80 % of n-hexane for which the molecular simulations underestimate noticeably the experimental value.

4.3.3 Speed of Sound and Excess Speed of Sound

In this section, simulation results were compared to experimental speed of sound. Numerical speed of sound was computed indirectly according to Newton-Laplace equation (equation (3.55)) using density, isothermal compressibility, isobaric thermal expansion and residual heat capacity directly estimated from Monte Carlo simulations. The use of this method, notwithstanding that it leads to important expanded uncertainties, provides generally acceptable results even if indirect[30]. The parity plot of Figure 4.9 shows that the MCCG force field is more efficient to predict the speed of sound than the TraPPE-ua. The latter, as depicted by Figure 4.10, systematically underestimates this property with a Bias of 6.1 % and an AAD of 6.1 % while for MCCG the Bias is of 0.1 % and the AAD is equal to 2.5 %.

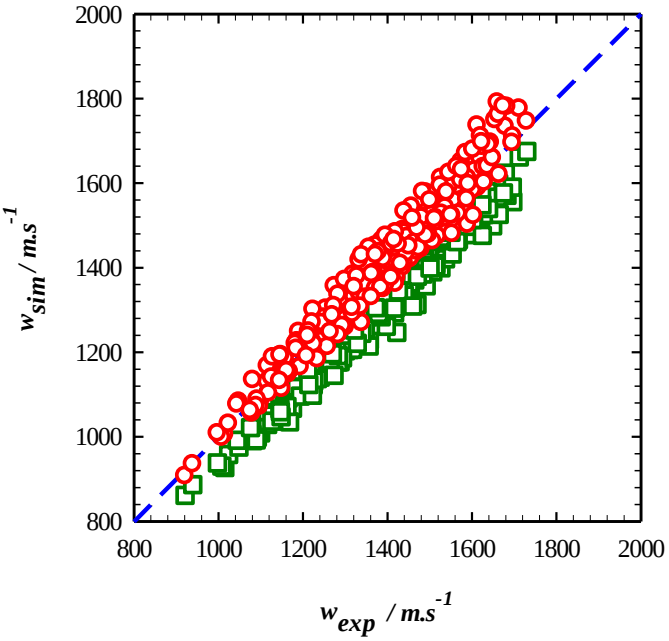

Figure 4.9 Calculated molecular simulation data of sound velocity w_{sim} as a function of experimental data w_{exp} for the mixture n-hexane + n-dodecane. Comparison between □: TraPPE-ua and ○: MCCG .

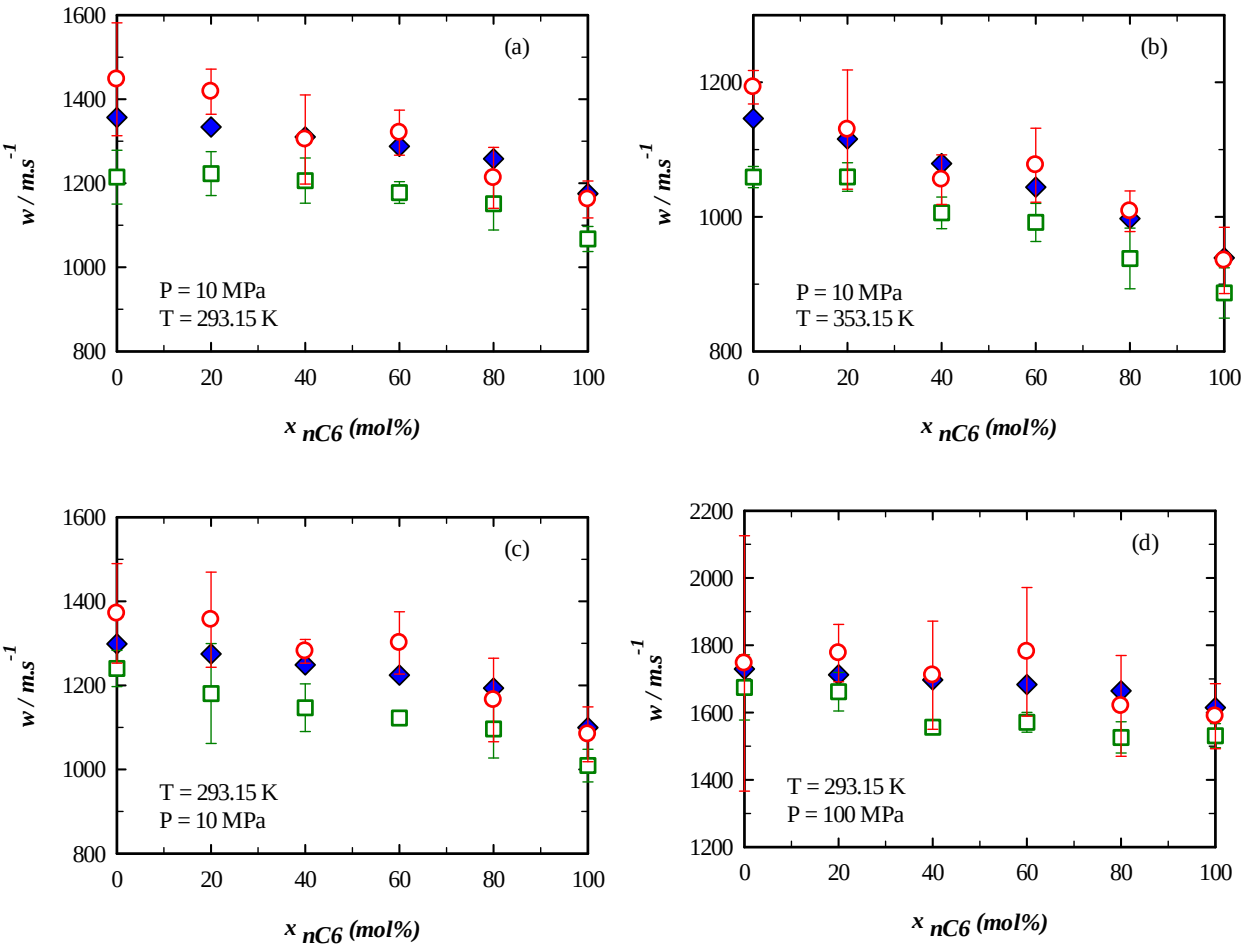

Figure 4.10 Speed of sound as a function of n-hexane concentration at different temperature and pressure conditions. Comparison between ◆: experimental data; □: TraPPE-ua and ○: MCCG.

Thereafter, we calculated excess speed of sound w^E from our experimental measurements. However, contrary to excess molar volume and excess isothermal compressibility, the calculation of w^E is not straightforward. The corresponding equation, which is presented in more details in a previous paper[31] is defined as follows:

$$w^E = w - \sqrt{\frac{\sum_i x_i \frac{M_i}{\rho_i}}{M\kappa_S^{id}}} \tag{4.5}$$

With

$$\kappa_S^{id} = \sum_i \emptyset_i \kappa_{T,i} - \frac{\left(\sum_i x_i \frac{M_i}{\rho_i}\right)\left(\sum_i \emptyset_i \alpha_{p,i}\right)^2}{\sum_i x_i \frac{M_i T \alpha_{p,i}^2}{\rho_i\left(\kappa_{T,i} - \kappa_{S,i}\right)}} \tag{4.6}$$

Where the subscript i denotes either n-hexane or n-dodecane. In addition to density ρ_i and isothermal compressibility $\kappa_{T,i}$, equation (4.6) also involves the isentropic compressibility $\kappa_{S,i}$

and the isobaric thermal expansion $\alpha_{p,i}$. The first one is calculated from the speed of sound and the density according to the following relation:

$$\kappa_S = \frac{1}{\rho w^2} \tag{4.7}$$

Concerning the isobaric thermal expansion, it was obtained from derivation of isobaric density measurements with respect to temperature by using the same Monte Carlo derivation method as the isothermal compressibility (cf. section 2.5.2).

The results show that the excess speed of sound values are positive. This behavior perfectly matches with our observation on excess molar volume and excess isothermal compressibility. Indeed, v^E and κ_T^E are shown to be negative, which means that the real mixture is denser than the ideal one, leading to higher speed of sound in the real mixture. In terms of amplitude, the excess sound velocity data can reach up to 6% of real mixture values.

Excess speed of sound were also calculated from simulation results by the mean of equations (4.5) and (4.6), leading to error bars than can be very large (up to 150 m/s). In Figure 4.9, simulation relative excess sound velocities are compared to experimental ones. Interestingly, the simulations values follow the trends depicted by the experimental results and are of the same order of magnitude despite the large error bars, showing the ability of the simulations to capture the weak non-ideal behavior of the mixture in terms of speed of sound.

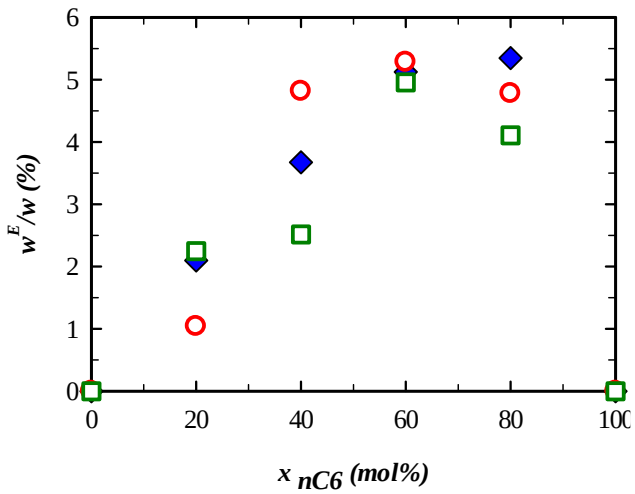

Figure 4.11 Relative excess sound velocity as a function of concentration of n-hexane at 333.15 K and 0.1MPa. Comparison between data calculated from ◆: experimental data; □: TraPPE-ua and ○: MCCG. For the sake of clarity, the large error bars are not represented.

4.4. A Transport Property: the Shear viscosity

As a further test of the capabilities of the chosen force fields, we evaluated their performance using Molecular Dynamic simulations combined to experimental measurements, to predict the viscosity of n-hexane and n-dodecane and their binary mixtures. The simulations were

performed at two temperatures (293.15 and 353.15 K) and five pressures (0.1, 10, 40,70 and 100 MPa). The simulation results with their corresponding numerical standard deviations for both TraPPE-ua and MCCG force fields are summarized in Tables B.10 and B.11 Appendix B. Compared to experimental data, as shown in Figures 4.12 and 4.13, it appears that the two force fields systematically underpredict the viscosity, with underestimation reaching 50 %. More precisely, for both molecular models, the denser (low temperature, high pressure, high content of n-dodecane) the system is, the higher are the deviations from experimental data as depicted by Figure 4.13.

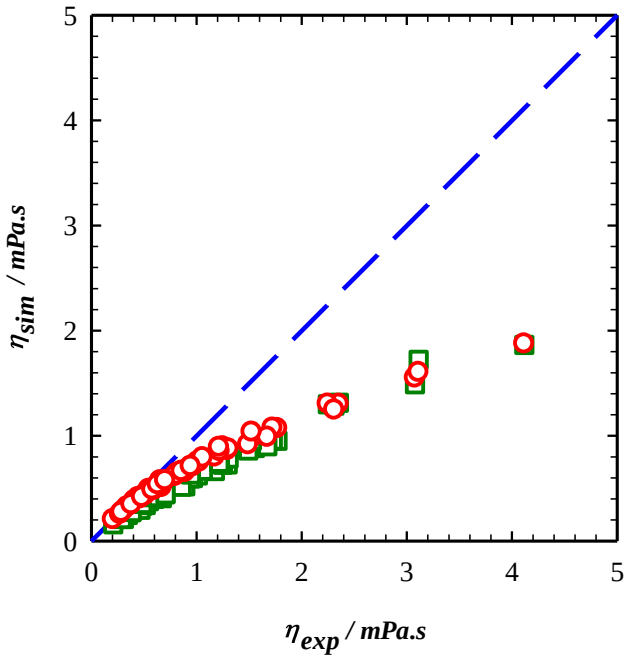

Figure 4.12 Molecular simulation data of viscosity η_{sim} as a function of experimental data η_{exp} for the mixture n-hexane + n-dodecane. Comparison between □: TraPPE-ua and ○: MCCG.

In details, the MCCG force field appears to be slightly more accurate than TraPPE-ua for low viscosities, see Figure 4.13. Quantitatively the experimental viscosities are underestimated by MCCG with an overall AAD of 24 %, a Bias of 24 % and a Max AD of 50 % whereas for TraPPE-ua we obtained an overall AAD of 35 %, a Bias of 35 % and a Max AD of 55 %.

Such a weakness of some force fields to yield correct transport properties has already been noticed by many authors[10,13,14,32–35] for n-alkanes systems. This inability of both force fields to capture correctly the density dependence of shear viscosity of such systems is probably related to the way the force fields describe the molecules' global rigidity[10,13], in particular the MCCG force field which is a fully flexible model. This weakness has to do as well with the way the force fields are usually defined. Indeed, such a result is not so surprising as most of the force fields, including TraPPE-ua, have been developed so as to mimic essentially equilibrium properties. However, it is known that phase equilibrium properties are usually less dependent to the internal rigidity than is viscosity[10] and so are not discriminative properties regarding the way internal degrees of freedom should be described.

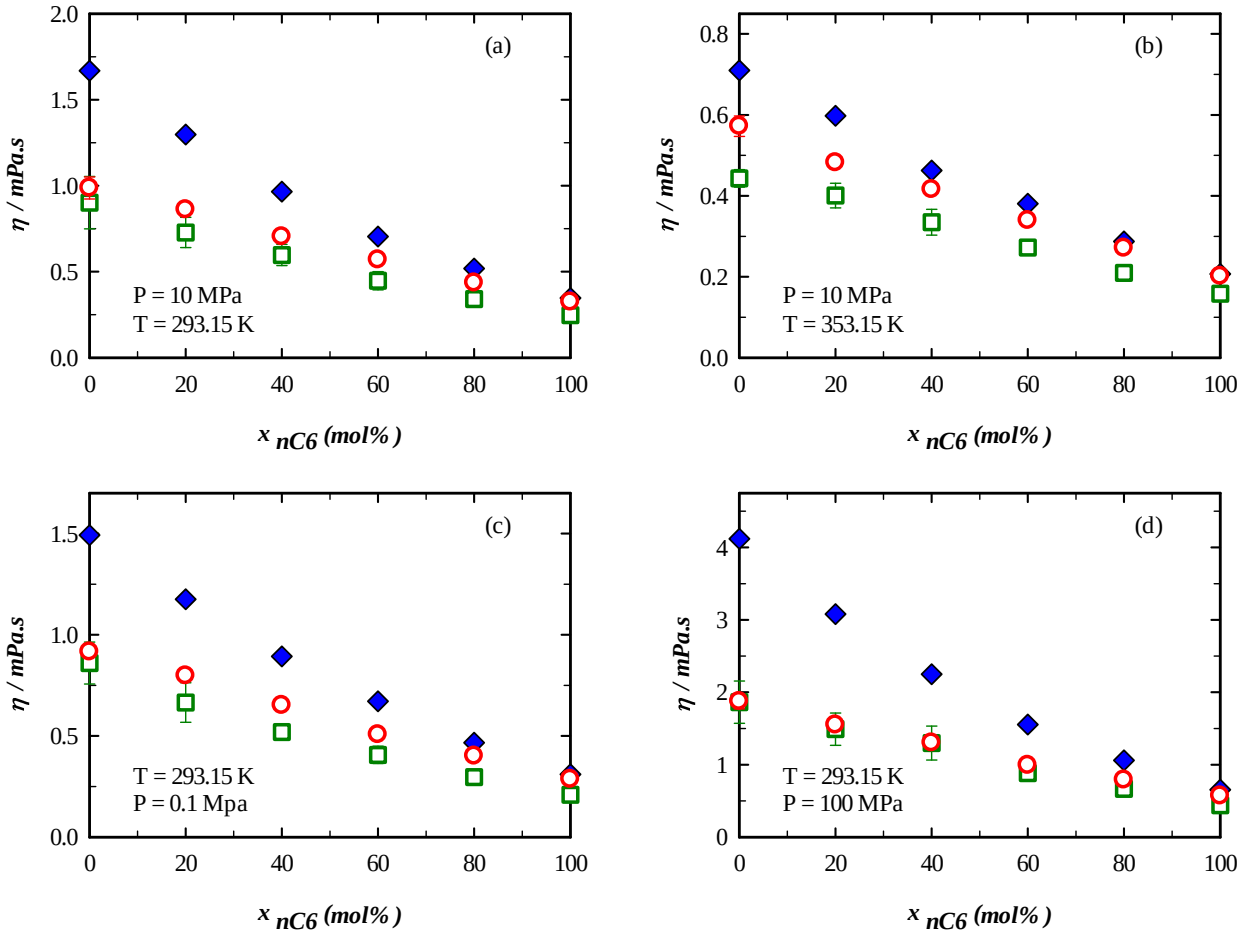

Figure 4.13 Viscosity as a function of n-hexane concentration at different temperature and pressure conditions. Comparison between ◆: experimental data; □: TraPPE-ua and ○: MCCG.

As for thermodynamic properties, we defined a viscosity deviation called excess viscosity of the binary mixture as the difference between the real mixture viscosity and a linear combination of pure compound viscosities[36]. It is given by the following correlation:

$$\eta^E = \eta - x_{nC6}\eta_{nC6} - (1 - x_{nC6})\eta_{nC12} \tag{4.8}$$

It should be noticed that such a deviation definition is not unique and has been chosen simply by analogy to the excess properties used to describe deviation from ideal mixtures on the volumetric properties as both quantities are strongly linked.

The experimental results show that the excess viscosities are negative, meaning that the ideal mixture is more viscous than the real mixture. The excess viscosities decrease in absolute values as the pressure decreased and the temperature is increased. Consequently , the maximum absolute values of η^E are observed at 293.15 K and 100 MPa, corresponding to the smallest values of v^E, κ_T^E and w^E . In these conditions, the excess viscosity can reach up to 35% of the real mixture viscosity.

Figure 4.14 compares the simulation relative excess viscosities to experimental values in the case of highest values of η^E . It appears that the excess viscosity is not well quantified by the

MCCG force field and is only qualitatively captured (noticeably underestimated in absolute value) by the TraPPE-ua. This misevaluation, even if small compared to the ones noticed on pure fluids, adds to the limitations of these force field to predict accurately viscosity for the densest systems studied here and may indicate a limitations of the combining rules used in this work. Such results indicate that viscosity is an interesting and sensitive property not only to evaluate the quality of force field but also the capabilities of combining rules to capture cross interactions for a given molecular model.

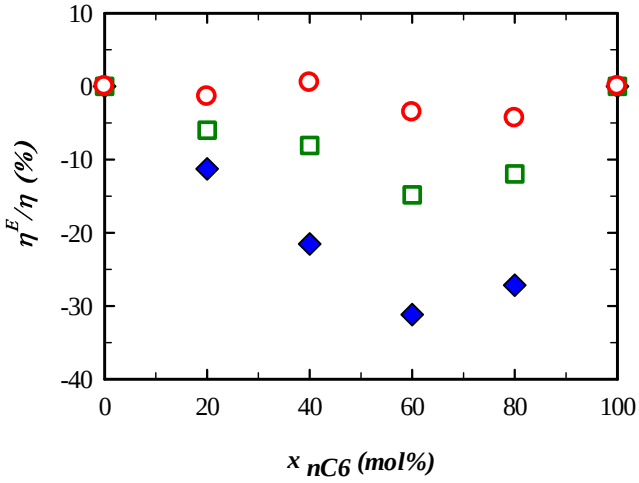

Figure 4.14 Relative excess viscosity as a function of concentration of n-hexane at 293.15 K and 100 MPa. Comparison between data calculated from ◆: experimental data; □: TraPPE-ua and ○: MCCG . For the sake of clarity, the large error bars are not represented.

4.5. Conclusions

In this work, we have evaluated the capabilities of two force fields, a united atom one (TraPPE-ua) and a coarse grained one (MCCG), to provide simultaneously thermodynamic properties, including derivative ones and excess quantities, and shear viscosity of simple liquid mixtures composed of n-hexane + n-dodecane over a wide range of thermodynamics conditions (from 293.15 to 353.15K and pressure up to 100 MPa). To achieve this test on a consistent and controlled set of data, we have performed accurate measurements of density, speed of sound and shear viscosity of these mixtures. From the simulation point of view, we have computed the aforementioned thermophysical properties at the same thermodynamic conditions using both classical Monte Carlo and Molecular Dynamics simulations combined with the two tested force fields and simple Lorentz-Berthelot combining rules.

The results obtained by the TraPPE-ua force field yield an AAD of 1.5 % for the density, 11.1 % for the isothermal compressibility, 6.1 % for the sound velocity and 35 % for the viscosity. Concerning the MCCG force field, it leads to slightly better results with an AAD of, 1.2 % for the density, 5.9 % for the isothermal compressibility, 2.5 % for the speed of sound and 24 % for the viscosity. An additional interesting point is that, when comparing the simulated excess properties to experimental values, the two force fields, using simple Lorentz-Berthelot

combining rules, are shown to capture rather well the weak non-ideality of the mixtures in terms of excess thermodynamic properties, but not in terms of excess viscosity. Thus, these results confirm that both TraPPE-ua and MCCG are able to yield results on direct and derivative thermodynamic properties in fair agreement with experimental ones. However, important deviations (systematic underestimation) from experimental data, up to around 50 %, are observed on viscosity for the densest systems. Such deviations confirm that, even on simple molecular systems such as n-alkane mixtures, force fields that are able to describe accurately fluid equilibrium properties are not always able to yield precise transport properties. Such results indicate that viscosity is an interesting property not only to evaluate the quality of force fields but also the capabilities/limitations of the combining rules to capture cross interactions for a given molecular model.

Further systematic tests are planned to deal with more asymmetric, and so more non-ideal mixtures[31,37], which are known to be even more difficult to model using classical equation of states and viscosity correlations, approaches [2].

4.6. References

(1) Lagache, M.; Ungerer, P.; and A. H. Fuchs, A. B. Prediction of Thermodynamic Derivative Properties of Fluids by Monte Carlo Simulation,. *Phys Chem Chem Phys* 2001, *3*.

(2) Hendriks, E.; Kontogeorgis, G. M.; Dohrn, R.; de Hemptinne, J.-C.; Economou, I. G.; Žilnik, L. F.; Vesovic, V. Industrial Requirements for Thermodynamics and Transport Properties. *Ind. Eng. Chem. Res.* 2010, *49* (22), 11131–11141.

(3) Wilhelmsen, Ø.; Aasen, A.; Skaugen, G.; Aursand, P.; Austegard, A.; Aursand, E.; Gjennestad, M. A.; Lund, H.; and M. Hammer, G. L. Thermodynamic Modeling with Equations of State: Present Challenges with Established Methods,. *Ind Eng Chem Res 56*, 3503–3515.

(4) Yang, T.; Fevang, Ø.; Ruhrgas, E. O.; Christoffersen, K.; Ivarrud, E. LBC Viscosity Modeling of Gas Condensate to Heavy Oil. *SPE* 9.

(5) Assael, M. *Experimental Thermodynamics Volume IX: Advances in Transport Properties of Fluids*; Goodwin, A. R., Vesovic, V., Wakeham, W. A., Eds.; Royal Society of Chemistry: Cambridge, 2014.

(6) Moore, J. D.; Gubbins, K. E. Molecular Modeling of Matter: Impact and Prospects in Engineering,. *Ind Eng Chem Res* 2010, *49*, 3026–3046.

(7) Ungerer, P.; Nieto-Draghi, C.; Rousseau, B.; Ahunbay, G.; Lachet, V. Molecular Simulation of the Thermophysical Properties of Fluids: From Understanding toward Quantitative Predictions. *J. Mol. Liq.* 2007, *134* (1–3), 71–89.

(8) Martin, M. G.; Siepmann, J. I. Transferable Potentials for Phase Equilibria. 1. United-Atom Description of n-Alkanes. *J. Phys. Chem. B* 1998, *102* (14), 2569–2577.

(9) Hoang, H.; Delage-Santacreu, S.; Galliero, G. Simultaneous Description of Equilibrium, Interfacial, and Transport Properties of Fluids Using a Mie Chain Coarse-Grained Force Field. *Ind. Eng. Chem. Res.* 2017, *56* (32), 9213–9226.

(10) Galliero, G. Equilibrium, Interfacial and Transport Properties of n-Alkanes: Towards the Simplest Coarse Grained Molecular Model. *Chem. Eng. Res. Des.* 2014, *92* (12), 3031–3037.

(11) Mejía, A.; Herdes, C.; Müller, E. A. Force Fields for Coarse-Grained Molecular Simulations from a Corresponding States Correlation. *Ind. Eng. Chem. Res.* 2014, *53* (10), 4131–4141.

(12) Lafitte, T.; Apostolakou, A.; Avendaño, C.; Galindo, A.; Adjiman, C. S.; Müller, E. A.; Jackson, G. Accurate Statistical Associating Fluid Theory for Chain Molecules Formed from Mie Segments. *J. Chem. Phys.* 2013, *139* (15), 154504.

(13) Nieto-Draghi, C.; Ungerer, P.; Rousseau, B. Optimization of the Anisotropic United Atoms Intermolecular Potential for N-Alkanes: Improvement of Transport Properties. *J. Chem. Phys.* 2006, *125* (4), 044517.

(14) Messerly, R. A.; Anderson, M. C.; Razavi, S. M.; Elliott, J. R. Improvements and Limitations of Mie λ-6 Potential for Prediction of Saturated and Compressed Liquid Viscosity. *Fluid Phase Equilibria* 2019, *483*, 101–115.

(15) Allen, M. P.; Tildesley, D. J. *Computer Simulation of Liquids*; Oxford University Press, 2017.

(16) Frenkel, D.; Smit, B. *Understanding Molecular Simulation*; Elsevier, 2002.

(17) Ungerer P., Tavitian B.; Boutin A. In Applications of molecular simulations in the oil and gas industry, Monte Carlo methods; Editions TECHNIP, 2005.

(18) Vlugt, T. J. H.; Martin, B. S. M. G.; and R. Krishna, Siepmann J. . Improving the Efficiency of the Configurational-Bias Monte Carlo Algorithm,. *Mol. Phys.* 1998, *94* (4), 727–733.

(19) Siepmann, J. I.; b, D. F. Configurational Bias Monte Carlo: A New Sampling Scheme for Flexible Chains,. *Mol. Phys.* 1992, *75* (1), 59–70.

(20) Wick, C. D.; Siepmann, J. I. Self-Adapting Fixed-End-Point Configurational-Bias Monte Carlo Method for the Regrowth of Interior Segments of Chain Molecules with Strong Intramolecular Interactions. *Macromolecules* 2000, *33* (19), 7207–7218.

(21) Tenney, C. M.; Maginn, E. J. Limitations and Recommendations for the Calculation of Shear Viscosity Using Reverse Nonequilibrium Molecular Dynamics. *J. Chem. Phys.* 2010, *132* (1), 014103.

(22) Nosé, S. A Unified Formulation of the Constant Temperature Molecular Dynamics Methods. *J. Chem. Phys.* 1984, *81* (1), 511–519.

(23) Evans, D. J.; Holian, B. L. The Nose–Hoover Thermostat. *J. Chem. Phys.* 1985, *83* (8), 4069–4074.

(24) Hoover, W. G. Canonical Dynamics: Equilibrium Phase-Space Distributions. *Phys. Rev. A* 1985, *31* (3), 1695–1697.

(25) Berendsen, H. J. C.; Postma, J. P. M.; van Gunsteren, W. F.; DiNola, A.; Haak, J. R. Molecular Dynamics with Coupling to an External Bath. *J. Chem. Phys.* 1984, *81* (8), 3684–3690.

(26) Andersen, H. C. Rattle: A "Velocity" Version of the Shake Algorithm for Molecular Dynamics Calculations. *J. Comput. Phys.* 1983, *52* (1), 24–34.

(27) Carreau, P. J. Rheological Equations from Molecular Network Theories. *Trans. Soc. Rheol.* 1972, *16* (1), 99–127.

(28) Treszczanowicz, A. J.; Kiyohara, O.; Benson, G. C. Excess Volumes for N-Alkanols +n-Alkanes IV. Binary Mixtures of Decan-1-Ol +n-Pentane, +n-Hexane, +n-Octane, +n-Decane, and +n-Hexadecane. *J. Chem. Thermodyn.* 1981, *13* (3), 253–260.

(29) Nakamura, M.; Chubachi, K.; Tamura, K.; Murakami, S. Excess Molar Volumes, Excess Isentropic and Isothermal Compressibilities, and Excess Molar Isochoric Heat Capacities

of [XCF3CH2OH + (1-x){HCON(CH3)2 or CH3CN}] at the Temperature 298.15 K. *J. Chem. Thermodyn.* 1993, *25* (4), 525–531.

(30) Fazelabdolabadi, B.; Bahramian, A. Prediction of Sound Velocity in Normal Alkanes: A Configurational-Bias Monte Carlo Simulation Approach. *Fluid Phase Equilibria* 2009, *284* (2), 129–136.

(31) Bazile, J.-P.; Nasri, D.; Saley Hamani, A. W.; Galliero, G.; Daridon, J.-L. Excess Volume, Isothermal Compressibility, Isentropic Compressibility and Speed of Sound of Carbon Dioxide + n-Heptane Binary Mixture under Pressure up to 70 MPa. I Experimental Measurements. *J. Supercrit. Fluids* 2018, *140*, 218–232.

(32) Galliero, G. Chapter 11. Computer Simulations. In *Experimental Thermodynamics Volume IX*; Assael, M. J., Goodwin, A. R. H., Vesovic, V., Wakeham, W. A., Eds.; Royal Society of Chemistry: Cambridge, 2014; pp 362–386.

(33) Allen, W.; Rowley, R. L. Predicting the Viscosity of Alkanes Using Nonequilibrium Molecular Dynamics: Evaluation of Intermolecular Potential Models. *J. Chem. Phys.* 1997, *106* (24), 10273–10281.

(34) Dysthe, D. K.; Fuchs, A. H.; Rousseau, B.; Durandeau, M. Fluid Transport Properties by Equilibrium Molecular Dynamics. II. Multicomponent Systems. *J. Chem. Phys.* 1999, *110* (8), 4060–4067.

(35) Rahman, S.; Lobanova, O.; Jiménez-Serratos, G.; Braga, C.; Raptis, V.; Müller, E. A.; Jackson, G.; Avendaño, C.; Galindo, A. SAFT-γ Force Field for the Simulation of Molecular Fluids. 5. Hetero-Group Coarse-Grained Models of Linear Alkanes and the Importance of Intramolecular Interactions. *J. Phys. Chem. B* 2018, *122* (39), 9161–9177.

(36) Garcia, B.; Ortega, J. C. Excess Viscosity .ηE, Excess Volume VE, and Excess Free Energy of Activation .ΔGE at 283, 293, 303, 313, and 323 K for Mixtures Acetonitrile and Alkyl Benzoates. *J. Chem. Eng. Data* 1988, *33* (2), 200–204.

(37) Regueira Muñiz, T.; Pantelide, G.; Yan, W.; Stenby, E. H. Density and Phase Equilibrium of the Binary System Methane + N-Decane under High Temperatures and Pressures. *Fluid Phase Equilibria* 2016, *428*, 48–61.

Chapter 5. Experimental Measurements of CO2+nC7 Mixtures

*Results in this chapter have been published in J. Sup. Flu. 140, 218-232, 2018

Contents

5.1. Mixtures studied 74
5.2. Volumetric Properties 75
5.2.1 Density 75
5.2.2 Excess volumes 81
5.3. Isothermal compressibility and excess isothermal compressibility 83
5.4. Acoustic properties 88
5.4.1 Speed of sound and isentropic compressibility 88
5.4.2 Excess isentropic compressibility and excess speed of sound 93
5.5. Conclusions 98
5.6. References 99

Introduction

To simulate enhance oil recovery processes as well as for seismic monitoring, volumetric and acoustic properties are key quantities. In particular, the knowledge of volumetric properties as a function CO_2 content in reservoir conditions is required to predict oil swelling and change in oil compressibility. With this aim in mind, an experimental and modelling investigation of thermophysical properties of binary liquid systems containing supercritical CO_2 and a hydrocarbon has been initiated in our laboratory. At the initial phase of this program, which forms this chapter, it was chosen to determine experimentally the excess volumetric and acoustic properties of carbon dioxide + n-heptane binary mixtures in various proportions at two temperatures (303 and 313 K) in the vicinity of the critical temperature of pure carbon dioxide (304.13 K) at pressures from 10 to 70 MPa, i.e. above the critical pressure of the pure components, by carrying out speed of sound and density measurements in the same mixtures. These specific thermodynamic conditions have been chosen so as to specifically analyze the expected influence of the proximity of the critical point of CO2 on the non-idealities of the studied mixture. As the second part of this study, molecular simulations of the same systems are performed and will be presented in detail in the next chapter. Speed of sound measurements were performed with a pulse echo technique whereas density was measured by using a U-shape tube density meter. By combination of density and speed of sound data, the isentropic compressibility was determined in the same pressure range. Moreover, the isothermal compressibility was evaluated from derivation of density measurements.
In the following the Chapter is structured as follow. Section 5.1 provides some details on the mixtures studied, Sections 5.2 and 5.3 embody the experimental results as well as the discussion on them, in particular from the excess volumetric properties point of view. Finally, the conclusion section summarizes the main outcomes of this study.

5.1. Mixtures Studied

Measurements were carried out along two isotherms around the critical temperature of CO_2 for several pressures ranging from 10 MPa to 70 MPa. Both speed of sound and density measurements were performed for pure n-heptane and five different mixtures ranging from 20 to 88.5 mol% of CO_2. The mixtures were first prepared in the speed of sound cell and then duplicated in the density measuring cell. Table 5.1 presents the different mixtures investigated along with their expended uncertainty $U(x_{co2})$ calculated with the conventional coverage factor k_P = 2 (Probability = 95 %). The difference in composition between the two sets was always much lower than the uncertainty in the mixture synthesis so that both datasets can be combined to enable estimation of derivative properties such as isentropic compressibility, and excess speed of sound. Figure 5.1 displays the experimental conditions of temperature and pressure as well as the *P*, *T* projection of the critical locus[7–9] that extends from the critical conditions of carbon dioxide to n-heptane critical point. The Binary system CO_2 +n-C_7 being of type II[10] with an Upper Critical End Point (UCEP) temperature of 222.7 K, the system is in single fluid phase state for all experimental conditions studied in this work. As can be seen in Figure 5.1 all the mixtures are in liquid state in the experimental conditions covered by the experiments whereas

in these conditions the CO_2 is either liquid in the vicinity of the critical temperature or supercritical.

Table 5.1 Composition in mol % of the different carbon dioxide + n-heptane binary mixtures investigated

Speed of sound	x_{co2} / mol%	20.14	40.02	60.00	83.26	88.50
measurements	$U(x_{co2})$ / mol%	0.01	0.01	0.01	0.01	0.01
Density	x_{co2} / mol%	20.14	40.00	60.00	83.26	88.49
measurements	$U(x_{co2})$ / mol%	0.07	0.05	0.04	0.03	0.03

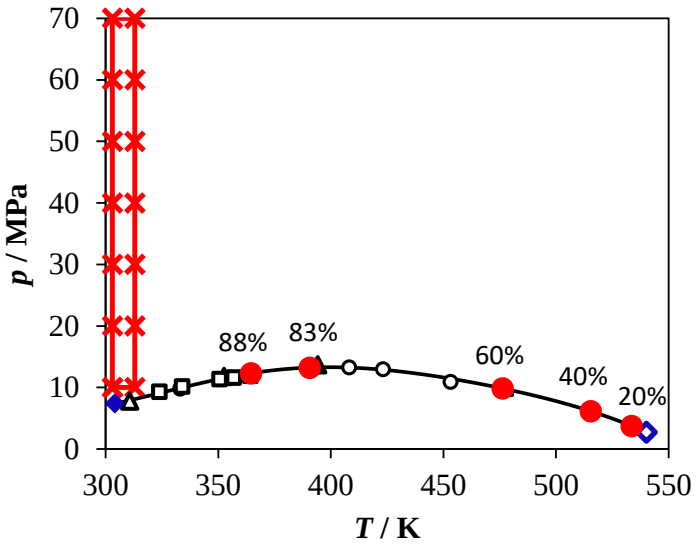

Figure 5.1 *P*, *T* projection of the carbon dioxide + n-heptane critical locus and experimental temperature and pressure conditions for the speed of sound and density measurements performed in this work. Δ: Kalra et al.[7]; ○: Chester and Haynes[8]; □: Choi an Yeo[9] ; ◆: CO_2 critical point; ◇: n-C_7 critical point; ●: critical conditions of the investigated mixtures estimated from interpolation of literature data; ×:experimental temperature and pressure conditions.

5.2. Volumetric Properties

5.2.1 Density

The volumetric mass density of the mixtures investigated as well as those of pure components are listed in Table 5.2 along with the expanded uncertainties $U(\rho)$, calculated by multiplying the combined standard uncertainty by the conventional coverage factor k_P = 2 (***Probability = 95 %).***

Densities of both pure components were measured previously under pressure by several authors and accurate correlations were developed to represent the volumetric properties of carbon

dioxide[11] and n-heptane[12] on an extended range. These correlations were used for comparisons with the present measurements. Comparison with Span and Wagner correlation gave for CO_2 an Average Absolute Deviation (AAD) of 0.04 % and a Maximum Deviation (MD) of 0.1 % corresponding to the lower pressure as can be observed in Figure 5.2. For n-heptane, comparison in Figure 5.3 of density data with the correlations shows that the equation of state developed by Lemmon and Span[12] is in agreement with the values reported here within the entire region of investigation. The maximum deviation observed is 0.1 % and the average absolute deviation is 0.05%. Larger deviations are observed with other correlations at higher pressure. Whatever the pressure, the deviation is lower than the expended uncertainty represented by a Chain-dotted curves in Figure 5.3.

Table 5.2 Density ρ and its expended uncertainty $U(\rho)$ in carbon dioxide + n-heptane binary mixtures as a function of temperature *T*, pressure *P* and composition x_{co2}

T	*P*	$\rho \pm U(\rho)$		$\rho \pm U(\rho)$		$\rho \pm U(\rho)$		$\rho \pm U(\rho)$	
K	MPa	kg.m^{-3}							
x_{co2} / mol%		0 %		20.14 %		40.00 %		60.00 %	
303.35	10.12	684.5	0.9	698.6	0.8	717.6	0.7	742.7	0.6
303.35	20.14	692.9	0.9	708.6	0.8	730.4	0.7	761.5	0.6
303.35	30.18	700.4	0.9	717.2	0.8	741.7	0.7	776.7	0.6
303.35	40.25	707.2	1.0	725.2	0.8	751.4	0.7	789.8	0.6
303.35	50.35	714.2	1.0	733.0	0.8	760.2	0.7	801.3	0.6
303.35	60.47	720.0	1.0	739.7	0.8	768.3	0.7	811.8	0.6
303.35	70.62	725.7	1.0	745.8	0.8	775.8	0.7	821.1	0.6
313.25	10.11	677.2	0.9	690.1	0.8	706.7	0.7	727.5	0.5
313.25	20.13	686.1	0.9	701.0	0.8	720.7	0.7	748.3	0.6
313.25	30.16	694.0	0.9	710.0	0.8	732.5	0.7	765.0	0.6
313.25	40.23	701.2	0.9	718.6	0.8	743.0	0.7	779.0	0.6
313.25	50.31	707.9	1.0	726.2	0.8	752.2	0.7	791.3	0.6
313.25	60.41	713.9	1.0	733.1	0.8	760.6	0.7	802.2	0.6
313.25	70.54	719.7	1.0	739.7	0.8	768.5	0.7	812.1	0.6
x_{co2} / mol%		83.26 %		88.49 %		100 %			
303.35	10.12	779.4	0.4	786.4	0.4	773.0	1.1		
303.35	20.14	818.3	0.5	837.6	0.5	890.8	0.4		
303.35	30.18	846.2	0.5	871.3	0.5	948.6	0.4		
303.35	40.25	868.1	0.5	897.2	0.6	988.1	0.4		
303.35	50.35	886.5	0.6	918.5	0.6	1019.9	0.4		
303.35	60.47	902.4	0.6	936.9	0.6	1046.3	0.4		
303.35	70.62	916.5	0.6	953.0	0.6	1068.9	0.4		
313.25	10.11	750.8	0.4	744.4	0.4	634.0	1.2		
313.25	20.13	794.8	0.5	809.2	0.4	840.2	0.4		
313.25	30.16	825.7	0.5	847.9	0.5	910.3	0.4		
313.25	40.23	849.6	0.5	876.6	0.5	956.6	0.4		
313.25	50.31	869.3	0.5	899.8	0.6	991.9	0.4		
313.25	60.41	886.3	0.6	919.5	0.6	1020.6	0.4		
313.25	70.54	901.2	0.6	936.8	0.6	1045.1	0.4		

Liquid density data were already reported for the binary mixture CO_2 + n-C_7 by Fenghour et al.[13] and Medina-Bermudez et al.[14]. However, these data cannot be compared with the present measurement as they do not cover the same experimental pressure and temperature conditions and the compositions of the investigated mixture are different.

Because of the proximity to the critical temperature of pure CO_2, the density of CO_2 varies largely between 10 and 70 MPa for both investigated temperatures. It results from this large change that isopleth density curves corresponding to high concentrations in CO_2 cross as can be seen in Figure 5.4.

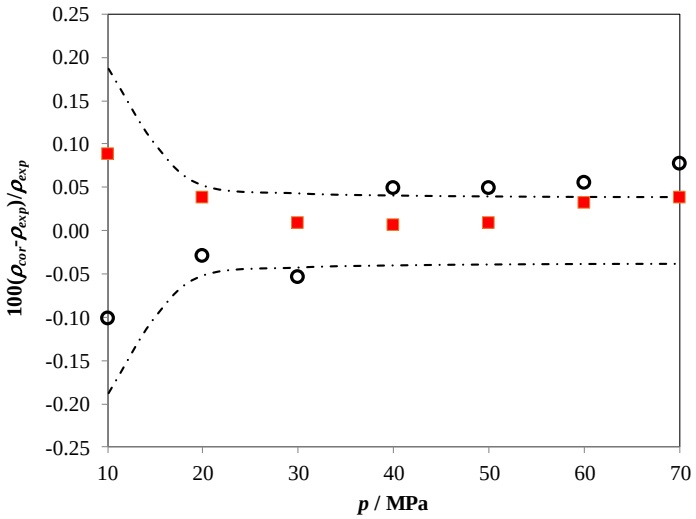

Figure 5.2 Deviations of the density data reported in Table 5.2 for CO_2 from correlation of Span and Wagner[11]: ○, 303.15 K; ■, 313.15 K; – · – · – : expanded uncertainty.

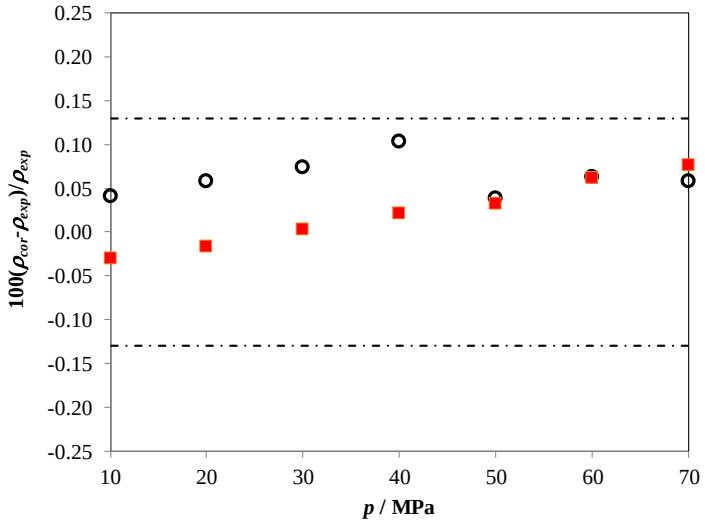

Figure 5.3 Deviations of the density data reported in Table 5.2 for n-C_7 from correlation of Lemmon and Span[12]: ○, 303.15 K; ■, 313.15 K; – · – · –: expanded uncertainty.

The influence of CO_2 content on density is presented in Figure 5.5 for the various isobars investigated at 313 K. It can be observed that, for pressures above 20 MPa, the isobaric curves monotonically increase from pure n-C_7 to pure CO_2 values whereas for the curve corresponding to 10 MPa the density of the mixture first increases with addition of CO_2 and then decreases above 80% of CO_2. This trend which is related to an important non ideal behavior at this specific pressure is observed for both investigated temperatures. However, by comparing panels (a) and

(b) of Figure 5.6 where the measurements performed at 10 MPa were compared to an ideal volumetric behavior for 303 K and 313 K respectively, it can be noted that the non-ideal behavior is more acute at 313 K.

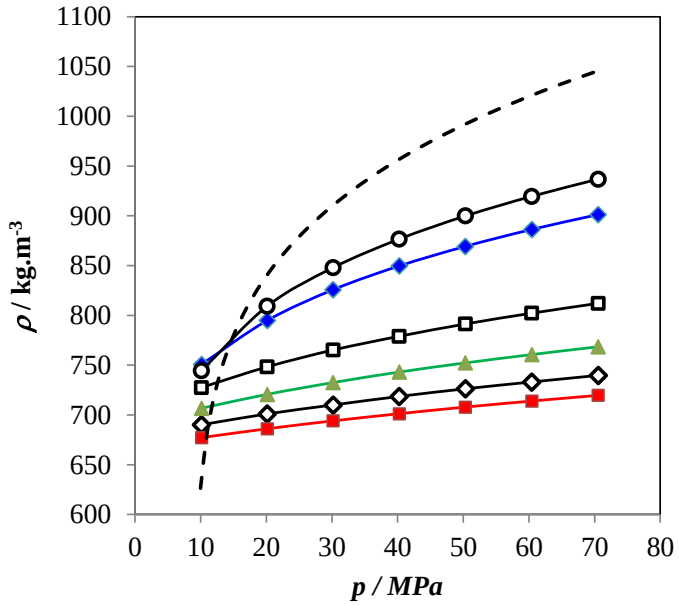

Figure 5.4 Density ρ as a function of pressure for different isopleths at 313 K. ■: pure n-C_7 ; ◇: 20 % CO_2 ; ▲: 40 % CO_2 ; □: 60 % CO_2 ; ◆: 83 % CO_2 ; ○: 88 % CO_2 ; - - - : pure CO_2.

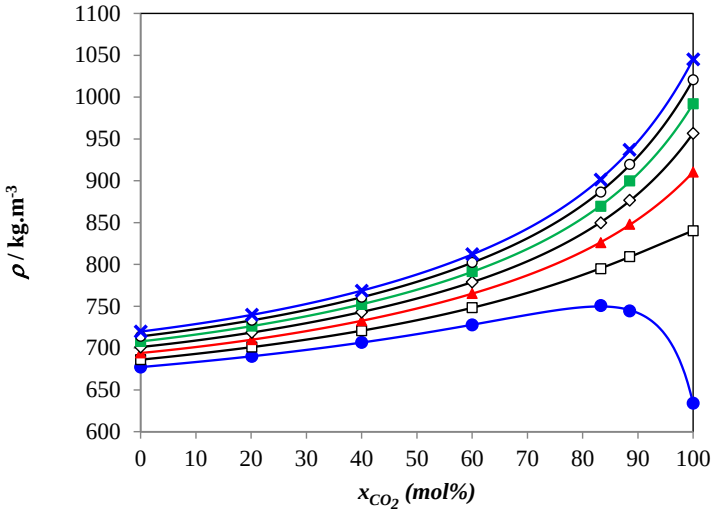

Figure 5.5 Density ρ as a function of concentration for different isobars at 313 K. ●: 10 MPa ; □: 20 MPa ; ▲: 30 MPa ; ◇: 40 MPa ; ■ 50 MPa ; ○: 60 MPa ; ×: 70 MPa.

This difference can be attributed to the relatively low density of pure CO_2 in this thermodynamic condition. At 313 K and 10 MPa the CO_2 is in supercritical state and has a density lower than n-heptane whereas at 303 K and 10 MPa the CO_2 is in a liquid state and is

denser than n-heptane. In both cases, at concentration below 60% of CO_2 in mole fraction the CO_2 behave in the mixture as an apparent component denser than pure CO_2.

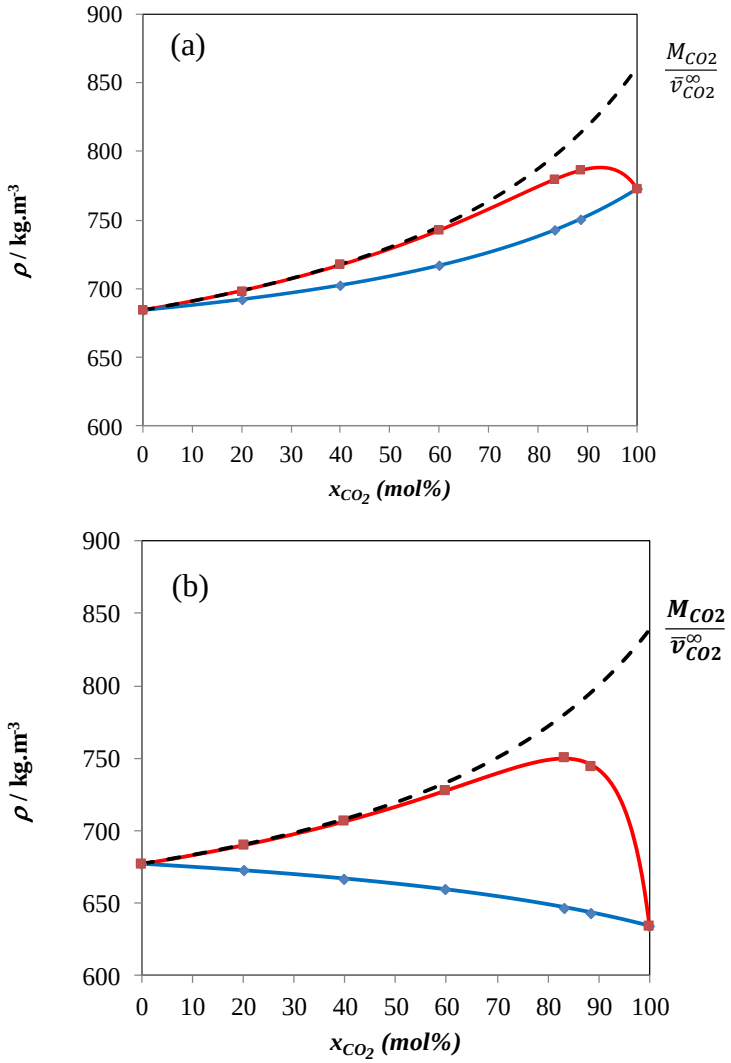

Figure 5.6 Density ρ as a function of concentration at 10 MPa and 303 K (panel a) and 313 K (panel b). Comparison between measurements (■) and ideal behavior (◆).- - - - : ideal solution with apparent density for CO_2 equal to $M_{CO2}/\bar{v}^{\infty}_{CO2}$.

This behavior can be highlighted by studying the partial molar volume $\bar{v}_{CO2}$. This quantity was determined by derivation with respect to CO_2 mole fraction of volume *v* obtained from density measurements:

$$\bar{v}_{CO2} = v + (1 - x_{CO2}) \left(\frac{\partial v}{\partial x_{CO2}}\right)_{P,T} \tag{5.1}$$

In this expression, the partial derivative was computed by first fitting the molar volume data at fixed pressure and temperature by an interpolation polynomial function. Subsequently the fitted function was differentiated analytically with respect to molar fraction. Results are plotted in Figure 5.7 for 10 MPa. It can be seen in this figure that indeed below 60% of CO_2 the partial molar volume of CO_2 appears to be nearly constant and equal to the partial molar volume of

CO_2 at infinite dilution $\bar{v}_{CO2}^{\infty}$. Its value is much lower than the molar volume v_{CO2} of pure CO_2. In addition, the partial volume of n-C_7 was calculated from the same derivative:

$$\bar{v}_{C7} = v - x_{CO2}\left(\frac{\partial v}{\partial x_{CO2}}\right)_{P,T} \tag{5.2}$$

and also plotted in Figure 5.7. For CO_2 concentration below 60 %, $\bar{v}_{C7}$ is independent of composition and is equal to the molar volume of pure n-heptane. Consequently, at low CO_2 content the volumetric behaviour of the system is similar to that of an ideal binary mixture with an apparent density of CO_2 equals to $M_{CO2}/\bar{v}_{CO2}^{\infty}$ as can be seen in panels (a) and (b) of Figure 5.6. Above 60 % of CO_2, the partial molar volume of n-C_7 tends to decrease, see Figure 5.7. This decrease in the partial molar volume of n-C_7 is more pronounced at 313 K than at 303 K. Interestingly, the partial molar volume at infinite dilution $\bar{v}_{C7}^{\infty}$ can even reach a negative value at 313 K as it can be seen in Figure 5.7. It should be noticed that such unusual change of sign of the partial molar volume of the n-heptane at infinite dilution is similar to what has been noticed by Eckert et al.[15] for naphthalene in CO_2 and by Chang and Randolph[16] for toluene in CO_2.

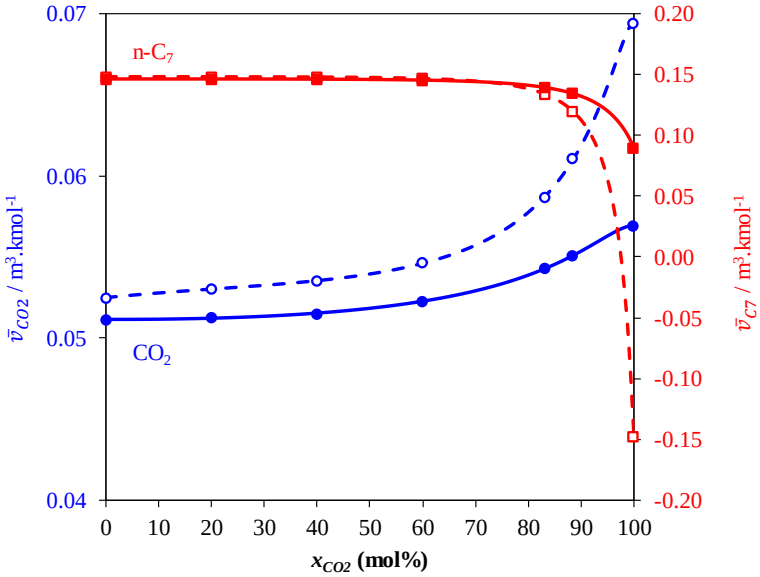

Figure 5.7 Partial molar volume of carbon dioxide and n-heptane as a function of CO_2 mol% at P = 10 MPa. ■: n-C_7 at 303 K; □: n-C_7 at 313 K; ●: CO_2 at 303 K; ○: CO_2 at 313 K.

This unusual behaviour of the n-C7 partial molar volume leads to a negative derivative of pressure with respect to n-heptane mole number at constant volume. Indeed, this derivative, which is related to both the partial molar volume and the isothermal compressibility by the following relation:

$$n\left(\frac{\partial p}{\partial n_{C7}}\right)_{T,V} = \frac{\bar{v}_{C7}}{v\kappa_T} \tag{5.3}$$

has the same sign than $\bar{v}_{C7}$. This means that an addition of an infinitesimal amount of n-heptane in CO_2 at fixed total volume and temperature leads to a contraction and a pressure drop in this condition. This behaviour, typical of dilute binary supercritical mixtures, can be interpreted by a microscopic picture[17,18]. More precisely, in near critical dilute mixtures, solvent molecules

may organize themselves around the diluted solute molecules, i.e. solvent molecules may form a cluster around solute molecules. Thus, in attractive supercritical mixtures, as in the studied mixture, a clustering process occurs whereby several CO_2 molecules structure themselves around diluted n-C_7 molecules, which in turns implies a negative $\bar{v}_{C7}$.

Such clustering phenomenon can be characterized and quantified by means of cluster size $\xi_{cluster}$ of CO_2 molecules surrounding one n-heptane molecule at infinite dilution, i.e. the excess number of CO2 molecules surrounding a n-C7 molecule with respect to a uniform distribution at bulk conditions. Debenedetti[19] has shown from the statistical mechanical theory of solutions of Kirkwood and Buff [20] that the cluster size can be related to the volumetric properties as follows:

$$\xi_{cluster} = \frac{RT\kappa_{T,CO2}}{v_{CO2}} - \frac{\bar{v}_{C7}^{\infty}}{v_{CO2}} \tag{5.4}$$

From this relation using experimental volumetric measurements, a mean value of 8 (CO_2 octomer, in excess) was obtained for 313 K and 10 MPa, thereby confirming a clustering process at this supercritical condition which is the closest to the critical point conditions of carbon dioxide. The rather limited clustering effect, compared to what can be found in the literature [17–19], simply reflects the non-negligible distance to the critical points of CO2 of the studied thermodynamic conditions.On the opposite at pressures higher than 30 MPa $\bar{v}_{C7}^{\infty}$ becomes greater than the molar volume of pure n-heptane v_{C7} for both 303 and 313 K isotherms as can be seen in Figure 5.8. This means that in such conditions the addition of an infinitesimal amount of n-heptane in CO_2 at fixed total volume and temperature leads to an expansion of the mixture higher than for the ideal mixture.

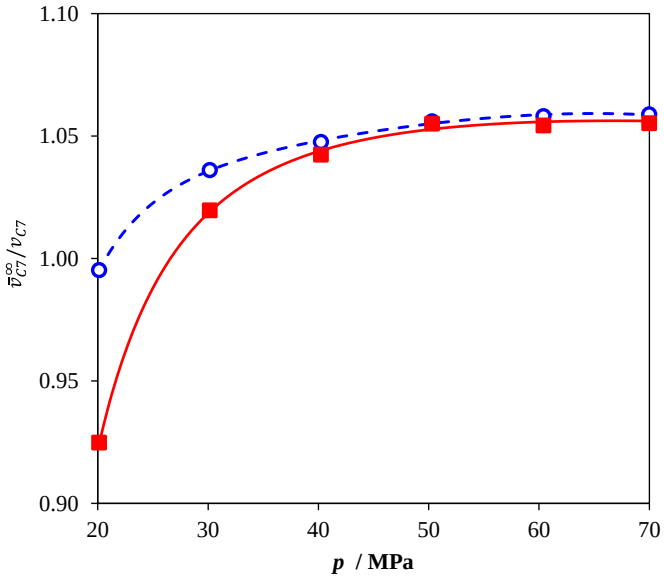

Figure 5.8 Ratio $\bar{v}_{C7}^{\infty}/v_{C7}$ as a function of pressure. ○: 303 K; ■: 313 K.

5.2.2 Excess Volumes

The excess property represents the difference between the thermodynamic property in a real mixture and that of an ideal mixture usually obtained from ideal combinations of pure component properties. To analyze the non-ideal behavior of the mixtures, the volumetric excess

properties have been determined for the different experimental conditions. The excess molar volume which is defined by:

$$v^E = \frac{x_{CO_2}M_{CO_2}+x_{C7}M_{C7}}{\rho} - \frac{x_{CO_2}M_{CO_2}}{\rho_{CO_2}} - \frac{x_{C7}M_{C7}}{\rho_{C7}} \quad (5.5)$$

was directly determined from the raw measurements, according to the following relation in order to minimize its uncertainty:

$$v^E = \frac{x_{CO_2}M_{CO_2}+x_{C7}M_{C7}}{A(\tau^2-\tau_w^2)+\rho_w} - \frac{x_{CO_2}M_{CO_2}}{A(\tau_{CO_2}^2-\tau_w^2)+\rho_w} - \frac{x_{C7}M_{C7}}{A(\tau_{C7}^2-\tau_w^2)+\rho_w} \quad (5.6)$$

The values obtained by this relation as well as the expanded standard uncertainty $U(v^E)$ calculated from uncertainty propagation from this relation are summarized in Table 5.3 and plotted along isobars in Figure 5.9 for 313 K.

Table 5.3 Excess molar volume v^E and its expended uncertainty $U(v^E)$ in carbon dioxide + n-heptane binary mixtures as a function composition x_{co2} for different temperatures *T* and pressures *p*.

T	*p*	$v^E \pm U(v^E)$		$v^E \pm U(v^E)$		$v^E \pm U(v^E)$		$v^E \pm U(v^E)$		$v^E \pm U(v^E)$	
K	MPa	$cm^3.mol^{-1}$									
x_{co2} / mol%		20.14 %		40.00 %		60.00 %		83.26 %		88.49 %	
303.35	10.12	-1.13	0.21	-2.28	0.16	-3.19	0.11	-3.37	0.09	-3.04	0.08
303.35	20.14	0.00	0.21	-0.11	0.15	-0.18	0.10	-0.07	0.05	-0.10	0.05
303.35	30.18	0.34	0.21	0.41	0.15	0.54	0.10	0.55	0.05	0.41	0.04
303.35	40.25	0.45	0.21	0.62	0.15	0.78	0.10	0.73	0.05	0.54	0.04
303.35	50.35	0.52	0.20	0.80	0.15	0.96	0.10	0.84	0.05	0.62	0.04
303.35	60.47	0.55	0.20	0.83	0.15	1.00	0.10	0.87	0.05	0.64	0.04
303.35	70.62	0.61	0.20	0.87	0.14	1.04	0.10	0.89	0.05	0.64	0.04
313.25	10.11	-3.34	0.22	-6.56	0.17	-9.45	0.13	-11.41	0.12	-10.65	0.12
313.25	20.13	-0.39	0.21	-0.73	0.16	-0.99	0.10	-0.85	0.06	-0.78	0.05
313.25	30.16	0.15	0.21	0.15	0.15	0.15	0.10	0.27	0.05	0.13	0.04
313.25	40.23	0.31	0.21	0.46	0.15	0.59	0.10	0.65	0.05	0.43	0.04
313.25	50.31	0.41	0.21	0.65	0.15	0.78	0.10	0.81	0.05	0.54	0.04
313.25	60.41	0.47	0.20	0.73	0.15	0.87	0.10	0.87	0.05	0.58	0.04
313.25	70.54	0.49	0.20	0.76	0.15	0.91	0.10	0.90	0.05	0.59	0.04

As observed previously by Medina-Bermudez et al.[14], the system presents a significant negative excess volume at the lowest investigated pressures, i.e. 10 and 20 MPa. This negative excess volume can represent up to 15% of the mixture volume at 10 MPa. Between 30 and 40 MPa the excess molar volume of the system become negligible, giving the impression that the system become ideal as pressure increases. In fact, at higher pressure the excess molar volume become positive with values that represent up to 1.5% of the volume The isobaric curves become much closer to each other as pressure increases meaning that beyond 60 MPa excess molar volume become less sensitive to changes in pressure. The same behavior is observed for 303 K. However, as can be noted in Figure 5.10 where excess volume curves corresponding to lower isobars are compared between 303 and 313 K, the amplitude of the effect is less pronounced for 303 K. Whatever the pressure and whatever the sign, the excess volume curves are asymmetric with extremum set towards the high CO_2 content domain around 70 to 80%.

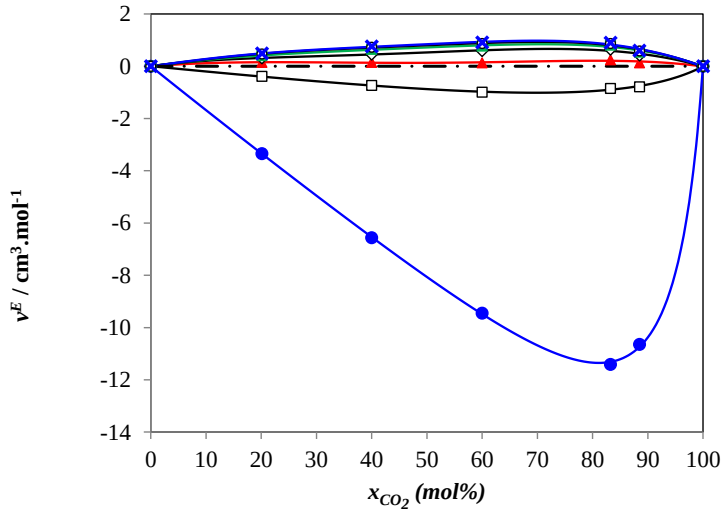

Figure 5.9 Excess molar volume as a function of concentration for different isobars at 313 K. ●: 10 MPa ; □: 20 MPa ; ▲: 30 MPa ; ◇: 40 MPa ; ■ 50 MPa ; ○: 60 MPa ; ×: 70 MPa.

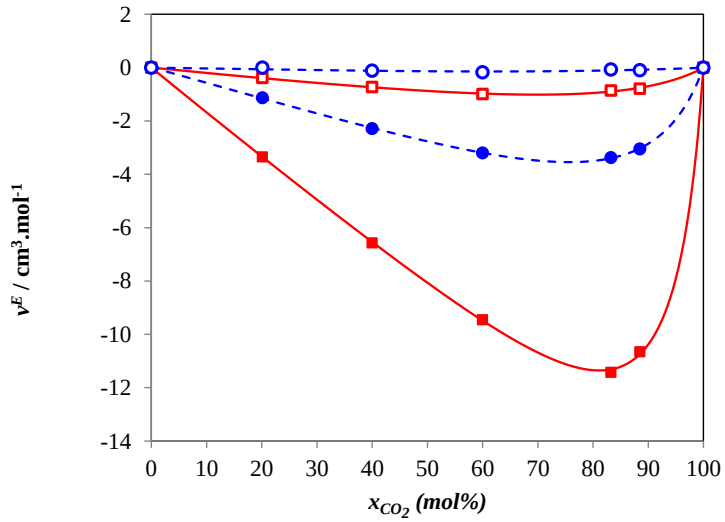

Figure 5.10 Comparison between excess molar volume curve at 303 and 313 K. as a function of concentration for different isobars at. ●: 303 K and 10 MPa ; ○: 303 K and 70 MPa ; ■ 313 K and 10 MPa ; □: 313 K and 70 MPa.

5.3. Isothermal Compressibility and Excess Isothermal Compressibility

The isothermal compressibility κ_T of both the pure components and binary mixtures were determined by derivation of density measurements according to its definition:

$$\kappa_T = \frac{1}{\rho}\left(\frac{\partial \rho}{\partial p}\right)_T \tag{5.7}$$

Such derivation was achieved by fitting empirical equations of state to the isothermal density data and by analytically deriving the fitted equations. A computation procedure[21] which is

presented in more details in section 2.5 and based on a Monte Carlo method with 5000 trials was used to obtain simultaneously the property and its expended standard uncertainty $U(\kappa_T)$.

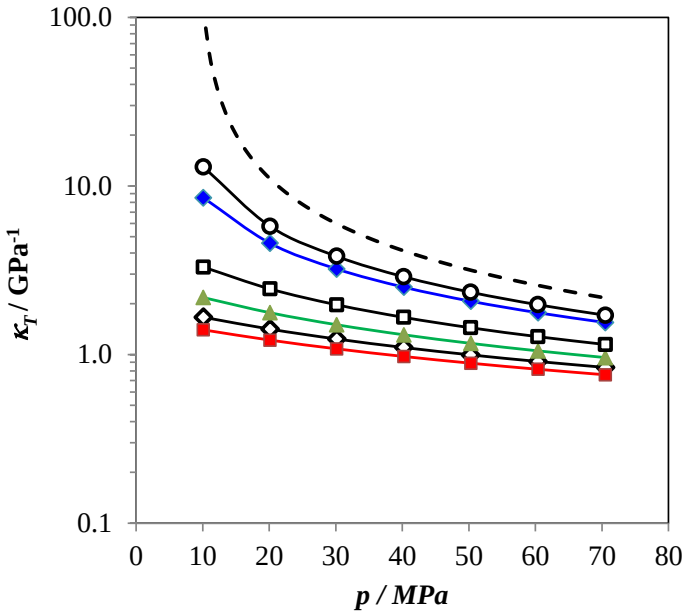

Figure 5.11 Isothermal compressibility κ_T as a function of pressure for different isopleths at 313 K. ■: pure n-C_7 ; ◇: 20 % CO_2 ; ▲: 40 % CO_2 ; □: 60 % CO_2 ; ◆: 83 % CO_2 ; ○: 88 % CO_2 ; - - - : pure CO_2.

According to the narrow pressure range investigated and the smooth shape of isobaric curves only three simple equations of state with a limited number of parameters (noted as capital letters *A*, *B* and *C*) were considered for fitting density data for systems with CO_2 concentration ranging from 0 to 83%. The first equation is the Hudleston's equation[22] written in terms of pressure:

$$P - P_{atm} = \frac{A-l}{l^2} exp\big(B + C(A-l)\big) \qquad \text{with } l = v^{1/3} \tag{5.8}$$

The second equation that expresses the tangent bulk modulus by a linear function of pressure correspond to the Murnaghan's equation[23] also rewritten in terms of pressure:

$$\rho = A\big(1 + B(P - P_{atm})\big)^C \tag{5.9}$$

The last equation assumed the derivative $(\partial p/\partial v)$ as a linear function of pressure. Integration by Tammann[24] of this linear function gave rise to the so-called Tait equation consider here in the following form:

$$\rho = \left(A - Cln\left(\frac{P - P_{atm} + B}{B}\right)\right)^{-1} \tag{5.10}$$

These 3 equations were randomly used for fitting the perturbed data points in the Monte Carlo procedure[21] and thus to calculate the derivative of density with respect to pressure for each of the 5000 trials. The mean and the standard deviation of the resulting compressibility distribution were evaluated to determine both the compressibility and its uncertainty. All these equations of state involve only three fitting coefficients allowing correlating density data with a maximum deviation less than the expanded uncertainty in density for the mixtures containing up to 83% of CO_2 in mol %. Above this concentration, a Benedict-Webb-Rubin (BWR) like equation of state[25] was required for representing the massive change in density with change in pressure at

low pressure. This 5 parameters (*A, B, C, E, F* and γ) equation correlates the compressibility factor of the mixture *Z* according to the following expression:

$$Z = 1 + A\rho_m + B\rho_m^2 + E\rho_m^5 + F\rho_m^2(1 + \gamma\rho_m^2)exp(-\gamma\rho_m^2) \quad (5.11)$$

where ρ_m is the molar density.

This equation allows correlating density data with a maximum deviation observed of 0.07% corresponding to pure carbon dioxide at 313 K and 10 MPa which represents the less dense state. The values of isothermal compressibilities determined in this way as well as the expended standard uncertainty $U(\kappa_T)$ are listed in Table 5.4.

Table 5.4 Isothermal compressibility κ_T and its expended uncertainty $U(\kappa_T)$ in carbon dioxide + n-heptane binary mixtures as a function of temperature *T*, pressure *P* and composition x_{co2}.

T	*p*	$\kappa_T \pm U(\kappa_T)$		$\kappa_T \pm U(\kappa_T)$		$\kappa_T \pm U(\kappa_T)$		$\kappa_T \pm U(\kappa_T)$	
K	MPa	GPa^{-1}							
x_{co2} / mol%		0 %		20.14 %		40.00 %		60.00 %	
303.35	10.12	1.340	0.039	1.507	0.045	1.943	0.056	2.807	0.071
303.35	20.14	1.174	0.017	1.314	0.025	1.623	0.034	2.192	0.032
303.35	30.18	1.046	0.011	1.167	0.015	1.397	0.014	1.806	0.013
303.35	40.25	0.944	0.015	1.051	0.013	1.229	0.014	1.539	0.014
303.35	50.35	0.861	0.019	0.957	0.014	1.097	0.019	1.343	0.018
303.35	60.47	0.792	0.022	0.879	0.017	0.993	0.023	1.192	0.020
303.35	70.62	0.733	0.024	0.813	0.019	0.906	0.026	1.073	0.022
313.25	10.11	1.430	0.038	1.653	0.052	2.155	0.062	3.231	0.073
313.25	20.13	1.235	0.016	1.414	0.036	1.769	0.034	2.448	0.030
313.25	30.16	1.089	0.011	1.238	0.015	1.505	0.014	1.981	0.012
313.25	40.23	0.975	0.015	1.102	0.015	1.312	0.015	1.668	0.013
313.25	50.31	0.883	0.019	0.995	0.021	1.164	0.020	1.443	0.017
313.25	60.41	0.807	0.021	0.907	0.025	1.048	0.023	1.273	0.019
313.25	70.54	0.744	0.023	0.834	0.029	0.953	0.025	1.140	0.019
x_{co2} / mol%		83.26 %		88.49 %		100 %			
303.35	10.12	6.191	0.096	8.85	0.12	28.90	0.20		
303.35	20.14	3.899	0.028	4.715	0.014	8.094	0.022		
303.35	30.18	2.870	0.011	3.304	0.013	4.887	0.013		
303.35	40.25	2.281	0.013	2.572	0.012	3.529	0.010		
303.35	50.35	1.896	0.015	2.118	0.010	2.770	0.009		
303.35	60.47	1.626	0.016	1.807	0.009	2.283	0.008		
303.35	70.62	1.424	0.016	1.579	0.008	1.944	0.007		
313.25	10.11	7.524	0.119	12.96	0.14	108.7	1.1		
313.25	20.13	4.472	0.032	5.764	0.018	11.12	0.05		
313.25	30.16	3.214	0.013	3.823	0.014	5.961	0.014		
313.25	40.23	2.518	0.014	2.892	0.012	4.106	0.010		
313.25	50.31	2.076	0.016	2.341	0.011	3.148	0.010		
313.25	60.41	1.769	0.016	1.973	0.010	2.560	0.009		
313.25	70.54	1.543	0.016	1.709	0.009	2.161	0.009		

The influence of pressure on this derived volumetric property is illustrated in Figure 5.11 for different isopleth at 313 K whereas the effect of CO_2 content at fixed temperature and pressure is shown in Figure 5.13 for 303 K. In this last figure the isothermal compressibility is not plotted as a function of mole concentration but in volume fraction $\emptyset_{CO2}$ as the compressibility of an ideal mixture is a linear function of volume fraction:

$$\kappa_T^{id} = \sum_i \emptyset_i \kappa_{T,i} \quad (5.12)$$

with the volume fraction defined by:

$$\emptyset_i = \frac{x_i M_i}{\rho_i \sum_i x_i \frac{M_i}{\rho_i}} \tag{5.13}$$

A linear behavior can be actually observed at 50 and 70 MPa but at the lowest pressures the curves depart significantly from a straight line, see Figure 5.13. As can be seen in Figure 5.14, where the real and ideal compressibilities are plotted as a function of volume fraction $\emptyset_{CO2}$ at 313 K and 10 MPa, the compression of the system departs significantly to ideality in this condition. At low to moderate CO_2 content, the compressibility of the system appears much lower than those of an ideal binary mixture. However, it can be noted in Figure 5.13 that between 0 and 40 % in volume fraction of CO_2, i.e. 0 and 60 in mol %, the compressibility appears as a linear function of volume fraction as for an ideal solution. Consequently, as for density, at low to moderate CO_2 content, the compressibility of the system is similar to that of an ideal binary mixture with a an apparent compressibility of CO_2 $\kappa_{T,CO2}^{\infty}$ much lower than the isothermal compressibility of pure CO_2. The ratio $\kappa_{T,CO2}^{\infty}/\kappa_{T,CO2}$ is equal to 0.05 for 313 K and to 0.2 for 313 K at this pressure.

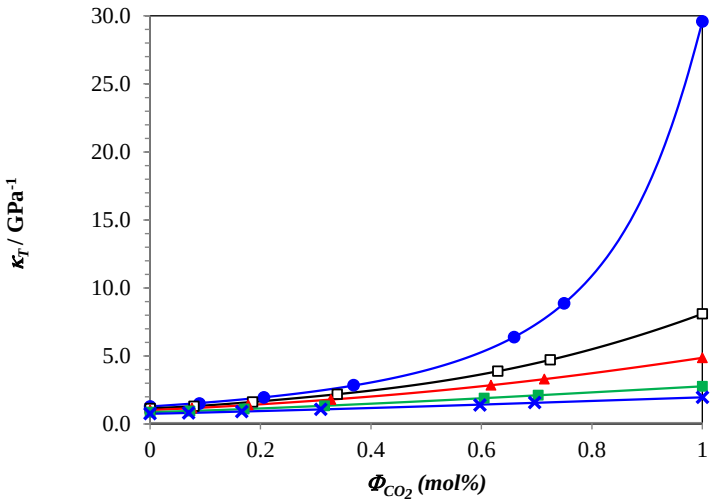

Figure 5.12 Isothermal compressibility κ_T as a function of volume fraction $\emptyset_{CO2}$ for different isobars at 303 K. ●: 10 MPa ; □: 20 MPa ; ▲: 30 MPa ; ■ 50 MPa ; ×: 70 MPa.

Beyond 70 % in volume of CO_2 compressibility increases largely to attain the compressibility value of pure carbon dioxide. Such significant increase of the compressibility is observed parallel to the large decrease in partial molar volume of n-heptane in Figure 5.7.

To highlight this non-ideal behavior, the excess isothermal compressibility was calculated from the following relation:

$$\kappa_T^E = \kappa_T - \emptyset_{CO2}\kappa_{T,CO2} - (1 - \emptyset_{CO2})\kappa_{T,C7} \tag{5.14}$$

The results are listed in Table 5.5 and plotted as a function in CO_2 concentration in Figure 5.14. The expanded standard uncertainties $U(\kappa_T^E)$ were calculated by propagating the uncertainty in composition determination as well as the uncertainty in density and compressibility.

As expected the excess isothermal compressibility is significant at 10 MPa and the non-ideal effects decrease as pressure increases. Whatever the pressure, the excess isothermal compressibility stays negative meaning that the real mixtures are denser than an ideal solution in the pressure range investigated. The excess isothermal compressibility curves appear

asymmetric with a minimum located towards high CO_2 concentration because in this range the compressibility itself is higher than for pure n-heptane

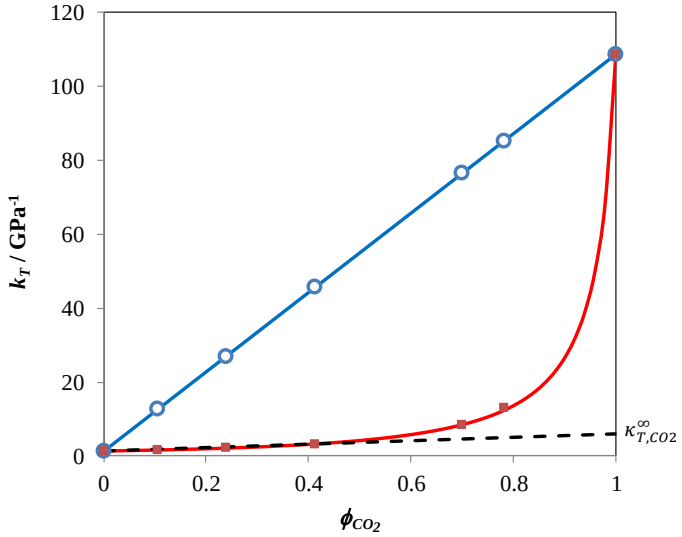

Figure 5.13 Comparison between measurements (■) and ideal behavior (○) of the isothermal compressibility as a function of volume fraction $\emptyset_{CO2}$ at 313 K and 10 MPa. - - - - : ideal solution with apparent compressibility $\kappa^{\infty}_{T,CO2}$ for CO_2.

Table 5.5 Excess isothermal compressibility κ^E_T and its expended uncertainty $U(\kappa^E_T)$ in carbon dioxide + n-heptane binary mixtures as a function composition x_{co2} for different temperatures T and pressures P.

T	p	$\kappa^E_T \pm U(\kappa^E_T)$		$\kappa^E_T \pm U(\kappa^E_T)$		$\kappa^E_T \pm U(\kappa^E_T)$		$\kappa^E_T \pm U(\kappa^E_T)$		$\kappa^E_T \pm U(\kappa^E_T)$	
K	MPa	GPa^{-1}									
x_{co2} / mol%		20.14 %		40.00 %		60.00 %		83.26 %		88.49 %	
303.35	10.12	-2.29	0.06	-5.07	0.08	-8.69	0.11	-13.31	0.16	-13.14	0.19
303.35	20.14	-0.408	0.029	-0.834	0.037	-1.33	0.03	-1.63	0.03	-1.47	0.02
303.35	30.18	-0.169	0.018	-0.332	0.017	-0.497	0.015	-0.547	0.014	-0.484	0.016
303.35	40.25	-0.083	0.018	-0.163	0.019	-0.234	0.017	-0.240	0.016	-0.201	0.014
303.35	50.35	-0.041	0.023	-0.088	0.025	-0.121	0.022	-0.119	0.018	-0.085	0.013
303.35	60.47	-0.019	0.027	-0.049	0.030	-0.065	0.025	-0.061	0.019	-0.028	0.013
303.35	70.62	-0.005	0.029	-0.027	0.033	-0.034	0.027	-0.032	0.019	0.003	0.012
313.25	10.11	-11.12	0.13	-24.82	0.27	-42.49	0.46	-68.97	0.76	-72.44	0.86
313.25	20.13	-0.641	0.039	-1.374	0.038	-2.246	0.036	-3.099	0.045	-2.729	0.040
313.25	30.16	-0.230	0.018	-0.473	0.017	-0.737	0.015	-0.919	0.016	-0.775	0.018
313.25	40.23	-0.107	0.020	-0.216	0.019	-0.327	0.017	-0.384	0.016	-0.313	0.015
313.25	50.31	-0.054	0.027	-0.110	0.025	-0.164	0.021	-0.186	0.018	-0.143	0.014
313.25	60.41	-0.027	0.032	-0.058	0.029	-0.087	0.024	-0.097	0.019	-0.066	0.013
313.25	70.54	-0.011	0.036	-0.029	0.032	-0.046	0.025	-0.052	0.019	-0.026	0.013

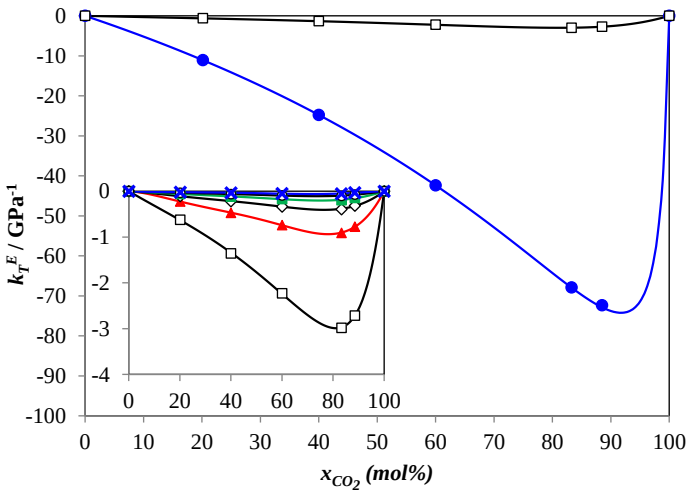

Figure 5.14 Excess Isothermal compressibility as a function of concentration for different isobars at 303 K. ●: 10 MPa ; □: 20 MPa ; ▲: 30 MPa ; ◇: 40 MPa ; ■ 50 MPa ; ○: 60 MPa ; ×: 70 MPa.

5.4. Acoustic Properties

5.4.1 Speed of Sound and Isentropic Compressibility

The speed of sound measurements are listed in Table 5.6. The values of the expanded uncertainty are also reported in Table 5.6 for each speed of sound measurement. Speed of sound measurements carried out in the different mixtures investigated are plotted as a function of pressure for 303 K in Figure 5.15. In agreement with the usual behavior in dense states, speed of sound curves are monotonically increasing with pressure. The isopleth curves corresponding to a CO_2 concentration lower than 80 % seems parallel with a slope that exhibits weak changes as pressure increase. On the opposite, the pressure has a significant impact on the slope of isopleths corresponding to high CO_2 content. A pronounced curvature is observed at low pressure in these curves. Similar trends are observed for both temperatures investigated. This effect is attributed to the large change in CO_2 compressibility in this *P*,*T* domain. To highlight this point, the acoustic behavior of pure CO_2 was added in Figure 5.15. Speed of sound values used for this representation were taken from literature[26,27] as it was not possible to detect any reflected echoes in our device. Actually, the large ultrasound absorption of carbon dioxide in the frequency domain corresponding to the pulse echo technique involves a poor or even no echoes detection by usual pulse echo technique. To overcome this drawback Lin and Trusler[26] have proposed an alternative method that consists in doping CO_2 with propane and in performing speed of sound measurements with various small quantities of dopant. Extrapolation of these measurements to a zero concentration of propane enabled them to determine CO_2 sound speed with an estimated relative uncertainty of 0.1% at temperatures between T = 248 to 373 K and pressures from 8 to 200 MPa. Rivas et al.[27] used the same method by considering methanol in order to get speed of sound data of pure CO_2 between 263 and 363 K for pressure up to 200 MPa. Both sets of data are consistent with each other within their reported uncertainties.

Table 5.6 Speed of sound *w* and its expended uncertainty $U(w)$ in liquid CO_2+ n-heptane binary mixtures as a function of temperature *T*, pressure *P* and composition x_{co2}.

T	*P*	$w \pm U(w)$		$w \pm U(w)$		$w \pm U(w)$	
K	MPa	m.s^{-1}					
x_{co2} / mol%		0 %		20.14 %		40.02 %	
303.35	10.12	1181.1	1.5	1085.6	1.4	973.0	1.3
303.35	20.14	1245.5	1.5	1155.5	1.4	1051.1	1.4
303.35	30.18	1305.5	1.5	1217.4	1.4	1118.4	1.3
303.35	40.25	1360.1	1.6	1275.0	1.5	1179.2	1.4
303.35	50.35	1411.0	1.6	1327.9	1.5	1232.6	1.4
303.35	60.47	1458.6	1.6	1376.2	1.5	1283.7	1.4
303.35	70.62	1502.5	1.7	1421.7	1.5	1330.0	1.4
313.25	10.11	1141.7	1.4	1042.6	1.4	927.3	1.3
313.25	20.13	1209.8	1.5	1116.1	1.4	1008.4	1.3
313.25	30.16	1271.4	1.5	1181.4	1.4	1080.3	1.3
313.25	40.23	1327.2	1.5	1240.3	1.4	1142.4	1.3
313.25	50.31	1378.5	1.6	1294.9	1.5	1198.8	1.3
313.25	60.41	1425.2	1.6	1344.5	1.5	1251.3	1.4
313.25	70.54	1471.6	1.6	1392.2	1.5	1298.9	1.4
x_{co2} / mol%		60.00 %		83.26 %		88.50 %	
303.35	10.12	826.3	1.3	605.6	1.5	544.6	1.5
303.35	20.14	918.6	1.2	728.1	1.2	680.4	1.2
303.35	30.18	994.0	1.2	817.8	1.1	773.5	1.1
303.35	40.25	1058.6	1.2	890.3	1.1	847.8	1.1
303.35	50.35	1117.0	1.2	953.1	1.1	911.1	1.1
303.35	60.47	1169.4	1.3	-	-	966.5	1.1
303.35	70.62	1216.3	1.1	-	-	1016.7	1.1
313.25	10.11	776.0	1.3	538.3	1.5	-	-
313.25	20.13	875.4	1.2	680.2	1.2	628.8	1.2
313.25	30.16	955.2	1.2	776.0	1.1	730.4	1.1
313.25	40.23	1023.3	1.2	852.5	1.1	808.4	1.1
313.25	50.31	1082.7	1.2	917.4	1.1	874.6	1.1
313.25	60.41	1137.4	1.2	974.5	0.9	932.2	1.1
313.25	70.54	1186.5	1.3	-	-	984.1	1.1

As the experimental conditions adopted by Lin and Trusler[26] and Rivas et al.[27] do not match ours, the data were interpolated to estimate speed of sound values corresponding to the experimental conditions of the present work. This interpolation generates an additional uncertainty lower than 0.1 % but unfortunately this interpolation does not cover the lowest pressures investigated here (10 and 20 MPa) for 303 and 313 K. For these conditions no reliable data are available in the open literature. Therefore, speed of sound values corresponding to these pressures were estimated by Span and Wagner[11,12] equation with an uncertainty claimed by the authors of 1 % in this *P*,*T* range. Figure 5.16 shows a plot of speed of sound versus CO_2 concentration at 313 K for different isobaric curves. It can be seen in this Figure that the curves are monotonically decreasing from pure n-C_7 to CO_2 values with a curvature that increases as *P*,*T* conditions get closer to CO_2 critical condition. The speed of sound has not been previously measured in binary CO_2 + n-C_7 but data were reported for pure n-heptane under pressure[28–31].

Comparison of the present measurements with a 2D-interpolation of literature data leads to an average absolute deviation of 0.08% with Boelhouwer[28], 0.19% with Muringer *et* al.[29], 0.14% with Daridon et al. [30], 0.26% with Dzida and Ernst[31] and 0.15 with Yebra et al.[32]. This interpolation was necessary because the measurement steps of pressure and temperature were not identical for the different data sets.

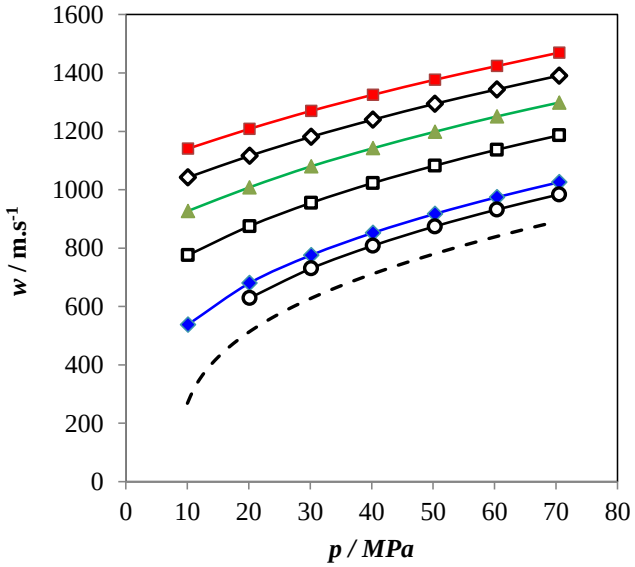

Figure 5.15 Speed of sound *w* as a function of pressure for different isopleths at 303 K. ■: pure n-C_7 ; ◇: 20 % CO_2 ; ▲: 40 % CO_2 ; □: 60 % CO_2 ; ◆: 83 % CO_2 ; ○: 88 % CO_2 ; - - - : pure CO_2.

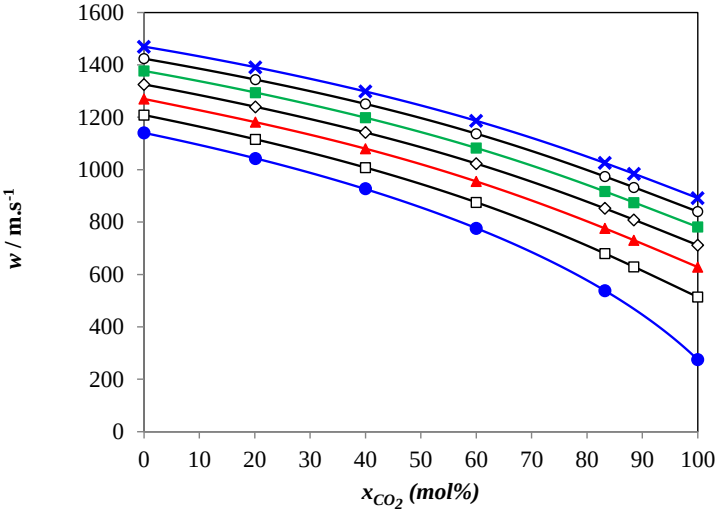

Figure 5.16 Speed of sound *w* as a function of concentration for different isobars at 313 K. ●: 10 MPa ; □: 20 MPa ; ▲: 30 MPa ; ◇: 40 MPa ; ■ 50 MPa ; ○: 60 MPa ; ×: 70 MPa.

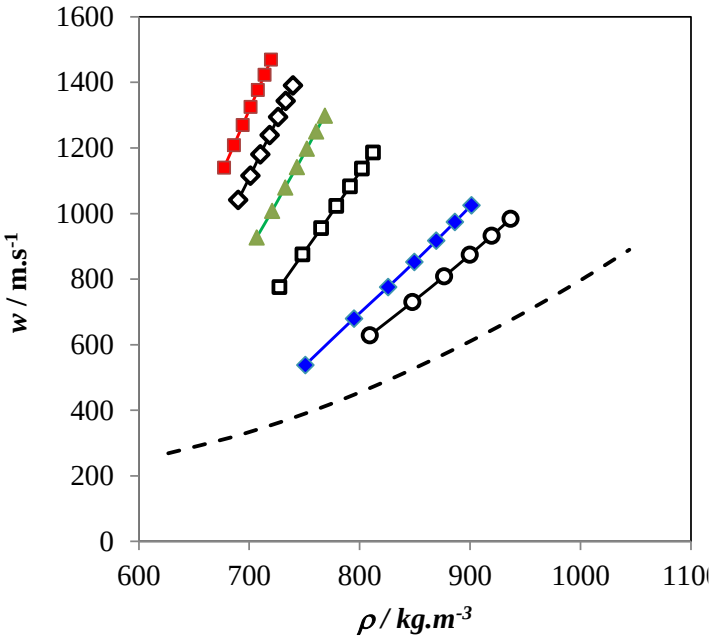

Figure 5.17 Speed of sound *w* as a function of as density for different isopleths at 303 K. ■: pure n-C_7 ; ◇: 20 % CO_2 ; ▲: 40 % CO_2 ; □: 60 % CO_2 ; ◆: 83 % CO_2 ; ○: 88 % CO_2 ; - - - : pure CO_2.

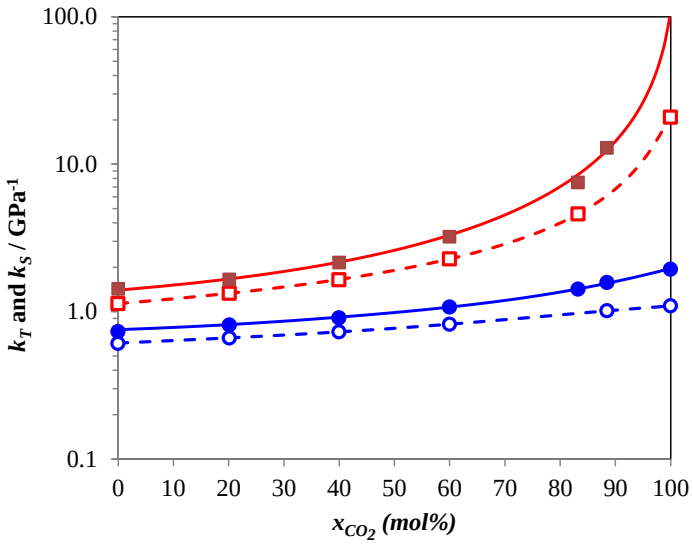

Figure 5.18 Comparison between isothermal and isentropic compressibility curves for extreme conditions. ●: κ_T at 303 K and 70 MPa ; ○: κ_s at 303 K and 70 MPa ; ■ : κ_T at 313 K and 10 MPa ; □: κ_s at 313 K and 10 MPa.

The simultaneous knowledge of density and speed of sound in the same *P*,*T* conditions does allow speed of sound to be plotted along isotherms as a function of the density instead of pressure. In this representation displayed in Figure 5.17, the isotherms put on view a regular and almost linear shape for all the mixtures. This linear trend is characteristic of dense systems. The positive slope of these curves decreases as CO_2 concentration increases and the linear trend disappears for pure CO_2 due to the high compressibility of CO_2 in the vicinity of the critical point.

In addition, the availability of speed of sound data and density measurements allows one to determine isentropic and isothermal compressibility according to the following relation:

$$\kappa_S = \frac{1}{\rho w^2} \tag{5.15}$$

The results are listed in Table 5.7 and both isothermal and isentropic compressibility were plotted as a function of CO_2 concentration in the same diagram (Figure 5.18) for the denser condition (303 K and 70 MPa) as well as for the less dense condition (313 K and 10 MPa). This figure shows a large increase of the difference between isothermal and isentropic compressibility with carbon dioxide content for the less dense condition whereas the increase is less pronounced for the denser case. This result is related to the augmentation of the non-adiabatic contribution in the isothermal compressibility due to a large increases of the isobaric expansion close to the critical conditions of carbon dioxide according to the relation:

$$\kappa_T = \kappa_s + \frac{T\alpha_P^2}{\rho c_P} \tag{5.16}$$

Where α_P is the isobaric expansion and c_p is the specific heat capacity at constant pressure.

Table 5.7 Isentropic compressibility κ_S and its expended uncertainty $U(\kappa_S)$ in carbon dioxide + n-heptane binary mixtures as a function of temperature *T*, pressure *P* and composition x_{co2}.

T	*P*	$\kappa_S \pm U(\kappa_S)$		$\kappa_S \pm U(\kappa_S)$		$\kappa_S \pm U(\kappa_S)$	
K	MPa	m.s^{-1}					
x_{co2} / mol%		0 %		20.14 %		40.00 %	
303.35	10.12	1.047	0.003	1.215	0.003	1.472	0.004
303.35	20.14	0.930	0.003	1.057	0.003	1.239	0.003
303.35	30.18	0.838	0.002	0.941	0.002	1.078	0.003
303.35	40.25	0.764	0.002	0.848	0.002	0.957	0.002
303.35	50.35	0.703	0.002	0.774	0.002	0.866	0.002
303.35	60.47	0.653	0.002	0.714	0.002	0.790	0.002
303.35	70.62	0.610	0.002	0.663	0.002	0.729	0.002
313.25	10.11	1.133	0.003	1.333	0.004	1.645	0.005
313.25	20.13	0.996	0.003	1.145	0.003	1.365	0.004
313.25	30.16	0.891	0.002	1.009	0.003	1.170	0.003
313.25	40.23	0.810	0.002	0.905	0.002	1.031	0.003
313.25	50.31	0.743	0.002	0.821	0.002	0.925	0.002
313.25	60.41	0.690	0.002	0.755	0.002	0.840	0.002
313.25	70.54	0.642	0.002	0.698	0.002	0.771	0.002
x_{co2} / mol%		60.00 %		83.26 %		88.49 %	
303.35	10.12	1.972	0.006	3.498	0.017	4.287	0.024
303.35	20.14	1.556	0.004	2.305	0.008	2.579	0.009
303.35	30.18	1.303	0.003	1.767	0.005	1.918	0.006
303.35	40.25	1.130	0.003	1.453	0.004	1.551	0.004
303.35	50.35	1.000	0.002	1.242	0.003	1.312	0.003
303.35	60.47	0.901	0.002	-	-	1.143	0.003
303.35	70.62	0.823	0.002	-	-	1.015	0.002
313.25	10.11	2.282	0.008	1.189	0.003	-	-
313.25	20.13	1.744	0.005	2.719	0.010	3.125	0.012
313.25	30.16	1.433	0.004	2.011	0.006	2.211	0.007
313.25	40.23	1.226	0.003	1.620	0.004	1.746	0.005
313.25	50.31	1.078	0.003	1.367	0.003	1.453	0.004
313.25	60.41	0.964	0.002	1.188	0.002	1.251	0.003
313.25	70.54	0.875	0.002	-	-	1.102	0.003

5.4.2 Excess Isentropic Compressibility and Excess Speed of Sound

The excess property represents the difference between the thermodynamic property in a real mixture and that of an ideal mixture usually obtained from ideal combinations of pure component properties. However, for both isentropic compressibility and speed of sound properties no simple combining rule exists for estimating ideal values[33]. Consequently, calculation of such ideal properties is not straightforward; it involves relating these properties to thermodynamic quantities readily calculable for ideal mixture. For that purpose, the isentropic compressibility was related to the isothermal compressibility, the density, the isobaric expansion and the molar heat capacity c_P according to equation (5.16) and the ideal isentropic compressibility is calculated by:

$$\kappa_S^{id} = \kappa_T^{id} - \frac{Tv^{id}\alpha_P^{id^2}}{c_P^{id}} \tag{5.17}$$

where κ_T^{id} and α_P^{id} are obtained by a linear combination in terms of volume fraction according to equation (5.12**)** for compressibility and to the following equation for expansion:

$$\alpha_P^{id} = \sum_i \emptyset_i \alpha_{P,i} \tag{5.18}$$

As for volume, the ideal molar heat capacity c_P^{id} can be determined by simple additivity on a mole fraction basis of molar heat capacity values of pure components :

$$c_P^{id} = \sum_i x_i c_{P,i} \tag{5.19}$$

However, in order to make all the properties of pure components used fully coherent with each other according to equation (5.16), pure component heat capacities were related to other thermodynamic properties through the following equation:

$$c_{P,i} = \frac{Tv_i\alpha_{P,i}^2}{\kappa_{T,i} - \kappa_{S,i}} \tag{5.20}$$

By considering such expression for the heat capacity of the pure components, the ideal isentropic compressibility was calculated by the relation:

$$\kappa_S^{id} = \sum_i \emptyset_i \kappa_{T,i} - \frac{\left(\sum_i x_i \frac{M_i}{\rho_i}\right)\left(\sum_i \emptyset_i \alpha_{P,i}\right)^2}{\sum_i x_i \frac{M_i T \alpha_{P,i}^2}{\rho_i\left(\kappa_{T,i} - \kappa_{S,i}\right)}} \tag{5.21}$$

which in turn allows calculating both the excess isentropic compressibility and the excess speed of sound as follows:

$$\kappa_S^E = \kappa_S - \kappa_S^{id} \tag{5.22}$$

$$w^E = w - \sqrt{\frac{\sum_i x_i \frac{M_i}{\rho_i}}{\sum_i x_i M_i \kappa_S^{id}}} \tag{5.23}$$

These last three relations involve the isobaric expansion of pure component in addition to the volumetric properties reported in Tables 5.2 and 5.4 as well as the acoustic properties listed in Tables 5.6 and 5.7. The required isobaric expansion values data were determined from derivation of density measurement with respect to temperature at constant pressure. As for compressibility, such derivation was carried out by the Monte Carlo method[21] detailed in section 2.5.2, that consists first in generating a 5000 data sets with density values randomly perturbed around the experimental measurements by using a normal probability distribution function centered on the experimental density values. Each density data set was then fitted to a

third degree polynomial function in order to determine analytically the derivatives. Finally, the averages and standard deviations of the resulting distributions were calculated in order to determine the isobaric expansion and its standard uncertainty for each experimental condition. In order to have enough experimental points for fitting the polynomial function, additional density data were required. These measurements, which are not reported here, were carried out at 293, 323, 333 and 343 K so as to extend both sides of the experimental range. According to the smooth shape of the isobaric curves for n-C_7 at all pressures investigated and for CO_2 below 20 MPa, a polynomial function $\rho(T)$ was used for fitting these isobars whereas a polynomial function $Z(\rho_m)$ was considered for CO_2 at 10 and 20 MPa. The value of isobaric expansion obtained by such procedure along with their uncertainties are reported in Table 5.8.

Table 5.8 Isobaric expansion α_P and its expended uncertainty $U(\alpha_P)$ in pure carbon dioxide and pure n-heptane as a function of pressure at p at 303.35 K and 313.25 K

T K	P MPa	$\alpha_p \pm U(\alpha_P)$		$\alpha_P \pm U(\alpha_P)$	
		$10^3 \times K^{-1}$			
		n-C_7		CO_2	
303.35	10.12	1.175	0.021	13.1	0.2
303.35	20.14	1.095	0.020	5.40	0.08
303.35	30.18	1.032	0.019	3.89	0.06
303.35	40.25	0.982	0.018	3.18	0.05
303.35	50.35	0.943	0.019	2.75	0.04
303.35	60.47	0.910	0.020	2.45	0.04
303.35	70.62	0.882	0.023	2.24	0.04
313.25	10.11	1.184	0.019	31.0	0.8
313.25	20.13	1.092	0.018	6.27	0.09
313.25	30.16	1.022	0.017	4.32	0.07
313.25	40.23	0.966	0.016	3.43	0.05
313.25	50.31	0.922	0.016	2.93	0.05
313.25	60.41	0.884	0.016	2.60	0.04
313.25	70.54	0.854	0.016	2.35	0.04

This supplementary information allows calculating the excess isentropic compressibility and excess speed of sound. The results as well as their uncertainties are reported in Tables 5.9 and 5.10 respectively.

Because of the complicated derivation of ideal isentropic compressibility by equation (5.21), the uncertainty in ideal compressibility obtained from error propagation law is significant. In comparison, when pressure increases and mixture tends to an ideal solution the excess value becomes rather small. Consequently, the relative uncertainty goes off in these conditions where non-ideal effects become smaller than uncertainty. This situation is achieved beyond 40 MPa

Table 5.9 Excess isentropic compressibility κ_S^E and its expended uncertainty $U(\kappa_S^E)$ in carbon dioxide + n-heptane binary mixtures as a function composition x_{co2} for different temperatures *T* and pressures *P*.

T	*P*	$\kappa_S^E \pm U(\kappa_S^E)$		$\kappa_S^E \pm U(\kappa_S^E)$		$\kappa_S^E \pm U(\kappa_S^E)$		$\kappa_S^E \pm U(\kappa_S^E)$		$\kappa_S^E \pm U(\kappa_S^E)$	
K	MPa	GPa^{-1}									
x_{co2} / mol%		20.14 %		40.00 %		60.00 %		83.26 %		88.49 %	
303.35	10.12	-1.59	0.13	-3.15	0.24	-4.45	0.39	-4.71	0.60	-4.20	0.67
303.35	20.14	-0.256	0.035	-0.526	0.048	-0.752	0.068	-0.73	0.11	-0.61	0.13
303.35	30.18	-0.094	0.022	-0.199	0.028	-0.279	0.036	-0.251	0.057	-0.203	0.067
303.35	40.25	-0.043	0.025	-0.093	0.029	-0.126	0.035	-0.109	0.046	-0.087	0.051
303.35	50.35	-0.021	0.030	-0.044	0.034	-0.061	0.039	-0.051	0.044	-0.040	0.045
303.35	60.47	-0.009	0.034	-0.022	0.037	-0.029	0.042	-	-	-0.017	0.043
303.35	70.62	-0.003	0.037	-0.010	0.040	-0.011	0.044	-	-	-0.007	0.043
313.25	10.11	-7.93	0.41	-14.2	1.0	-18.4	1.9	-21.7	3.7	-	-
313.25	20.13	-0.453	0.036	-0.933	0.055	-1.366	0.086	-1.38	0.15	-1.16	0.18
313.25	30.16	-0.152	0.023	-0.318	0.030	-0.459	0.042	-0.431	0.070	-0.352	0.082
313.25	40.23	-0.071	0.026	-0.150	0.032	-0.218	0.040	-0.202	0.055	-0.163	0.060
313.25	50.31	-0.039	0.031	-0.083	0.036	-0.120	0.043	-0.113	0.053	-0.093	0.054
313.25	60.41	-0.024	0.034	-0.053	0.039	-0.078	0.046	-0.075	0.054	-0.064	0.053
313.25	70.54	-0.016	0.036	-0.033	0.040	-0.051	0.047	-	-	-0.048	0.053

Table 5.10 Excess speed of sound w^E and its expended uncertainty $U(w^E)$ in carbon dioxide + n-heptane binary mixtures as a function of temperature *T*, pressure *P* and composition x_{co2}.

T	*P*	$w^E \pm U(w^E)$		$w^E \pm U(w^E)$		$w^E \pm U(w^E)$		$w^E \pm U(w^E)$		$w^E \pm U(w^E)$	
K	MPa	m.s^{-1}									
x_{co2} / mol%		20.14 %		40.00 %		60.00 %		83.26 %		88.49 %	
303.35	10.12	368	16	418	15	360	14	201	15	148	16
303.35	20.14	119	14	170	12	164	11	93	12	68	12
303.35	30.18	58	12	93	11	95	10	56	11	41	12
303.35	40.25	34	18	57	16	59	14	37	13	27	13
303.35	50.35	20	25	35	22	39	20	26	16	19	15
303.35	60.47	12	33	23	29	25	26	-	-	13	18
303.35	70.62	7	40	14	36	16	32	-	-	10	21
313.25	10.11	642	9	620	10	505	13	799	21	-	-
313.25	20.13	170	11	229	9	216	9	122	10	88	11
313.25	30.16	81	11	123	10	125	9	73	10	53	11
313.25	40.23	48	16	78	14	84	13	53	12	38	12
313.25	50.31	32	22	54	20	61	18	42	16	31	15
313.25	60.41	24	29	42	26	49	24	36	20	28	18
313.25	70.54	18	35	32	32	40	29	-	-	26	22

.

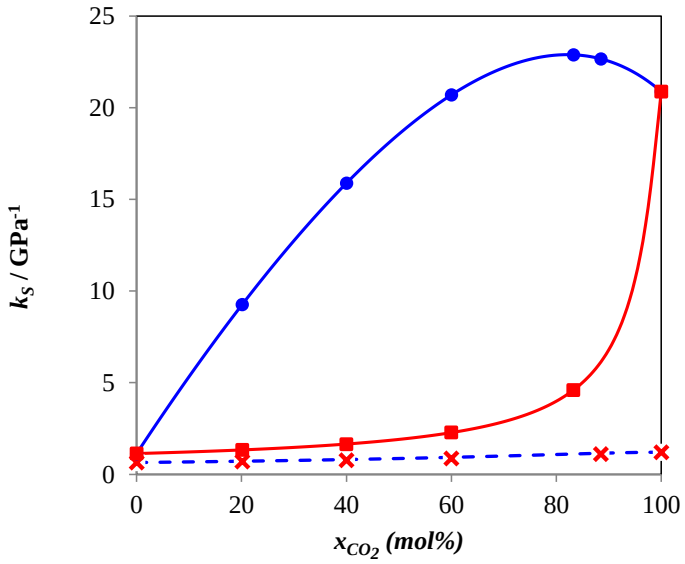

Figure 5.19 Comparison between measurements and ideal behavior of the isentropic compressibility as a function of CO_2 mol %. ■ : experimental at 313 K and 10 MPa ; ●: ideal behavior at 313 K and 10 MPa ; × : experimental at 313 K and 70 MPa ; - - - - : ideal behavior at 313 K and 70 MPa.

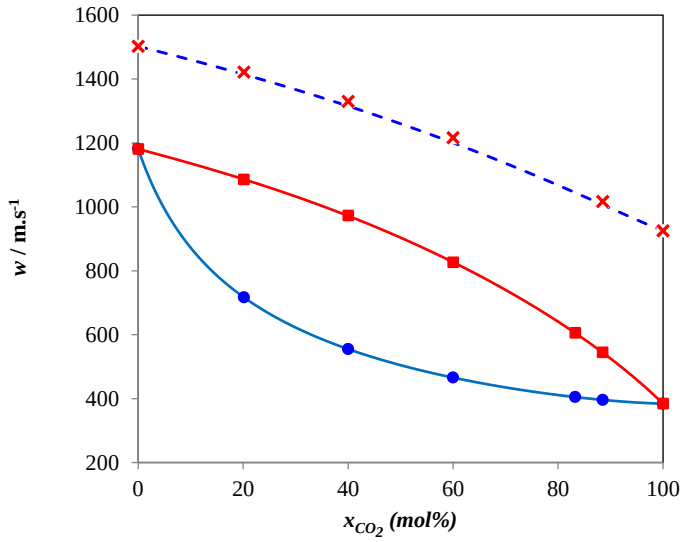

Figure 5.20 Comparison between measurements and ideal behavior of speed of sound as a function of CO_2 mol %. ■ : experimental at 313 K and 10 MPa ; ●: ideal behavior at 313 K and 10 MPa ; × : experimental at 313 K and 70 MPa ; - - - - : ideal behavior at 313 K and 70 MPa.

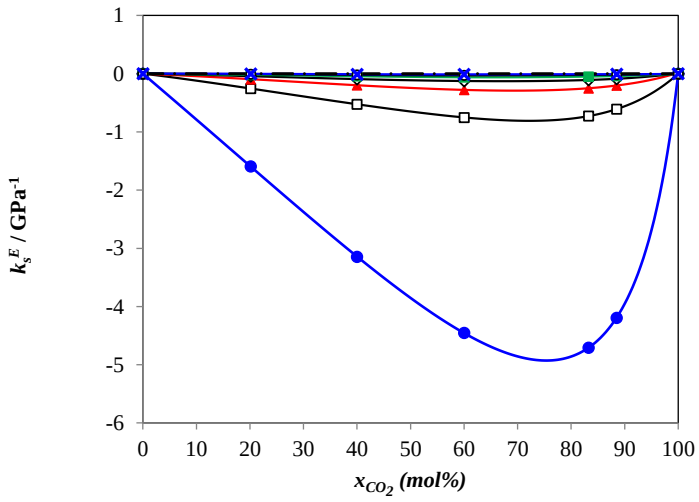

Figure 5.21 Excess isentropic compressibility as a function of concentration for different isobars at 303 K. ●: 10 MPa ; □: 20 MPa ; ▲: 30 MPa ; ◇: 40 MPa ; ■ 50 MPa ; ○: 60 MPa ; ×: 70 MPa.

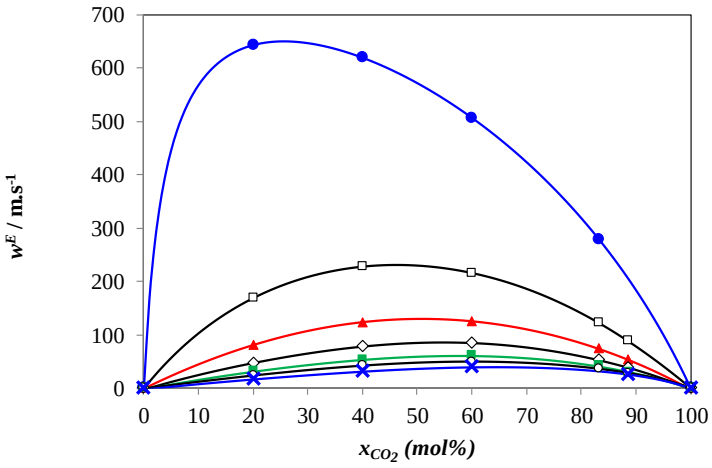

Figure 5.22 Excess speed of sound as a function of concentration for different isobars at 313 K. ●: 10 MPa ; □: 20 MPa ; ▲: 30 MPa ; ◇: 40 MPa ; ■ 50 MPa ; ○: 60 MPa ; ×: 70 MPa.

The experimental and ideal compressibility are plotted in Figure 5.19 for the extreme pressures at 313K whereas experimental and ideal speed of sound are compared in Figure 5.20 for both 10 and 70 MPa at 313K. The same trend can be seen in both figures. At 70 MPa the real and the ideal curves overlap within the error bar whereas at 10 MPa the deviation between both curves is very large. Moreover, the curvatures of both the real and the ideal curves at 10 MPa are opposite in Figure 5.20. The ideal behavior predicts a large impact of CO_2 injection in pure n-heptane on speed of sound with a decrease of 500 m.s^{-1} for a CO_2 injection of 20 % whereas the actual value is only 100 m.s^{-1}. The difference leads to a large excess value in this condition of pressure and temperature. The excess curves are plotted in Figures 5.21 and 5.22 for compressibility and speed of sound respectively. From these figures, it can be noticed that the excess isentropic curves display the same behavior than excess isothermal compressibility.

Both property exhibit asymmetric curves with minimum located in the high CO_2 content range. On the opposite the excess speed of sound shows an asymmetry with a maximum in the high n-C_7 content domain as the speed of sound in pure n-heptane is higher than that of pure CO_2. To summarize and compare the influence of the non-ideality on the different properties, relative excess curves have been plotted on the same figure, see Figure 5.23. This figure clearly shows that the impact of non-ideality is magnified on derivative property such as k_T. Although the excess volume only represents 5% of the actual volume, the excess compressibility can be higher than 300% of the compressibility. This difference is related to significant contrast between pure component compressibilities at this *P,T* condition. It also leads to a significant effect on speed of sound for which relative deviation can reach 50 % of the actual speed of sound. Finally, it should be pointed out that the asymmetry observed on the excess curves in Figures 5.14, 5.21 and 5.22 is considerably reduced in a relative representation, see Figure 5.23.

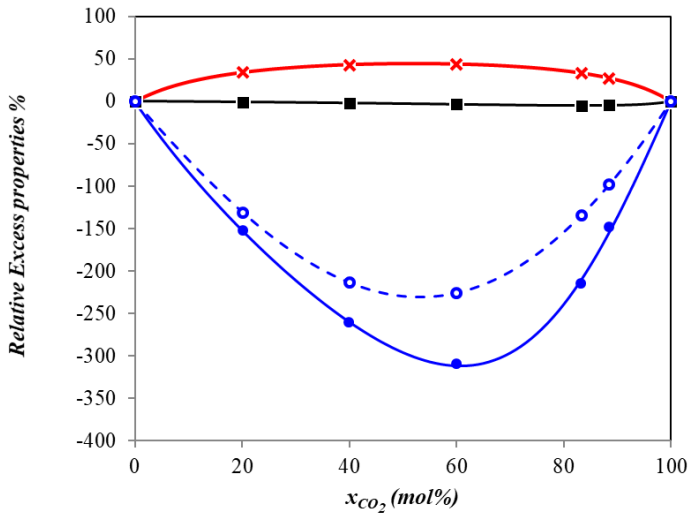

Figure 5.23 Relative excess properties in % as a function of concentration at 313 K and 10 MPa. ■ : v^E/v ; ●: κ_T^E/κ_T ; ○: κ_S^E/κ_S ; ×: w^E/w.

5.5. Conclusions

In this work, which forms the first part of a more complete study that includes molecular simulations that will be presented in the next chapter, accurate speed of sound and density measurements have been achieved on carbon dioxide and n-heptane binary mixtures at two temperatures (303 and 313 K) and at pressures from 10 to 70 MPa. This mixture has been chosen because of its interest as a simple proxy to CO_2 enhanced oil recovery systems and these specific thermodynamic conditions have been chosen so as to specifically analyze the expected influence of the proximity of the critical point of CO_2 on the non-idealities of the studied mixture in terms of density, speed of sound, isentropic and isothermal compressibilities excess properties, the latter being deduced from density measurements and reliable empirical equation of states.

Because of the large variations of CO_2 density with pressure on the studied isotherms, it has been noticed that isopleth density curves corresponding to high concentrations in CO_2 could cross at the lowest pressure (i.e. between 10 and 20 MPa). In other words, density, at the lowest pressure, does not behave monotonously with CO_2 concentration which is a signature of an important non ideal behavior of such near critical mixtures.
Interestingly, it has been noticed, at T = 313 K and P = 10 MPa, a change of sign, from positive to negative, of the partial molar volume of n-heptane when going towards infinite dilution. Such contraction behaviour is typical of near critical dilute mixture and can be interpreted as the organisation of the solvent molecules (CO_2) around the solute molecule which may form cluster. In this precise case the cluster size (in excess) is about 8 molecules of solvent.
In addition, all measured (or derived) mixtures properties have been compared directly to their ideal counterpart. For the highest pressures the supercritical mixtures behave as nearly ideal ones, however for P =1 0 MPa, compressibilities (isothermal and isentropic) and speed of sound are much lower than those of an ideal binary mixture whereas density is higher than that of an ideal binary mixture. Interestingly, it has been found that these mixtures properties, for low to moderate CO_2 content, could be well described by an ideal binary mixture where the actual CO_2 properties are replaced by their infinite CO_2 dilution values.
Interpreted in terms of excess properties, the results show that excess molar volume, excess isothermal and isentropic compressibilities and excess sound velocities are significant at the lowest pressure, i.e. P = 10 MPa, and high CO_2 content (about 80 % in mol) as expected regarding the proximity of the CO_2 critical point for such conditions. When these excess properties are expressed as relative (to the mixture properties) quantities, it has been noticed that non-idealities are more pronounced on the derivative properties. Thus, although the excess volume only represents 5% of the actual volume, the excess compressibility can be higher than 300% of the compressibility and the excess speed of sound can be of the order of 50 % of the actual speed of sound. All these results emphasized the fact that assuming ideality for such supercritical mixtures, in particular when the thermodynamic conditions are close to that of CO_2, may lead to important misevaluation of the mixtures volumetric properties.

5.6. References

(1) Holm, L. W.; Josendal, V. A. Mechanisms of Oil Displacement By Carbon Dioxide. J. Pet. Technol. 1974, 26 (12), 1 427-1 438.

(2) Al-Abri, A.; Amin, R. Phase Behaviour, Fluid Properties and Recovery Efficiency of Immiscible and Miscible Condensate Displacements by SCCO2 Injection: Experimental Investigation. Transp. Porous Media 2010, 85 (3), 743–756.

(3) Badamchi-Zadeh, A.; Yarranton, H. W.; Maini, B. B.; Satyro, M. A. Phase Behaviour and Physical Property Measurements for VAPEX Solvents: Part II. Propane, Carbon Dioxide and Athabasca Bitumen. J. Can. Pet. Technol. 2009, 48 (03), 57–65.

(4) Varet, G.; Montel, F.; Nasri, D.; Daridon, J.-L. Gas Solubility Measurement in Heavy Oil and Extra Heavy Oil at Vapor Extraction (VAPEX) Conditions. Energy Fuels 2013, 27 (5), 2528–2535.

(5) Dunn, S. G.; Nenniger, E. H.; Rajan, V. S. V. A Study of Bitumen Recovery by Gravity Drainage Using Low Temperature Soluble Gas Injection. Can. J. Chem. Eng. 1989, 67 (6), 978–991.

(6) Torabi, F.; Jamaloei, B. Y.; Stengler, B. M.; Jackson, D. E. The Evaluation of CO2-Based Vapour Extraction (VAPEX) Process for Heavy-Oil Recovery. J. Pet. Explor. Prod. Technol. 2012, 2 (2), 93–105.

(7) Kalra, H.; Kubota, H.; Robinson, D. B.; Ng, H.-J. Equilibrium Phase Properties of the Carbon Dioxide-n-Heptane System. J. Chem. Eng. Data 1978, 23 (4), 317–321.

(8) Chester, T. L.; Haynes, B. S. Estimation of Pressure-Temperature Critical Loci of CO2 Binary Mixtures with Methyl-Tert-Butyl Ether, Ethyl Acetate, Methyl-Ethyl Ketone, Dioxane and Decane. J. Supercrit. Fluids 1997, 11 (1), 15–20.

(9) Choi, E.-J.; Yeo, S.-D. Critical Properties for Carbon Dioxide + N-Alkane Mixtures Using a Variable-Volume View Cell. J. Chem. Eng. Data 1998, 43 (5), 714–716.

(10) Cismondi, M.; Rodríguez-Reartes, S. B.; Milanesio, J. M.; Zabaloy, M. S. Phase Equilibria of CO_2 + n -Alkane Binary Systems in Wide Ranges of Conditions: Development of Predictive Correlations Based on Cubic Mixing Rules. Ind. Eng. Chem. Res. 2012, 51 (17), 6232–6250.

(11) Span, R.; Wagner, W. A New Equation of State for Carbon Dioxide Covering the Fluid Region from the Triple-Point Temperature to 1100 K at Pressures up to 800 MPa. J. Phys. Chem. Ref. Data 1996, 25 (6), 1509–1596.

(12) Lemmon, E. W.; Span, R. Short Fundamental Equations of State for 20 Industrial Fluids. J. Chem. Eng. Data 2006, 51 (3), 785–850.

(13) A, F.; Jpm, T.; Wa, W. Densities and bubble points of binary mixtures of carbon dioxide and n-heptane and ternary mixtures of n-butane, n-heptane and n-hexadecane. Fluid Phase Equilibria 2001, 185 (1–2), 349–358.

(14) Medina-Bermúdez, M.; Saavedra-Molina, L. A.; Escamilla-Tiburcio, W.; Galicia-Luna, L. A.; Elizalde-Solis, O. (P, ρ, T) Behavior for the Binary Mixtures Carbon Dioxide + Heptane and Carbon Dioxide + Tridecane. J. Chem. Eng. Data 2013, 58 (5), 1255–1264.

(15) Eckert, C. A.; Ziger, D. H.; Johnston, K. P.; Kim, S. Solute Partial Molal Volumes in Supercritical Fluids. J. Phys. Chem. 1986, 90 (12), 2738–2746.

(16) Chang, C. J.; Randolph, A. D. Solvent Expansion and Solute Solubility Predictions in Gas-Expanded Liquids. AIChE J. 1990, 36 (6), 939–942.

(17) Eckert, C. A.; Ziger, D. H.; Johnston, K. P.; Ellison, T. K. The Use of Partial Molal Volume Data to Evaluate Equations of State for Supercritical Fluid Mixtures. Fluid Phase Equilibria 1983, 14, 167–175.

(18) Wu, R. S.; Lee, L. L.; Cochran, H. D. Structure of Dilute Supercritical Solutions: Clustering of Solvent and Solute Molecules and the Thermodynamic Effects. Ind. Eng. Chem. Res. 1990, 29 (6), 977–988.

(19) [222]detti, P. G. Clustering in Dilute, Binary Supercritical Mixtures: A Fluctuation Analysis. Chem. Eng. Sci. 1987, 42 (9), 2203–2212.

(20) Kirkwood, J. G.; Buff, F. P. The Statistical Mechanical Theory of Solutions. I. J. Chem. Phys. 1951, 19 (6), 774–777.

(21) Daridon, J.-L.; Bazile, J.-P. Computation of Liquid Isothermal Compressibility from Density Measurements: An Application to Toluene. J. Chem. Eng. Data 2018, 63 (6), 2162–2178.

(22) Hudleston, L. J. Intermolecular Forces of Normal Liquids. Trans. Faraday Soc. 1937, 33 (0), 97–103.

(23) Murnaghan, F. D. The Compressibility of Media under Extreme Pressures. Proc. Natl. Acad. Sci. 1944, 30 (9), 244–247.

(24) Tammann, G. Ueber Die Abhängigkeit Der Volumina von Lösungen Vom Druck. Z. Für Phys. Chem. 1895, 17U (1), 620–636.

(25) Benedict, M.; Webb, G. B.; Rubin, L. C. An Empirical Equation for Thermodynamic Properties of Light Hydrocarbons and Their Mixtures II. Mixtures of Methane, Ethane, Propane, and n-Butane. J. Chem. Phys. 1942, 10, 747–758.

(26) Lin, C.-W.; Trusler, J. P. M. Speed of Sound in (Carbon Dioxide + Propane) and Derived Sound Speed of Pure Carbon Dioxide at Temperatures between (248 and 373) K and at Pressures up to 200 MPa. J. Chem. Eng. Data 2014, 59 (12), 4099–4109.

(27) Rivas, C.; Gimeno, B.; Velasco, I.; Artal, M.; Fernández, J.; Blanco, S. T. High-pressure speed of sound in pure CO2 and in CO2 with SO2 as an impurity using methanol as a doping agent. In International Journal of Greenhouse Gas Control; 2016.

(28) Boelhouwer, J. W. M. Sound Velocities in and Adiabatic Compressibilities of Liquid Alkanes at Various Temperatures and Pressures. Physica 1967, 34 (3), 484–492.

(29) Muringer, M. J. P.; Trappeniers, N. J.; Biswas, S. N. The Effect of Pressure on the Sound Velocity and Density of Toluene and N-Heptane up to 2600 Bar. Phys. Chem. Liq. 1985, 14 (4), 273–296.

(30) Daridon, J. L.; Lagourette, B.; Lagrabette, A. Acoustic Determination of Thermodynamic Properties of Ternary Liquid Mixtures Up to 150 Mpa. Phys. Chem. Liq. 1999, 37 (2), 137–160.

(31) Dzida, M.; Ernst, S. Speed of Sound in Propan-1-Ol + Heptane Mixtures under Elevated Pressures. J. Chem. Eng. Data 2003, 48 (6), 1453–1457.

(32) Yebra, F.; Troncoso, J.; Romaní, L. Fully Automatized Apparatus for Determining Speed of Sound for Liquids in the Temperature and Pressure Interval (283.15–343.15)K and (0.1–95)MPa. J. Chem. Thermodyn. 2017, 104, 102–109.

(33) Benson, G. C.; Kiyohara, O. Evaluation of Excess Isentropic Compressibilities and Isochoric Heat Capacities. J. Chem. Thermodyn. 1979, 11 (11), 1061–1064.

Chapter 6. Molecular Simulations of CO_2+nC7 Mixtures

Contents

6.1. Preliminary Results 103
6.1.1 Prediction of Pure CO_2 Phase Behaviour by MCCG 103
6.1.2 Prediction of CO_2 + n-C_7 Mixtures Phase Behaviour by MCCG 104
6.2. Molecular Simulation Details 107
6.2.1 Thermodynamic Properties 107
6.2.2 Structural Properties 107
6.3. Thermodynamic Properties 108
6.3.1 Density and Derivative Properties 108
6.3.2 Excess Properties 111
6.4. Kirkwood Buff Integrals and Partial Molar Volumes 112
6.5. Microscopic Analysis of CO_2 Clusters 114
6.5.1 Definition of Clusters 115
6.5.2 Static Property of Cluster 119
6.5.3 Dynamic Properties of Cluster 120
6.6. Conclusions 121
6.7. References 122

Introduction

In chapter 5, an experimental investigation of volumetric and acoustic properties of a simple model system consisting of a binary mixture of carbon dioxide + n-heptane has been presented. The measurements were performed for two isotherms in the vicinity of CO_2 critical point (303 and 313 K) at pressure from 10 to 70 MPa. The experimental results obtained highlighted an important non-ideal behavior of the mixture for high CO_2 content, especially at the lowest pressure of investigation (10 MPa). This non ideal behavior has been attributed to a clustering phenomenon consisting of the organization of clusters of CO_2 molecules around n-heptane molecules, the cluster size being deduced from the partial molar volumes of the mixtures components at infinite dilution conditions close to the CO_2 critical point[1].

To shed further light on these experimental findings, we have carried out in this chapter molecular simulations associated to Kirkwood Buff theory of solutions[2] on the same systems to simulate the aforementioned thermophysical properties and to provide additional information about the mixture microscopic structure.

The chapter is structured as follows. The section 6.1 contains preliminary results on the prediction of phase behavior by the MCCG force field. The section 6.2 is devoted to the molecular simulation details. Sections 6.3 to 6.5 contain results of our investigations. Molecular simulation results of thermodynamic properties are first presented and compared to experimental data. Then, a microscopic analysis of CO_2 clustering is provided. Finally, the main outcomes of this study are summarized in the conclusion.

6.1. Preliminary Results

6.1.1 Prediction of Pure CO_2 Phase Behaviour by MCCG

In this chapter, we performed molecular simulations of thermodynamic and structural properties of CO_2 + n-C7 mixture in the vicinity of CO_2 critical point using the MCCG force field. Therefore, it was first essential to check how MCCG predicts the critical temperature T_c and pressure P_c of CO_2. For that purpose, Gibbs Ensemble Monte Carlo (GEMC) simulations were performed in the NVT ensemble to compute equilibrium liquid-vapor densities of pure carbon dioxide at a given temperature. The results of these simulations are shown in Figure 6.1 which compares the simulation results to experimental data taken from the NIST database[3]. Observation of the figure clearly shows that the liquid–vapor coexistence curve is remarkably well predicted by the MCCG force field. Critical temperature T_c and density ρ_c were then extrapolated from these simulation results by the mean of scaling laws[4] defined as follow:

$$\rho_L - \rho_V = A(T - T_c)^{\beta} \tag{6.1}$$

$$\frac{\rho_L + \rho_V}{2} - \rho_c = B(T - T_c) \tag{6.2}$$

Where ρ_L and ρ_V are respectively the coexistence liquid and vapor density, $\beta \approx 0.325$ is a characteristic universal exponent[5], *A* and *B* are constants.

Quantitatively, we obtained from such extrapolations critical values of $T_c = 304.09\ K$ and $\rho_c = 463.60\ Kg.m^{-3}$. The critical pressure were then determined by extrapolating[4] the Clapeyron law to $1/T_c$. From this method, a P_c value of $7.52\ MPa$ was obtained. Compared to experimental values of CO_2 critical data ($T_c^{exp} = 304.13\ K$ and $P_c^{exp} = 7.37\ MPa$), the MCCG force field leads to a suitable critical temperature and pressure with an AAD of 0.02% and 2.0% respectively. Regarding the critical temperature, such a good result is not surprising as critical temperature is used to parameterize the force field parameters (cf. section 3.2.1.3)

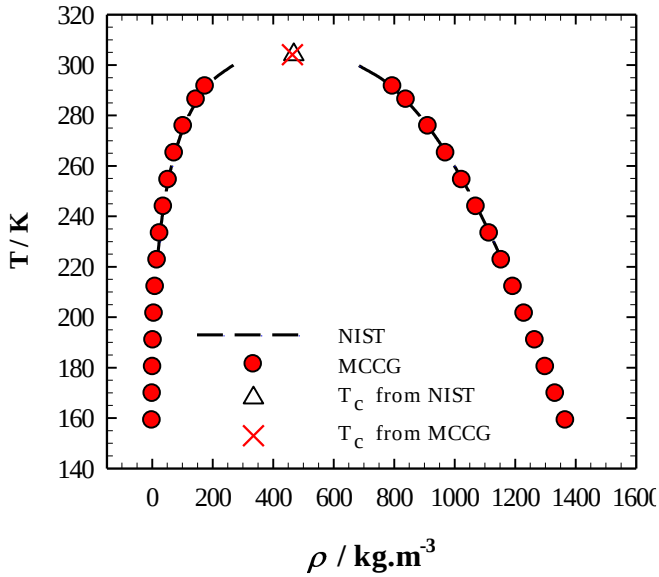

Figure 6.1 Phase diagram of CO_2 . Comparison between GEMC simulations with MCCG and experimental data taken from the NIST database.

6.1.2 Prediction of CO_2 + n-C_7 Mixtures Phase Behaviour by MCCG

Considering the high asymmetry[6] of the CO_2 + n-C_7 mixture, and the fact that the quadrupolar moment of CO_2 is not taken into account by the MCCG model, it is not obvious that the classical Lorentz-Berthelot combining rule defined by equations (3.23) and (3.24) could be sufficient to accurately describe the cross interaction mixture parameters[7]. To check this point, we have performed a preliminary study to assess the capacity of the force field to predict vapor–liquid equilibrium phases composition and Henry's law constant of CO_2 in CO_2 + n-C_7 mixture, the latter being defined[8] as:

$$H_{CO_2} = \lim_{x_{CO_2}^{liq} \to 0} \left[\frac{f_{CO_2}^{liq}}{x_{CO_2}^{liq}} \right] = \rho_{nC7}^{liq}\, k_B T exp\left(\frac{\mu_{CO_2}^{ex}}{k_B T}\right) \tag{6.3}$$

Where f_{CO2}^{liq} and x_{CO2}^{liq} are respectively the fugacity and the mole fraction of CO_2 in liquid mixture, ρ_{nC7}^{liq} the number density of the liquid n-heptane and μ_{CO2}^{ex} is the excess chemical potential of CO_2 in the liquid mixture. Phase equilibrium properties were computed by carrying out Gibbs Ensemble Monte Carlo (GEMC) simulations, whereas μ_{CO2}^{ex}, were computed by using the Widom method[9,10] during MC simulations (cf. equation 3.61).

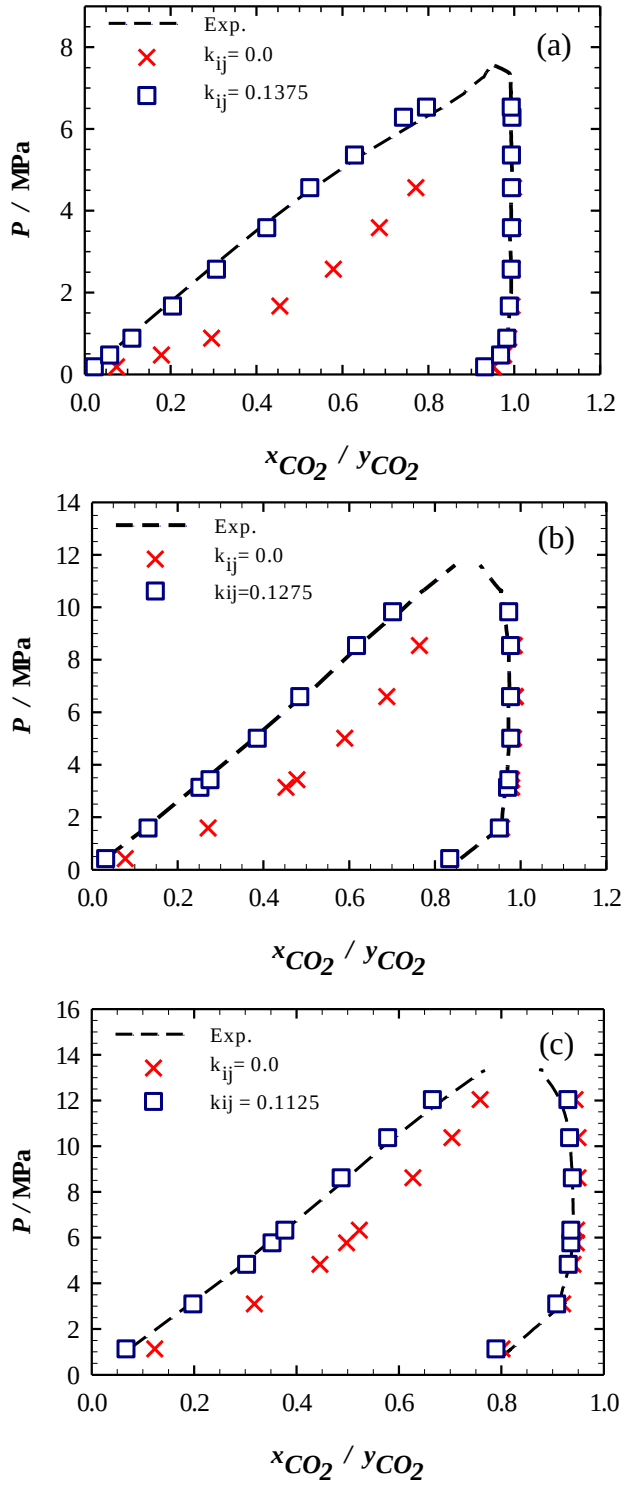

Figure 6.2 Equilibrium phase compositions for the CO_2+n-C_7 binary systems at different temperatures. Panel (a): 310.65 K, panel (b): 352.6 K and panel (c): 394.26 K. Comparison between experimental data provided by Kalra et al.[11]and GEMC simulation with and without k_{ij}.

Figures 6.2 and 6.3 show comparisons between the simulation and experimental results. It is clear that these combining rules combined with the MCCG force field do not correctly capture the cross interactions of the studied mixture of CO_2 + n-C_7 binary system. To overcome this

problem, the potential well depth combining rule given by equation (3.24) was corrected using a binary interaction parameter k_{ij}:

$$\varepsilon_{ij} = (1 - k_{ij})\sqrt{\varepsilon_{ii}\varepsilon_{jj}} \tag{6.4}$$

assuming that fluid-phase equilibria are dominated by the energetic contributions to the interactions rather than by specific molecular shape[7,12]. The correction protocol consists in choosing a k_{ij}value leading to the right prediction of the aforementioned phase equilibrium properties. To determine the appropriate binary coefficient, whose value range between 0.1 and 0.15, an error minimization method that consists in minimizing the deviation between experimental and numerical phase composition then Henry's law constant at fixed temperature was employed.

As observed in the different panels of Figures 6.2 and 6.3, both VLE and Henry's law constant numerical results are in good agreement with experimental data[11] for k_{ij} equals 0.1375, 0.1275 and 0.1125 at 310.6, 352.6 and 394.3 K, respectively. k_{ij} values were then fitted as a linear function of temperature as usually done in the literature[13]. Hereafter, this correlation is used to calculate k_{ij} at the temperatures of interest for this work, that is 303.35 K ($k_{ij} = 0.14$) and 313.25 K ($k_{ij} = 0.1375$) .

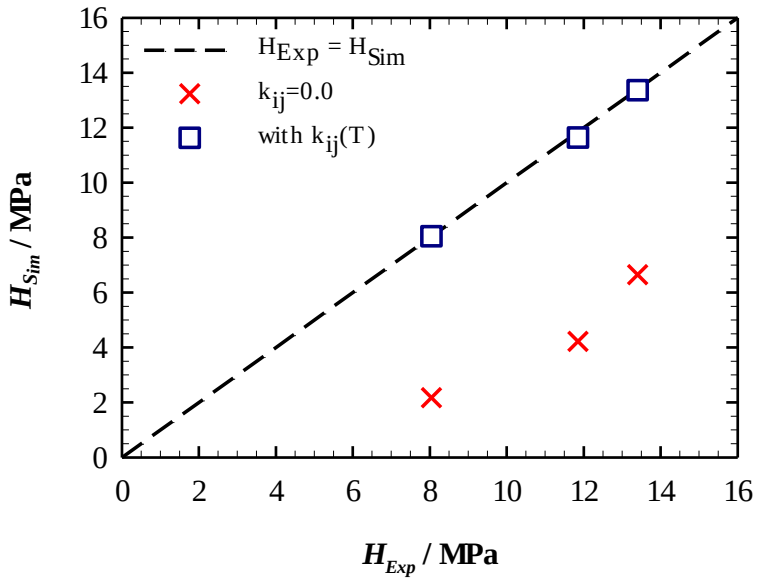

Figure 6.3 Henry's law constant calculated by molecular simulation as a function of experimental values taken from Kalra et al.[11] for carbon dioxide + n-heptane mixture. Comparison are made between simulation results with and without binary coefficient correction.

6.2. Molecular Simulation Details

6.2.1 Thermodynamic Properties

Equilibrium thermodynamic properties such as density, isothermal compressibility, speed of sound and isentropic compressibility were computed by performing Monte Carlo simulations (cf. section 3.3.1) using the binary interaction parameters (k_{ij}) obtained in the section 6.1.2. These MC simulations were performed in the isothermal isobaric ensemble (NPT) using a cubic simulation box containing at least 500 molecules for conditions far from the critical point of pure CO_2 (i.e. $x_{CO2} \leq 60$ mol% and P ≥30 MPa) and 1000 molecules for other mixtures. The periodic boundary conditions were applied in all the directions. The Mie λ-6 potential was truncated at a cut-off radius r_C and long range corrections were included. Details about chosen r_C values are provided in the following section. To generate new configurations, four MC moves were implemented: volume change, molecular translation, molecular rotation and configurational-bias MC partial regrowth. In these simulations, the system is first equilibrated by carrying out at least 3×10^7 MC moves followed by a period of more than 2.10^8 moves during which the sampling is carried out to determine the thermodynamic properties. During the equilibration stage, the maximum amplitudes of first three MC moves are adjusted so that their acceptance are approximately equal to 50%**.**

6.2.2 Structural Properties

To compute the microscopic structure such as the radial distribution functions, Molecular Dynamic simulations in NPT ensemble were performed with binary interaction parameters in the section 6.1.2. The simulation systems were made up of cubic boxes composed of at least 3000 molecules for conditions far from the critical point of pure CO_2 (i.e. $x_{CO2} \leq 60$ mol% and P ≥ 30 MPa) and at least 5000 molecules for other mixtures. In particular, for simulation performed at infinite dilution of CO_2, the system was composed of 5000 molecules of CO_2 and 1 molecule of n-heptane. In addition, classical periodic boundary conditions were applied in all three directions.

During MD simulations, the equations of motion were integrated using the velocity-Verlet algorithm[14]. The temperature and pressure were kept constant using a Berendsen thermostat and barostat, respectively. The classical RATTLE algorithm[15] was employed to constrain the bond length in the MCCG force field.

Similarly to the MC simulations, the non-bonded Mie λ-6 potential was truncated at a cut-off radius r_C and the long range corrections were included. It should be noted that, even if long range corrections are included, the cut-off radius has a strong effect on thermodynamic properties of the mixtures close to the critical point. This is because the correlation length in such mixtures are known to be large[16,17]. Therefore, to choose adequate values of r_C, we have investigated its effect on simulation results of density It was observed that a r_C value of 4σ is able to provide good results for conditions far from the critical point of pure CO_2, whereas a r_C value of 7σ was found adequate for the other mixtures, as shown in Figure 6.4 for pureCO_2 close to its critical point.. It should be noticed that such values of r_C have been used in both MC and MD simulations to compute the thermodynamic and structural properties.

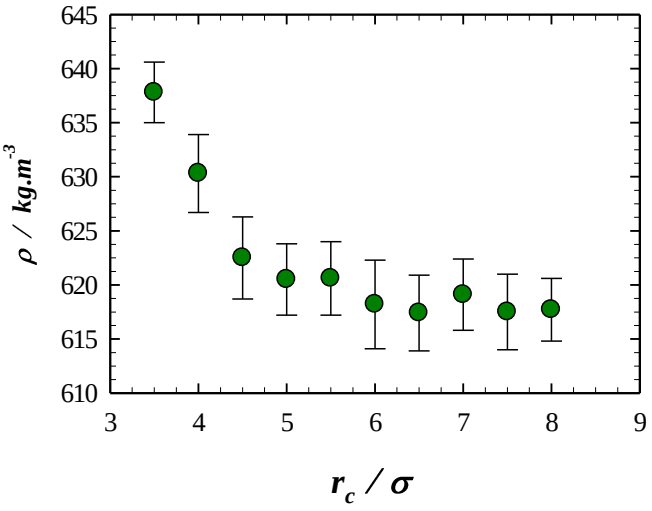

Figure 6.4 Effect of the cut off radius r_C value on the accuracy of simulation results of density near the CO_2 critical point for pure CO2 at 313.15 K and 10.11 MPa. The computed density decreases by increasing r_C until it reaches a plateau around $r_C = 7\sigma$.

6.3. Thermodynamic Properties

In this section, we compare molecular simulation results of thermodynamic properties to experimental results previously reported in chapter 5. To allow comparison, Monte Carlo simulations on pure carbon dioxide, n-heptane and their mixtures with CO_2 mole fractions of 20, 40, 60, 83.26, 88.49 mol% were carried out at the same conditions as experimental measurements, that is for pressure from 10.11 to 70 MPa and on two isotherms at 303.35 and 313.25 K. For further investigations, simulations were also performed for two additional compositions (95 to 99 mol%), where experimental measurements were rather difficult, and for some properties (speed of sound, isentropic compressibility) even impossible to perform with our experimental devices.

6.3.1 Density and Derivative Properties

MC Simulation results of density are reported in Table C.1 of appendix C. Compared to experimental results, numerical density data are globally in good agreement. In details, for conditions far from the critical point (i.e. $x_{CO2} \leq 60$ mol% and P ≥30 MPa), simulation results remarkably matches with experimental ones with an AAD not greater than 1%, whereas for near-critical conditions, deviations from experimental data are much more pronounced and reach up to 4% for pure CO_2 at 313.15 K and 10.11 MPa, i.e. the closest condition to CO_2 critical point. From these observations, it is clear that the deviations mostly arise from the proximity to the CO_2 critical point, and the difficulties to describe this region with molecular simulations combined with the limitations of the chosen force fields.

In Figure 6.5, numerical densities are plotted as a function of CO_2 content at 313.25 K and 10.11 MPa and compared to experimental data. It can be noted that the non-monotonic behavior, synonym of an important non ideal behavior, is well captured by MC simulations. In

addition, this trend is confirmed by simulation results for mixture with higher content of CO_2 (95 and 99mol%) where experimental measurements were not achieved.

Simultaneously to density, MC simulations provide isothermal compressibility values of the system by analyzing volume fluctuations. Such data are available in Table C.2 of appendix C. Similarly to density, this derivative property is rather well predicted by molecular simulations with the chosen force fields. As expected, the AAD deviations to experimental values depict the same trend as density. Deviations vary between 0.5% for pure n-heptane and 10% for mixture with high CO2 content at 10.11 MPa. However, comparison of simulation results of k_T with experimental result around the critical point should be taken with care due to the high sensitivity of this property to density fluctuations[17].

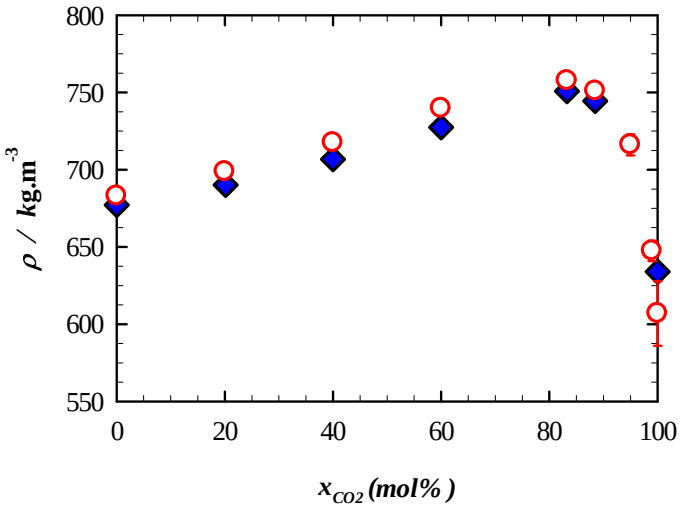

Figure 6.5 Density ρ as a function of CO_2 molar concentration at 313.25 K and 10.11 MPa. Comparison between ◆ **:** experimental measurement and ○: molecular MC simulation.

Figure 6.6 represents numerical and experimental results of isothermal compressibility at 313.25 K and 10.11 MPa as a function of numerical and experimental volume fractions of CO_2, respectively. By comparing the two plots, we observed that the significant departure of k_T to linearity, experimentally pointed out for mixtures with higher CO_2 content near the pure CO_2 critical point, is well depicted by molecular simulation results.

In addition, isentropic compressibility k_s and speed of sound w were indirectly calculated from molecular simulation results of density, isothermal compressibility, isobaric thermal expansion and molar heat capacity using standard thermodynamic relationships defined by equations (3.54) and (3.55), respectively. Both k_s and w calculated data can be found in appendix B. Interestingly, despite not being directly computed by simulations, the calculated data are shown to be in good agreement with experimental results, see Figures 6.7 and 6.8**.** An additional very interesting point is that the simulations allow to provide acoustic thermodynamic properties for CO_2 rich mixtures close to the critical point of CO_2. Indeed, for such conditions, it was found, in chapter 5, that experimental measurements were not possible to perform with the pulse echoes technique used due to the strong dissipation of acoustic waves that results in the inability to detect any reflected echoes in the measurement device.

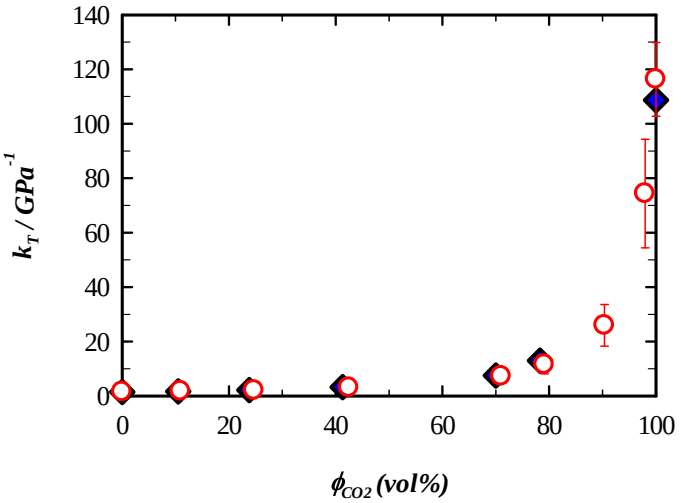

Figure 6.6 Isothermal compressibility k_T as a function of CO_2 volume concentration at 313.25 K and 10.11 MPa. Comparison between ◆ **:** experimental measurement and ○: molecular MC simulation.

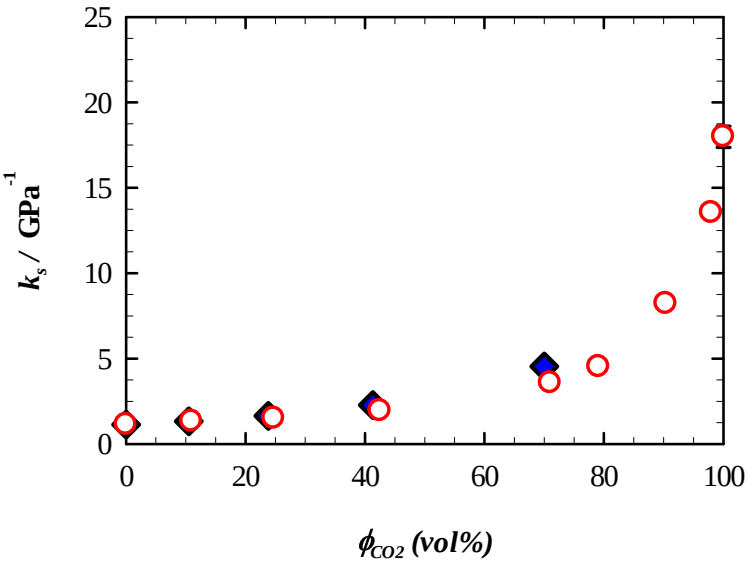

Figure 6.7 Isentropic compressibility k_s as a function of CO_2 volume concentration at 313.25 K and 10.11 MPa. Comparison between ◆ : experimental measurement and ○: molecular MC simulation.

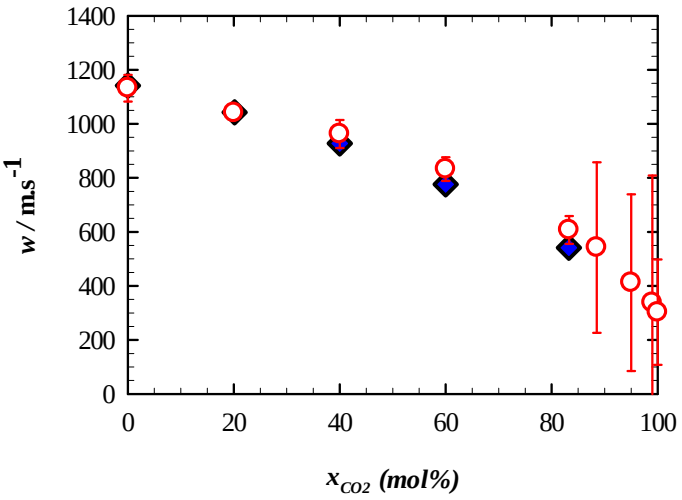

Figure 6.8 Speed of sound w as a function of CO_2 molar concentration at 313.25 K and 10.11 MPa. Comparison between ◆ : experimental measurement and ○: molecular MC simulation.

6.3.2 Excess Properties

To go further in our investigations, excess volumetric and acoustic properties of the studied mixtures were estimated from molecular simulation results. To do so, excess properties were calculated by the general correlation:

$$y^E = y - y^{id} \tag{6.5}$$

Where y denotes either V_m , κ_T , κ_S or w and the superscript id the corresponding ideal properties estimated using the following equations[18] :

$$V^{id} = \sum_i x_i \frac{M_i}{\rho_i} \tag{6.6}$$

$$\kappa_T^{id} = \sum_i \emptyset_i \kappa_{T,i} \tag{6.7}$$

$$\kappa_S^{id} = \sum_i \emptyset_i \kappa_{T,i} - \frac{\left(\sum_i x_i \frac{M_i}{\rho_i}\right)\left(\sum_i \emptyset_i \alpha_{p,i}\right)^2}{\sum_i x_i \frac{M_i T \alpha_{p,i}^2}{\rho_i (\kappa_{T,i} - \kappa_{S,i})}} \tag{6.8}$$

$$w^{id} = \frac{\sum_i x_i \frac{M_i}{\rho_i}}{M \kappa_S^{id}} \tag{6.9}$$

Where the subscript i denotes either CO_2 or n-C_7 .

Evaluation of these excess properties is very important since it highlights how the non-ideal behavior of the mixture is treated by simulation for the corresponding property. It is worth noting that excess properties calculations may be affected by large errors bars, especially for indirectly estimated properties such as κ_S^E and w^E . Despite such large error bars, the results are shown to be quantitatively well estimated by simulations. For example, simulation of excess properties are compared to experimental values at 313.15 K and 10.11 MPa in Figure 6.9 where panels a, b, c, d represent respectively V_m^E, κ_T^E, κ_S^E and w^E as a function of CO2 mol% fraction.

Both simulation results of excess properties are fully consistent with experimental values. In addition, the asymmetric trend is perfectly described by molecular simulations.

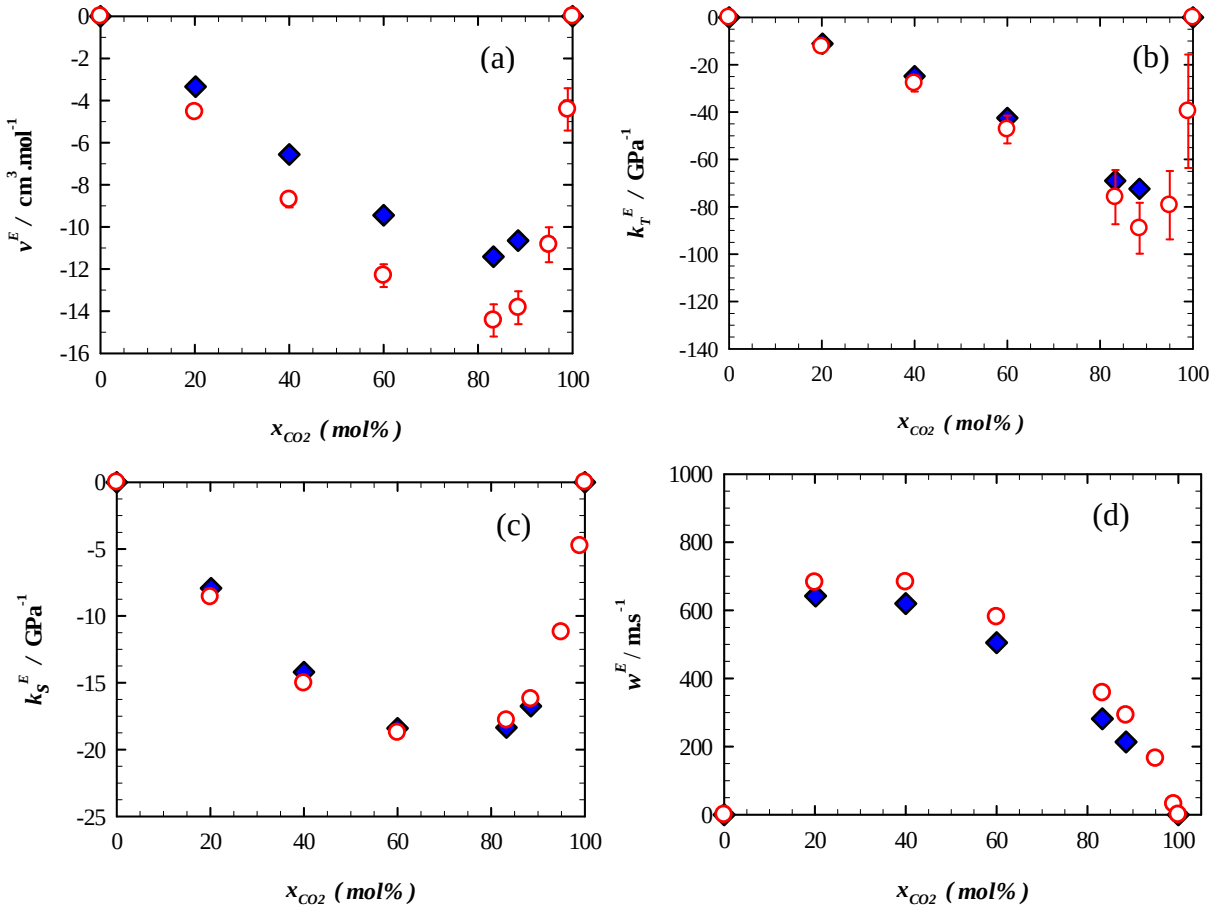

Figure 6.9 Excess properties as a function of CO_2 molar concentration at 313.25 K and 10 MPa. Comparison between ◆ : experimental measurement and ○: molecular MC simulation. For κ_S^E and w^E, wide expanded error bars have not been plotted for the sake of clarity of corresponding curves.

6.4. Kirkwood Buff Integrals and Partial Molar Volumes

To investigate more deeply non-idealities highlighted above by experimental and numerical excess properties, the calculation of experimental partial molar volume of the mixture components turned out to be very informative regarding the fluid behavior at the microscopic level[1]. The most straightforward way to compute such partial property is, as we have done in our experimental investigations, to fit and analytically derive molar volumes. However, this method is subject to high uncertainties related to the choice of the fitting polynomial function and the number of mixture compositions close to the boundary conditions (x_{CO2} = 0% and 100%). Furthermore, when applying this fitting method to simulation molar volumes to determine partial molar volume as done by several authors [19], the results are influenced by the wide molar volume fluctuations, especially for near-critical systems . To overcome these

drawbacks, partial molar volumes were directly computed from the Kirkwood and Buff Integrals (KBIs) previously defined in section 3.3.3.2.

KBIs computed by MD simulations are listed in Tables C.4 to C.7of appendix C along with the corresponding standard deviations. To validate the reported data, isothermal compressibilities have been calculated from these KBIs, using equation (3.73) and compared to MC simulation results of k_T obtained by the fluctuation theory at 313.25 K and 10.11 MPa, see Figure 6.10.

Interestingly, the two sets of data are very consistent within error bars, except for the mixture containing 99 mol% of CO_2 and pure CO_2. However, as previously discussed, comparisons of isothermal compressibility in such near-critical conditions is always very difficult to achieve, due to high density fluctuations. Furthermore, the results were obtained using two different molecular simulations scheme (and system size), MC and MD, which are probably not fully equivalent close to critical conditions.

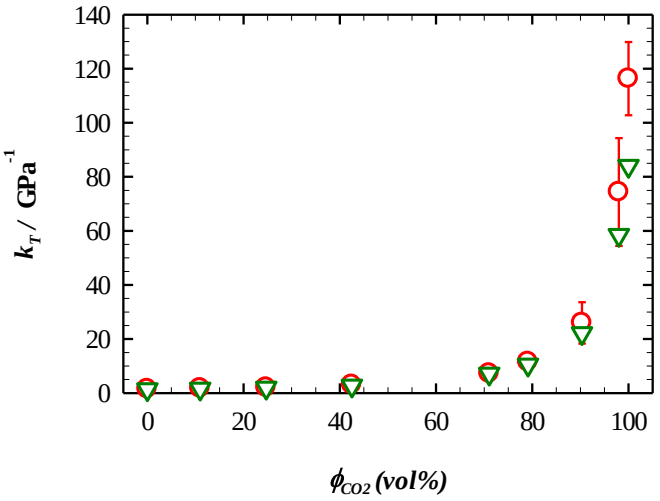

Figure 6.10 Comparison of molecular simulations results of isothermal compressibility of CO2 + n-C_7 mixtures at 313.25 K and 10.11 MPa. ○: molecular MC simulation and ▽: from KBIs.

Then, partial molar volumes of CO_2 ($\bar{v}_{CO2}$) and n-heptane ($\bar{v}_{nC7}$) have been calculated using equation (3.74). Figure 6.11 compares, at 313.25 K and 10.11 MPa, experimental and numerical partial molar volumes of CO2 and n-heptane. It shows a very good match of computed values with experimental fitted results. The sharp decrease of n-C_7 partial molar volume by increasing CO_2 content in the mixture experimentally pointed out, is also observed for simulation results. This trend is confirmed by additional simulation results of mixtures with CO_2 molar fractions from 90 mol% to infinite dilution. The values obtained for infinite dilution of n-heptane ($\bar{v}^{\infty}{}_{nC7}$) overestimates (in absolute value) the experimental value by 60%. This large difference comes from both the large fluctuations observed in molecular simulation in this domain and the experimental uncertainty caused by the high sensitivity to the limit number of data point close to the boundary condition.

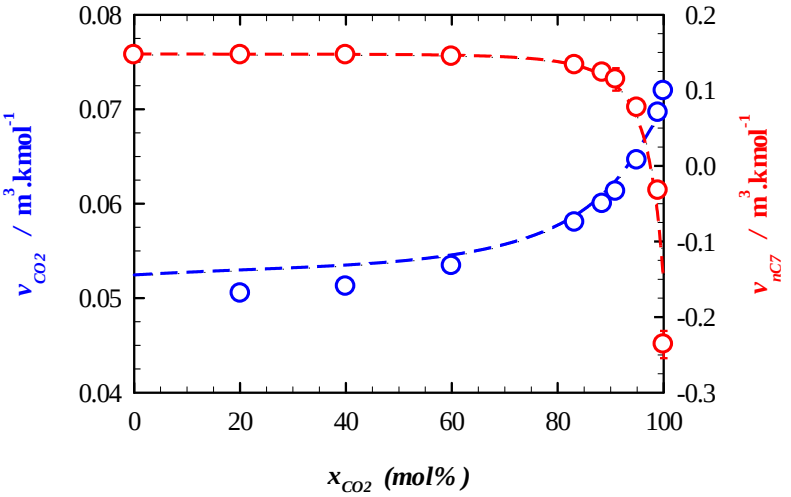

Figure 6.11 Partial molar volume of CO_2 (blue) and n-heptane (red) as a function of CO_2 molar fraction at 313.25 K and 10.11 MPa. Comparison between **- - -** : fit of experimental measurements and **O**: calculation from KBIs.

6.5. Microscopic Analysis of CO_2 Clusters

For mixtures with $x_{CO2} \geq 98$ mol% , the partial molar volume of n-heptane computed from KBIs are negative, as observed from experimental investigations. This result is the macroscopic signature of the formation of CO_2 clusters around n-C_7 molecules at infinite dilution as predicted by Debenedetti and co-workers[1] on binary systems,. The average size of these clusters $\xi_{cluster}$, defined as the excess number of solvent molecules surrounding a solute molecule with respect to a uniform (ideal gas) distribution is given[1] by:

$$\xi_{cluster} \equiv \rho_{CO2} 4\pi \int_0^{\infty} [g^{\infty}_{CO2-nC7}(r) - 1] r^2 dr = \rho^{\infty}_{CO2} \cdot G^{\infty}_{co2-nC7} \qquad (6.10)$$

where the superscript ∞ refers to infinite dilution, ρ_{CO2} is the CO_2 density number $g_{CO2-nC7}(r)$ is the radial distribution function between CO_2 and n-C_7 and $G_{co2-nC7}$ is the corresponding Kirkwood Buff Integral.

Quantitatively, for n-C_7 solute infinitely diluted in CO_2 solvent,(1 molecule of n-C_7 for 5000 molecules of CO_2), we obtained from equation (6.10) a cluster size of $\xi_{cluster} = 6.3$ with a standard deviation of 1.7 at 313.25 K and 10.11 MPa corresponding to the experimental condition for which clustering was observed from density measurements. Interestingly, this cluster size (in excess) estimated numerically from the Kirkwood Buff Integral at infinite dilution of n-C_7 is of the same order as the value obtained from the extrapolation of the experimental data[6], which is around 8.

To gain further microscopic insight of such clusters referred as cluster of type I, we have additionally studied, the static and dynamic properties of such cluster in infinite dilute mixture using Molecular Dynamics, In addition, to quantify the effect of solute molecules on the organization of clusters, we have also estimated the structure of CO_2 cluster formed in pure

supercritical CO_2 fluid [20,21], referred as cluster of type II. It is worth noting that using equation (6.10) leads to a cluster size (in excess) of $\xi_{cluster} = 2.04$ for this cluster of type II at T = 313.25 K and P = 10.11 MPa. This indicates that the clustering effect of type I is roughly 3 times larger than that of type II at this particular condition.

6.5.1 Definition of Clusters

Before proceeding further in the investigation of cluster organization, terms with respect to cluster formation should be unambiguously defined. There are a non-negligible number of different definitions proposed in the literature[22–28]. In general, such cluster is referred to a concentration of solvent molecules around a central molecule[25](either solute in type I or solvent molecule in type II) as depicted in Figure 6.12. Molecules can be either directly or indirectly "bonded» to the central molecule. A molecule is considered to have a direct bond if it satisfies a given criterion, often an energetic or a geometric criterion[25,28]. An indirect bonded molecule is connected to the central molecule through intermediate molecules of cluster, i.e. it is directly bonded to at least one bonded molecule of the cluster but not to the central molecule[25,28]. The magnitude of these cluster (N_{cluster}) should not be confused with the fluctuation-based cluster size $\xi_{cluster}$ previously defined by equation (6.10).

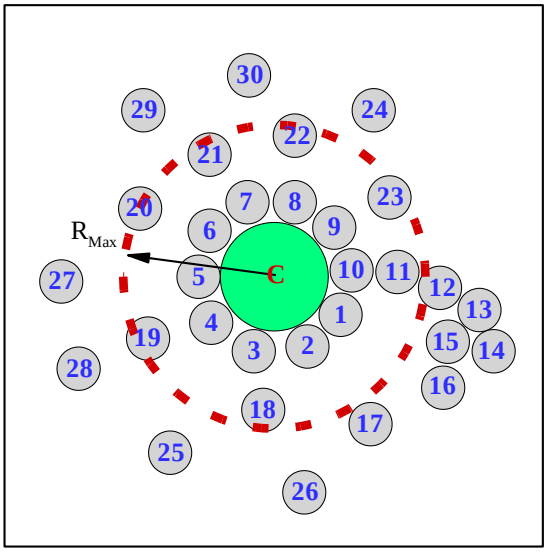

Figure 6.12 A scheme to determine molecules belonging to the cluster. (Green color) Large circle corresponds to the solute molecule, i.e. central molecule. (Dark color) Small circles are the solvent molecules. The 1st to 10th solvent molecules are directly connected to the center molecule, so they are accounted for as belonging to the cluster. The 11th to 16th solvent molecules are indirectly connected to the center molecule, but only the 11th solvent molecule is considered to be in the cluster due to the added criterion of a limited region defined by R_{Max}.

In our study, we have employed a geometric criterion to determine pairs of directly bonded molecules. More precisely, in this work, two molecules separated by a distance less than the radius of the first minimum of the corresponding RDF are considered to be directly bonded[24,28].

For the indirectly bonded molecules, an efficient algorithm based on computation of connectivity matrix[25] have been used. In addition, we have limited the number of molecules belonging to the cluster by defining a spherical region, defined by a radius R_{Max}, surrounding the central molecule[27] as shown in Figure 6.12. However, the definition of such a domain size to catch the appropriate cluster magnitude, is not simple [24].

To define R_{Max}, it is somewhat intuitive to rely on the RDF, i.e. choosing R_{Max} as the corresponding distance beyond which $g(r)$ is nearly constant and equal to 1.0. Results shown in Figure 6.13 indicate that R_{Max} should be in range from 25 Å to 30 Å for the cluster of type I and from 20 Å to 25 Å for the cluster of type II. However, the RDFs may not be adequate to characterize the clustering region[26], even though it already provides important information on clustering. Indeed, the slow decay to 1 and the relatively low peaks confirm that the cluster occurs but it is rather weak. Therefore, to determine the clustering region, we have tried to alternatively estimate R_{Max} by analyzing its effect on the dynamic properties of clusters, assuming that the molecules belonging to the cluster should exhibit dynamic behaviors different from molecules that do not belong to the cluster. More precisely, for that purpose, we have considered two dynamic properties: the autocorrelation function of excess number of molecules in the cluster and the residence time.

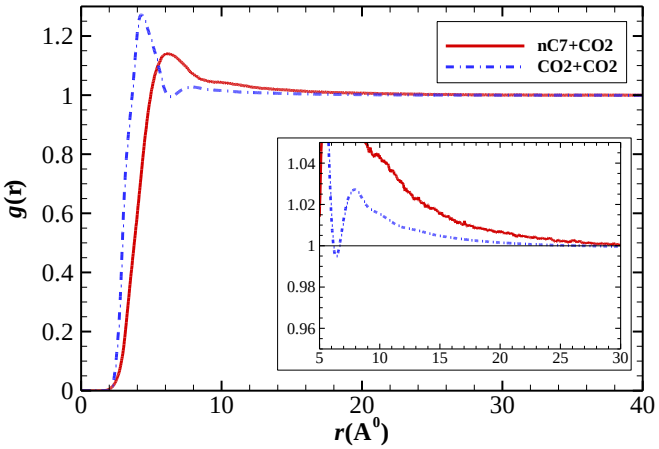

Figure 6.13 The radial distribution functions (RDF) of infinite dilute mixture of CO_2 + n-C_7 at T = 313.25 K and P = 10.11 MPa.

The autocorrelation function (ACF) of excess number of molecules in the cluster, C(t), is defined as:

$$C(t) = \left[N_{\text{cluster}}(t=0) - N_{\text{cluster}}^{\text{Ideal}}\right] \times \left[N_{\text{cluster}}(t) - N_{\text{cluster}}^{\text{Ideal}}\right] \qquad (6.11)$$

where N_{cluster} is the number of CO_2 molecules belonging to the cluster, $N_{\text{cluster}} = \sum_i \delta_i$ with $\delta_i = 1$ if the i^{th} molecule of the simulation box belongs to the cluster region defined by R_{Max} and $\delta_i = 0$ if not, and $N_{\text{cluster}}^{\text{Ideal}} = \left(\frac{4}{3}\pi R_{\text{Max}}^3\right) \times \left(\frac{\rho_{CO_2}}{M_{CO_2}}\right) N_a$ is the reference number of CO_2 molecules in an ideal representation.

Figure 6.14 shows the effect of R_{Max} on normalized ACF, $C_N(t) = [C(t)/C(t=0)]$, for the cluster-types I and II. It is found that $C_N(t)$ converges when R_{Max} increases. The adequate value of R_{Max} should be the one for which $C_N(t)$ is no longer affected by the choice of the R_{Max} value. As shown in Figure 6.14, the converging value of R_{Max} is in the range from 25 Å to 30 Å for the cluster-type I and from 20 Å to 25 Å for the cluster-type II, both in agreement with what has been deduced from the RDFs.

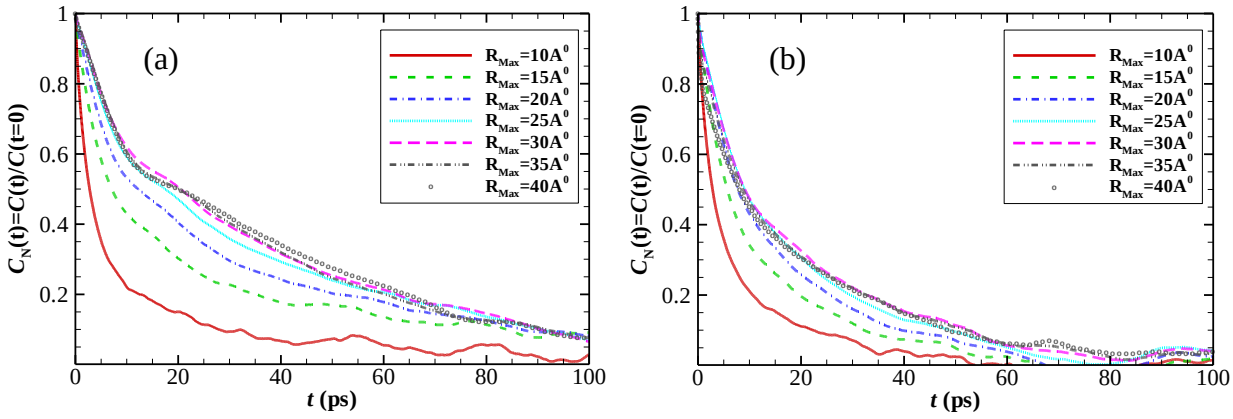

Figure 6.14 Effect of R_{Max} on the normalized autocorrelation functions of excess number of molecules in the cluster $C_N(t) = [C(t)/C(t=0)]$. Panel (a): The cluster-type I in CO_2 + n-C_7. Panel (b): The cluster-type II in CO_2 + CO_2.

The residence time τ_0 is a quantity used to measure how long molecules reside in the cluster[27]. To compute τ_0, we have estimated the number of molecules remaining in the cluster during the time window 0 to t $N_{\mathrm{remain}}(t)$ that is defined as:

$$N_{\mathrm{remain}}(t) = \sum_i \delta_i^0(t) \tag{6.12}$$

where, $\delta_i^0(t) = 1$ if the i^{th} molecule resides in the cluster domain defined by R_{Max} during the time interval [0,t], and $\delta_i^0(t) = 0$ otherwise. Figure 6.15 shows the time evolution of $N_{\mathrm{remain}}(t)/N_{\mathrm{remain}}(t=0)$, for various values of R_{Max} for the cluster-types I and II. It is interesting to notice that $N_{\mathrm{remain}}(t)$ exponentially decays with the time for all R_{Max} studied. In addition, the same behavior was obtained for the cluster-type II. The residence time τ_0 can so be calculated from the following equation:

$$N_{\mathrm{remain}}(t) = N_{\mathrm{remain}}(t=0) \times \exp\left[-\frac{t}{\tau_0}\right] \tag{6.13}$$

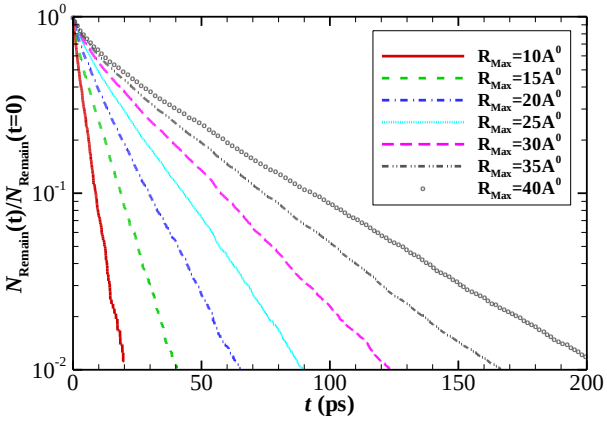

Figure 6.15 Time dependence of $N_{\mathrm{Remain}}(t)/N_{\mathrm{Remain}}(t=0)$ for various values of R_{Max} for the cluster-type I, i.e. CO_2 + n-C_7.

Figure 6.16 displays dependence of τ_0 on R_{Max} for both cluster-types I and II. Results indicate that there are two regions, the transition from the first region to the second one defining two regimes in terms of residence time and so the adequate value of R_{Max}. The adequate value of R_{Max} obtained from the residence time is in the range from 25 Å to 30 Å for the cluster-type I and from 20 Å to 25 Å for the cluster-type II, see Figure 6.16, in agreement with previous findings.

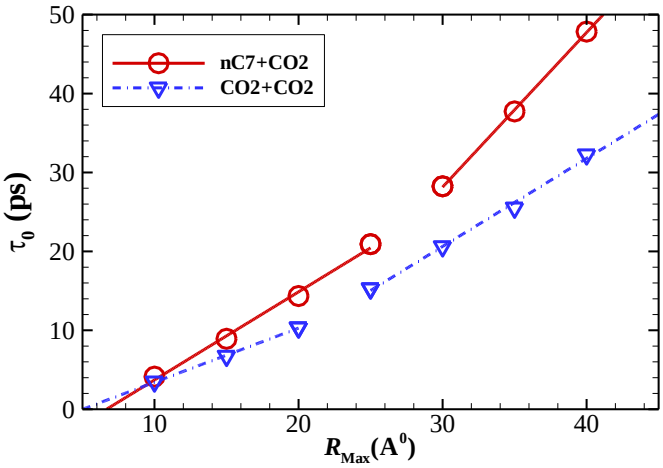

Figure 6.16 Dependence of residence time on R_{Max} for the cluster-types I and II, i.e. n-C_7+CO_2 and CO_2+CO_2 respectively.

In summary, it has been found that the adequate value of R_{Max} obtained from three different approaches are consistent with each other. Thus, in the following we will use $R_{\mathrm{Max}} = 30$ Å for the cluster-type I and $R_{\mathrm{Max}} = 25$ Å for the cluster-type II. Indeed, more precise values of R_{Max} could be obtained by using a finer range of R_{Max}. However, results would not be significantly modified compared with statistical uncertainties.

6.5.2 Static Property of Cluster

To study the "static" property of cluster, we have computed the probability density distribution of the instantaneous cluster magnitude (N_{cluster}). Results are provided in Figure 6.17. It appears that both distributions have a Gaussian form. More precisely, the mode of the distribution (i.e. the most likely value of the cluster magnitude) of cluster-type I is approximately 955, which is nearly 2 times that of cluster type II (around 550). This result indicates that the molecule aggregate formed in cluster-type I is stronger than the one in cluster-type II.

For a fair comparison of the variability of cluster-types I and II, we have also computed the density distribution of the relative number of cluster molecules $N^R(t)$ that is defined as:

$$N^R(t) = \frac{N_{\text{cluster}}(t)}{N_{\text{Cluster}}^{\text{Ave}}} \tag{6.14}$$

where $N_{\text{Cluster}}^{\text{Ave}}$ is the average number of solvent molecules within a sphere of radius R_{Max}. Results are provided in Figure 6.18. This figure shows once again Gaussian distributions, in which the standard deviations are roughly equal to 0.058 and 0.081 respectively for cluster-types I and II. This result indicates that the cluster-type I is somewhat more stable (less relative variability) than the cluster-type II.

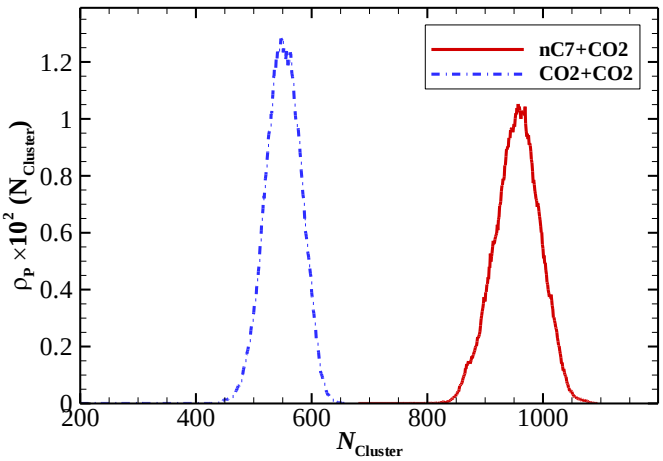

Figure 6.17 A comparison between probability density (ρ_P) distributions of number of molecules N_{cluster} of the cluster-types I and II

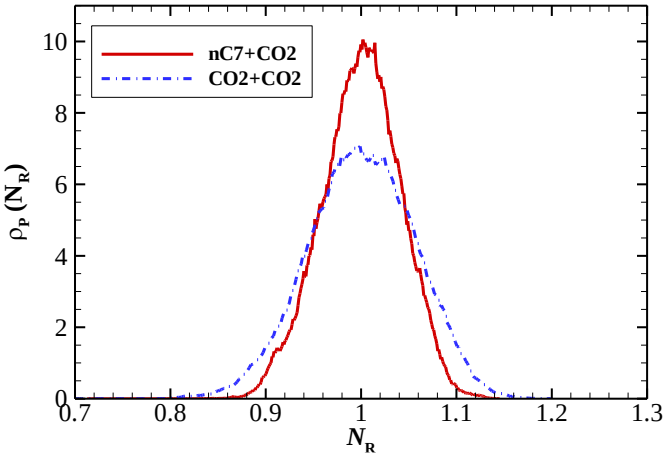

Figure 6.18 A comparison between probability density (ρ_P) distributions of relative number of cluster N^{R} of the cluster-types I and II.

6.5.3 Dynamic Properties of Cluster

Figure 6.19 shows $C_N(t)$ and $N_{\mathrm{Remain}}(t)$ for the cluster-types I and II. As expected from the static property, both of $C_N(t)$ and $N_{\mathrm{Remain}}(t)$ decay more slowly in the cluster-type I than in the cluster-type II. More precisely, the residence time of the former $\tau_0^I = 28.5\,ps$ is roughly two times greater than that of the latter $\tau_0^{II} = 15.3ps$. These results are further evidences that the cluster-type I is more stable than the cluster-type II.

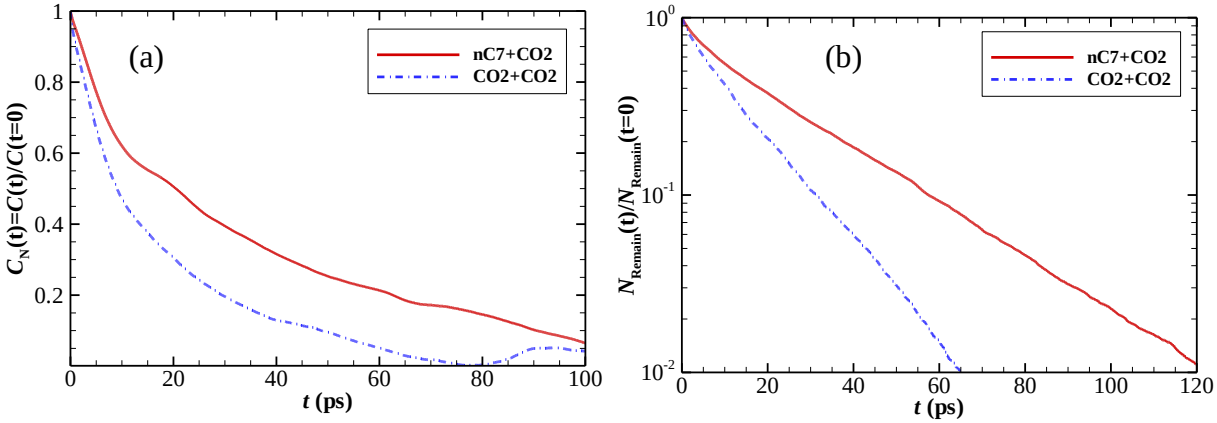

Figure 6.19 Panel (a) : A comparison between the normalized autocorrelation functions of excess number of molecules in the clusters $C_N(t) = [C(t)/C(t=0)]$ of cluster-types I and II. Panel (b): A comparison between normalizations of $N_{\mathrm{Remain}}(t)$, i.e. $\left[N_{\mathrm{Remain}}(t)/N_{\mathrm{Remain}}(t=0)\right]$, of cluster-types I and II.

In Figure 6.20 the instantaneous number $N_{\mathrm{cluster}}(t)$ of CO_2 molecules belonging to the cluster type I and the number N_{Remain} of CO_2 molecules remaining member of the cluster in the window time 0 to t. This plot clearly shows, as has been discussed by Liew et al.[27] and Petsche and Debenedetti [26], that the structure of cluster is maintained as time proceeds; however, cluster

initial members are replaced by new ones. There is an exchange between the molecules of the cluster and the rest of the system.

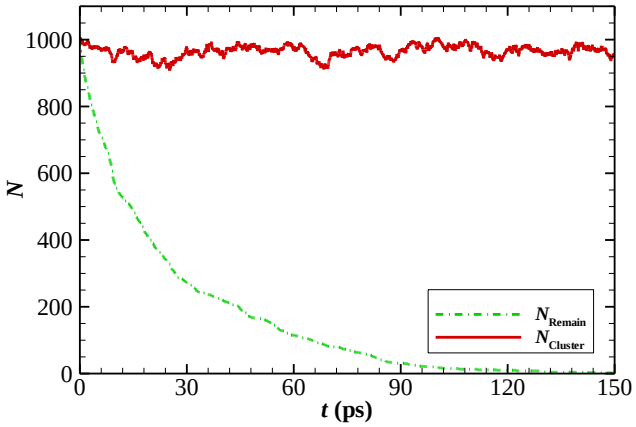

Figure 6.20 Number of CO_2 molecules in cluster of type I as a function of time.

6.6. Conclusions

In this work, which form the second part of a combined experimental and numerical study of binary mixtures composed of carbon dioxide and n-heptane at two temperatures (303.35 and 313.25 K) and at pressures from 10 to 70 MPa, we have performed molecular simulations of thermodynamic and structural properties of the studied mixture using a coarse grained force field named MCCG.

First, a systematic comparison between predicted thermodynamic properties and experimental results previously reported has been performed. It appears that through a simple correction to the Lorentz–Berthelot combining rules by the mean of a binary interaction parameter, molecular simulations with MCCG were able to predict thermophysical properties such as density, isothermal compressibility, speed of sound, isentropic compressibility and the corresponding excess properties of such an asymmetric mixture. However, results slightly deteriorate in conditions near to the CO_2 critical point, mainly due to high density fluctuations and limitations of the force field used.

Second, we have accurately estimated from the radial distribution function the so-called Kirkwood Buff Integrals. From the KBI values, partial molar volumes of CO_2 and n-heptane have been then directly calculated. Interestingly, the results obtained are in very good agreement with experimental values, except at infinite dilution of CO_2 where simulations provide greater partial molar volume of n-C_7 than experimental measurements. As deduced from extrapolation of experiments, for very CO_2-rich mixture (about 98 mol%), the partial molar volume of n-heptane at 313.15 K and 10.11 MPa are negative, indicating the formation of CO_2 clusters around diluted n-heptane molecules. From simulations, we obtained a cluster size of about 6 molecules (in excess), which is of the same order as the value obtained by experimental indirect estimation.

In the last part of this chapter, we have proceeded to a microscopic study of the CO_2 clusters. Having chosen a geometric criterion to define the cluster, we determined the spatial limit of the

clustering from 3 different methods: (1) from the RDF, (2) from the autocovariance of the excess number of molecules in the cluster and (3) from the residence time of the molecules in the cluster. The results obtained by these 3 methods proved to be similar and showed that the clustering effect is contained in a sphere of radius R_{clust}≈30 Å. Once the clustering region and the cluster's molecules have been identified, its static behavior has been determined by computing the probability density distribution of the total and relative numbers of CO_2 molecules in the cluster. The results are a Gaussian distribution indicating that the most likely value of the number of CO2 molecules aggregate around the central solute n-C7 molecule is about 955. Concerning the dynamic behavior of the cluster, we have estimated the residence time of molecules belonging to the cluster. It was shown that the CO_2 molecules remain on average 28.5 ps in the cluster around the central n-C_7 molecule confirming the weak stability of such cluster. So, as time proceeds, the aggregate lost their identity by exchanging molecules with non-clustering region, but keep their integrity.

For a comparison purpose, we have also studied clusters formed in pure CO_2 under the same thermodynamic conditions. The results show that, due to the addition of an infinitesimal quantity of n-heptane, CO_2 clusters formed in the mixture at infinite dilution are larger and more stable than those existing in pure supercritical CO_2. Additional investigations are planned to check the effect of the distance to the CO_2 critical point as well as the effect of the length of the solute n-alkane chain on the clustering of CO_2 molecules.

6.7. References

(1) Debenedetti, P. G. Clustering in Dilute, Binary Supercritical Mixtures: A Fluctuation Analysis. *Chem. Eng. Sci.* 1987, *42* (9), 2203–2212.

(2) Kirkwood, J. G.; Buff, F. P. The Statistical Mechanical Theory of Solutions. I. *J. Chem. Phys.* 1951, *19* (6), 774–777.

(3) Lemmon, E.W., Bell, I.H., Huber, M.L., McLinden, M.O. NIST Standard Reference Database 23: Reference Fluid Thermodynamic and Transport Properties-REFPROP, Version 10.0, National Institute of Standards and Technology, Standard Reference Data Program, Gaithersburg, 2018

(4) Ungerer P., Tavitian B.; Boutin A. In Applications of molecular simulations in the oil and gas industry, Monte Carlo methods; Editions TECHNIP, 2005.

(5) Wilding, N. B. Critical-Point and Coexistence-Curve Properties of the Lennard-Jones Fluid: A Finite-Size Scaling Study. *Phys. Rev. E* 1995, *52* (1), 602–611.

(6) Bazile, D. N. J.-P.; Hamani, A. W. S.; and J.-L. Daridon, G. G. "Excess Volume, Isothermal Compressibility, Isentropic Compressibility and Speed of Sound of Carbon Dioxide + n-Heptane Binary Mixture under Pressure up to 70 MPa. *Exp. Meas. J. Supercrit. Fluids* 2018, *140*, 218–232.

(7) Müller, E. A.; Gelb, L. D. Molecular Modeling of Fluid-Phase Equilibria Using an Isotropic Multipolar Potential. *Ind. Eng. Chem. Res.* 2003, *42* (17), 4123–4131.

(8) Shing, K. S.; Gubbins, K. E.; Lucas, K. Henry Constants in Non-Ideal Fluid Mixtures. *Mol. Phys.* 1988, *65*, 1235–1252.

(9) Widom, B. Some Topics in the Theory of Fluids. *J. Chem. Phys.* 1963, *39* (11), 2808–2812.

(10) Widom, B. Potential-Distribution Theory and the Statistical Mechanics of Fluids. *J. Phys. Chem.* 1982, *86* (6), 869–872.

(11) Kalra, H.; Kubota, H.; Robinson, D. B.; Ng, H.-J. Equilibrium Phase Properties of the Carbon Dioxide-n-Heptane System. *J. Chem. Eng. Data* 1978, *23* (4), 317–321.

(12) Avendaño, C.; Lafitte, T.; Galindo, A.; Adjiman, C. S.; Jackson, G.; Müller, E. A. SAFT-γ Force Field for the Simulation of Molecular Fluids. 1. A Single-Site Coarse Grained Model of Carbon Dioxide. *J. Phys. Chem. B* 2011, *115* (38), 11154–11169.

(13) Privat R. and Jaubert J.N (2012). Thermodynamic Models for the Prediction of Petroleum-Fluid Phase Behaviour, Crude Oil Emulsions- Composition Stability and Characterization, Editions InTech, 2012.

(14) Verlet, L. Computer "Experiments" on Classical Fluids. I. Thermodynamical Properties of Lennard-Jones Molecules. *Phys. Rev.* 1967, *159* (1), 98–103.

(15) Andersen, H. C. Rattle: A "Velocity" Version of the Shake Algorithm for Molecular Dynamics Calculations. *J. Comput. Phys.* 1983, *52* (1), 24–34.

(16) Saitow, K.; Kajiya, D.; Nishikawa, K. Dynamics of Density Fluctuation of Supercritical Fluid Mapped on Phase Diagram. *J. Am. Chem. Soc.* 2004, *126* (2), 422–423.

(17) Parris, P. MOLECULAR SIMULATION STUDIES IN THE SUPERCRITICAL REGION, 2010, Doctoral thesis, University College London.

(18) Bazile, J.-P.; Nasri, D.; Saley Hamani, A. W.; Galliero, G.; Daridon, J.-L. Density, Speed of Sound, Compressibility, and Excess Properties of Carbon Dioxide + n-Dodecane Binary Mixtures from 10 to 70 MPa. *J. Chem. Eng. Data* 2019, *64* (7), 3187–3204.

(19) Stubbs, J. M.; Drake-Wilhelm, D. D.; Siepmann, J. I. Partial Molar Volume and Solvation Structure of Naphthalene in Supercritical Carbon Dioxide: A Monte Carlo Simulation Study. *J. Phys. Chem. B* 2005, *109* (42), 19885–19892.

(20) Sedunov, B. The Analysis of the Equilibrium Cluster Structure in Supercritical Carbon Dioxide. *Am. J. Anal. Chem.* 2012, *3* (12), 899–904.

(21) Mareev, E.; Aleshkevich, V.; Potemkin, F.; Bagratashvili, V.; Minaev, N.; Gordienko, V. Anomalous Behavior of Nonlinear Refractive Indexes of CO_2 and Xe in Supercritical States. *Opt. Express* 2018, *26* (10), 13229–13238.

(22) Hill, T. L. Statistical Mechanics: Principles and Selected Applications; Courier Corporation, 1956.

(23) Hill, T. L. Molecular Clusters in Imperfect Gases. *J. Chem. Phys.* 1955, *23* (4), 617–622.

(24) Stillinger, F. H. Rigorous Basis of the Frenkel-Band Theory of Association Equilibrium. *J. Chem. Phys.* 1963, *38* (7), 1486–1494.

(25) Sevick, E. M.; Monson, P. A.; Ottino, J. M. Monte Carlo Calculations of Cluster Statistics in Continuum Models of Composite Morphology. *J. Chem. Phys.* 1988, *88* (2), 1198–1206.

(26) Petsche, I. B.; Debenedetti, P. G. Solute–Solvent Interactions in Infinitely Dilute Supercritical Mixtures: A Molecular Dynamics Investigation. *J. Chem. Phys.* 1989, *91* (11), 7075–7084.

(27) Liew, C. C.; Inomata, H.; Saito, S. Molecular Dynamics Study on Solvent Clustering in Supercritical Fluid Solutions Based on Particle Radial Kinetic Energy. *Fluid Phase Equilibria* 1995, *104*, 317–329.

(28) Ingebrigtsen, T.; Toxvaerd, S. Contact Angles of Lennard-Jones Liquids and Droplets on Planar Surfaces. *J. Phys. Chem. C* 2007, *111* (24), 8518–8523.

Chapter 7. Conclusions and Perspectives

Contents

7.1. Conclusions 125
7.2. Perspectives and Recommendation for Future Works 126

In this chapter, we present general conclusions on the work developed in this manuscript as well as perspectives and recommendation for future works.

7.1. Conclusions

It should be recall that the objective of this work, combining experimental measurements and molecular simulations, is on the one hand to provide reliable experimental data on asymmetric mixtures, in particular on those of interest for CO_2-EOR processes, and on the other hand to evaluate the performance of molecular simulation techniques to quantitatively predict these thermophysical properties and provide microscopic insight on the microscopic structure of the studied mixtures.

In the first chapter, we carried out experimental measurements and molecular simulations on a simple asymmetric liquid mixture composed of n-hexane + n-dodecane. This study allows evaluating the capability of Mie Chain Coarse Grained force field, comparatively to a fine grained force field (TraPPE-ua), to simultaneously predict thermodynamic properties (density and derivative properties) and a transport properties (viscosity). From our results, it appears that both force fields combined with molecular simulation techniques are able to predict quantitatively the studied thermodynamic properties and their associated excess properties for this simple system by using classical Lorentz-Berthelot combining rules. However, the transferability of these force fields to the prediction of viscosity and its excess values is not straightforward even for such a simple mixture. It can be concluded from these observations that viscosity is an interesting property not only to evaluate the quality of force fields but also the capabilities of the combining rules to capture cross interactions for a given molecular model.

Then, in the following chapter, we have chosen to study a more complex system, consisting of CO_2 and n-heptane for two temperatures (303 and 313 K) and pressures ranging from 10 to 70 MPa, i.e. around the critical point of CO_2. This mixture has been chosen because of its interest as a proxy for CO_2 enhanced oil recovery systems and these specific thermodynamic conditions have been chosen so as to specifically analyze the expected influence of the proximity of the critical point of CO_2 on the non-idealities of the studied mixture. First, we enrich existing data bases by providing accurate experimental data of density, speed of sound and their derivative (isothermal and isentropic compressibility) but also the excess volumetric and acoustic properties. It should be point out that such type of data is very rare in the open literature on gas+liquid systems. In more details, we observed that density, at the lowest pressure (10 MPa), does not behave monotonously with CO_2 concentration, which is a signature of a significant non ideal behavior of such near critical mixtures. In addition, it has been noticed, at T = 313 K and P = 10 MPa, a change of sign, from positive to negative, of the partial molar volume of n-heptane when going towards infinite dilution. Such contraction behaviour, typical of near critical dilute mixture, can be interpreted as the organisation of the solvent molecules (CO_2) around the solute molecule which may form cluster. Moreover, by comparing mixtures volumetric properties to ideal mixtures ones, it has been found that these mixtures volumetric properties, for low to moderate CO_2 content, could be well described by an ideal binary mixture where the actual CO_2 properties are replaced by their infinite CO_2 dilution values.

To go further in our investigations on the studied CO_2 + n-C_7 mixtures, in chapter 6 we performed molecular simulations using the MCCG force field. It appears that through a simple correction to the Lorentz–Berthelot combining rules, by the mean of a binary interaction parameter, molecular simulations were able to predict thermophysical properties in good agreement with experimental data. A very interesting point in this context is that, molecular simulations are able to provide some thermodynamic properties while they cannot be measured experimentally. This was the case, for example, for sound velocity in CO_2-rich mixtures. Furthermore, molecular simulations have been combined to Kirkwood-Buff theory of solution to provide partial molar volumes of the mixtures components which were found to be consistent with those deduced from experimental data. Finally, the clustering phenomenon highlighted experimentally has been studied by Molecular Dynamics to improve the understanding of its microscopic nature. It was found that different definitions of the clustering all yield cluster radius of about 30 Å. Moreover, it was shown that the CO_2 molecules remain on average 28.5 ps in the cluster radius around the central n-C_7 molecule confirming the weak stability of such cluster. So, as time proceeds, the aggregate lost their identity by exchanging molecules with non-clustering region, but keep their integrity.

7.2. Perspectives and Recommendation for Future Works

The perspectives and recommendations for future short term works can be grouped under the following headings:

- **On experimental measurements**. Despite the strong growth of databases containing thermophysical properties of asymmetric mixtures, it still seems necessary to continue to produce experimental data on such systems, especially for specific conditions where models need to be improved. In this context, additional measurements on binary systems composed of CO_2 and longer n-alkanes and composed of methane and long n-alkanes continue to be carried out in our laboratory (cf. Appendix A). These studies should also be extended to transport properties such as viscosity which is another very important property for which the database is still rather sparse.

- **On molecular simulations**. In the short term, it would be interesting to continue investigating the clustering phenomenon observed in chapters 5 and 6. For this purpose, we have already performed a set of molecular simulations on CO_2 + n-C_7 systems closer to the critical point to see the effect of the distance to the CO_2 critical point on cluster formation. In addition, a systematic study on the effect of the length of n-alkane molecules on the clustering should be conducted, in parallel with the experiments. All these results could be then used to assess the limitations of the SAFT-Mie Equation of state (Lafitte and co-workers) which is based on the MCCG model, to tackle subtle thermodynamic behavior such as the clustering.

In the medium and long-term an interesting research topic could be the development of simple molecular models that simultaneously predict both thermodynamic and transport properties. For that, a coarse grained approach, like the one used for the MCCG force field used in this work, remains a good base because it is a quite simple model with few number

of parameters. However, it must be enriched by improving for example the way molecules rigidity is described while keeping its simplicity. The ultimate goal could be its declination in an equation of state (SAFT-like), requiring fewer resources than molecular simulations and being so more compatible with engineering requirements. A new project with this subject as one of its objectives has just started in our laboratory.

Appendix A . Density, Speed of Sound, Compressibility and Excess Properties of Carbon Dioxide + n-Dodecane.

*Results presented in this Appendix have been published in J. Chem. Eng. Data 2019, 64, 7, 3187

Contents

A .1 Chemicals 129
A .2 Speed of Sound and Density 129
A .3 Derivative Properties 137
A .4 Excess Properties 143
A .5 Partial Molar Volume 150
A .6 Conclusion 156
A .7 References 157

Introduction

The knowledge of volumetric and acoustic properties of reservoir fluids as a function of temperature, pressure and composition is important for simulating oil recovery processes as well as seismic monitoring. Indeed, these thermodynamic data correspond to key properties for tuning the equations of state used for representing thermodynamic properties of such mixtures. The need for such thermophysical data on systems containing carbon dioxide in addition to hydrocarbons has increased with the growing trend towards injecting CO_2 into reservoir to enhance oil recovery by solvent miscible flooding processes.

Therefore, a program is underway in our laboratory to quantify density and speed of sound in CO_2 + hydrocarbon systems with a focus on the influence of hydrocarbon chain length on the non-ideal behavior of such binary systems at near-critical or supercritical CO_2 conditions. The CO_2 + n-heptane system was already studied and the results are reported in a previous article[1]. In this article, the investigation is extended to mixtures composed of carbon dioxide and n-dodecane. The work will be continued and reinforced by studying the CO_2 + n-heptadecane and CO_2 + n-docosane binary systems in the near future.

Thus, densities were measured for various compositions covering the whole range of molar percentage (0-100%) at several pressures ranging from 10 to 70 MPa and at two temperatures around the critical temperature of carbon dioxide, i.e (303.15, 313.15) K. These temperatures were chosen so as to focus on the influence of the vicinity of the critical point of CO_2 on the non-ideality of the studied mixtures. The isothermal compressibility was then deduced from these measurements using a numerical Monte-Carlo procedure. Additionally, acoustic measurements have been carried out so as to determine the speed of sound of these mixtures for the same the experimental conditions than density measurements. By combining both volumetric and speed of sound data sets, the isentropic compressibility was determined. Finally, excess quantities associated with each property were evaluated from experimental measurements so as to quantify and highlight the deviations to ideality in such CO_2-n-dodecane mixtures

A .1 Chemicals

Carbon dioxide was purchased from LINDE with a nominal purity of 99.995%. Normal-dodecane was supplied by Sigma-Aldrich with a purity of 99.6 mol % confirmed with a certificate of analysis. Both components were used without any further treatment. Details on pure components are listed in Table A.1.

A .2 Speed of Sound and Density

Speed of sound and density measurements were performed for pure n-dodecane and five different mixtures ranging from 20 to 85 mol% of CO_2. In addition, as shown in Table A.2, three mixtures with high CO_2 contents and pure carbon dioxide were investigated in the densitometer for the purpose to determine the partial molar volume of n-dodecane at infinite dilution in carbon dioxide. Mixtures were first prepared in the acoustic cell and then reproduced for density measurement. Table A.2 lists the composition of the different mixtures investigated

along with their expanded uncertainty $U(x_{co2})$ obtained by multiplying by the conventional coverage factor k_P = 2 (P = 95 %) the combined standard uncertainty $u_c(x_{co2})$ calculated from equation (2.19).

Table.Appendix A.1 Sample Description

Chemical Name	CAS	Source	Purity	Water content	Purification Method
Carbon dioxide	124-38-9	Linde	0.99995	< 5 ppm	None
n-dodecane	112-40-3	Sigma-Aldrich	0.996	<0.01%	None

Table.Appendix A.2 Mole fraction x_{co2} and its expanded uncertainty $U(x_{co2})$ (level of confidence = 0.95, k = 2) of the different sample mixtures investigated of the binary system (Carbon Dioxide + n-dodecane).

Speed of sound measurements	x_{co2}	0.2032	0.3989	0.6007	0.7498	0.85278	-	-	-
	$U(x_{co2})$	0.0004	0.0004	0.0002	0.0001	0.00006	-	-	-
Density measurements	x_{co2}	0.205	0.400	0.6008	0.7497	0.8530	0.9348	0.9771	0.9877
	$U(x_{co2})$	0.002	0.001	0.0009	0.0006	0.0005	0.0003	0.0003	0.0003

It can be verified from this Table that the difference between the compositions of the mixtures prepared for speed of sound and density measurements are always less than the expanded uncertainty. Moreover, density and speed of sound measurement were performed in the same P,T conditions. This is a prerequisite for the determination of isentropic compressibility as well as excess isentropic compressibility and excess speed of sound. Measurements were carried out every 10 MPa steps from (10 up to 70) MPa at (303.15 and 313.15) K, two isotherms that surround the critical temperature of CO_2. Experimental results are presented in Table A.3 for speed of sound and Tables A.4 and A.5 for density ρ. Density of pure n-dodecane was previously measured by several authors and an exhaustive review of available experimental data was carried out by Lemmon and Huber[2] who developed an accurate equation of state for representing thermodynamic properties of n-dodecane under pressure with a claimed uncertainty of 0.2%. The present measurements were only compared to the density calculated from this equation and to the measurement of Valencia et al.[3] that exactly match our experimental conditions up to 60 MPa. It results from these comparisons an Average Absolute Deviation (AAD%) of 0.09% and a Maximum Deviation (MD%) of 0.1% with predictions of Lemmon and Huber equation of state. Moreover, the density difference between the present measurements and the experimental data of Valencia et al. [12] does not exceed 0.08% with an absolute average of 0.03%.

Table.Appendix A.3 Values of speed of sound w and its expanded uncertainty *U(w)* (level of confidence = 0.95, k = 2) at Temperatures T, and Pressures p, and Mole Fraction x_co2 for (Carbon Dioxide + n-Dodecane)

T/K	*p*/MPa	x_{co2}	$w \pm U(w)$/m.s^{-1}		x_{co2}	$w \pm U(w)$/m.s^{-1}		x_{co2}	$w \pm U(w)$/m.s^{-1}	
303.15	10	0	1318.5	1.5	0.2032	1245.6	1.4	0.3989	1152.2	1.1
303.15	20	0	1372.4	1.5	0.2032	1304.1	1.4	0.3989	1214.9	1.3
303.15	30	0	1421.4	1.5	0.2032	1356.4	1.5	0.3989	1272.0	1.4
303.15	40	0	1468.5	1.6	0.2032	1404.4	1.5	0.3989	1323.0	1.4
303.15	50	0	1512.3	1.6	0.2032	1449.9	1.5	0.3989	1370.3	1.4
303.15	60	0	1553.7	1.6	0.2032	1492.5	1.5	0.3989	1414.9	1.4
303.15	70	0	1593.3	1.7	0.2032	1532.6	1.6	0.3989	1456.7	1.5
313.15	10	0	1281.7	1.5	0.2032	1209.7	1.4	0.3989	1114.6	1.3
313.15	20	0	1337.9	1.5	0.2032	1269.6	1.4	0.3989	1180.3	1.3
313.15	30	0	1389.6	1.5	0.2032	1322.9	1.4	0.3989	1238.8	1.3
313.15	40	0	1436.8	1.5	0.2032	1373.3	1.4	0.3989	1291.0	1.4
313.15	50	0	1481.5	1.6	0.2032	1419.2	1.5	0.3989	1339.9	1.4
313.15	60	0	1524.2	1.6	0.2032	1462.4	1.5	0.3989	1385.2	1.4
313.15	70	0	1564.6	1.6	0.2032	1503.9	1.5	0.3989	1427.5	1.4
303.15	10	0.6007	1011.6	1.3	0.7498	845.5	1.3	0.85278	680.5	1.2
303.15	20	0.6007	1084.4	1.2	0.7498	937.0	1.2	0.85278	800.1	1.2
303.15	30	0.6007	1147.4	1.2	0.7498	1010.4	1.2	0.85278	885.8	1.2
303.15	40	0.6007	1204.4	1.3	0.7498	1073.3	1.2	0.85278	955.4	1.1
303.15	50	0.6007	1256.0	1.3	0.7498	1128.9	1.2	0.85278	1015.3	1.1
303.15	60	0.6007	1303.2	1.3	0.7498	1179.5	1.2	0.85278	1068.3	1.1
303.15	70	0.6007	1346.4	1.3	0.7498	1225.4	1.2	0.85278	1116.7	1.2
313.15	10	0.6007	969.6	1.2	0.7498	793.2	1.3	0.85278	630.0	1.2
313.15	20	0.6007	1046.4	1.2	0.7498	893.3	1.2	0.85278	751.2	1.2
313.15	30	0.6007	1112.9	1.2	0.7498	971.4	1.2	0.85278	843.1	1.1
313.15	40	0.6007	1170.9	1.3	0.7498	1037.1	1.2	0.85278	917.2	1.1
313.15	50	0.6007	1224.3	1.3	0.7498	1095.2	1.2	0.85278	979.7	1.1
313.15	60	0.6007	1272.9	1.3	0.7498	1147.0	1.2	0.85278	1034.9	1.1
313.15	70	0.6007	1317.9	1.3	0.7498	1195.2	1.2	0.85278	1084.8	1.1

[a] Standard uncertainties *u* are $u(T) = 0.1$ K, $u(p) = 0.0002p$.

The density data of pure carbon dioxide were compared with the values predicted by the equation of state developed by Span and Wagner.[4] An AAD% of 0.07 % and a MD% of 0.13 % was observed with this equation of state. The density of the binary mixture CO_2 + n-C_{12} was previously investigated by different authors. Ashcroft and Isa[5] first studied the effect of dissolved CO_2 on the density of n-dodecane at atmospheric pressure. Then, Cumicheo et al.[6] measured the density at saturation pressures. Zhang et al.[7] measured the density of this mixture in liquid phase up to 18 MPa. Unfortunately, neither experimental pressure and temperature conditions nor compositions of the investigated mixtures coincide with the present study. Therefore, a triple interpolation of these data had to be conducted for comparison with the present measurements at 313.15 K and 10 MPa. The result shows a good agreement with an average absolute deviation of 0.17 % and a maximum deviation 0.3% over the CO_2 composition range from 0.25 to 0.85. Finally, Zambrano et al.[8] measured the volumetric properties of mixtures ranging from 0.1 to 0.6 CO_2 mole fraction in an extended range of temperature (283.15 to 393.15) K and pressure (10 to 100) MPa. Comparison with these data at 313.15 K shows that our experimental data are significantly higher with an average deviation of about 1.80 % and a maximum deviation of 3.5% corresponding to the mixture with the higher CO_2 content (0.6) as

can be seen in Figure A.1 where density deviations from data reported by different authors are plotted in the same graph at 313.15 and 10 MPa.

Table.Appendix A.4 Values of density ρ and its expanded uncertainty $U(\rho)$ (level of confidence = 0.95, k = 2) at Temperatures T, and Pressures p, and Mole Fraction x_{co2} for (Carbon Dioxide + n-Dodecane)[a]

T / K	p / MPa	x_{co2}	$\rho \pm U(\rho)$ / kg.m^{-3}		x_{co2}	$\rho \pm U(\rho)$ / kg.m^{-3}		x_{co2}	$\rho \pm U(\rho)$ / kg.m^{-3}	
303.15	10	0	748.5	0.8	0.205	756.3	0.7	0.400	767.4	0.6
303.15	20	0	755.1	0.8	0.205	763.6	0.7	0.400	776.3	0.6
303.15	30	0	761.3	0.9	0.205	770.5	0.8	0.400	784.3	0.7
303.15	40	0	766.9	0.9	0.205	776.8	0.8	0.400	791.6	0.7
303.15	50	0	772.0	0.9	0.205	782.5	0.8	0.400	798.2	0.7
303.15	60	0	776.8	0.9	0.205	787.9	0.8	0.400	804.4	0.7
303.15	70	0	781.4	0.9	0.205	793.2	0.8	0.400	810.2	0.7
313.15	10	0	741.6	0.8	0.205	748.8	0.7	0.400	758.7	0.6
313.15	20	0	748.5	0.8	0.205	756.5	0.7	0.400	768.1	0.6
313.15	30	0	754.8	0.8	0.205	763.6	0.7	0.400	776.4	0.6
313.15	40	0	760.8	0.9	0.205	770.3	0.8	0.400	784.2	0.7
313.15	50	0	766.3	0.9	0.205	776.4	0.8	0.400	791.2	0.7
313.15	60	0	771.5	0.9	0.205	782.1	0.8	0.400	797.6	0.7
313.15	70	0	776.4	0.9	0.205	787.4	0.8	0.400	803.6	0.7
303.15	10	0.6008	784.3	0.5	0.7497	802.5	0.5	0.8530	815.6	0.4
303.15	20	0.6008	796.3	0.6	0.7497	820.5	0.5	0.8530	844.1	0.5
303.15	30	0.6008	806.8	0.6	0.7497	835.2	0.5	0.8530	865.6	0.5
303.15	40	0.6008	816.0	0.6	0.7497	847.6	0.5	0.8530	883.1	0.6
303.15	50	0.6008	824.4	0.6	0.7497	858.7	0.5	0.8530	898.1	0.6
303.15	60	0.6008	832.1	0.6	0.7497	868.7	0.6	0.8530	911.4	0.7
303.15	70	0.6008	839.3	0.6	0.7497	878.0	0.6	0.8530	923.3	0.7
313.15	10	0.6008	773.3	0.5	0.7497	786.6	0.5	0.8530	790.9	0.7
313.15	20	0.6008	786.1	0.5	0.7497	806.5	0.5	0.8530	824.1	0.4
313.15	30	0.6008	797.2	0.6	0.7497	822.5	0.5	0.8530	847.6	0.5
313.15	40	0.6008	807.2	0.6	0.7497	836.1	0.5	0.8530	866.6	0.5
313.15	50	0.6008	816.1	0.6	0.7497	848.0	0.5	0.8530	882.5	0.6
313.15	60	0.6008	824.2	0.6	0.7497	858.7	0.5	0.8530	896.4	0.6
313.15	70	0.6008	831.6	0.6	0.7497	868.2	0.5	0.8530	908.7	0.7

[a] Standard uncertainties u are $u(T)$ = 0.05 K, $u(p)$ =0.0002p.

A literature survey reveals that speed of sound of the binary system CO_2 + n-C_{12} are so far inexistent but several measurements were reported for pure n-dodecane under pressure in the same conditions.[9–11] Comparison of the present measurements with literature data leads to an average absolute deviation of 0.07% (MD% = 0.14%) with Boelhouwer[9] , 0.08% (MD% = 0.13%) with Khasanshin an Shchemelev[11] and 0.12% (MD%=0.30%) with Dzida and Cempa.[12] Figure A.2 presents the speed of sound data at a 303.15 K as a function of composition at various pressures whereas Figure A.3 illustrates the volumetric behavior of this binary system at the same temperature over the entire composition range investigated.

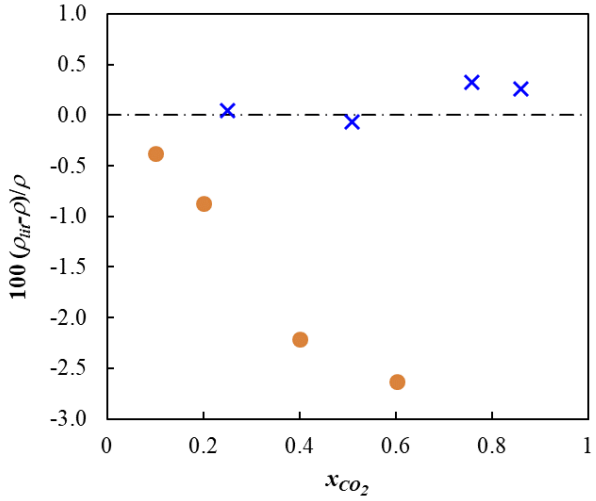

Figure.Appendix A.1 Deviation $100(\rho_{lit} - \rho)/\rho$ of the interpolated literature density value ρ_{lit} from density data reported in Table A.3 as function of a function of mole fraction x_{co2} at temperature T = 313.15 K and pressure P = 10 MPa. ✖, Zhang et al.[7]; ●, Zambrano et al. [8].

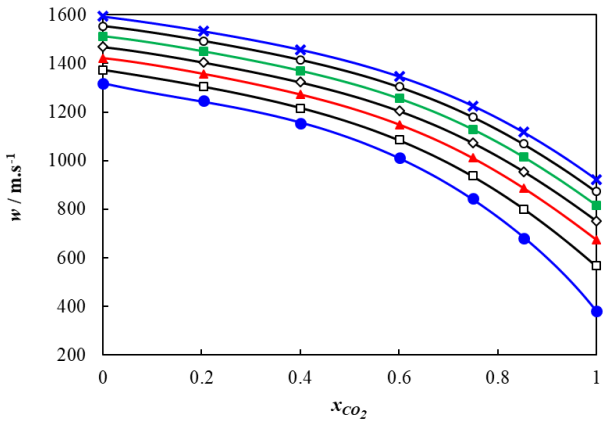

Figure.Appendix A.2 Speed of sound w in the binary system carbon dioxide + n-dodecane as a function of mole fraction x_{co2} at temperature T = 303.15 K and at various pressures p: ●, 10 MPa;. □, 20 MPa; ▲, 30 MPa; ◇, 40 MPa; ■, 50 MPa; O, 60 MPa; ✖, 70 MPa.

To complement our data, speed of sound data of the literature for pure carbon dioxide were added in Figure A.2. These data were obtained from works of Lin and Trusler[13] and Rivas et al.[14] for pressure higher than 20 MPa, with an uncertainty of 0.2%, whereas speed of sound values corresponding to (10 and 20) MPa were estimated by Span and Wagner equation[4] with an uncertainty given by the authors of 1 % in this *P*,*T* range. Comparison of Figures A.2 and C.3 shows an opposite trend with CO_2 mole fraction. Speed of sound monotonically falls as CO_2 content increases whereas density tends to increase with addition of carbon dioxide at this temperature for isobars higher than 10 MPa. This abnormal behavior, related to the high density and high compressibility of carbon dioxide in the studied *P*,*T* range, leads to a negative slope

of $w(\rho)$ isobaric curves as can be noticed in Figure A.4. Speed of sound decreases as the system becomes denser due to CO_2 addition.

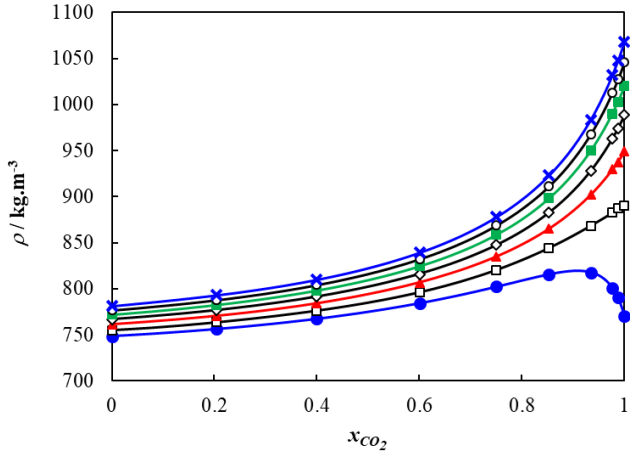

Figure.Appendix A.3 Density ρ in the binary system carbon dioxide + n-dodecane as a function of mole fraction x_{co2} at temperature T = 303.15 K and at various pressures p: ●, 10 MPa;. □, 20 MPa; ▲, 30 MPa; ◇, 40 MPa; ■, 50 MPa; O, 60 MPa; ✖, 70 MPa

Table.Appendix A.5 Values of density ρ and its expanded uncertainty $U(\rho)$ (level of confidence = 0.95, k = 2) at Temperatures T, and Pressures P, and Mole Fraction x_{co2} for the high CO_2 content mixtures of the binary (Carbon Dioxide + n-Dodecane)[a]

T / K	P / MPa	x_{co2}	$\kappa_T \pm U(\kappa_T)$ / GPa^{-1}		x_{co2}	$\kappa_T \pm U(\kappa_T)$ / GPa^{-1}	
303.15	10	0.9348	8.79	0.14	0.9771	17.42	0.37
303.15	20	0.9348	4.56	0.14	0.9771	6.36	0.37
303.15	30	0.9348	3.190	0.066	0.9771	4.11	0.10
303.15	40	0.9348	2.488	0.045	0.9771	3.084	0.059
303.15	50	0.9348	2.053	0.035	0.9771	2.491	0.045
303.15	60	0.9348	1.755	0.029	0.9771	2.099	0.036
303.15	70	0.9348	1.536	0.025	0.9771	1.819	0.031
313.15	10	0.9348	14.74	0.25	0.9771	37.53	0.71
313.15	20	0.9348	5.58	0.25	0.9771	8.33	0.71
313.15	30	0.9348	3.686	0.084	0.9771	4.93	0.12
313.15	40	0.9348	2.809	0.053	0.9771	3.551	0.070
313.15	50	0.9348	2.292	0.041	0.9771	2.798	0.051
313.15	60	0.9348	1.947	0.034	0.9771	2.318	0.040
313.15	70	0.9348	1.698	0.030	0.9771	1.985	0.033
303.15	10	0.9877	21.03	0.42	1	30.56	0.58
303.15	20	0.9877	7.12	0.42	1	8.19	0.12
303.15	30	0.9877	4.45	0.10	1	4.898	0.070
303.15	40	0.9877	3.282	0.064	1	3.534	0.050
303.15	50	0.9877	2.615	0.047	1	2.781	0.040
303.15	60	0.9877	2.182	0.038	1	2.301	0.033
303.15	70	0.9877	1.877	0.032	1	1.967	0.028
313.15	10	0.9877	55.38	0.95	1	123.0	3.1
313.15	20	0.9877	9.55	0.95	1	11.01	0.16
313.15	30	0.9877	5.41	0.14	1	5.945	0.084
313.15	40	0.9877	3.810	0.077	1	4.126	0.059
313.15	50	0.9877	2.958	0.055	1	3.181	0.046
313.15	60	0.9877	2.425	0.043	1	2.599	0.038
313.15	70	0.9877	2.060	0.035	1	2.203	0.032

At the lowest studied pressure the curve $\rho(x_{co2})$ goes through a maximum above 80% of carbon dioxide. This phenomenon corresponds to a significant change of the partial molar properties of the carbon dioxide as a function of molar fraction at this pressure. This maximum is also observed at 313 K, see Figure A.5. It is all the more important at this temperature as pure CO_2 is supercritical in this condition and has a density lower than n-dodecane as can be seen in Figure A.5. Density corresponding to ideal mixture were added in this figure for the purpose of comparing experimental measurement to ideal behavior. This comparison shows a large deviation of volumetric properties from ideal behavior in this particular condition of pressure and temperature. However, it can be observed in this figure that the system behave like an ideal mixture (dash line) at low CO_2 content by considering an apparent density significantly denser ($\rho_{CO2}^{\infty} = 880.2\ kg.m^{-3}$) than pure CO_2 ($\rho_{CO2}^{*} = 628.9\ kg.m^{-3}$).

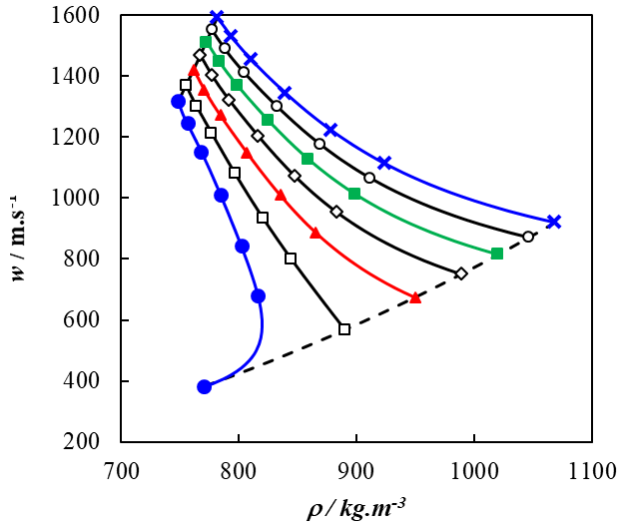

Figure.Appendix A.4 Speed of sound *w* in the binary system carbon dioxide + n-dodecane as a function of Density ρ at temperature T = 303.15 K and at various pressures *p*: ●, 10 MPa;. □, 20 MPa; ▲, 30 MPa; ◇, 40 MPa; ■, 50 MPa; O, 60 MPa; ×, 70 MPa; - - - -, Pure CO_2; _____, Pure n-dodecane.

An uncommon comportment is also observed in Figure A.4 where isobar 10 MPa presents two distinct behaviors corresponding to different signs of the slope of the $w(\rho)$ curve. In such circumstances there is no bijection between density and speed of sound at fixed pressure and temperature, which may be problematic for seismic monitoring.

Finally, it can be observed in Figure A.6 that the vicinity of the critical condition of pure carbon dioxide (304.13 K, 7.38 MPa) profoundly affects the compressibility of the CO_2-rich mixture. A large change in density with respect to pressure is observed between 10 and 20 MPa for isopleths corresponding to mole fractions higher than 80% in CO_2. This effect disappears as the CO_2 content reduces. It follows from this difference of behavior between poor and rich CO_2 mixtures a crossover of isopleths as can be noted in Figure A.6 between (10 and 20) MPa.

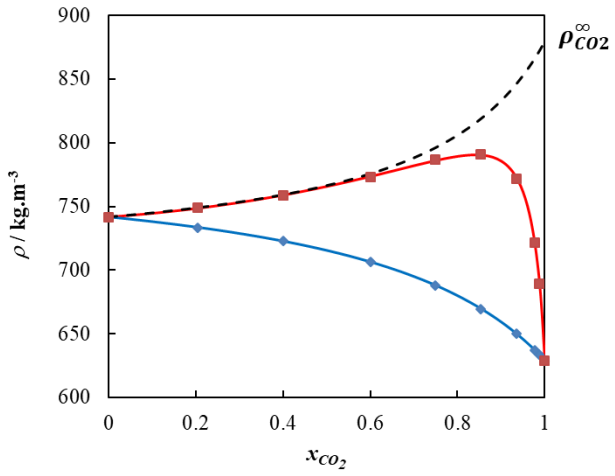

Figure.Appendix A.5 Comparison between ideal and real Density ρ in the binary system carbon dioxide + n-dodecane as a function of mole fraction x_{co2} at temperature T = 313.15 K and pressure P = 10 MPa. ■, measurements; ◆, ideal behavior; .- - - - : ideal solution with an apparent density for CO_2 equal to $M_{CO2}/\bar{v}^{\infty}_{CO2}$.

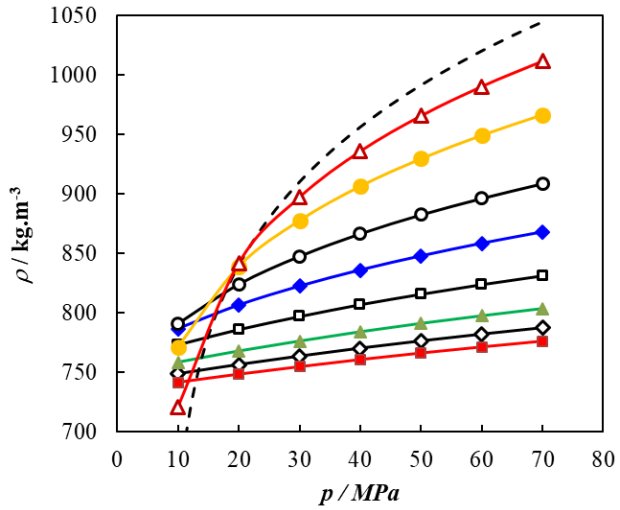

Figure.Appendix A.6 Density ρ in the binary system carbon dioxide + n-dodecane as a function of pressure p at temperature T = 313.15 K and for various CO_2 contents: ■, 0%; ◇, 20%; ▲, 40%; □, 60%; ◆, 75 %; ○, 85%; ●, 93%; ; △: 98 %; - - - , 100%.

A .3 Derivative Properties

Derivative thermodynamic properties were determined from the density and speed of sound data for all mixtures. The isothermal compressibility κ_T of this binary system as well as its expanded uncertainty $U(\kappa_T)$ were first obtained by a numerical differentiation of density data using a computation technique developed in a previous article.[15] This method, based on a Monte Carlo technique with 5000 trials, consists in perturbing randomly the data according to their combined uncertainties. The perturbed data are then fitted with equations of state used randomly, as described below. Finally, the fitted equations are analytically differentiated to compute the compressibility for each of the 5000 trials. The mean and the standard deviation of the resulting compressibility distribution were evaluated to determine both the compressibility and its standard uncertainty in the computation procedure $u_{comp}(\kappa_T)$.

Table.Appendix A.6 Values of isothermal compressibility κ_T and its expanded uncertainty $U(\kappa_T)$ (level of confidence = 0.95, k = 2) at Temperatures T, and Pressures p, and Mole Fraction x_{co2} for (Carbon Dioxide + n-Dodecane)

T / K	P / MPa	x_{co2}	$\kappa_T \pm U(\kappa_T)$ / GPa^{-1}		x_{co2}	$\kappa_T \pm U(\kappa_T)$ / GPa^{-1}		x_{co2}	$\kappa_T \pm U(\kappa_T)$ / GPa^{-1}	
303.15	10	0	0.924	0.028	0.205	1.030	0.033	0.400	1.239	0.035
303.15	20	0	0.834	0.015	0.205	0.929	0.033	0.400	1.088	0.035
303.15	30	0	0.760	0.009	0.205	0.846	0.018	0.400	0.971	0.017
303.15	40	0	0.700	0.010	0.205	0.778	0.011	0.400	0.878	0.010
303.15	50	0	0.648	0.013	0.205	0.720	0.011	0.400	0.802	0.011
303.15	60	0	0.604	0.016	0.205	0.671	0.014	0.400	0.739	0.014
303.15	70	0	0.566	0.018	0.205	0.629	0.017	0.400	0.685	0.016
313.15	10	0	0.974	0.029	0.205	1.097	0.035	0.400	1.324	0.037
313.15	20	0	0.881	0.015	0.205	0.982	0.035	0.400	1.154	0.037
313.15	30	0	0.805	0.009	0.205	0.890	0.018	0.400	1.025	0.017
313.15	40	0	0.741	0.011	0.205	0.814	0.011	0.400	0.923	0.010
313.15	50	0	0.688	0.014	0.205	0.751	0.011	0.400	0.840	0.011
313.15	60	0	0.642	0.016	0.205	0.697	0.014	0.400	0.772	0.014
313.15	70	0	0.602	0.019	0.205	0.651	0.017	0.400	0.714	0.016
303.15	10	0.6008	1.652	0.036	0.7497	2.465	0.036	0.8530	4.177	0.074
303.15	20	0.6008	1.401	0.036	0.7497	1.954	0.036	0.8530	2.863	0.074
303.15	30	0.6008	1.219	0.016	0.7497	1.625	0.020	0.8530	2.220	0.043
303.15	40	0.6008	1.081	0.011	0.7497	1.394	0.016	0.8530	1.831	0.032
303.15	50	0.6008	0.972	0.011	0.7497	1.223	0.013	0.8530	1.566	0.027
303.15	60	0.6008	0.884	0.013	0.7497	1.091	0.012	0.8530	1.373	0.023
303.15	70	0.6008	0.811	0.016	0.7497	0.985	0.015	0.8530	1.226	0.020
313.15	10	0.6008	1.808	0.039	0.7497	2.855	0.042	0.8530	5.29	0.10
313.15	20	0.6008	1.514	0.039	0.7497	2.189	0.042	0.8530	3.29	0.10
313.15	30	0.6008	1.306	0.016	0.7497	1.783	0.022	0.8530	2.450	0.048
313.15	40	0.6008	1.151	0.012	0.7497	1.509	0.020	0.8530	1.977	0.035
313.15	50	0.6008	1.030	0.012	0.7497	1.310	0.015	0.8530	1.669	0.029
313.15	60	0.6008	0.933	0.014	0.7497	1.160	0.012	0.8530	1.450	0.024
313.15	70	0.6008	0.853	0.015	0.7497	1.041	0.014	0.8530	1.285	0.021

According to the difference observed in Figure A.6 between the isopleths of CO_2 rich mixtures (i.e. > 85%) and the other one, distinct equations were considered for fitting the density data according to the CO_2 content. Three simple equations of state proposed respectively by Hudleston[16], Murnaghan[17] and Tammann[18] for describing liquid state were considered for systems with CO_2 content below 85% in mol. Above this concentration, a Benedict-Webb-

Rubin[19] type equation of state involving five parameters was required for representing the high compressibility of the system in these conditions. This equation expresses the compressibility factor of the mixture *Z* of the molar density according to the following expression:

$$Z = 1 + A\rho_m + B\rho_m^2 + E\rho_m^5 + F\rho_m^2(1 + \gamma\rho_m^2)exp(-\gamma\rho_m^2) \qquad (A.1)$$

Table.Appendix A.7 Values of isothermal compressibility κ_T and its expanded uncertainty $U(\kappa_T)$ (level of confidence = 0.95, $k = 2$) at Temperatures *T*, and Pressures *p*, and Mole Fraction x_{co2} for the high CO_2 content mixtures of the binary (Carbon Dioxide + n-Dodecane)

T / K	*P* / MPa	x_{co2}	$\kappa_T \pm U(\kappa_T)$ / GPa^{-1}		x_{co2}	$\kappa_T \pm U(\kappa_T)$ / GPa^{-1}	
303.15	10	0.9348	8.79	0.14	0.9771	17.42	0.37
303.15	20	0.9348	4.56	0.14	0.9771	6.36	0.37
303.15	30	0.9348	3.190	0.066	0.9771	4.11	0.10
303.15	40	0.9348	2.488	0.045	0.9771	3.084	0.059
303.15	50	0.9348	2.053	0.035	0.9771	2.491	0.045
303.15	60	0.9348	1.755	0.029	0.9771	2.099	0.036
303.15	70	0.9348	1.536	0.025	0.9771	1.819	0.031
313.15	10	0.9348	14.74	0.25	0.9771	37.53	0.71
313.15	20	0.9348	5.58	0.25	0.9771	8.33	0.71
313.15	30	0.9348	3.686	0.084	0.9771	4.93	0.12
313.15	40	0.9348	2.809	0.053	0.9771	3.551	0.070
313.15	50	0.9348	2.292	0.041	0.9771	2.798	0.051
313.15	60	0.9348	1.947	0.034	0.9771	2.318	0.040
313.15	70	0.9348	1.698	0.030	0.9771	1.985	0.033
303.15	10	0.9877	21.03	0.42	1	30.56	0.58
303.15	20	0.9877	7.12	0.42	1	8.19	0.12
303.15	30	0.9877	4.45	0.10	1	4.898	0.070
303.15	40	0.9877	3.282	0.064	1	3.534	0.050
303.15	50	0.9877	2.615	0.047	1	2.781	0.040
303.15	60	0.9877	2.182	0.038	1	2.301	0.033
303.15	70	0.9877	1.877	0.032	1	1.967	0.028
313.15	10	0.9877	55.38	0.95	1	123.0	3.1
313.15	20	0.9877	9.55	0.95	1	11.01	0.16
313.15	30	0.9877	5.41	0.14	1	5.945	0.084
313.15	40	0.9877	3.810	0.077	1	4.126	0.059
313.15	50	0.9877	2.958	0.055	1	3.181	0.046
313.15	60	0.9877	2.425	0.043	1	2.599	0.038
313.15	70	0.9877	2.060	0.035	1	2.203	0.032

The values of isothermal compressibility determined in this way as well as the expanded standard uncertainty $U(\kappa_T)$ are listed in Tables A.6 and A.7. This last uncertainty takes into account, with a conventional coverage factor $k_P = 2$ (*Probability* = 95 %), both the combined standard uncertainty in compressibility computation $u_{comp}(\kappa_T)$ and the uncertainty $u_x(\kappa_T)$ caused by mixture preparation and sample purities. Isothermal compressibility of pure n-dodecane was compared with previous reported literature values[3] and with the prediction of the Lemmon and Huber equation of state[11] in the same conditions. The resultant absolute average deviations were 1.9% and 0.9% respectively with maximum deviations of 4.9% and 2.0%. For pure carbon dioxide, the comparison between the present work and value obtained

from Span and Wagner[4] correlation reveal and absolute average deviation of 0.8% with a maximum of 2.3%. All these deviations are consistent with the estimated uncertainties of both sets of values. No literature value was found for comparison with mixtures compressibility.

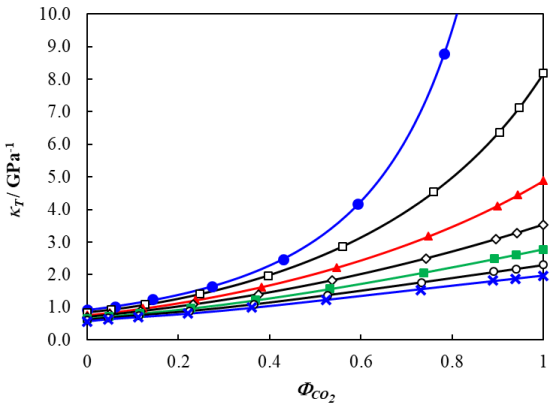

Figure.Appendix A.7 Isothermal compressibility κ_T in the binary system carbon dioxide + n-dodecane as a function of volume fraction $\emptyset_{CO2}$ for different isobars at temperature T = 303.15 K. ●, 10 MPa ; □, 20 MPa ; ▲, 30 MPa ; ◇, 40 MPa ; ■, 50 MPa ; O, 60 MPa ; ×, 70 MPa.

The influence of CO_2 content on this derived volumetric property at 303.15 K was plotted along various isobars in Figure A.7. In this figure the isothermal compressibility is not plotted as a function of mole fraction but as a function of volume fraction $\emptyset_{CO2}$ as the compressibility of an ideal mixture does not varies as a linear function of molar fraction but obeys to the following linear combination :

$$\kappa_T^{id} = \sum_i \emptyset_i \kappa_{T,i}^* \tag{A.2}$$

where the volume fraction $\emptyset_i$ of the *i* component is given by:

$$\emptyset_i = \frac{x_i M_i}{\rho_i^* \sum_k x_k \frac{M_k}{\rho_k^*}} \tag{A.3}$$

A linear behavior is actually observed in Figure A.7 for the highest isobar whereas the behavior significantly departs from linearity for the lowest pressures. Comparison in Figure A.8 of real and ideal isothermal compressibility plotted in the same graphic as a function of volume fraction $\emptyset_{CO2}$ at 10 MPa reveals a large deviation of experimental compressibility data from ideality for both temperatures investigated. Nevertheless, it can be noticed in this figure that isothermal compressibility behaves linearly as a function of volume fraction for low concentrations (below 60% in mol%). The extrapolation of this linear trend to $\emptyset_{CO2} = 1$ leads to a y-intercept significantly different from the compressibility of the pure CO_2. Its value noted $\kappa_{T,CO2}^{\infty}$ is 10 times smaller than pure CO_2 isothermal compressibility at 303 K and 10 MPa and even 30 times smaller at 313 K and 10 MPa.

The speed of sound and density data compiled in Tables A.3 and A.4 for the same conditions of temperature and pressure were used to calculate the isentropic compressibility from the Newton Laplace relation:

$$\kappa_S = \frac{1}{\rho w^2} \tag{A.4}$$

The values of κ_S obtained by this relation over the whole composition range are provided in Table A.8 with their expanded uncertainties. The effect of CO_2 content on this property is presented graphically in Figures A.9 and C.10 for two different conditions 303.15, 70 MPa and 313.15 K, 10 MPa corresponding to the densest and the lightest conditions. As for previous properties, ideal curves were added in these figures so as to compare real to ideal behavior. The way this ideal isentropic compressibility is computed is described in the following paragraph. Comparison of Figures A.9 and A.10 reveals an important contrast between both experimental conditions. At 10 MPa and 313.15 K the experimental isentropic compressibility data departs significantly from the ideal behavior whereas a weak deviation is observed at 303.15 K and 70 MPa between real and ideal curves.

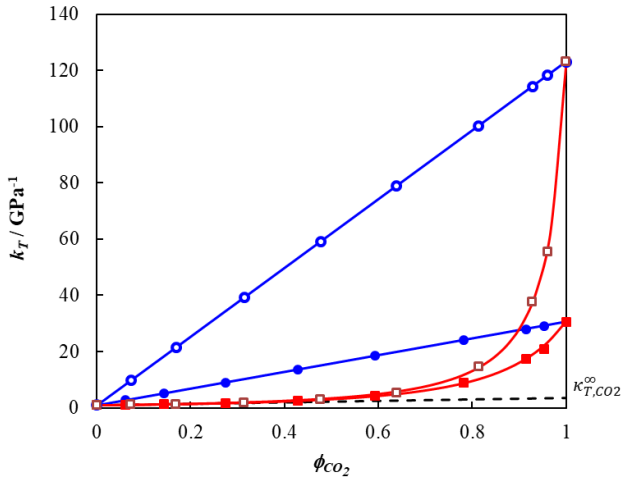

Figure.Appendix A.8 Comparison between ideal and real isothermal compressibility κ_T in the binary system carbon dioxide + n-dodecane as a function of volume fraction $\emptyset_{CO2}$ at pressure P = 10 MPa for different temperatures. ■, measurement at T = 303.15 K, ● ideal behavior at T = 303.15 K; □, measurement at T = 313.15 K, ○ ideal behavior at T = 313.15 K; - - - - , ideal solution with apparent compressibility $\kappa^{\infty}_{T,CO2}$ for CO_2.

As the isentropic compressibility is not merely related to volumetric properties but to energetic and entropic effects, the isentropic compressibility of an ideal mixture cannot be calculated by a simple combination of isentropic compressibility of pure components. In the present work, it was obtained from the thermodynamic equation that related the isentropic to the isothermal compressibility:

$$\kappa_S^{id} = \kappa_T^{id} - \frac{TV_m^{id}(\alpha_p^{id})^2}{C_{pm}^{id}} \quad (A.5)$$

using the following theoretical expressions for molar volume V_m^{id}, isobaric expansion α_p^{id} and molar heat capacity C_{pm}^{id} :

$$V_m^{id} = \sum_i x_i \frac{M_i}{\rho_i^*} \quad (A.6)$$

$$\alpha_P^{id} = \sum_i \emptyset_i \alpha_{p,i}^* \quad (A.7)$$

$$C_{pm}^{id} = \sum_i x_i \frac{M_i(\alpha_{p,i}^*)^2}{\rho_i^*(\kappa_{T,i}^* - \kappa_{S,i}^*)} \quad (A.8)$$

This set of equations is function of four physical quantities ρ_i, $\kappa_{T,i}$, $\kappa_{S,i}$ and $\alpha_{p,i}$, that must be determined for each component. Density and isothermal compressibility of both components were taken from Tables A.4 to A.6. Isentropic compressibility of n-dodecane was obtained from Table A.8 whereas those of pure carbon dioxide were determined from density measurement of Table A.5 and from speed of sound data taken from literature.[4,13,1413, 22-23] Finally, the isobaric expansion of both components was obtained by derivation of density data by a numerical method based on a perturbation Monte Carlo technique similar to those introduced for isothermal compressibility.

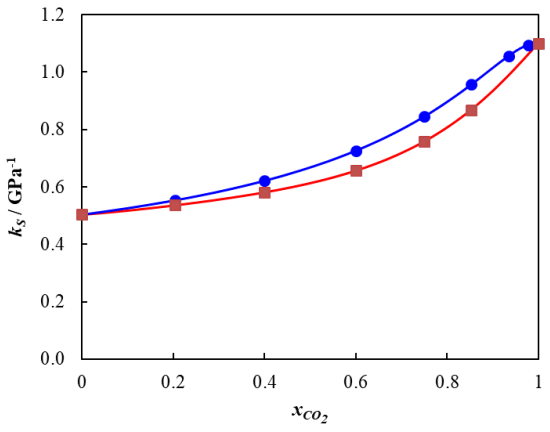

Figure.Appendix A.9 Comparison between ideal and real isentropic compressibility κ_S as a function of mole fraction x_{co2} at temperature T = 303.15 K and pressure P = 70 MPa. ■, measurement , ● ideal behavior.

Table.Appendix A.8 Values of isentropic compressibility κ_S and its expanded uncertainty $U(\kappa_S)$ (level of confidence = 0.95, k = 2) at Temperatures T, and Pressures p, and Mole Fraction x_{co2} for (Carbon Dioxide + n-Dodecane)[a]

T / K	p / MPa	x_{co2}	$\kappa_S \pm U(\rho\kappa_S)$ / GPa^{-1}		x_{co2}	$\kappa_S \pm U(\kappa_S)$ / GPa^{-1}		x_{co2}	$\kappa_S \pm U(\kappa_S)$ / GPa^{-1}	
303.15	10	0	0.7685	0.0019	0.205	0.8523	0.0021	0.400	0.9816	0.0020
303.15	20	0	0.7031	0.0017	0.205	0.7700	0.0018	0.400	0.8728	0.0020
303.15	30	0	0.6501	0.0016	0.205	0.7054	0.0017	0.400	0.7881	0.0018
303.15	40	0	0.6046	0.0015	0.205	0.6527	0.0015	0.400	0.7217	0.0016
303.15	50	0	0.5664	0.0014	0.205	0.6079	0.0014	0.400	0.6671	0.0015
303.15	60	0	0.5333	0.0013	0.205	0.5697	0.0013	0.400	0.6210	0.0014
303.15	70	0	0.5041	0.0012	0.205	0.5367	0.0012	0.400	0.5817	0.0013
313.15	10	0	0.8208	0.0021	0.205	0.9127	0.0022	0.400	1.0609	0.0026
313.15	20	0	0.7464	0.0018	0.205	0.8200	0.0020	0.400	0.9346	0.0022
313.15	30	0	0.6861	0.0017	0.205	0.7484	0.0018	0.400	0.8393	0.0019
313.15	40	0	0.6367	0.0015	0.205	0.6884	0.0016	0.400	0.7652	0.0017
313.15	50	0	0.5945	0.0014	0.205	0.6395	0.0015	0.400	0.7040	0.0016
313.15	60	0	0.5580	0.0013	0.205	0.5979	0.0014	0.400	0.6534	0.0014
313.15	70	0	0.5262	0.0012	0.205	0.5615	0.0013	0.400	0.6107	0.0013
303.15	10	0.6008	1.2460	0.0032	0.7497	1.7432	0.0055	0.8530	2.6479	0.0094
303.15	20	0.6008	1.0680	0.0026	0.7497	1.3881	0.0037	0.8530	1.8506	0.0057
303.15	30	0.6008	0.9414	0.0022	0.7497	1.1729	0.0029	0.8530	1.4723	0.0040
303.15	40	0.6008	0.8448	0.0019	0.7497	1.0241	0.0024	0.8530	1.2407	0.0031
303.15	50	0.6008	0.7689	0.0017	0.7497	0.9138	0.0020	0.8530	1.0801	0.0025
303.15	60	0.6008	0.7076	0.0015	0.7497	0.8275	0.0018	0.8530	0.9615	0.0022
303.15	70	0.6008	0.6573	0.0014	0.7497	0.7584	0.0016	0.8530	0.8685	0.0019
313.15	10	0.6008	1.3754	0.0036	0.7497	2.0207	0.0066	0.8530	3.186	0.012
313.15	20	0.6008	1.1617	0.0028	0.7497	1.5538	0.0043	0.8530	2.1504	0.0069
313.15	30	0.6008	1.0128	0.0023	0.7497	1.2886	0.0032	0.8530	1.6597	0.0046
313.15	40	0.6008	0.9036	0.0020	0.7497	1.1120	0.0026	0.8530	1.3716	0.0034
313.15	50	0.6008	0.8176	0.0018	0.7497	0.9831	0.0022	0.8530	1.1805	0.0028
313.15	60	0.6008	0.7488	0.0016	0.7497	0.8852	0.0019	0.8530	1.0417	0.0024
313.15	70	0.6008	0.6924	0.0015	0.7497	0.8063	0.0017	0.8530	0.9351	0.0021

Additional density measurements, not reported here, were performed to extend the temperature range from (293 to 343) K and the number of experimental points used for describing an isobar before derivation. A polynomial function $\rho(T)$ was used for fitting isobaric data of pure n-dodecane before derivation whereas a polynomial function of type $Z(\rho_m)$ was required for describing CO_2 data and the calculation of the derivatives with respect to temperature. The value of isobaric expansion obtained by such procedure for the pure components are tabulated along with their uncertainties in Table A.9. So as to support the isobaric expansion values obtained through this numerical method, a comparison with literature data[3] and correlation[2,4] predictions was carried out. This comparison reveals an AAD% of 1.2 and a MD% of 3.2 with data reported by Valencia et al.[3] for n-dodecane. Finally, absolute average deviations observed with correlation are 1.7% and 0.7% for n-dodecane[2] and carbon dioxide[4] respectively.

Table.Appendix A.9 Values of isobaric expansion α_P^* and its expanded uncertainty $U(\alpha_P^*)$ (level of confidence = 0.95, k = 2) at Temperatures T, and Pressures p, for pure Carbon Dioxide and n-Dodecane.

T / K	p / MPa	$\alpha_{P,C12}^* \pm U(\alpha_{P,C12}^*)$ / 10^{-3} K^{-1}		$\alpha_{P,CO2}^* \pm U(\alpha_{P,CO2}^*)$ / 10^{-3} K^{-1}	
303.15	10	0.921	0.034	13.40	0.21
303.15	20	0.942	0.035	32.73	0.68
303.15	30	0.860	0.034	5.469	0.081
303.15	40	0.888	0.034	6.399	0.093
303.15	50	0.812	0.033	3.920	0.060
303.15	60	0.846	0.034	4.306	0.063
303.15	70	0.767	0.033	3.217	0.050
313.15	10	0.810	0.034	3.430	0.050
313.15	20	0.739	0.033	2.789	0.045
313.15	30	0.771	0.033	2.917	0.043
313.15	40	0.713	0.032	2.501	0.041
313.15	50	0.740	0.033	2.584	0.039
313.15	60	0.688	0.032	2.284	0.038
313.15	70	0.717	0.033	2.327	0.036

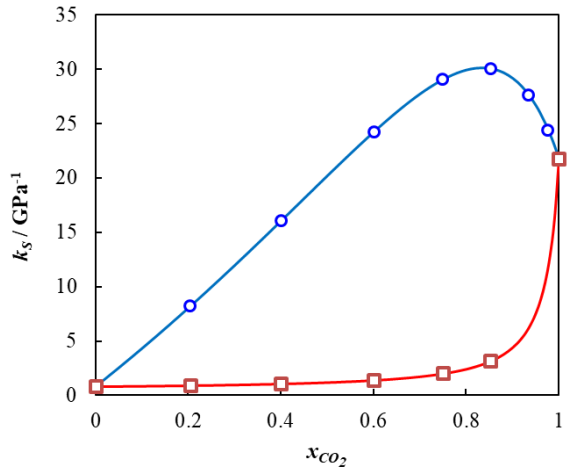

Figure.Appendix A.10 Comparison between ideal and real isentropic compressibility κ_S as a function of mole fraction x_{co2} at temperature T = 313.15 K and pressure P = 10 MPa. □, measurement ; ○, ideal behavior.

A .4 Excess Properties

To highlight the deviation to ideality, excess properties related to molar volume (V_m^E), isothermal compressibility (κ_T^E), isentropic compressibility (κ_S^E) and speed of sound (w^E) were calculated and plotted along different isobars. These quantities are defined as the difference between the actual value of the thermodynamic property considered and its theoretical value corresponding to an ideal solution in the same conditions of composition, temperature and

pressure. Thus, for any property, excess values were obtained indirectly through the calculation of the thermodynamic property corresponding an ideal mixture:

$$y^E = y - y^{id} \tag{A.9}$$

where y represents here either V_m , κ_T , κ_S or w. The formulae selected for calculating ideal molar volume and ideal isothermal and isentropic compressibilities correspond to Eq. A.6, Eq. A.2 and Eq. A.5 respectively whereas the speed of sound in an ideal mixture was calculated indirectly from V_m^{id} and κ_S^{id} using Newton-Laplace equation (Eq.A.4). The values of the excess properties and their corresponding uncertainties are given in Tables A.10 and A.11. The expanded standard uncertainties were calculated by propagating both the uncertainties in measurement and in ideal properties calculations.

Because of the complicated determination of the isentropic compressibility for an ideal mixture, cf. Eq. A.5, the uncertainties in excess isentropic compressibility and consequently in excess speed of sound become significant after propagation of all sources of uncertainties.

Consequently, the relative uncertainty associated to these excess properties turn out to be significant when deviation to ideality become less and less marked. Despite these significant relative uncertainties, the evolution with the mole fraction of the excess properties determined by this method appears regular and smooth (Figures A.11 to A.18). Due to the large difference in amplitude between the diverse isobaric excess curves, they cannot be depicted in the same graph. Therefore, excess properties calculated for 10 MPa were plotted in Figures A.11 to A.14 as a function of composition for both temperatures whereas other isobars are displayed in Figures A.15 to A.18 at only one temperature (303.15 K). The solid curves drawn across the experimental data in all these figures were determined by only interpolating experimental molar volume V_m , speed of sound w and isothermal compressibility κ_T and by calculating all other properties from the interpolation values of these properties.

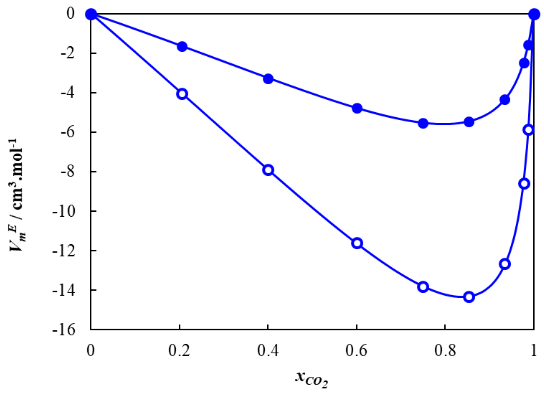

Figure.Appendix A.11 Excess volume V_m^E as a function of mole fraction x_{co2} at pressure P = 10 MPa and at different temperatures. ●, 303.15 K; ○, 313

Table.Appendix A.10 Excess molar volume V_m^E, excess isothermal compressibility κ_T^E, excess isentropic compressibility κ_S^E, excess speed of sound w^E and their expanded uncertainty (level of confidence = 0.95, k = 2) at Temperatures T, and Pressures p, and Mole Fraction x_{co2} for (Carbon Dioxide + n-Dodecane)

T /K	p /MPa	x_{co2}	$V_m^E \pm U(V_m^E)$ / cm^{-3}.mol^{-1}		$\kappa_T^E \pm U(\kappa_T^E)$ GPa^{-1}		$\kappa_S^E \pm U(\kappa_S^E)$ / GPa^{-1}		$w^E \pm U(w^E)$ / m.s^{-1}	
303.15	10	0.205	-1.63	0.28	-1.691	0.055	-1.37	0.10	471	18
303.15	20	0.205	-0.33	0.27	-0.298	0.036	-0.242	0.034	166	19
303.15	30	0.205	0.08	0.27	-0.124	0.020	-0.107	0.022	93	17
303.15	40	0.205	0.24	0.27	-0.061	0.015	-0.059	0.022	60	20
303.15	50	0.205	0.31	0.27	-0.030	0.017	-0.037	0.024	43	26
303.15	60	0.205	0.36	0.26	-0.013	0.021	-0.025	0.027	33	33
303.15	70	0.205	0.34	0.26	-0.003	0.024	-0.017	0.030	26	40
313.15	10	0.205	-4.03	0.28	-8.75	0.23	-7.208	0.383	800	10
313.15	20	0.205	-0.75	0.28	-0.466	0.038	-0.385	0.037	220	16
313.15	30	0.205	-0.18	0.27	-0.184	0.020	-0.150	0.024	115	16
313.15	40	0.205	0.09	0.27	-0.097	0.015	-0.081	0.023	75	19
313.15	50	0.205	0.23	0.27	-0.059	0.017	-0.049	0.025	52	25
313.15	60	0.205	0.30	0.27	-0.038	0.021	-0.032	0.028	39	32
313.15	70	0.205	0.36	0.26	-0.026	0.024	-0.022	0.031	31	39
303.15	10	0.400	-3.27	0.20	-3.934	0.093	-2.94	0.22	570	16
303.15	20	0.400	-0.79	0.20	-0.684	0.040	-0.535	0.050	256	17
303.15	30	0.400	-0.03	0.20	-0.292	0.021	-0.238	0.030	157	16
303.15	40	0.400	0.27	0.19	-0.156	0.015	-0.131	0.027	107	19
303.15	50	0.400	0.44	0.19	-0.092	0.017	-0.083	0.029	80	25
303.15	60	0.400	0.55	0.19	-0.058	0.020	-0.056	0.031	63	31
303.15	70	0.400	0.61	0.19	-0.038	0.023	-0.040	0.034	51	38
313.15	10	0.400	-7.89	0.21	-20.25	0.52	-14.5	1.1	816	10
313.15	20	0.400	-1.53	0.20	-1.076	0.044	-0.852	0.060	323	14
313.15	30	0.400	-0.45	0.20	-0.423	0.021	-0.337	0.033	191	15
313.15	40	0.400	0.03	0.20	-0.227	0.016	-0.180	0.029	130	18
313.15	50	0.400	0.29	0.20	-0.141	0.017	-0.110	0.030	95	23
313.15	60	0.400	0.46	0.19	-0.096	0.021	-0.073	0.033	73	30
313.15	70	0.400	0.57	0.19	-0.070	0.023	-0.051	0.035	59	36
303.15	10	0.6008	-4.75	0.14	-7.40	0.16	-4.78	0.42	543	16
303.15	20	0.6008	-1.16	0.13	-1.258	0.047	-0.904	0.079	282	16
303.15	30	0.6008	-0.12	0.13	-0.525	0.024	-0.400	0.043	186	16
303.15	40	0.6008	0.33	0.13	-0.276	0.018	-0.221	0.036	134	18
303.15	50	0.6008	0.54	0.13	-0.162	0.018	-0.141	0.037	104	23
303.15	60	0.6008	0.68	0.13	-0.101	0.020	-0.097	0.039	85	30
303.15	70	0.6008	0.75	0.13	-0.066	0.022	-0.070	0.042	71	37
313.15	10	0.6008	-11.60	0.16	-37.53	0.96	-21.6	2.2	721	12
313.15	20	0.6008	-2.22	0.13	-1.976	0.058	-1.44	0.10	341	14
313.15	30	0.6008	-0.70	0.13	-0.753	0.027	-0.569	0.049	220	14
313.15	40	0.6008	-0.05	0.13	-0.391	0.020	-0.305	0.040	158	17
313.15	50	0.6008	0.30	0.13	-0.235	0.019	-0.188	0.040	122	22
313.15	60	0.6008	0.50	0.13	-0.154	0.021	-0.125	0.041	97	28
313.15	70	0.6008	0.64	0.13	-0.108	0.022	-0.090	0.043	82	34
303.15	10	0.7497	-5.54	0.11	-11.18	0.25	-6.00	0.63	433	17
303.15	20	0.7497	-1.355	0.086	-1.797	0.059	-1.15	0.11	239	16
303.15	30	0.7497	-0.204	0.085	-0.721	0.034	-0.501	0.060	164	15
303.15	40	0.7497	0.275	0.084	-0.369	0.026	-0.272	0.049	121	18
303.15	50	0.7497	0.498	0.084	-0.213	0.021	-0.172	0.048	96	23
303.15	60	0.7497	0.627	0.083	-0.133	0.020	-0.119	0.050	81	29
303.15	70	0.7497	0.684	0.083	-0.088	0.022	-0.087	0.052	69	36
313.15	10	0.7497	-13.80	0.13	-56.35	1.5	-25.1	3.3	562	14
313.15	20	0.7497	-2.499	0.088	-2.830	0.079	-1.84	0.15	281	14
313.15	30	0.7497	-0.815	0.086	-1.032	0.040	-0.715	0.071	189	14
313.15	40	0.7497	-0.114	0.085	-0.523	0.031	-0.379	0.055	141	16
313.15	50	0.7497	0.241	0.084	-0.311	0.024	-0.231	0.052	111	21
313.15	60	0.7497	0.436	0.084	-0.205	0.021	-0.153	0.052	90	27
313.15	70	0.7497	0.572	0.083	-0.146	0.022	-0.111	0.053	78	32
303.15	10	0.8530	-5.450	0.091	-14.32	0.35	-6.15	0.79	294	17
303.15	20	0.8530	-1.196	0.059	-2.09	0.10	-1.15	0.15	166	16
303.15	30	0.8530	-0.138	0.060	-0.799	0.057	-0.492	0.078	118	15
303.15	40	0.8530	0.257	0.061	-0.393	0.042	-0.265	0.061	90	18
303.15	50	0.8530	0.435	0.062	-0.216	0.035	-0.169	0.058	74	22
303.15	60	0.8530	0.533	0.063	-0.125	0.030	-0.118	0.059	64	27
303.15	70	0.8530	0.583	0.063	-0.073	0.027	-0.089	0.061	58	34
313.15	10	0.8530	-14.33	0.14	-73.6	2.0	-24.8	4.3	399	18
313.15	20	0.8530	-2.243	0.060	-3.39	0.13	-1.86	0.20	193	14
313.15	30	0.8530	-0.625	0.059	-1.205	0.067	-0.706	0.093	134	14
313.15	40	0.8530	0.015	0.060	-0.606	0.048	-0.373	0.069	104	16
313.15	50	0.8530	0.337	0.061	-0.358	0.038	-0.225	0.063	84	20
313.15	60	0.8530	0.519	0.062	-0.233	0.033	-0.149	0.061	70	25
313.15	70	0.8530	0.638	0.063	-0.161	0.029	-0.109	0.061	63	30

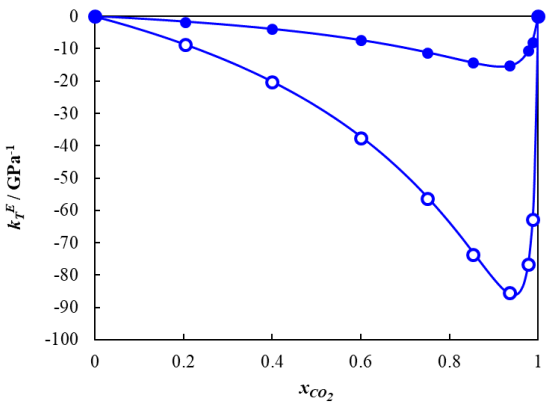

Figure.Appendix A.12 Excess isothermal compressibility κ_T^E as a function of mole fraction x_{co2} at pressure P = 10 MPa and at different temperatures T. ●, 303.15 K; ○, 313.15 K.

It can be seen in Figure A.11 that the system shows a large negative deviation from ideality at both investigated temperatures indicating a drastic contraction caused by mixing. The excess volumes curves are asymmetric implying a contraction all the more significant than CO_2 mole fraction is higher. As pressure increases, this behavior disappears and the excess molar volume becomes small and positive. Deviation to ideality is more prominent in the compressibility plot (Figures A.12, A.13, A.16 and A.17) for which negative excess value become very important as pressure decreases. Negative excess values were observed for both the isothermal and isentropic compressibility over the entire temperature and pressure ranges investigated.

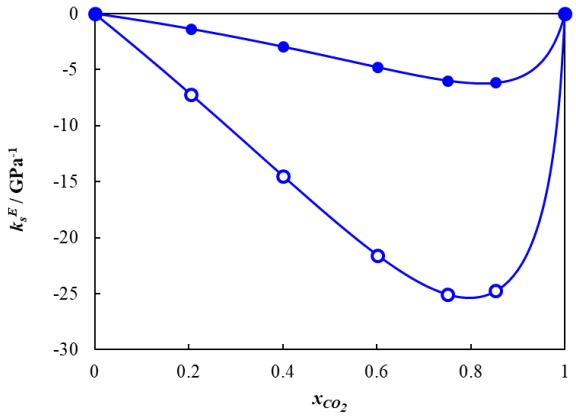

Figure.Appendix A.13 Excess isentropic compressibility κ_S^E as a function of mole fraction x_{co2} at pressure P = 10 MPa and at different temperatures T. ●, 303.15 K; ○, 313.15 K..

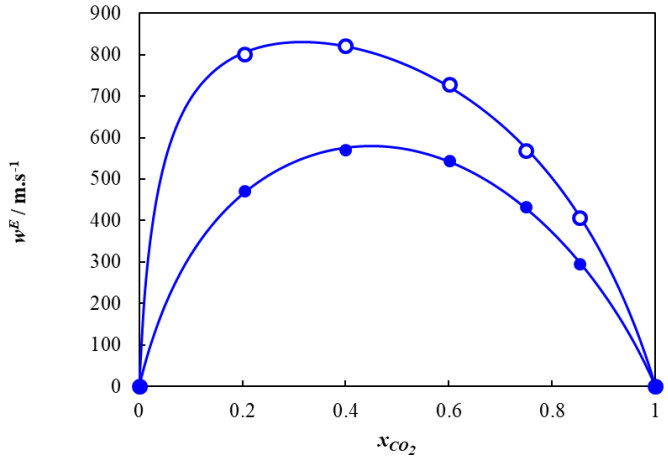

Figure.Appendix A.14 Excess speed of sound w^E as a function of mole fraction x_{co2} at pressure P = 10 MPa and at different temperatures T. ●, 303.15 K; ○, 313.15 K..

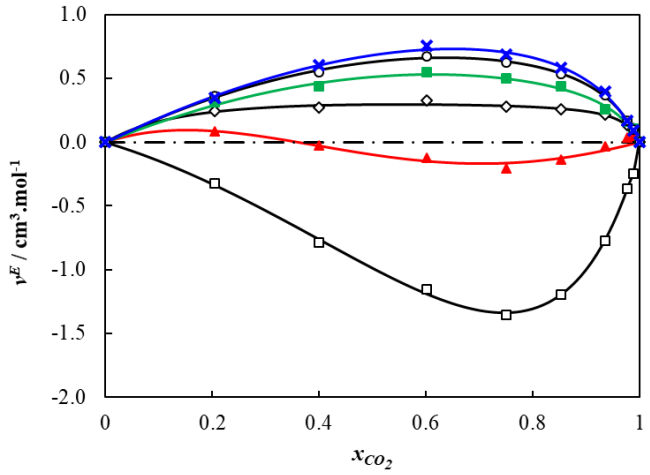

Figure.Appendix A.15 Excess volume V_m^E as a function of mole fraction x_{co2} at temperature T = 303.15 K and at various pressures p. □, 20 MPa ; ▲, 30 MPa ; ◇, 40 MPa ; ■, 50 MPa ; ○, 60 MPa ; ×, 70 MPa.

The excess compressibility curves present an acute asymmetry partly caused by the significant difference of compressibility between pure carbon dioxide and n-dodecane. This asymmetry is reduced when adopting a relative representation of excess property as shown in Figure A.19. It can be noticed from this figure that deviation to ideality can be ten times higher than the value of the compressibility itself at 10 MPa. The magnitude of excess compressibilities decreases with pressure increase from (20 to 70) MPa. The extent of the deviation is linked to the compressibility contrast between the pure and the apparent compressibility of CO_2 at infinite dilution in n-dodecane. It also leads to a drastic effect on speed of sound for which relative deviation can reach 60 % of the actual speed of sound.

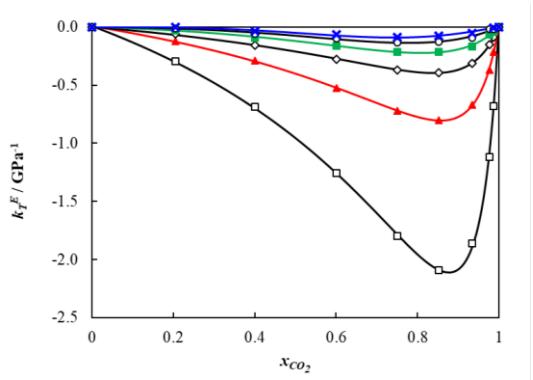

Figure.Appendix A.16 Excess isothermal compressibility κ_T^E as a function of mole fraction x_{co2} at temperature T = 303.15 K and at various pressures p. □, 20 MPa ; ▲, 30 MPa ; ◇, 40 MPa ; ■ 50 MPa ; ○, 60 MPa ; ×, 70 MPa.

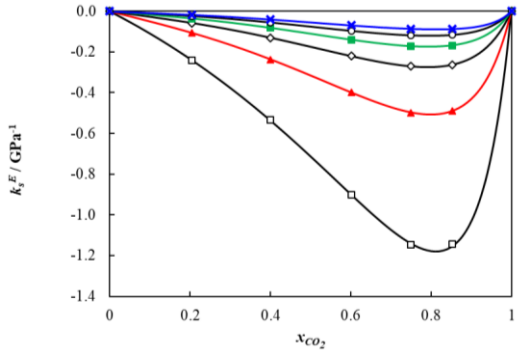

Figure.Appendix A.17 Excess isentropic compressibility κ_S^E as a function of mole fraction x_{co2} at temperature T = 303.15 K and at various pressures p. □, 20 MPa ; ▲, 30 MPa ; ◇, 40 MPa ; ■ 50 MPa ; ○, 60 MPa ; ×, 70 MPa.

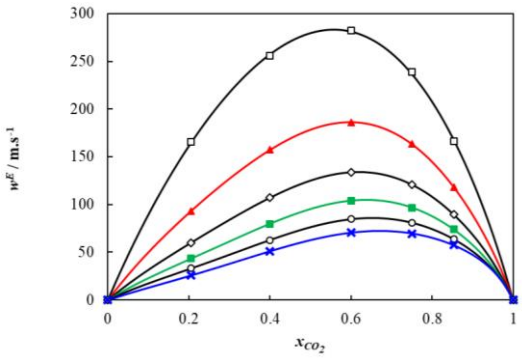

Figure.Appendix A.18 Excess speed of sound w^E as a function of mole fraction x_{co2} at temperature T = 303.15 K and at various pressures p. □, 20 MPa ; ▲, 30 MPa ; ◇, 40 MPa ; ■ 50 MPa ; ○, 60 MPa ; ×, 70 MPa

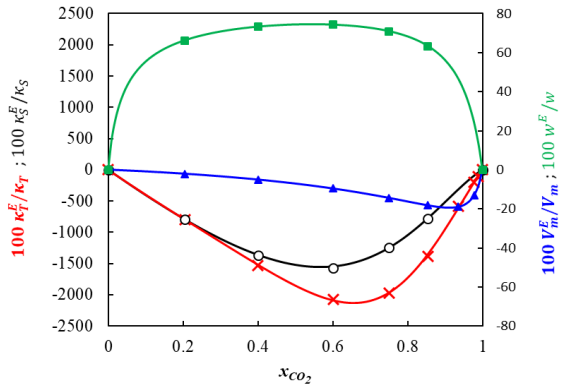

Figure.Appendix A.19 Relative excess properties in the binary system carbon dioxide + n-dodecane as a function of mole fraction x_{co2} at temperature T = 313.15 K and pressure p. ▲, 30 $100\ V_m^E/V_m$; ■ 50 $100\ w^E/w$; ×, $100\ \kappa_T^E/\kappa_T$. ; ○, $100\ \kappa_S^E/\kappa_S$.

Table.Appendix A.11 Excess molar volume V_m^E, excess isothermal compressibility κ_T^E and their expanded uncertainty (level of confidence = 0.95, k = 2) at Temperatures T, and Pressures p for the high CO_2 content mixtures of the binary (Carbon Dioxide + n-Dodecane)

T / K	p / MPa	x_{co2}	$V_m^E \pm U(V_m^E)$ / cm^3.mol^{-1}		$\kappa_T^E \pm U(\kappa_T^E)$ / GPa^{-1}		x_{co2}	$V_m^E \pm U(V_m^E)$ / cm^3.mol^{-1}		$\kappa_T^E \pm U(\kappa_T^E)$ / GPa^{-1}	
303.15	10	0.9348	-4.344	0.088	-15.32	0.47	0.9771	-2.47	0.10	-10.61	0.64
303.15	20	0.9348	-0.772	0.040	-1.86	0.16	0.9771	-0.368	0.034	-1.12	0.38
303.15	30	0.9348	-0.032	0.038	-0.667	0.084	0.9771	0.035	0.033	-0.37	0.11
303.15	40	0.9348	0.217	0.038	-0.315	0.059	0.9771	0.132	0.033	-0.153	0.074
303.15	50	0.9348	0.256	0.038	-0.168	0.046	0.9771	0.158	0.033	-0.062	0.057
303.15	60	0.9348	0.371	0.038	-0.094	0.038	0.9771	0.168	0.033	-0.017	0.047
303.15	70	0.9348	0.394	0.038	-0.053	0.033	0.9771	0.167	0.033	0.007	0.040
313.15	10	0.9348	-12.67	0.14	-85.5	2.5	0.9771	-8.60	0.18	-76.7	2.9
313.15	20	0.9348	-1.577	0.043	-3.08	0.28	0.9771	-0.746	0.039	-1.75	0.73
313.15	30	0.9348	-0.429	0.039	-0.998	0.11	0.9771	-0.193	0.033	-0.51	0.14
313.15	40	0.9348	-0.017	0.038	-0.460	0.069	0.9771	-0.019	0.032	-0.228	0.088
313.15	50	0.9348	0.173	0.038	-0.244	0.053	0.9771	0.066	0.032	-0.121	0.065
313.15	60	0.9348	0.264	0.038	-0.138	0.044	0.9771	0.102	0.032	-0.071	0.053
313.15	70	0.9348	0.323	0.038	-0.079	0.038	0.9771	0.131	0.033	-0.044	0.044
303.15	10	0.9877	-1.59	0.11	-8.13	0.69					
303.15	20	0.9877	-0.246	0.034	-0.68	0.43					
303.15	30	0.9877	0.049	0.031	-0.21	0.12					
303.15	40	0.9877	0.104	0.031	-0.088	0.079					
303.15	50	0.9877	0.103	0.031	-0.039	0.060					
303.15	60	0.9877	0.101	0.031	-0.016	0.049					
303.15	70	0.9877	0.094	0.031	-0.004	0.042					
313.15	10	0.9877	-5.85	0.21	-62.8	3.1					
313.15	20	0.9877	-0.439	0.039	-0.95	0.96					
313.15	30	0.9877	-0.109	0.032	-0.26	0.16					
313.15	40	0.9877	-0.004	0.031	-0.123	0.095					
313.15	50	0.9877	0.036	0.031	-0.077	0.070					
313.15	60	0.9877	0.051	0.031	-0.057	0.056					
313.15	70	0.9877	0.066	0.031	-0.046	0.047					

A .5 Partial Molar Volume

The partial molar quantities are key thermodynamic properties for studying non ideal behavior of binary mixtures as their values refer to an individual constituent in its surrounding solution. Of particular interest are the partial molar volumes. They indicate how the components are integrated in a mixture. They can be determined from derivation of density measurements according to the following relations:

$$V_{CO2} = V_m + (1 - x_{CO2}) \left(\frac{\partial V_m}{\partial x_{CO2}}\right)_{p,T} \quad \text{(A.10)}$$

$$V_{C12} = V_m - x_{CO2} \left(\frac{\partial V_m}{\partial x_{CO2}}\right)_{p,T} \quad \text{(A.11)}$$

where derivatives of molar volume with respect to mole fraction were determined by first fitting the molar volume data by a Padé approximant of order 2/3:

$$V_m = \frac{a_0 + a_1 x_{CO2} + a_2 x_{CO2}^2}{1 + b_1 x_{CO2} + b_2 x_{CO2}^2 + b_3 x_{CO2}^3} \quad \text{(A.12)}$$

whose coefficients are listed in Table A.12. The results obtained for V_{CO2} and V_{C12} at 303.15 K

Table.Appendix A.12 Coefficients of 2/3 Padé Approximant (Eq. A.12) for Correlating Molar Volume V_m as a Function of Mole Fraction x_{co2} at Fixed temperature *T* and Pressure *p*.

T / K	*p* / MPa	a_0 / $m^3.kmol^{-1}$	a_1 / $m^3.kmol^{-1}$	a_2 / $m^3.kmol^{-1}$	b_1	b_2	b_3
303.15	10	0.227590	-0.393429	0.169186	-0.942555	0.001203	0
303.15	20	0.225582	-0.360510	0.144792	-0.811115	0.010726	0
303.15	30	0.223733	-0.128498	-0.038074	0.213170	0.018392	0
303.15	40	0.222133	-0.397690	0.175983	-0.995445	0.005001	0
303.15	50	0.220723	-0.398587	0.177864	-1.009916	0.009920	0
303.15	60	0.219277	-0.380508	0.164220	-0.936265	0.007287	0
303.15	70	0.217969	-0.370250	0.156774	-0.897189	0.006240	0
313.15	10	0.229661	-0.398441	0.170725	-0.960442	0.032997	-0.044760
313.15	20	0.227572	-0.377694	0.157103	-0.874076	0.007248	0
313.15	30	0.225667	-0.330066	0.120694	-0.674681	0.011474	0
313.15	40	0.223876	0.689837	-0.688355	3.866870	0.025153	0
313.15	50	0.222292	-0.385904	0.166428	-0.940189	0.003564	0
313.15	60	0.220807	-0.381092	0.163603	-0.928378	0.005246	0
313.15	70	0.219417	-0.375554	0.160079	-0.912264	0.005783	0

Concerning the partial molar volume of n-dodecane, it can be seen in Figure A.20 that for pressure higher than 30 MPa, V_{CO2} slightly drops as CO_2 mole fraction increases. V_{CO2} is higher than V_{CO2}^{*} at these pressures, reflecting that CO_2 appears less dense when it is surrounded by n-dodecane molecules than in pure conditions. This result is in agreement with the positive excess volume observed at these pressures, see Figure A.15. At lower pressures, V_{CO2} first decreases and then increases to reach V_{CO2}^{*}. In these conditions V_{CO2}^{∞} is lower than V_{CO2}^{*}. Consequently, the carbon dioxide appears much denser than pure CO_2 at infinite dilution under low pressure. For example, the ratio $V_{CO2}^{*}/V_{CO2}^{\infty}$ calculated at 313.15 K and 10 MPa reaches the value 1.4 at 10 MPa. This value is in agreement with the apparent density estimated from Figure A.5.

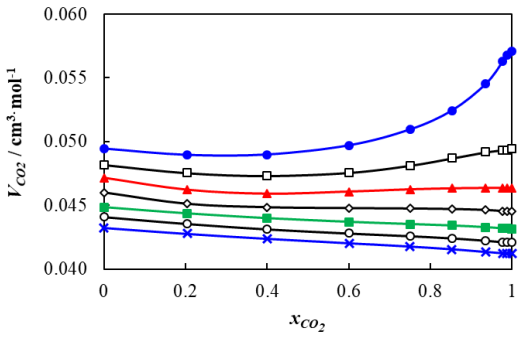

Figure.Appendix A.20 Partial molar volume of carbon dioxide V_{CO2} in the binary system Carbon Dioxide + n-Dodecane as a function of mole fraction x_{CO2} for different isobars at temperature T = 303.15 K. ●, 10 MPa ; □, 20 MPa ; ▲, 30 MPa ; ◇, 40 MPa ; ■, 50 MPa ; ○, 60 MPa ; ×, 70 MPa.

Concerning the molar volume of n-dodecane, it can be seen in Figure A.21 that, whatever the pressure, the partial molar volume of n-dodecane V_{C12} remain steady up to 60% of carbon dioxide meaning that n-dodecane does not seem to be affected by the presence of CO_2 in this composition range. Beyond this range, addition of carbon dioxide causes either an increase or decrease depending of the pressure range. The highest isobars, i.e. above 30 MPa, increases at high CO_2 content so that V_{C12} becomes greater than the molar volume of pure n-dodecane V_{C12}^{*}. Therefore, in such conditions, an addition of an infinitesimal amount of n-dodecane in CO_2 leads to an expansion of the mixture which is higher than for an ideal mixture. On the opposite, the lowest isobars, i.e. below 30 MPa, decreases at high CO_2 content leading to a crossover of isobars between 80 and 90 % in Figure A.21. V_{C12} drastically reduces at 10 MPa for high molar proportions of CO_2 leading to a partial molar volume of n-dodecane much lower than its pure molar volume V_{C12}^{*}. The fall in n-dodecane partial molar volume is so pronounced at 313 K and 10 MPa that V_{C12} reaches a negative value in these conditions as shown in Figure A.22. This phenomenon already observed for toluene[20], naphthalene[21] and n-heptane[11] implies the intersection of $V_{CO2}(x_{CO2})$ and $V_{C12}(x_{CO2})$ curves for high values of x_{CO2}. At the intersection point, the partial molar volumes of both components are equal $(V_{CO2} = V_{C12})$ and take the same value than the molar volume as:

$$V_m = x_{CO2}V_{CO2} + (1 - x_{CO2})V_{C12} = V_{CO2} \quad \text{(A.13)}$$

Consequently, at this specific point, the three curves $V_m\,(x_{CO2})$, $V_{CO2}(x_{CO2})$ and $V_{C12}(x_{CO2})$ intersect as can be observed in Figure A.23. Moreover, at this particular point, the molar volume passes through a minimum as its derivative with respect to mole fraction becomes null:

$$\left(\frac{\partial V_m}{\partial x_{CO2}}\right)_{p,T} = \frac{V_{CO2} - V_m}{1 - x_{CO2}} = 0 \quad \text{(A.14)}$$

A negative value of the partial molar volume of solute n-dodecane at infinite dilution in carbon dioxide indicates that an insertion of n-dodecane in CO_2 contracts the systems. The derivative of pressure with respect to solute mole number n_{C12} at constant volume V is negative as :

$$\left(\frac{\partial p}{\partial n_{C12}}\right)_{T,V} = \frac{V_{C12}}{V\kappa_T} < 0 \quad \text{(A.15)}$$

Therefore, in such conditions, an addition of n-dodecane in a fixed total volume of CO_2 reduces the pressure of the overall system. The mixture has a lower overall volume than carbon dioxide alone. This uncommon contraction phenomenon can be interpreted in the light of fluctuation theory**.**

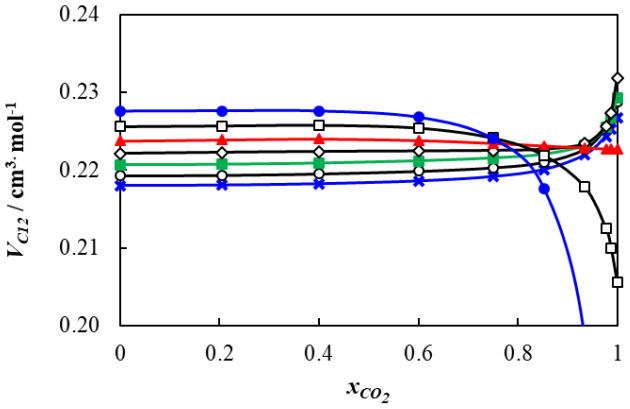

Figure.Appendix A.21 Partial molar volume of n-dodecane V_{C12} in the binary system carbon dioxide + n-dodecane as a function of mole fraction x_{CO2} for different isobars at temperature T = 303.15 K. ●, 10 MPa ; □, 20 MPa ; ▲, 30 MPa ; ◇, 40 MPa ; ■, 50 MPa ; ○, 60 MPa ; ×, 70 MPa

Such effect is quantified by means of a cluster size $\xi_{cluster}$ corresponding to an average number of CO_2 molecules surrounding one solute molecule at infinite dilution. According to the statistical mechanical theory of solutions of Kirkwood and Buff[22], this quantity can be estimated [23] from volumetric measurements as follows:

$$\xi_{cluster} = \frac{RT\kappa^*_{T,CO2}}{V^*_{CO2}} - \frac{V^\infty_{C12}}{V^*_{CO2}} \quad \text{(A.16)}$$

where V^∞_{C12} corresponds to the partial molar volume at infinite dilution.

This peculiar behavior that leads to deviation from a linear behavior of molar volume with respect to mole fraction requires a careful approach for calculating this property from density measurements. For that purpose, additional density measurements were carried out for CO_2 compositions ranging from 93% to 99% as well as in pure carbon dioxide (Table A.5). The partial molar at infinite dilution V_{C12}^{∞} was obtained from extrapolation of these measurements to infinite dilution. The results are plotted in Figure A.24 as a function of pressure at 313.15 K. From the value obtained for V_{C12}^{∞} and from the application Eq. A.16, a cluster size of 17 was determined for the particular condition 313 K and 10 MPa. Such value, higher than those calculated in the same condition for the binary mixture CO_2 + n-heptane[1] ($\xi_{cluster} = 8$) reveals that CO_2 clustering effect increases with increasing the carbon chain length of the solute for a given thermodynamic state. This result in turn further suggests that excess properties in such CO_2 + n-alkane binary systems increase with the chain length of the n-alkane. This conclusion is illustrated in Figure A.25 where excess molar volume and speed of sound of both CO_2 + n-C_7[1] and CO_2 + n-C_{12} are compared.

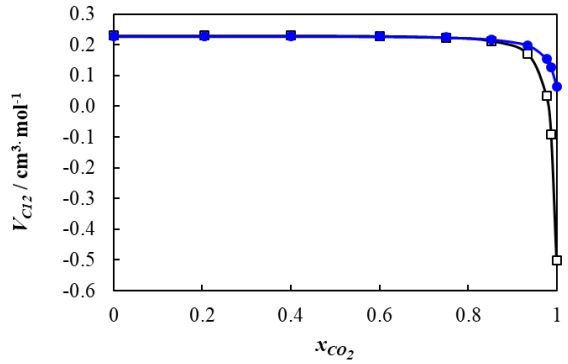

Figure.Appendix A.22 Partial molar volume of n-dodecane V_{C12} in the binary system carbon dioxide + n-dodecane as a function of mole fraction x_{CO2} at pressure P = 10 MPa for different temperatures T. ●, 303.15 K ; □, 313.15 K.

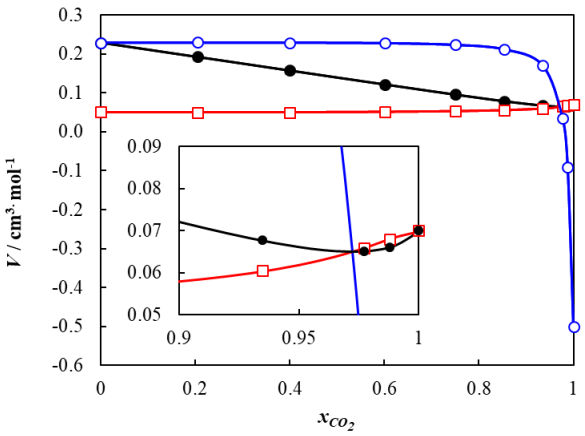

Figure.Appendix A.23 Molar volume V_m , partial molar volumes of carbon dioxide V_{CO2} and n-dodecane V_{C12} in the binary system carbon dioxide + n-dodecane as a function of mole fraction x_{CO2} at temperature T = 313.15 K and pressure P = 10 MPa. ●, V_m ; □, V_{CO2}; ○, V_{C12}.

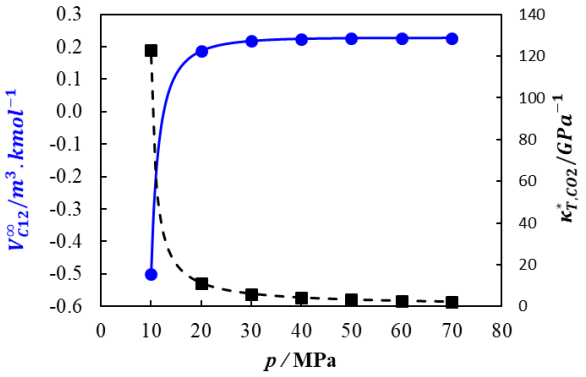

Figure.Appendix A.24 Cross-plot of partial molar volumes of n-dodecane at infinite dilution in carbon dioxide V_{C12}^{∞} in the binary system carbon dioxide + n-dodecane and isothermal compressibility of pure carbon dioxide $\kappa_{T,CO2}^{*}$as a function of pressure p. ●, V_{C12}^{∞} ; ■, $\kappa_{T,CO2}^{*}$.

It should be noticed that the partial molar volume of n-dodecane at infinite dilution in carbon dioxide was previously determined by Spicka et al. [33] who reported data at 313.15 K and at various pressures from (8 to 28) MPa obtained indirectly from supercritical fluid chromatography. Comparison of the present values (-0.501 and 0.187 $m^3.kmol^{-1}$) with reported data[22] (-1.15 and -0.11 $m^3.kmol^{-1}$) at (10 and 20) MPa do not exhibit a good match. The difference is significant and the trend is even opposite at 20 MPa as can be observed in Figure A.26 where the slope of the experimental molar volume versus mole fraction calculated from data of Spicka et al.[22] using Eq. A.14 is plotted in the same graph than the experimental molar volume. The compressibility of pure carbon dioxide was added in Figure A.24 so as to observed a cross-plot of the solvent compressibility $\kappa_{T,CO2}^{*}$ and the partial molar volume at infinite dilution V_{C12}^{∞}. This cross-plot suggests a strong (anti-)correlation between the partial molar volume at infinite dilution and the isothermal compressibility of solvent. In order to highlight such correlation between partial molar volume and fluid compressibility, the partial molar volumes determined for both temperatures up to 30 MPa (the pressure corresponding to the limit of negative excess volumes conditions) was represented in Figure A.27 as a function of the fluid isothermal compressibility. In this graph all the experiments superpose following a master curve of quasi-linear shape. This result confirms the strong correlation between partial molar volume and isothermal compressibility and suggests that the deviation to ideality is related to the high compressibility of the system near the critical conditions of carbon dioxide.

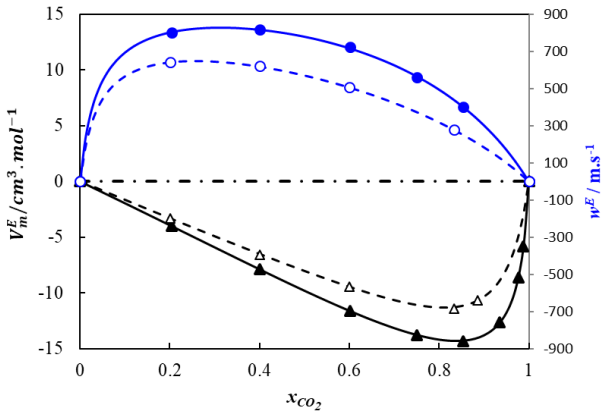

Figure.Appendix A.25 Comparison between CO_2 + n-C_7 [1] and CO_2 + n-C_{12} excess properties. △, V_m^E of CO_2 + n-C_7; ▲, V_m^E of CO_2 + n-C_{12} ; ○, w^E of CO_2 + n-C_7 ; ●, w^E of CO_2 + n-C_{12}

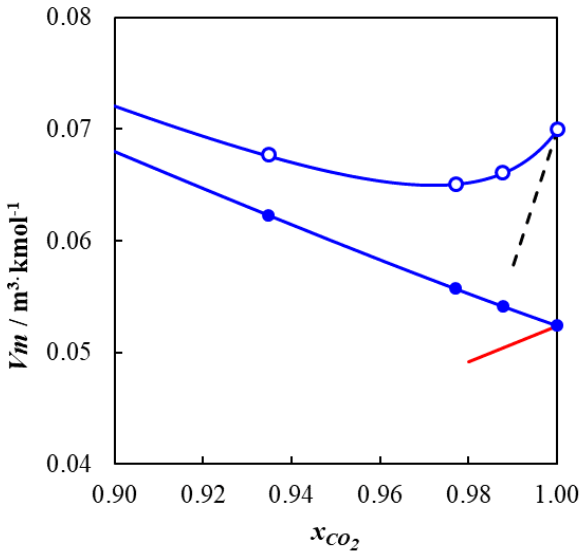

Figure.Appendix A.26 Molar volume V_m in the binary system carbon dioxide + n-dodecane as a function of mole fraction x_{CO2} at temperature T = 313.15 K and different pressures p. ○, 10 MPa; ●, 20 MPa ; - - - -, slope calculated from data of Spicka et al. [33] at 10 MPa ; ————, slope calculated from data of Spicka et al. [33] at 20 MPa ;

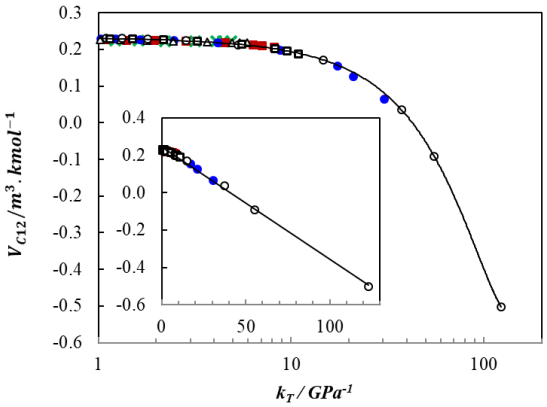

Figure.Appendix A.27 Partial molar volumes of n-dodecane V_{C12} in the binary system carbon dioxide + n-dodecane as a function of fluid isothermal compressibilityκ_T for various condition of temperature T and pressure p. ●, T = 303.15 K and P = 10 MPa ; O, T = 313.15 K and P = 10 MPa ; ■, T = 303.15 K and P = 20 MPa ; □, T = 313.15 K and P = 20 MPa ; ×, T = 303.15 K and p = 30 MPa ; △, T = 313.15 K and P = 30 MPa ;————, master curve.

A .6 Conclusion

In this work, speed of sound and density measurements have been performed on carbon dioxide and n-dodecane binary mixtures at two temperatures (303 and 313 K) and at pressures from 10 to 70 MPa. Measurements were achieved on pure n-decane and five different mixtures with a CO_2 content varying from 20% to 85 % in mole. Such system has been chosen because of its interest to mimic CO_2 enhanced oil recovery systems. The choice of the thermodynamic conditions was guided by the idea of evaluating the expected influence of the proximity of the critical point of CO_2 on the non-idealities of the studied mixture. In addition, by comparison with a similar work on carbon dioxide – n-heptane mixture[1], this work allows to evaluate the effect of the chain length on the non-idealities.

Regarding the measured properties, i.e. density and speed of sound, it has been noticed that the speed of sound monotonically falls as CO_2 content increases at T=303.15K whereas density tends to increase with addition of carbon dioxide at this temperature for isobars higher than 10 MPa. This abnormal behavior is related to the high density and high compressibility of carbon dioxide in the studied thermodynamic conditions. At the lowest pressure studied, i.e. 10 MPa, density goes through a maximum at high CO_2 content at both temperatures, indicating a significant change of the partial molar properties of CO_2 in such conditions.

Compressibilities (isothermal and isentropic) were deduced from density and speed of sound measurements. Both emphasize the large deviations from the ideal behavior for both temperatures investigated at the lowest pressure, P =10 MPa, i.e. for the conditions the closest to the critical point of CO_2. On the contrary, for the highest pressures studied here, P =70 MPa, only a weak deviation from ideality was observed.

All these results were confirmed by analysing the excess properties. It has been noticed that excess molar volume, excess isothermal and isentropic compressibilities and excess sound velocities are largest the lowest pressure, i.e. P = 10 MPa, and high CO_2 content.

To better understand such non ideal behavior, partial molar volumes have been computed. Results reflect that CO_2 appears less dense when it is surrounded by n-dodecane molecules than in pure conditions for high pressures conditions (above 30 MPa), whereas this is the contrary at the lowest pressure. In other words, at P =10 MPa , a small addition of n-dodecane in a fixed total volume of CO_2 reduces the pressure of the overall system. This behavior was interpreted as the macroscopic manifestation of a microscopic clustering of CO_2 around n-dodecane at high CO_2 content, as already noticed on CO_2 + n-heptane mixture but in an amplified manner. This result suggests that clustering in such CO_2 + n-alkane binary systems, and consequently excess properties, increases with the chain length of the n-alkane.

Another interesting results is that it has been noticed that there exists a strong correlation between partial molar volume and isothermal compressibility of the studied mixtures for both temperatures up to 30 MPa. This suggests that the deviation to ideality is related to the high compressibility (or more precisely the asymmetry in compressibilities between CO_2 and n-dodecane) of the system near the critical conditions of carbon dioxide.

A .7 References

(1) Bazile, D. N. J.-P.; Hamani, A. W. S.; and J.-L. Daridon, G. G. "Excess Volume, Isothermal Compressibility, Isentropic Compressibility and Speed of Sound of Carbon Dioxide + n-Heptane Binary Mixture under Pressure up to 70 MPa. *Exp. Meas. J. Supercrit. Fluids* 2018, *140*, 218–232.

(2) Lemmon, E. W.; Huber, M. L. Thermodynamic Properties of N-Dodecane. *Energy Fuels* 2004, *18* (4), 960–967.

(3) Valencia, J. L.; González-Salgado, D.; Troncoso, J.; Peleteiro, J.; Carballo, E.; Romaní, L. Thermophysical Characterization of Liquids Using Precise Density and Isobaric Heat Capacity Measurements As a Function of Pressure. *J. Chem. Eng. Data* 2009, *54* (3), 904–915.

(4) Span, R.; Wagner, W. A New Equation of State for Carbon Dioxide Covering the Fluid Region from the Triple-Point Temperature to 1100 K at Pressures up to 800 MPa. *J. Phys. Chem. Ref. Data* 1996, *25* (6), 1509–1596.

(5) Ashcroft, S. J.; Isa, M. B. Effect of Dissolved Gases on the Densities of Hydrocarbons. *J. Chem. Eng. Data* 1997, *42* (6), 1244–1248.

(6) Cumicheo, C.; Cartes, M.; Segura, H.; Müller, E. A.; Mejía, A. High-Pressure Densities and Interfacial Tensions of Binary Systems Containing Carbon Dioxide+n-Alkanes: (N-Dodecane, n-Tridecane, n-Tetradecane). *Fluid Phase Equilibria* 2014, *380*, 82–92.

(7) Zhang, Y.; Liu, Z.; Liu, W.; Zhao, J.; Yang, M.; Liu, Y.; Wang, D.; Song, Y. Measurement and Modeling of the Densities for CO2 + Dodecane System from 313.55 K to 353.55 K and Pressures up to 18 MPa. *J. Chem. Eng. Data* 2014, *59* (11), 3668–3676.

(8) Zambrano, J.; Gómez-Soto, F. V.; Lozano-Martín, D.; Martín, M. C.; Segovia, J. J. Volumetric Behaviour of (Carbon Dioxide+hydrocarbon) Mixtures at High Pressures. *J. Supercrit. Fluids* 2016, *110*, 103–109.

(9) Boelhouwer, J. W. M. Sound Velocities in and Adiabatic Compressibilities of Liquid Alkanes at Various Temperatures and Pressures. *Physica* 1967, *34* (3), 484–492.
(10) Takagi, T.; Teranishi, H. Ultrasonic Speeds and Thermodynamics for Binary Solutions of N-Alkanes under High Pressures. *Fluid Phase Equilibria* 1985, *20*, 315–320.
(11) Khasanshin, T. S.; Samuilov, V. S.; Shchemelev, A. P. The Sound Velocity in Liquid Binary Mixtures of N-Alkanes. *High Temp.* 2009, *47* (4), 527–532.
(12) Dzida, M.; Cempa, M. Thermodynamic and Acoustic Properties of (Heptane+dodecane) Mixtures under Elevated Pressures. *J. Chem. Thermodyn.* 2008, *40* (10), 1531–1541.
(13) Lin, C.-W.; Trusler, J. P. M. Speed of Sound in (Carbon Dioxide + Propane) and Derived Sound Speed of Pure Carbon Dioxide at Temperatures between (248 and 373) K and at Pressures up to 200 MPa. *J. Chem. Eng. Data* 2014, *59* (12), 4099–4109.
(14) Rivas, C.; Gimeno, B.; Artal, M.; Blanco, S. T.; Fernández, J.; Velasco, I. High-Pressure Speed of Sound in Pure CO2 and in CO2 with SO2 as an Impurity Using Methanol as a Doping Agent. *Int. J. Greenh. Gas Control* 2016, *54*, 737–751.
(15) Daridon, J.-L.; Bazile, J.-P. Computation of Liquid Isothermal Compressibility from Density Measurements: An Application to Toluene. *J. Chem. Eng. Data* 2018, *63* (6), 2162–2178.
(16) Hudleston, L. J. Intermolecular Forces of Normal Liquids. *Trans. Faraday Soc.* 1937, *33* (0), 97–103.
(17) Murnaghan, F. D. The Compressibility of Media under Extreme Pressures. *Proc. Natl. Acad. Sci.* 1944, *30* (9), 244–247.
(18) Tammann, G. Ueber Die Abhängigkeit Der Volumina von Lösungen Vom Druck. *Z. Für Phys. Chem.* 1895, *17U* (1), 620–636.
(19) Benedict, M.; Webb, G. B.; Rubin, L. C. An Empirical Equation for Thermodynamic Properties of Light Hydrocarbons and Their Mixtures II. Mixtures of Methane, Ethane, Propane, and n-Butane. *J. Chem. Phys.* 1942, *10*, 747–758.
(20) Chang, C. J.; Randolph, A. D. Solvent Expansion and Solute Solubility Predictions in Gas-Expanded Liquids. *AIChE J.* 1990, *36* (6), 939–942.
(21) Eckert, C. A.; Ziger, D. H.; Johnston, K. P.; Ellison, T. K. The Use of Partial Molal Volume Data to Evaluate Equations of State for Supercritical Fluid Mixtures. *Fluid Phase Equilibria* 1983, *14*, 167–175.
(22) Kirkwood, J. G.; Buff, F. P. The Statistical Mechanical Theory of Solutions. I. *J. Chem. Phys.* 1951, *19* (6), 774–777.
(23) Debenedetti, P. G. Clustering in Dilute, Binary Supercritical Mixtures: A Fluctuation Analysis. *Chem. Eng. Sci.* 1987, *42* (9), 2203–2212.

Appendix B . Experimental Measurements and Molecular Simulations Data of n-C_6 + n-C_{12}.

Contents

B .1 Experimental Measurement data 160
B .1 .1 Density Measurement data 160
B .1 .2 Experimental Isothermal Compressibility data 163
B .1 .3 Experimental Speed of sound data 163
B .1 .4 Experimental viscosity data 165
B .2 Molecular Simulation Results 170
B .2 .1 Molecular Simulation Density Results 170
B .2 .2 Isothermal Compressibility 172
B .2 .3 Molecular Simulation Results of Viscosity 174
B .3 References 175

Introduction

In this appendix, are provided the experimental measurements and molecular simulations data of thermophysical properties of the binary mixture n-hexane + n-dodecane used in chapter 4. In section B.1, we present the experimental data of density, isothermal compressibility, speed of sound and viscosity. Then, section B.2 depicts molecular simulation data of density, isothermal compressibility and viscosity for both MCCG and TraPPE-ua force fields.

B .1 Experimental Measurement Data

B .1 .1 Density Measurement Data

Table B.1 presents the experimental density data of pure n-hexane and n-dodecane and four binary mixtures of these components at percentage mole fractions of 20, 40, 60 and 80 % of n-hexane. Measurements were carried out along four isotherms spaced at 20 K intervals in the temperature range of 293.15-353.15 K at pressures ranging from 0.1 to 100 MPa by steps of 10 MPa. Along with experimental data of density, we presented the corresponding expanded standard deviations with the conventional coverage factor $k_P = 2$ (*Probability* = 95 %) estimated from the working equations , according to the GUM of NIST [1] (cf. section 2.4)

Liquid densities of n-hexane, n-dodecane and their binary mixtures were previously measured under pressure and/or correlated by several authors[2–6]. When compared to literature data, our density measurements are shown to be in good agreement as can be seen on Figures B.1 and B.2 for pure n-hexane and n-dodecane, respectively.

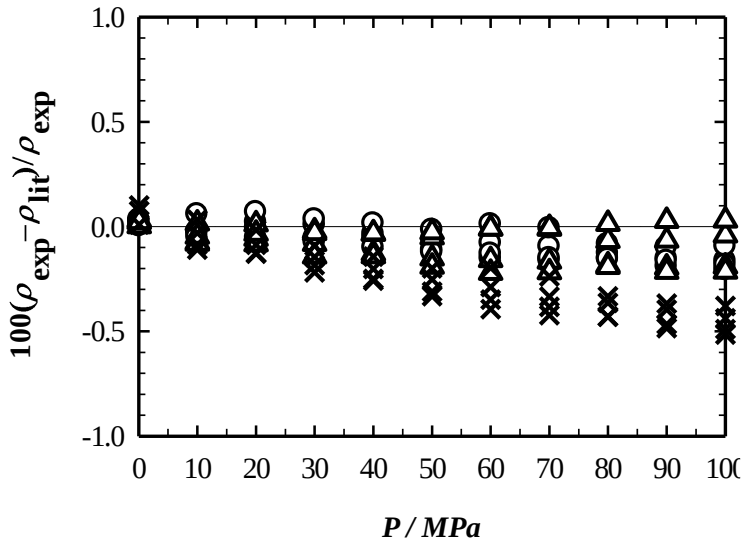

Figure.Appendix B.1 Deviations of our experimental density data of n-hexane with those from ○: Cibulka et al. [2]; △: Assael et al.[3] and data from ×:REFPROP [4]

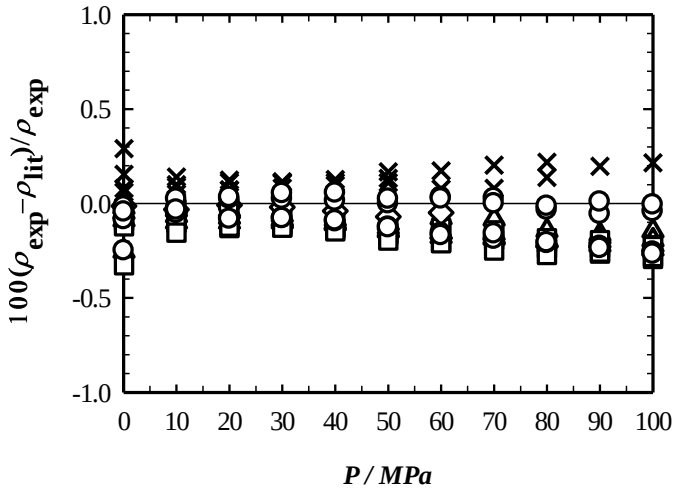

Figure.Appendix B.2 Deviations of our density data of n-dodecane with data from ○: Cibulka et al.[2], △: Assael et al.[3]; □: Caudwell et al. [5]; ◇: Bazile et al. [6] and ×: REFPROP [4].

Table.Appendix B.1 Experimental density data for the binary mixtures n-hexane + n-dodecane

T/K	P/MPa	ρ + U_c(ρ)											
		$kg.m^{-3}$											
x_{n-C6}/mol%		0		20		40		60		80		100	
293.15	0.10	748.28	0.24	738.21	0.22	725.16	0.24	710.23	0.24	688.66	0.24	659.43	0.24
293.15	10.00	755.58	0.24	745.34	0.23	732.77	0.24	718.30	0.24	697.56	0.24	668.85	0.24
293.15	20.00	762.00	0.24	751.80	0.23	739.41	0.24	725.53	0.24	705.26	0.24	677.78	0.24
293.15	30.00	767.55	0.24	757.74	0.23	745.62	0.24	731.83	0.24	712.25	0.24	685.47	0.24
293.15	40.00	772.99	0.24	763.24	0.23	751.35	0.24	737.82	0.24	718.56	0.24	692.28	0.24
293.15	50.00	778.04	0.24	768.54	0.23	756.70	0.24	743.49	0.25	724.54	0.25	698.64	0.25
293.15	60.00	782.74	0.24	773.29	0.23	761.60	0.25	748.64	0.25	729.91	0.25	704.60	0.25
293.15	70.00	787.19	0.25	777.67	0.23	766.27	0.25	753.50	0.25	735.83	0.25	710.15	0.25
293.15	80.00	791.48	0.25	782.14	0.23	770.82	0.25	758.27	0.25	740.04	0.25	715.26	0.25
293.15	90.00	795.64	0.25	786.31	0.24	775.07	0.25	762.67	0.25	744.57	0.25	720.11	0.26
293.15	100.00	799.48	0.25	790.21	0.24	779.13	0.25	766.86	0.25	749.05	0.26	724.80	0.26
313.15	0.10	734.20	0.24	723.69	0.25	710.25	0.25	694.56	0.25	672.27	0.26	641.30	0.23
313.15	10.00	741.50	0.25	730.92	0.24	718.25	0.24	703.17	0.24	681.90	0.24	652.10	0.23
313.15	20.00	748.27	0.25	738.09	0.24	725.79	0.24	711.12	0.24	690.46	0.24	662.08	0.24
313.15	30.00	754.74	0.25	744.70	0.24	732.50	0.24	718.44	0.24	698.29	0.24	670.46	0.24
313.15	40.00	760.65	0.24	750.79	0.24	738.92	0.24	724.97	0.24	705.21	0.24	678.32	0.24
313.15	50.00	765.99	0.24	756.43	0.24	744.55	0.24	731.41	0.25	711.60	0.25	685.10	0.24
313.15	60.00	770.96	0.24	761.55	0.24	750.07	0.25	737.13	0.25	717.71	0.25	691.41	0.24
313.15	70.00	776.02	0.25	766.61	0.25	755.26	0.25	742.34	0.25	723.71	0.25	697.46	0.25
313.15	80.00	780.40	0.25	771.25	0.25	760.15	0.25	747.25	0.25	728.68	0.25	703.25	0.25
313.15	90.00	784.66	0.25	775.69	0.25	764.79	0.25	752.10	0.25	733.63	0.25	708.34	0.25
313.15	100.00	788.72	0.25	779.98	0.25	769.14	0.25	756.52	0.25	738.45	0.26	713.29	0.26
333.15	0.10	719.29	0.23	708.62	0.24	694.27	0.24	678.02	0.24	655.53	0.24	622.26	0.24
333.15	10.00	727.98	0.24	718.35	0.24	703.82	0.24	688.47	0.24	665.54	0.24	635.67	0.25
333.15	20.00	735.51	0.24	726.31	0.24	712.39	0.24	697.36	0.24	675.52	0.24	646.99	0.25
333.15	30.00	742.40	0.24	733.40	0.24	719.79	0.24	705.49	0.24	684.12	0.24	656.56	0.26
333.15	40.00	748.71	0.24	739.76	0.24	726.57	0.24	712.73	0.24	691.91	0.24	665.11	0.24
333.15	50.00	754.54	0.24	745.62	0.24	732.90	0.24	719.32	0.25	698.70	0.25	672.75	0.24
333.15	60.00	760.36	0.25	751.99	0.24	739.33	0.25	725.73	0.25	705.71	0.25	680.08	0.24
333.15	70.00	765.56	0.25	757.29	0.25	744.98	0.25	731.43	0.25	711.85	0.25	686.55	0.25
333.15	80.00	770.06	0.25	761.86	0.25	749.74	0.25	736.69	0.25	717.16	0.25	692.15	0.25
333.15	90.00	774.59	0.25	766.39	0.25	754.39	0.25	741.55	0.25	722.41	0.26	697.76	0.25
333.15	100.00	779.18	0.25	771.20	0.25	759.05	0.26	746.51	0.26	727.37	0.26	703.17	0.26
353.15	0.10	702.97	-	-	-	-	-	-	-	-	-	-	-
353.15	10.00	713.52	0.24	703.00	0.24	688.81	0.24	672.89	0.24	649.18	0.24	617.70	0.25
353.15	20.00	722.19	0.25	711.58	0.24	698.26	0.24	682.92	0.24	660.11	0.24	630.61	0.26
353.15	30.00	729.79	0.25	719.49	0.24	706.71	0.24	692.01	0.24	669.85	0.24	641.47	0.26
353.15	40.00	736.66	0.24	726.83	0.24	714.14	0.24	700.01	0.24	678.47	0.24	650.89	0.24
353.15	50.00	742.76	0.24	733.14	0.24	721.12	0.24	707.22	0.24	685.96	0.25	659.30	0.24
353.15	60.00	748.68	0.24	739.42	0.24	727.09	0.25	713.63	0.25	693.14	0.25	666.97	0.25
353.15	70.00	754.03	0.25	745.14	0.25	733.02	0.25	719.65	0.25	699.76	0.25	673.90	0.25
353.15	80.00	759.16	0.25	750.38	0.25	738.76	0.25	725.54	0.25	705.62	0.25	680.38	0.25
353.15	90.00	764.27	0.25	755.50	0.25	743.78	0.25	731.03	0.25	711.42	0.26	686.39	0.26
353.15	100.00	768.84	0.25	760.17	0.25	748.79	0.25	736.15	0.26	716.62	0.26	691.93	0.26

B .1 .2 Experimental Isothermal Compressibility Data

Table B.2 presents isothermal compressibility data obtained by applying the derivation procedure presented in section 2.5.

Table.Appendix B.2 Experimental isothermal compressibility of the binary mixtures n-hexane + n-dodecane

T/K	P/MPa	$\kappa_T + U_c(\kappa_T)$											
		GPa^{-1}											
x_{n-c6}/mol%		0		20		40		60		80		100	
293.15	0.10	1.01	0.02	1.02	0.02	1.10	0.02	1.20	0.02	1.36	0.02	1.59	0.03
293.15	10.00	0.89	0.01	0.91	0.01	0.97	0.01	1.05	0.01	1.18	0.01	1.35	0.01
293.15	20.00	0.80	0.01	0.83	0.01	0.87	0.01	0.94	0.01	1.05	0.01	1.18	0.01
293.15	30.00	0.73	0.00	0.75	0.00	0.80	0.00	0.85	0.00	0.94	0.00	1.05	0.00
293.15	40.00	0.67	0.00	0.70	0.00	0.73	0.00	0.78	0.00	0.86	0.00	0.95	0.00
293.15	50.00	0.62	0.00	0.65	0.00	0.68	0.00	0.72	0.00	0.79	0.00	0.87	0.00
293.15	60.00	0.59	0.00	0.61	0.00	0.63	0.00	0.67	0.00	0.73	0.00	0.80	0.01
293.15	70.00	0.55	0.00	0.57	0.00	0.60	0.01	0.63	0.01	0.68	0.01	0.74	0.01
293.15	80.00	0.52	0.01	0.54	0.01	0.56	0.01	0.60	0.01	0.64	0.01	0.69	0.01
293.15	90.00	0.50	0.01	0.51	0.01	0.54	0.01	0.57	0.01	0.60	0.01	0.65	0.01
293.15	100.00	0.48	0.01	0.49	0.01	0.51	0.01	0.54	0.01	0.57	0.01	0.62	0.01
313.15	0.10	1.08	0.02	1.12	0.02	1.22	0.02	1.36	0.02	1.54	0.03	1.88	0.03
313.15	10.00	0.97	0.01	1.01	0.01	1.08	0.01	1.19	0.01	1.33	0.01	1.57	0.01
313.15	20.00	0.88	0.01	0.91	0.01	0.98	0.01	1.07	0.01	1.18	0.01	1.35	0.01
313.15	30.00	0.80	0.00	0.84	0.00	0.89	0.00	0.96	0.00	1.05	0.00	1.19	0.00
313.15	40.00	0.74	0.00	0.77	0.00	0.82	0.00	0.88	0.00	0.96	0.00	1.07	0.00
313.15	50.00	0.69	0.00	0.72	0.00	0.76	0.00	0.81	0.00	0.88	0.00	0.97	0.00
313.15	60.00	0.64	0.00	0.67	0.01	0.71	0.00	0.75	0.00	0.81	0.00	0.89	0.01
313.15	70.00	0.60	0.00	0.63	0.01	0.66	0.01	0.70	0.01	0.75	0.01	0.82	0.01
313.15	80.00	0.57	0.01	0.59	0.01	0.62	0.01	0.65	0.01	0.71	0.01	0.76	0.01
313.15	90.00	0.53	0.01	0.56	0.01	0.59	0.01	0.61	0.01	0.66	0.01	0.71	0.01
313.15	100.00	0.51	0.01	0.52	0.00	0.56	0.01	0.58	0.01	0.63	0.01	0.67	0.01
333.15	0.10	1.27	0.02	1.42	0.02	1.48	0.02	1.65	0.03	1.78	0.03	2.58	0.04
333.15	10.00	1.11	0.01	1.20	0.01	1.28	0.01	1.40	0.01	1.53	0.01	2.01	0.02
333.15	20.00	0.99	0.01	1.05	0.01	1.13	0.01	1.22	0.01	1.34	0.01	1.65	0.01
333.15	30.00	0.89	0.00	0.94	0.00	1.01	0.00	1.08	0.00	1.19	0.00	1.41	0.00
333.15	40.00	0.81	0.00	0.85	0.00	0.91	0.00	0.98	0.00	1.07	0.00	1.23	0.00
333.15	50.00	0.75	0.00	0.78	0.00	0.83	0.00	0.89	0.00	0.97	0.00	1.09	0.00
333.15	60.00	0.70	0.00	0.72	0.00	0.77	0.00	0.82	0.00	0.89	0.00	0.99	0.01
333.15	70.00	0.65	0.01	0.67	0.01	0.71	0.01	0.76	0.01	0.82	0.01	0.90	0.01
333.15	80.00	0.61	0.01	0.63	0.01	0.66	0.01	0.70	0.01	0.76	0.01	0.83	0.01
333.15	90.00	0.58	0.01	0.60	0.01	0.62	0.01	0.66	0.01	0.71	0.01	0.77	0.01
333.15	100.00	0.55	0.01	0.57	0.01	0.59	0.01	0.62	0.01	0.66	0.01	0.71	0.01
353.15	0.10	1.60	0.03	-	-	-	-	-	-	-	-	-	-
353.15	10.00	1.32	0.01	1.32	0.02	1.48	0.02	1.63	0.02	1.84	0.03	2.39	0.02
353.15	20.00	1.13	0.01	1.16	0.01	1.27	0.01	1.39	0.01	1.55	0.02	1.91	0.01
353.15	30.00	0.99	0.00	1.04	0.01	1.11	0.01	1.21	0.01	1.35	0.01	1.60	0.00
353.15	40.00	0.89	0.00	0.94	0.00	1.00	0.00	1.08	0.00	1.19	0.00	1.38	0.00
353.15	50.00	0.81	0.00	0.86	0.00	0.91	0.00	0.97	0.00	1.07	0.00	1.22	0.00
353.15	60.00	0.75	0.00	0.80	0.00	0.83	0.00	0.89	0.00	0.98	0.01	1.09	0.01
353.15	70.00	0.70	0.01	0.74	0.01	0.77	0.01	0.82	0.01	0.89	0.01	0.99	0.01
353.15	80.00	0.66	0.01	0.69	0.01	0.72	0.01	0.77	0.01	0.83	0.01	0.90	0.01
353.15	90.00	0.62	0.01	0.65	0.01	0.68	0.01	0.72	0.01	0.77	0.01	0.83	0.01
353.15	100.00	0.59	0.01	0.61	0.01	0.64	0.01	0.68	0.01	0.72	0.01	0.78	0.01

B .1 .3 Experimental Speed of Sound Data

In this section, are listed in the Table B.3, the experimental speed of sound data of the binary mixture composed of n-hexane + n-dodecane at percentage mole fractions of 0, 20, 40, 60, 80 and 100% of n-hexane. Measurements were carried out along four isotherms spaced at 20 K

intervals in the temperature range of 293.15-353.15 K at pressures ranging from 0.1 to 100 MPa by steps of 10 MPa. To validate our measurements, the results of pure compounds were compared to data reported by other authors in the literature. For n-hexane, as shown in Figure B.3, our data are in very good agreement with data provided by Boelhouwer [7] and Daridon et al. [8] with absolute deviations not greater than 0.07%. However, we observed more important absolute deviations with Ball and Trusler [9] at atmospheric pressure (up to 1%). For n-dodecane, our data match very well with those provided by Boelhouwer [7], Kasanshin and Shchemelev [10] and Plantier et al. [11] with an AAD around 0.1%, see Figure B.4.

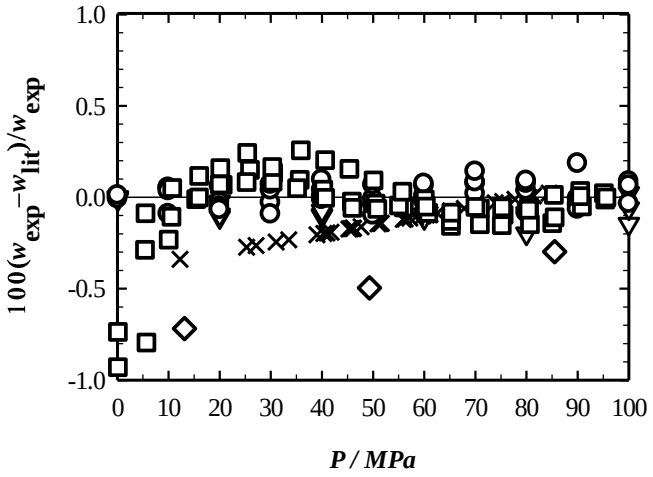

Figure.Appendix B.3 Deviations of our experimental speed of sound data of n-hexane with literature data of ×: Kasanshin et Shchemelev [10]; ▽: Boelhouwer [7]; △: Kagramanyan and Badalyan [12] ; ▼: Kiriakov and Panin [13]; ◇: Takagi et al. [14]; □: Ball and Trusler [9]; ○: Daridon et al. [8].

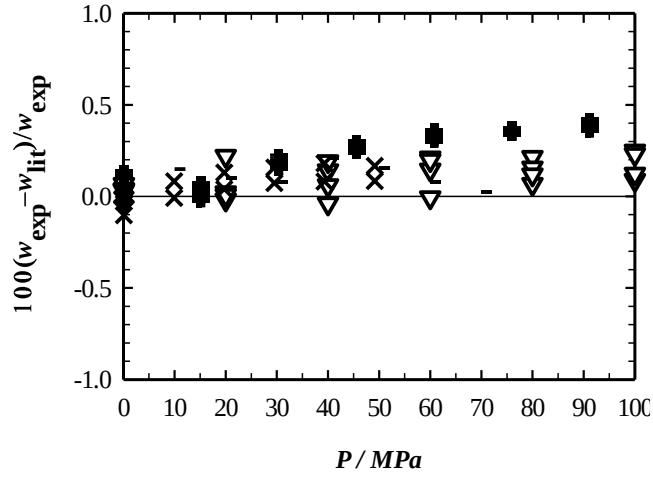

Figure.Appendix B.4 Deviations of our experimental speed of sound data of n-dodecane with literature data of × : Kasanshin and Shchemelev [10]; ▽: Boelhouwer [7]; ✚: Dzida and Cempa. [15] ; - : Bazile et al. [6]; and ◆ : Plantier et al. [11].

Table.Appendix B.3 Experimental sound velocity data of the binary mixtures of n-hexane+n-dodecane

T/K	P/MPa	$W + U_c$(w)											
		$m.s^{-1}$											
x_{n-c6}/mol%		0		20		40		60		80		100	
293.15	0.10	1298.9	1.6	1274.9	1.62	1248.8	1.6	1224.3	1.6	1193.7	1.5	1099.8	1.40
293.15	10.00	1356.5	1.7	1333.5	1.69	1309.9	1.7	1287.9	1.6	1258.1	1.6	1175.2	1.49
293.15	20.00	1410.1	1.8	1387.1	1.76	1365.5	1.7	1345.4	1.7	1317.5	1.7	1240.8	1.58
293.15	30.00	1457.4	1.9	1436.6	1.82	1416.4	1.8	1397.8	1.8	1372.1	1.7	1300.4	1.65
293.15	40.00	1503.1	1.9	1482.8	1.88	1463.8	1.9	1446.3	1.8	1422.1	1.8	1354.6	1.72
293.15	50.00	1546.1	2.0	1526.4	1.94	1508.3	1.9	1491.6	1.9	1469.8	1.9	1404.4	1.78
293.15	60.00	1585.9	2.0	1567.7	1.99	1550.3	2.0	1534.3	1.9	1514.3	1.9	1452.7	1.84
293.15	70.00	1624.6	2.1	1606.8	2.04	1590	2.0	1574.6	2.0	1553.1	2.0	1496.6	1.90
293.15	80.00	1660.3	2.1	1643.9	2.09	1627.7	2.1	1612.8	2.0	1591.7	2.0	1537.4	1.95
293.15	90.00	1695.4	2.2	1679	2.13	1663.2	2.1	1648.9	2.1	1629.4	2.1	1575.7	2.00
293.15	100.00	1729.6	2.2	1712	2.17	1696.8	2.2	1683	2.1	1664.5	2.1	1614.5	2.05
313.15	0.10	1222.2	1.6	1190.2	1.51	1158.6	1.5	1128.7	1.4	1091.9	1.4	1009.5	1.28
313.15	10.00	1283.6	1.6	1254.4	1.59	1226	1.6	1199.3	1.5	1168.2	1.5	1092.3	1.39
313.15	20.00	1339.3	1.7	1312.5	1.67	1286.5	1.6	1262.2	1.6	1234.3	1.6	1165.2	1.48
313.15	30.00	1390.7	1.8	1365.5	1.73	1341.5	1.7	1319	1.7	1293.7	1.6	1230.5	1.56
313.15	40.00	1439.8	1.8	1414.7	1.80	1392.1	1.8	1371.1	1.7	1347.7	1.7	1287.7	1.64
313.15	50.00	1483.8	1.9	1460.7	1.86	1439.3	1.8	1419.5	1.8	1397.3	1.8	1338.9	1.70
313.15	60.00	1525.4	1.9	1504	1.91	1483.6	1.9	1464.7	1.9	1444.6	1.8	1389.9	1.77
313.15	70.00	1565	2.0	1545	1.96	1525.4	1.9	1507.3	1.9	1487	1.9	1436.2	1.82
313.15	80.00	1602.7	2.0	1583.6	2.01	1564.7	2.0	1547.4	2.0	1528.3	1.9	1479.9	1.88
313.15	90.00	1639.4	2.1	1620.1	2.06	1601.9	2.0	1585.2	2.0	1567.3	2.0	1519.1	1.93
313.15	100.00	1674.5	2.1	1654.4	2.10	1636.9	2.1	1620.8	2.1	1604.1	2.0	1557.6	1.98
333.15	0.10	1148.2	1.5	1116.5	1.42	1081.6	1.4	1048.2	1.3	1007.7	1.3	920.7	1.17
333.15	10.00	1214	1.5	1186.3	1.51	1155.4	1.5	1126.3	1.4	1089.4	1.4	1014.8	1.29
333.15	20.00	1273.7	1.6	1248.6	1.59	1220.9	1.6	1194.9	1.5	1162.1	1.5	1094	1.39
333.15	30.00	1328.4	1.7	1305.1	1.66	1279.8	1.6	1256.2	1.6	1225.8	1.6	1163.1	1.48
333.15	40.00	1378.9	1.8	1357.1	1.72	1333.6	1.7	1312	1.7	1283.7	1.6	1224.3	1.55
333.15	50.00	1425.9	1.8	1405.4	1.78	1383.5	1.8	1363.3	1.7	1336.1	1.7	1279.7	1.63
333.15	60.00	1470.6	1.9	1450.7	1.84	1430	1.8	1411.1	1.8	1384.9	1.8	1330.6	1.69
333.15	70.00	1511.9	1.9	1493.3	1.90	1473.7	1.9	1455.8	1.8	1431.2	1.8	1379.7	1.75
333.15	80.00	1550.5	2.0	1533.4	1.95	1514.8	1.9	1497.8	1.9	1474.4	1.9	1422.4	1.81
333.15	90.00	1588.2	2.0	1571.2	2.00	1553.4	2.0	1537.4	2.0	1514.5	1.9	1464.9	1.86
333.15	100.00	1623.4	2.1	1606.7	2.04	1589.7	2.0	1574.5	2.0	1552.5	2.0	1507.5	1.91
353.15	0.10	1075.8	1.4	-	-	-	-	-	-	-	-	-	-
353.15	10.00	1146.2	1.5	1115.9	1.42	1079.2	1.4	1044.2	1.3	997.5	1.3	938.9	1.19
353.15	20.00	1211.8	1.5	1182.6	1.50	1149.9	1.5	1118.9	1.4	1075.7	1.4	1024.2	1.30
353.15	30.00	1269.6	1.6	1242.5	1.58	1212.8	1.5	1184.9	1.5	1145.7	1.5	1097.6	1.39
353.15	40.00	1321.8	1.7	1297.2	1.65	1269.9	1.6	1244.4	1.6	1209	1.5	1164.5	1.48
353.15	50.00	1371.8	1.7	1347.8	1.71	1322.4	1.7	1298.8	1.6	1264.9	1.6	1222.9	1.55
353.15	60.00	1416.4	1.8	1395	1.77	1371.2	1.7	1349.2	1.7	1316.7	1.7	1276.9	1.62
353.15	70.00	1459.8	1.9	1439.2	1.83	1416.7	1.8	1396.1	1.8	1362.2	1.7	1328.1	1.69
353.15	80.00	1500.9	1.9	1480.8	1.88	1459.5	1.9	1440	1.8	1409.4	1.8	1373.8	1.74
353.15	90.00	1539.8	2.0	1519.9	1.93	1499.6	1.9	1481.2	1.9	1451.2	1.8	1419.1	1.80
353.15	100.00	1576	2.0	1556.6	1.98	1537.3	2.0	1519.8	1.9	1490.7	1.9	1459	1.85

B .1 .4 Experimental Viscosity Data

In this section, are reported the experimental data of dynamic viscosity for pure compounds of n-hexane and n-dodecane and their binary mixtures at percentage mole fractions of 20, 40, 60 and 80 % of n-hexane. Measurements were carried out along four isotherms spaced at 20 K intervals in the temperature range of 293.15-353.15 K at pressures ranging from 0.1 to 100 MPa by steps of 10 MPa.

Liquid viscosities in n-hexane and n-dodecane were published by many authors [5,16–22]. For comparison purpose with literature data reported at temperature and pressure conditions

different from our experimental ones, experimental viscosities were correlated as a function of temperature T and pressure P. For atmospheric pressure, we used a Vogel-Fulcher-Tammann [23–25] like equation defined as follows:

$$\eta_{0,VFT} = A\ exp\left[\frac{B}{T-C}\right] \tag{B.1}$$

Concerning high pressure viscosity data, they were correlated as a function of T and the relative pressure $\tilde{P} = P - P_{atm}$ according to the following correlation [26]:

$$ln\left(\frac{\eta}{\eta_{0,VFT}}\right) = D\tilde{P} + (E_O + E_1 T) + ln\left(\frac{\tilde{P}+F_0+F_1 T}{F_0+F_1 T}\right) \tag{B.2}$$

These fitting equations, which coefficients are reported in Table B.4, presented an overall average absolute deviation with experimental data of 0.3 % for n-hexane and 0.5 % for n-dodecane.

As demonstrated by the graphs of Figures B.5 and B.6, the experimental results are in very good agreement with the literature data with deviations not exceeding the experimental uncertainties (around 3%).

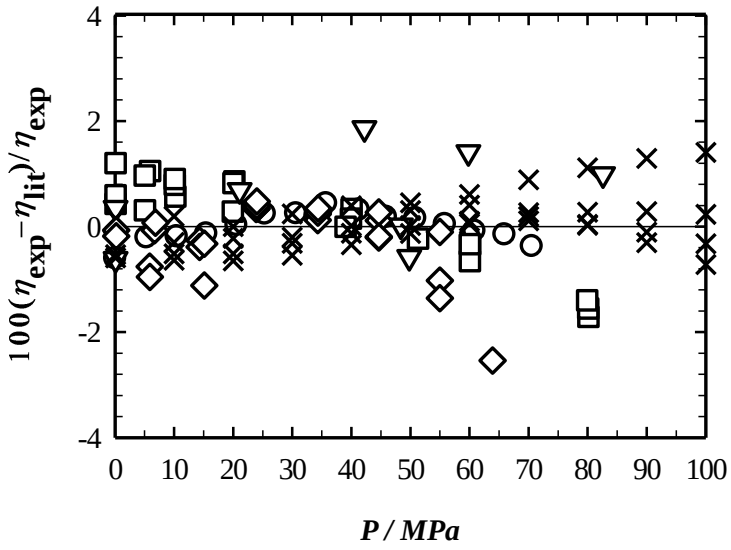

Figure.Appendix B.5 Deviations between n-hexane viscosity correlation of this work and literature data of ○: Assael et al.[17]; □**:** Oliveira and Wakeham [18]; ▽**:** Dymond and Awan [19]; ×**:** Michailidou et al.[27] and ◇ **:** Kiran and Sen [20]

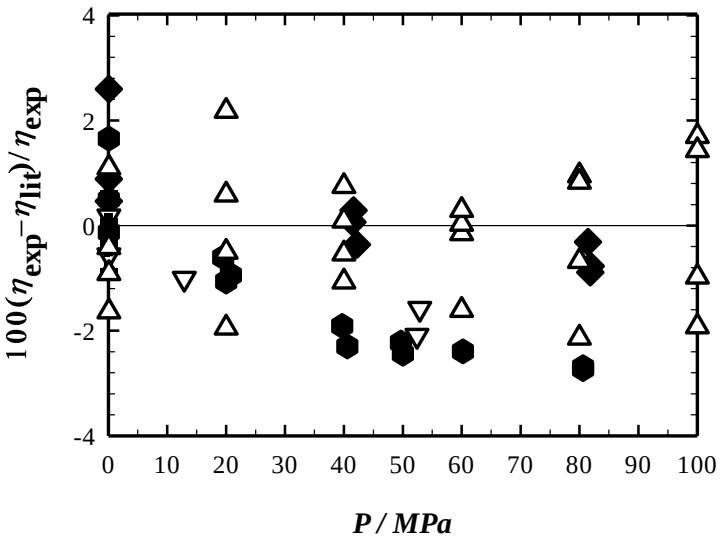

Figure.Appendix B.6 Deviations between n-dodecane viscosity correlation of this work and literature data from △: Ducoulombier et al. [16] ;▽**:** Dymond and Awan [19] ; ⬢ : Tanaka et al. [21] ; ✚ : Knapstad et al. [22] ; and ◆ : Caudwell et al.[5].

In addition, to check the consistency of the experimental measurements for mixtures, viscosity of mixtures are correlated as a function of temperature T, pressure P and the mixture's composition, using a Grunberg-Nissan [3] equation as follows:

$$\ln\left(\eta_{mix}(T,P,x_1)\right) = x_1 \ln(\eta_1) + (1-x_1)\ln(\eta_2) + x_1(1-x_1)G(T,P) \quad \text{(B.3)}$$

where η_{mix} is the predicted viscosity of the mixture , $\eta_1$and η_2 are the viscosity calculated with equations (B.1) and (B.2) for n-hexane and n-dodecane respectively, x_1 is the molar fraction of n-hexane in the binary mixture and G is a function of T and P , depending only on the two pure components and defined by the following equation:

$$G(T,P) = g_0 + g_1 T + g_2 T^2 + g_3 \Delta P + g_4 \Delta P^2 + g_5 \Delta P^3 \quad \text{(B.4)}$$

The coefficients g_i, i=1;5 are listed in Table B.4 along with the AAD, the Bias and the Max AAD between the mixtures' viscosity calculated with equations (B.3) and (B.4) and the experimental values. We observe that the predicted viscosity values are in very good agreement with the experimental data with an AAD of 1.15 %, lower than the experimental uncertainty (3%).

Table.Appendix B.4 Parameters of Eq. B.1, B.2 and B.4 from 293.15 to 353.15 K and for a pressure range of 0.1 MPa-100 MPa and relative deviations (Bias%), absolute average deviation (AAD%) and maximum deviation (Max AD%) between predicted viscosities and experimental data.

parameters	$nC6$	$nC12$	$G(T,P)$
A	9.16861E-03	3.90493E-02	
B	1.22041E+03	7.14673E+02	
C	-5.31455E+01	9.70135E+01	
E_0	-1.37904E-03	-1.17797E-01	
E_1	8.67170E-06	3.66823E-04	
F_0	1.25757E+02	-1.03375E+02	
F_1	-1.28652E-01	7.37556E-01	
D	-2.00900E-04	3.75856E-03	
g_0			-1.49493E+00
g_1			1.16706E-02
g_2			-1.68730E-05
g_3			-4.28871E-03
g_4			7.22547E-05
g_5			-2.25200E-07
Deviation with experimental values			
Bias%	0.32	0.43	-0.06
AAD%	0.32	0.48	1.15
Max AD%	1.04	1.51	5.52

Table.Appendix B.5 . Experimental viscosity data of n-hexane + n-dodecane binary mixture

T/K	P/MPa	$\eta + U_c(\eta)$											
		$m.Pa.s$											
x_{n-c6}/mol%		0		20		40		60		80		100	
293.15	0.10	1.49	0.03	1.18	0.02	0.89	0.02	0.67	0.01	0.47	0.01	0.31	0.01
293.15	10.00	1.67	0.03	1.30	0.03	0.97	0.02	0.71	0.01	0.52	0.01	0.35	0.01
293.15	20.00	1.87	0.04	1.44	0.03	1.07	0.02	0.78	0.02	0.57	0.01	0.38	0.01
293.15	30.00	2.08	0.04	1.60	0.03	1.18	0.02	0.86	0.02	0.62	0.01	0.41	0.01
293.15	40.00	2.31	0.05	1.77	0.04	1.31	0.03	0.94	0.02	0.68	0.01	0.45	0.01
293.15	50.00	2.56	0.05	1.95	0.04	1.44	0.03	1.03	0.02	0.74	0.01	0.48	0.01
293.15	60.00	2.83	0.06	2.15	0.04	1.57	0.03	1.12	0.02	0.80	0.02	0.52	0.01
293.15	70.00	3.11	0.06	2.35	0.05	1.73	0.03	1.22	0.02	0.86	0.02	0.55	0.01
293.15	80.00	3.42	0.07	2.58	0.05	1.89	0.04	1.33	0.03	0.92	0.02	0.58	0.01
293.15	90.00	3.76	0.08	2.82	0.06	2.06	0.04	1.44	0.03	0.99	0.02	0.62	0.01
293.15	100.00	4.12	0.08	3.08	0.06	2.25	0.04	1.56	0.03	1.06	0.02	0.66	0.01
313.15	0.10	1.07	0.02	0.87	0.02	0.69	0.01	0.53	0.01	0.38	0.01	0.26	0.01
313.15	10.00	1.19	0.02	0.97	0.02	0.73	0.01	0.55	0.01	0.41	0.01	0.29	0.01
313.15	20.00	1.32	0.03	1.07	0.02	0.81	0.02	0.61	0.01	0.45	0.01	0.32	0.01
313.15	30.00	1.47	0.03	1.18	0.02	0.90	0.02	0.68	0.01	0.49	0.01	0.35	0.01
313.15	40.00	1.62	0.03	1.30	0.03	0.99	0.02	0.74	0.01	0.54	0.01	0.37	0.01
313.15	50.00	1.78	0.04	1.42	0.03	1.09	0.02	0.81	0.02	0.58	0.01	0.40	0.01
313.15	60.00	1.95	0.04	1.55	0.03	1.19	0.02	0.88	0.02	0.63	0.01	0.43	0.01
313.15	70.00	2.13	0.04	1.68	0.03	1.29	0.03	0.96	0.02	0.67	0.01	0.46	0.01
313.15	80.00	2.32	0.05	1.83	0.04	1.41	0.03	1.04	0.02	0.72	0.01	0.49	0.01
313.15	90.00	2.53	0.05	1.98	0.04	1.52	0.03	1.12	0.02	0.77	0.02	0.52	0.01
313.15	100.00	2.74	0.05	2.14	0.04	1.65	0.03	1.21	0.02	0.82	0.02	0.55	0.01
333.15	0.10	0.81	0.02	0.67	0.01	0.55	0.01	0.43	0.01	0.31	0.01	0.22	0.00
333.15	10.00	0.90	0.02	0.74	0.01	0.57	0.01	0.46	0.01	0.33	0.01	0.24	0.00
333.15	20.00	1.00	0.02	0.82	0.02	0.64	0.01	0.51	0.01	0.37	0.01	0.27	0.01
333.15	30.00	1.10	0.02	0.91	0.02	0.71	0.01	0.56	0.01	0.41	0.01	0.29	0.01
333.15	40.00	1.21	0.02	1.00	0.02	0.78	0.02	0.62	0.01	0.45	0.01	0.32	0.01
333.15	50.00	1.32	0.03	1.09	0.02	0.85	0.02	0.67	0.01	0.49	0.01	0.34	0.01
333.15	60.00	1.44	0.03	1.18	0.02	0.93	0.02	0.73	0.01	0.53	0.01	0.37	0.01
333.15	70.00	1.57	0.03	1.28	0.03	1.01	0.02	0.79	0.02	0.57	0.01	0.39	0.01
333.15	80.00	1.70	0.03	1.39	0.03	1.09	0.02	0.84	0.02	0.61	0.01	0.42	0.01
333.15	90.00	1.84	0.04	1.49	0.03	1.17	0.02	0.90	0.02	0.65	0.01	0.44	0.01
333.15	100.00	1.99	0.04	1.60	0.03	1.26	0.03	0.97	0.02	0.69	0.01	0.46	0.01
353.15	0.10	0.63	0.01	-	-	-	-	-	-	-	-	-	-
353.15	10.00	0.70	0.01	0.60	0.01	0.49	0.01	0.38	0.01	0.29	0.01	0.21	0.00
353.15	20.00	0.78	0.02	0.66	0.01	0.54	0.01	0.42	0.01	0.32	0.01	0.23	0.00
353.15	30.00	0.86	0.02	0.73	0.01	0.59	0.01	0.46	0.01	0.35	0.01	0.25	0.01
353.15	40.00	0.95	0.02	0.80	0.02	0.64	0.01	0.51	0.01	0.38	0.01	0.27	0.01
353.15	50.00	1.03	0.02	0.87	0.02	0.70	0.01	0.55	0.01	0.42	0.01	0.30	0.01
353.15	60.00	1.12	0.02	0.94	0.02	0.76	0.02	0.60	0.01	0.45	0.01	0.32	0.01
353.15	70.00	1.22	0.02	1.01	0.02	0.82	0.02	0.65	0.01	0.48	0.01	0.34	0.01
353.15	80.00	1.32	0.03	1.09	0.02	0.89	0.02	0.70	0.01	0.52	0.01	0.36	0.01
353.15	90.00	1.42	0.03	1.17	0.02	0.96	0.02	0.75	0.02	0.55	0.01	0.39	0.01
353.15	100.00	1.53	0.03	1.25	0.03	1.03	0.02	0.80	0.02	0.58	0.01	0.41	0.01

B .2 Molecular Simulation Results

In this section, the simulation data of density, isothermal compressibility, speed of sound and viscosity are listed for both MCCG and TraPPE-ua

B .2 .1 Molecular Simulation Density Results

Table.Appendix B.6 . Molecular simulation density and standard deviation data with TraPPE-ua for the binary mixtures n-hexane + n-dodecane

T/K	P/MPa	ρ + σ (ρ) $kg.m^{-3}$											
x_{n-C6}/mol%		0		20		40		60		80		100	
293.15	0.10	758.12	0.23	747.12	0.46	732.48	0.66	715.25	0.42	693.03	1.01	663.01	0.13
293.15	10.00	765.17	0.51	754.71	0.35	741.20	0.19	724.64	0.00	702.77	0.27	674.47	0.31
293.15	20.00	772.39	0.38	762.44	1.59	749.19	0.12	732.57	0.33	711.64	0.85	684.55	0.19
293.15	30.00	779.98	0.87	769.80	0.58	755.69	0.63	740.25	0.16	719.38	0.65	693.21	0.14
293.15	40.00	786.67	0.88	775.70	0.27	763.50	0.05	747.12	0.03	727.47	0.52	701.01	0.21
293.15	50.00	793.30	1.71	781.07	0.81	768.94	0.26	753.52	0.10	734.01	0.36	708.36	0.12
293.15	60.00	797.82	0.95	787.33	0.21	774.52	0.12	760.08	0.01	740.63	1.06	715.10	0.42
293.15	70.00	802.92	0.28	791.85	0.57	779.86	0.01	765.80	0.11	746.73	0.17	721.45	0.28
293.15	80.00	807.50	0.71	798.61	1.78	785.59	0.76	771.00	0.31	752.13	0.45	727.12	0.28
293.15	90.00	813.19	1.03	803.20	1.79	791.63	0.54	775.42	0.17	757.34	0.41	732.82	0.11
293.15	100.00	823.62	0.94	807.79	1.43	795.34	1.29	780.48	0.12	761.84	0.75	737.89	0.02
313.15	0.10	743.49	0.52	731.70	0.22	717.37	0.11	699.47	0.33	676.08	0.73	644.42	0.33
313.15	10.00	751.88	0.91	740.91	0.34	726.86	0.12	710.09	0.99	687.11	1.03	657.58	0.23
313.15	20.00	759.81	0.48	748.75	0.17	735.88	0.70	718.82	0.25	697.26	0.19	668.81	0.07
313.15	30.00	766.81	0.67	756.55	0.19	743.41	0.14	727.00	0.20	706.43	0.54	678.75	0.05
313.15	40.00	774.17	0.61	763.07	0.90	751.18	0.07	734.27	0.66	714.02	0.36	687.41	0.27
313.15	50.00	779.81	0.31	770.10	0.38	757.30	0.13	740.97	0.17	720.84	0.68	695.42	0.01
313.15	60.00	785.89	0.56	776.19	0.29	763.68	0.20	747.94	0.18	727.97	0.37	702.70	0.36
313.15	70.00	791.18	0.31	781.60	0.24	769.60	0.66	754.34	0.63	734.62	0.36	709.12	0.05
313.15	80.00	796.12	0.42	786.85	1.09	774.62	0.29	759.68	0.31	740.58	0.54	715.66	0.13
313.15	90.00	801.52	0.50	791.97	0.53	780.30	0.08	765.02	0.27	746.07	0.27	721.50	0.46
313.15	100.00	806.73	0.59	796.91	0.14	784.75	0.47	769.95	0.15	751.34	0.96	727.11	0.25
333.15	0.10	729.26	0.07	716.47	0.64	701.69	0.27	682.28	0.23	658.50	0.77	625.05	0.02
333.15	10.00	738.45	0.55	726.28	0.72	712.33	0.39	694.91	0.12	671.18	0.69	640.30	0.08
333.15	20.00	746.82	0.02	735.43	0.13	722.56	0.53	704.52	0.20	683.34	1.14	653.00	0.42
333.15	30.00	754.70	0.09	744.42	0.62	730.51	0.18	713.44	0.13	692.42	0.79	664.03	0.42
333.15	40.00	761.88	0.34	751.07	0.15	738.54	0.11	722.13	0.12	700.65	0.86	673.74	0.09
333.15	50.00	768.85	0.47	758.42	0.02	745.16	0.16	729.70	0.14	709.66	0.76	682.42	0.10
333.15	60.00	775.08	0.32	764.41	0.29	751.39	0.37	736.13	0.08	715.56	0.56	690.15	0.15
333.15	70.00	781.00	0.26	770.35	0.46	758.08	0.09	742.64	0.00	723.30	0.41	697.48	0.41
333.15	80.00	785.94	0.01	776.48	0.40	764.21	0.39	748.71	0.25	729.39	0.37	704.34	0.20
333.15	90.00	790.87	0.38	781.92	0.48	769.74	0.26	754.50	0.23	734.69	0.28	710.69	0.45
333.15	100.00	796.31	0.35	786.79	0.63	775.34	0.01	760.29	0.19	740.83	0.40	716.21	0.21
353.15	0.10	713.37	0.82	701.28	0.46	684.69	0.16	665.57	0.08	639.94	0.82	-	-
353.15	10.00	724.25	0.71	712.43	0.89	697.87	0.11	678.59	0.79	654.65	0.59	622.84	0.46
353.15	20.00	734.11	0.47	722.93	0.43	708.27	0.33	690.88	0.26	667.50	0.77	637.30	0.73
353.15	30.00	742.54	0.29	730.99	0.88	717.76	0.13	700.66	0.14	678.47	0.59	649.63	0.28
353.15	40.00	750.46	0.57	739.88	0.41	725.92	0.02	709.38	0.02	688.26	0.68	660.39	0.36
353.15	50.00	756.57	0.04	746.60	0.37	733.55	0.18	717.66	0.10	696.74	0.44	669.48	0.42
353.15	60.00	764.12	0.25	753.69	0.51	740.55	0.44	724.78	0.08	704.48	0.58	677.97	0.56
353.15	70.00	769.04	0.99	759.93	0.59	747.82	0.03	731.47	0.32	712.44	0.42	685.54	0.42
353.15	80.00	775.97	0.38	765.73	0.68	753.20	0.45	738.12	0.21	718.92	0.47	692.85	0.36
353.15	90.00	781.83	0.35	771.84	0.23	759.05	0.83	744.28	0.16	725.14	0.48	699.19	0.37
353.15	100.00	786.72	0.72	777.19	1.18	764.55	0.74	749.58	0.38	731.18	0.48	705.80	0.26

Table.Appendix B.7 Molecular Simulation density and standard deviation data with MCCG for the binary mixtures n-hexane + n-dodecane

T/K	P/MPa	ρ + σ(ρ)											
		$kg.m^{-3}$											
x_{n-C6}/mol%		0		20		40		60		80		100	
293.15	0.10	764.43	0.98	752.73	0.59	738.13	1.04	719.20	1.98	695.40	1.69	663.20	1.15
293.15	10.00	771.20	0.26	760.50	1.01	745.40	0.62	727.30	1.62	704.40	1.05	674.10	1.00
293.15	20.00	777.23	0.59	765.90	0.87	751.47	1.36	734.50	1.68	713.50	1.81	682.60	0.73
293.15	30.00	784.10	1.30	772.23	0.60	758.73	0.40	742.70	1.07	720.90	0.84	691.60	1.23
293.15	40.00	787.93	2.11	778.63	1.16	765.47	0.25	748.20	1.10	728.10	1.03	699.20	0.71
293.15	50.00	795.60	3.40	783.60	0.72	770.33	0.38	753.80	1.64	733.80	1.06	706.20	1.10
293.15	60.00	799.97	0.25	788.73	0.57	776.17	0.40	760.80	1.00	739.60	0.47	713.00	0.38
293.15	70.00	803.80	1.37	793.23	0.40	781.37	0.70	765.70	1.12	745.60	0.58	719.30	0.76
293.15	80.00	807.27	2.84	798.20	0.35	786.07	0.42	770.40	2.22	750.90	0.78	725.50	1.00
293.15	90.00	811.33	2.76	802.37	0.23	790.40	0.40	775.00	1.65	755.80	1.71	730.30	0.81
293.15	100.00	814.20	3.73	806.37	0.95	795.10	0.25	779.00	2.69	761.00	1.70	735.80	0.33
313.15	0.10	747.70	0.87	735.40	0.46	720.30	0.85	702.10	1.12	676.80	1.22	643.50	0.71
313.15	10.00	756.07	0.64	742.80	0.46	729.50	0.85	709.90	2.53	686.90	1.04	655.90	0.73
313.15	20.00	762.00	0.79	751.10	0.72	737.15	0.07	719.50	1.23	696.80	1.11	665.20	0.83
313.15	30.00	769.07	1.16	757.87	0.78	743.70	0.42	726.70	1.79	704.80	0.94	675.20	0.92
313.15	40.00	774.07	0.76	763.80	0.70	749.55	1.20	734.20	0.71	711.90	1.64	683.80	0.94
313.15	50.00	780.83	0.61	769.83	0.32	756.57	0.29	738.90	0.80	718.80	1.11	691.30	0.56
313.15	60.00	785.23	0.31	775.60	0.26	762.37	0.12	745.90	1.40	725.30	0.99	699.20	0.64
313.15	70.00	790.90	1.39	780.00	0.00	767.13	0.68	752.80	3.40	732.00	1.13	705.40	0.77
313.15	80.00	795.03	0.91	785.63	0.67	772.80	0.44	757.40	2.18	737.40	0.64	711.40	0.92
313.15	90.00	799.57	2.06	790.07	0.25	777.83	0.12	763.80	2.37	743.30	1.78	717.40	0.76
313.15	100.00	805.23	0.25	795.17	1.33	782.03	0.31	767.40	1.09	748.90	1.43	723.00	0.94
333.15	0.10	731.47	0.98	718.43	0.25	702.70	0.50	682.60	1.61	657.30	1.29	622.60	0.72
333.15	10.00	740.03	0.65	727.27	0.06	712.43	0.21	693.90	1.23	669.10	0.63	636.00	0.62
333.15	20.00	746.80	0.79	735.73	0.06	721.00	0.17	702.40	1.45	679.30	0.60	647.90	0.58
333.15	30.00	754.27	0.29	742.60	0.26	728.83	0.06	711.20	0.36	688.80	0.77	658.40	1.21
333.15	40.00	760.53	0.42	749.93	0.25	736.23	0.68	718.50	0.77	696.60	1.50	668.60	0.82
333.15	50.00	766.67	0.55	756.37	0.80	742.47	0.21	726.60	0.52	704.90	0.90	676.60	0.35
333.15	60.00	771.90	0.46	761.93	0.57	748.90	0.71	731.10	1.62	711.50	1.01	684.30	0.44
333.15	70.00	778.73	0.80	767.77	0.21	754.70	0.14	738.20	0.96	718.10	0.88	691.20	0.72
333.15	80.00	783.50	0.69	772.47	0.21	760.40	0.14	744.20	0.57	724.60	1.07	698.00	0.27
333.15	90.00	788.40	0.61	777.45	0.07	765.20	0.28	749.90	1.32	730.90	1.10	704.30	0.93
333.15	100.00	791.73	1.12	782.90	0.28	770.70	0.57	754.70	1.32	736.00	1.01	710.40	0.58
353.15	0.10	713.93	0.31	701.30	1.42	685.13	0.21	664.40	0.47	637.90	0.89	-	-
353.15	10.00	723.67	0.15	711.10	1.11	695.80	0.26	676.50	2.07	651.30	1.38	617.10	0.57
353.15	20.00	731.77	0.51	719.90	1.25	705.63	0.42	686.50	0.68	662.00	1.28	630.90	0.84
353.15	30.00	739.73	0.47	727.60	2.05	713.90	0.42	696.20	0.86	673.00	0.58	642.60	0.68
353.15	40.00	747.03	0.50	735.30	1.84	721.90	0.28	704.60	0.36	682.40	0.75	653.10	0.38
353.15	50.00	753.57	0.31	742.20	1.43	728.40	0.71	712.30	1.18	690.60	1.53	661.90	0.41
353.15	60.00	759.63	0.25	749.50	1.18	735.45	0.21	719.20	0.68	698.30	0.35	670.70	0.45
353.15	70.00	764.63	1.17	755.20	0.65	741.55	0.64	724.90	1.41	705.10	0.65	677.90	0.50
353.15	80.00	770.67	0.35	761.10	1.30	747.65	0.07	732.70	1.20	711.70	0.51	685.10	0.68
353.15	90.00	775.97	0.06	766.10	3.47	753.40	0.42	737.90	2.01	718.30	0.87	691.60	0.53
353.15	100.00	780.80	0.60	770.90	1.73	758.55	0.21	743.70	0.50	723.40	0.68	697.70	0.61

B .2 .2 Isothermal Compressibility

Table.Appendix B.8 Molecular Simulation isothermal compressibility and standard deviation data with TraPPE-ua for the binary mixtures n-hexane + n-dodecane

T/K	P/MPa	$\kappa_T + \sigma(\kappa_T)$ / GPa^{-1}											
$x_{nC6}/\%mol$		0		20		40		60		80		100	
293.15	0.10	1.05	0.05	1.18	0.15	1.27	0.08	1.34	0.02	1.47	0.13	1.92	0.08
293.15	10.00	1.03	0.09	1.06	0.05	1.11	0.08	1.20	0.04	1.32	0.08	1.61	0.07
293.15	20.00	0.84	0.08	0.95	0.04	0.99	0.03	1.08	0.07	1.15	0.08	1.38	0.04
293.15	30.00	0.77	0.06	0.87	0.06	0.91	0.06	0.96	0.01	1.00	0.07	1.25	0.01
293.15	40.00	0.73	0.03	0.74	0.02	0.81	0.02	0.86	0.04	1.09	0.09	1.09	0.02
293.15	50.00	0.69	0.04	0.79	0.01	0.75	0.02	0.86	0.03	0.93	0.05	0.98	0.03
293.15	60.00	0.64	0.06	0.70	0.07	0.68	0.01	0.77	0.02	0.80	0.07	0.93	0.01
293.15	70.00	0.57	0.14	0.64	0.07	0.64	0.01	0.68	0.01	0.77	0.04	0.81	0.01
293.15	80.00	0.59	0.05	0.58	0.02	0.61	0.01	0.67	0.02	0.70	0.06	0.76	0.01
293.15	90.00	0.54	0.07	0.55	0.03	0.56	0.02	0.67	0.02	0.67	0.06	0.72	0.01
293.15	100.00	0.49	0.04	0.52	0.02	0.58	0.01	0.58	0.02	0.65	0.03	0.67	0.03
313.15	0.10	1.32	0.24	1.35	0.04	1.44	0.02	1.56	0.02	1.82	0.12	2.26	0.05
313.15	10.00	1.10	0.06	1.10	0.09	1.21	0.02	1.33	0.06	1.63	0.04	1.80	0.02
313.15	20.00	1.03	0.08	1.06	0.08	1.11	0.02	1.19	0.02	1.33	0.09	1.55	0.03
313.15	30.00	0.85	0.08	0.94	0.01	0.96	0.08	1.08	0.02	1.20	0.04	1.34	0.12
313.15	40.00	0.83	0.05	0.94	0.02	0.91	0.02	0.97	0.03	1.06	0.07	1.19	0.00
313.15	50.00	0.78	0.01	0.80	0.07	0.88	0.02	0.92	0.05	1.02	0.05	1.05	0.05
313.15	60.00	0.66	0.01	0.70	0.01	0.78	0.02	0.83	0.04	0.87	0.02	0.97	0.01
313.15	70.00	0.68	0.03	0.71	0.08	0.73	0.01	0.79	0.01	0.79	0.05	0.88	0.00
313.15	80.00	0.62	0.07	0.64	0.04	0.67	0.03	0.73	0.03	0.72	0.05	0.87	0.04
313.15	90.00	0.59	0.04	0.63	0.04	0.62	0.02	0.66	0.01	0.73	0.03	0.79	0.02
313.15	100.00	0.61	0.02	0.58	0.03	0.58	0.04	0.65	0.03	0.69	0.06	0.75	0.01
333.15	0.10	1.43	0.08	1.54	0.09	1.73	0.01	1.84	0.06	2.17	0.23	2.73	0.08
333.15	10.00	1.23	0.13	1.35	0.03	1.40	0.01	1.63	0.02	1.87	0.23	2.27	0.02
333.15	20.00	1.21	0.15	1.13	0.00	1.19	0.01	1.34	0.02	1.58	0.14	1.84	0.05
333.15	30.00	0.99	0.00	1.09	0.08	1.14	0.00	1.14	0.03	1.38	0.06	1.50	0.05
333.15	40.00	0.93	0.04	1.02	0.08	0.97	0.03	1.07	0.05	1.21	0.04	1.36	0.05
333.15	50.00	0.83	0.10	0.85	0.04	0.92	0.01	0.97	0.01	1.04	0.05	1.21	0.04
333.15	60.00	0.79	0.04	0.80	0.08	0.84	0.02	0.87	0.02	0.97	0.05	1.09	0.06
333.15	70.00	0.72	0.05	0.73	0.02	0.79	0.01	0.80	0.06	0.91	0.02	0.99	0.03
333.15	80.00	0.63	0.00	0.72	0.03	0.69	0.06	0.79	0.01	0.81	0.07	0.90	0.03
333.15	90.00	0.59	0.03	0.68	0.05	0.68	0.01	0.75	0.02	0.81	0.06	0.86	0.02
333.15	100.00	0.60	0.01	0.65	0.02	0.67	0.05	0.69	0.04	0.72	0.03	0.80	0.03
353.15	0.10	1.60	0.04	1.63	0.02	1.87	0.10	2.17	0.01	2.61	0.07	-	-
353.15	10.00	1.38	0.02	1.45	0.03	1.65	0.07	1.78	0.08	2.07	0.16	2.56	0.16
353.15	20.00	1.16	0.03	1.32	0.08	1.43	0.03	1.40	0.08	1.72	0.12	2.04	0.11
353.15	30.00	1.07	0.03	1.12	0.04	1.22	0.08	1.35	0.05	1.54	0.08	1.69	0.12
353.15	40.00	0.99	0.01	1.03	0.05	1.11	0.05	1.21	0.05	1.24	0.09	1.44	0.11
353.15	50.00	0.90	0.03	0.98	0.02	1.07	0.02	1.07	0.02	1.21	0.05	1.28	0.03
353.15	60.00	0.89	0.01	0.92	0.06	0.87	0.00	0.97	0.05	1.04	0.05	1.22	0.09
353.15	70.00	0.90	0.05	0.79	0.03	0.90	0.03	0.87	0.01	0.95	0.04	1.01	0.03
353.15	80.00	0.73	0.02	0.76	0.04	0.81	0.02	0.83	0.02	0.87	0.07	0.96	0.08
353.15	90.00	0.63	0.00	0.71	0.03	0.74	0.02	0.77	0.06	0.86	0.03	0.96	0.07
353.15	100.00	0.62	0.04	0.64	0.00	0.68	0.01	0.71	0.03	0.82	0.04	0.84	0.03

Table.Appendix B.9 Molecular Simulation isothermal compressibility and standard deviation data with MCCG for the binary mixtures n-hexane + n-dodecane.

T/K P/MPa		$\kappa_T + \sigma(\kappa_T)$ GPa^{-1}											
$x_{nC6}/\%mol$		0		20		40		60		80		100	
293.15	0.10	0.92	0.10	0.94	0.10	1.06	0.03	1.02	0.09	1.41	0.15	1.74	0.13
293.15	10.00	0.79	0.02	0.84	0.04	1.06	0.11	1.00	0.05	1.28	0.10	1.47	0.07
293.15	20.00	0.81	0.07	0.78	0.02	0.89	0.07	0.92	0.13	1.09	0.05	1.27	0.15
293.15	30.00	0.69	0.02	0.76	0.05	0.87	0.15	0.85	0.09	0.97	0.05	1.20	0.09
293.15	40.00	0.67	0.05	0.77	0.07	0.74	0.02	0.77	0.09	0.87	0.03	0.99	0.07
293.15	50.00	0.59	0.10	0.62	0.08	0.68	0.00	0.64	0.08	0.83	0.04	0.89	0.03
293.15	60.00	0.55	0.10	0.65	0.02	0.61	0.08	0.72	0.12	0.74	0.04	0.89	0.03
293.15	70.00	0.59	0.02	0.59	0.07	0.65	0.05	0.58	0.08	0.79	0.02	0.81	0.04
293.15	80.00	0.47	0.11	0.56	0.04	0.61	0.03	0.50	0.03	0.64	0.06	0.75	0.03
293.15	90.00	0.56	0.02	0.53	0.10	0.49	0.00	0.58	0.06	0.64	0.05	0.73	0.04
293.15	100.00	0.51	0.13	0.49	0.03	0.56	0.07	0.48	0.08	0.62	0.08	0.67	0.06
313.15	0.10	1.10	0.08	1.11	0.03	1.29	0.02	1.28	0.06	1.65	0.09	2.08	0.11
313.15	10.00	0.96	0.02	1.02	0.09	1.07	0.01	1.24	0.10	1.43	0.08	1.73	0.02
313.15	20.00	0.81	0.13	0.96	0.01	0.95	0.02	1.09	0.21	1.34	0.15	1.49	0.06
313.15	30.00	0.87	0.04	0.79	0.05	0.93	0.01	0.88	0.08	1.14	0.05	1.30	0.11
313.15	40.00	0.67	0.08	0.81	0.04	0.82	0.05	0.88	0.05	1.01	0.04	1.19	0.06
313.15	50.00	0.62	0.10	0.76	0.09	0.81	0.07	0.74	0.05	0.95	0.09	1.17	0.06
313.15	60.00	0.60	0.03	0.67	0.05	0.73	0.01	0.78	0.07	0.83	0.06	1.01	0.07
313.15	70.00	0.58	0.09	0.68	0.05	0.69	0.05	0.70	0.09	0.77	0.08	0.92	0.08
313.15	80.00	0.54	0.08	0.62	0.04	0.64	0.06	0.63	0.05	0.71	0.05	0.84	0.04
313.15	90.00	0.53	0.04	0.58	0.07	0.65	0.10	0.70	0.09	0.71	0.05	0.81	0.04
313.15	100.00	0.47	0.08	0.49	0.05	0.58	0.03	0.52	0.03	0.73	0.07	0.77	0.03
333.15	0.10	1.23	0.03	1.28	0.01	1.40	0.06	1.59	0.03	2.00	0.07	2.62	0.06
333.15	10.00	1.08	0.02	1.16	0.03	1.33	0.10	1.39	0.12	1.69	0.10	2.03	0.06
333.15	20.00	0.98	0.07	1.05	0.11	1.12	0.04	1.24	0.09	1.40	0.09	1.69	0.01
333.15	30.00	0.87	0.04	0.89	0.05	1.03	0.06	1.08	0.10	1.22	0.06	1.43	0.09
333.15	40.00	0.77	0.05	0.89	0.05	0.94	0.05	1.02	0.10	1.17	0.06	1.30	0.06
333.15	50.00	0.78	0.07	0.78	0.04	0.80	0.02	0.88	0.06	1.03	0.03	1.16	0.06
333.15	60.00	0.72	0.02	0.73	0.03	0.81	0.02	0.89	0.12	0.95	0.04	1.06	0.04
333.15	70.00	0.70	0.08	0.68	0.05	0.67	0.02	0.83	0.08	0.86	0.06	0.94	0.06
333.15	80.00	0.71	0.14	0.67	0.01	0.67	0.00	0.75	0.04	0.81	0.04	0.95	0.03
333.15	90.00	0.67	0.11	0.61	0.03	0.72	0.03	0.68	0.06	0.72	0.04	0.85	0.06
333.15	100.00	0.52	0.05	0.58	0.04	0.72	0.07	0.62	0.05	0.72	0.05	0.81	0.06
353.15	0.10	1.40	0.08	1.43	0.08	1.74	0.08	1.90	0.16	2.44	0.16	-	-
353.15	10.00	1.20	0.03	1.40	0.16	1.52	0.08	1.59	0.12	1.93	0.08	2.41	0.18
353.15	20.00	1.11	0.09	1.14	0.07	1.31	0.08	1.54	0.20	1.71	0.03	1.89	0.09
353.15	30.00	1.00	0.03	1.04	0.10	1.12	0.01	1.21	0.09	1.46	0.09	1.73	0.09
353.15	40.00	0.88	0.05	1.02	0.13	1.01	0.02	1.07	0.10	1.29	0.11	1.45	0.08
353.15	50.00	0.78	0.11	0.86	0.18	0.93	0.02	1.08	0.07	1.15	0.07	1.24	0.06
353.15	60.00	0.75	0.01	0.86	0.10	0.86	0.09	0.96	0.08	1.03	0.06	1.17	0.07
353.15	70.00	0.68	0.06	0.72	0.15	0.81	0.04	0.74	0.08	1.00	0.05	1.08	0.06
353.15	80.00	0.64	0.03	0.70	0.10	0.75	0.04	0.85	0.02	0.91	0.07	0.97	0.08
353.15	90.00	0.63	0.09	0.72	0.02	0.72	0.04	0.70	0.06	0.80	0.04	0.96	0.04
353.15	100.00	0.57	0.00	0.66	0.04	0.66	0.03	0.71	0.09	0.77	0.06	0.85	0.04

B .2 .3 Molecular Simulation Results of Viscosity

Table.Appendix B.10 Molecular Simulation viscosity and standard deviation data with TraPPE-ua for the binary mixtures n-hexane + n-dodecane

T/K	P/MPa	$\eta + \sigma(\eta)$ $mPa.s$											
$x_{nC6}/\%mol$		0		20		40		60		80		100	
293.15	0.10	0.86	0.10	0.67	0.10	0.52	0.04	0.41	0.04	0.30	0.02	0.21	0.01
293.15	10.00	0.90	0.15	0.73	0.09	0.60	0.06	0.45	0.05	0.34	0.02	0.25	0.02
293.15	40.00	1.29	0.14	0.95	0.14	0.78	0.07	0.59	0.06	0.44	0.03	0.32	0.02
293.15	70.00	1.72	0.42	1.32	0.24	0.96	0.16	0.75	0.06	0.52	0.04	0.38	0.03
293.15	100.00	1.86	0.29	1.49	0.22	1.30	0.23	0.88	0.11	0.67	0.09	0.44	0.05
353.15	0.10	0.42	0.04	0.38	0.03	0.30	0.01	0.25	0.02	0.19	0.02	-	-
353.15	10.00	0.44	0.02	0.40	0.03	0.33	0.03	0.27	0.01	0.21	0.01	0.16	0.01
353.15	40.00	0.63	0.06	0.53	0.04	0.43	0.04	0.37	0.04	0.28	0.01	0.22	0.02
353.15	70.00	0.74	0.08	0.62	0.04	0.56	0.04	0.45	0.02	0.35	0.04	0.27	0.01
353.15	100.00	0.95	0.11	0.72	0.09	0.68	0.08	0.54	0.04	0.42	0.04	0.31	0.01

Table.Appendix B.11 Molecular Simulation viscosity and standard deviation data with MCCG for the binary mixtures n-hexane + n-dodecane

T/K P/MPa		$\eta + \sigma(\eta)$ $mPa.s$											
$x_{nC6}/\%mol$		0		20		40		60		80		100	
293.15	0.10	0.9156	0.0241	0.80	0.02	0.65	0.02	0.51	0.01	0.40	0.01	0.29	0.01
293.15	10.00	0.9868	0.0641	0.86	0.02	0.70	0.03	0.57	0.02	0.44	0.02	0.32	0.01
293.15	40.00	1.2429	0.0762	1.07	0.05	0.88	0.02	0.70	0.02	0.55	0.02	0.41	0.02
293.15	70.00	1.6024	0.1007	1.30	0.04	1.07	0.04	0.85	0.03	0.66	0.02	0.49	0.02
293.15	100.00	1.8730	0.1009	1.55	0.07	1.30	0.04	0.99	0.04	0.79	0.02	0.57	0.02
353.15	0.10	0.5335	0.0175	0.45	0.02	0.38	0.01	0.30	0.00	0.24	0.00	-	-
353.15	10.00	0.5720	0.0254	0.48	0.01	0.42	0.01	0.34	0.00	0.27	0.01	0.20	0.01
353.15	40.00	0.7087	0.0493	0.61	0.03	0.52	0.01	0.44	0.00	0.34	0.00	0.25	0.01
353.15	70.00	0.8903	0.0641	0.75	0.02	0.64	0.02	0.53	0.01	0.42	0.01	0.32	0.01
353.15	100.00	1.0354	0.0533	0.90	0.02	0.75	0.02	0.62	0.01	0.48	0.02	0.38	0.01

B .3 References

(1) C. E. Kuyatt, B. N. Taylo. “Guidelines for Evaluating and Expressing the Uncertainty of NIST Measurement Results” NIST Technical Note 1297; 1994.

(2) L. Hnnedkovsky, I. Cibulka. Liquid Densities at Elevated Pressures of N-Alkanes from C5 to C16:A Critical Evaluation of Experimental Data,. J Chem Eng Data 1996, 41.

(3) Assael, M. J.; and D. Exadaktilou, J. H. D. An Improved Representation for N-Alkane,. Int. J. Thermophys. 1994, 15 (1).

(4) Lemmon, E.W., Bell, I.H., Huber, M.L., McLinden, M.O. NIST Standard Reference Database 23: Reference Fluid Thermodynamic and Transport Properties-REFPROP, Version 10.0, National Institute of Standards and Technology, Standard Reference Data Program, Gaithersburg, 2018

(5) Caudwell, D. R.; Trusler, J. P. M.; Vesovic, V.; Wakeham, W. A. The Viscosity and Density of N-Dodecane and n-Octadecane at Pressures up to 200 MPa and Temperatures up to 473 K. Int. J. Thermophys. 2004, 25 (5), 1339–1352.

(6) Bazile, J.-P.; Nasri, D.; SALEY HAMANI, A. W. Density, Speed of Sound, Compressibility and Excess Properties of Carbon Dioxide + n-Dodecane Binary Mixture.

(7) Boelhouwer, J. W. M. Sound Velocities in and Adiabatic Compressibilities of Liquid Alkanes at Various Temperatures and Pressures. Physica 1967, 34 (3), 484–492.

(8) kalra.

(9) Ball, S. J.; Trusler, J. P. M. Speed of Sound of N-Hexane and n-Hexadecane at Temperatures Between 298 and 373 K and Pressures up to 100 MPa. 17.

(10) Khasanshin, T. S.; Shchemelev, A. P. Sound Velocity in Liquid N-Alkanes. 2001, 39 (1), 8.

(11) Plantier, F.; Daridon, J.-L.; Lagourette, B.; Boned, C. Isentropic Thermophysical Properties of Pure N-Paraffins as a Function of Temperature and Chain Length. High Temp.-High Press. 2000, 32 (3), 305–310.

(12) Kagramanyan, L. S.; Badalyan, A. L. Pulsed experimental arrangement for measurement of ultrasound velocity in liquids under pressure up to 2000 atm.13th ed. Izv. Akad. Nauk. Arm. USSR Fiz 1978, p 478.

(13) Kiriakov, B. S.; Panin, P. P. Thermodynamic properties of liquid n-hexane up to 2000 atm. Nauk. Tr. Kursk. Cos Pedagog. Inst. 1972.

(14) Takagi, T.; Teranishi, H. Ultrasonic Speeds and Thermodynamics for Binary Solutions of N-Alkanes under High Pressures. Fluid Phase Equilibria 1985, 20, 315–320.

(15) Dzida, M.; Cempa, M. Thermodynamic and Acoustic Properties of (Heptane+dodecane) Mixtures under Elevated Pressures. J. Chem. Thermodyn. 2008, 40 (10), 1531–1541.

(16) Ducoulombier, D.; Zhou, H.; Boned, C.; Peyrelasse, J.; Saint-Guirons, H.; Xans, P. Pressure (1-1000 Bars) and Temperature (20-100.Degree.C) Dependence of the Viscosity of Liquid Hydrocarbons. J. Phys. Chem. 1986, 90 (8), 1692–1700.

(17) Assael, M. J.; Dymond, J. H.; Papadaki, M.; Patterson, P. M. Correlation and Prediction of Dense Fluid Transport Coefficients. III. n-Alkane Mixtures. Int. J. Thermophys. 1992, 13 (4), 659–669.

(18) Oliveira, C. M. B. P.; Wakeham, W. A. The Viscosity of Five Liquid Hydrocarbons at Pressures up to 250 MPa. Int. J. Thermophys. 1992, 13 (5), 773–790.

(19) Dymond, J. H.; Awan, M. A. Correlation of High-Pressure Diffusion and Viscosity Coefficients for n-Alkanes. Int. J. Thermophys. 1989, 10 (5), 941–951.

(20) Kiran, E.; Sen, Y. L. High-Pressure Viscosity and Density of n-Alkanes. Int. J. Thermophys. 1992, 13 (3), 411–442.

(21) Tanaka, Y.; Hosokawa, H.; Kubota, H.; Makita, T. Viscosity and Density of Binary Mixtures of Cyclohexane with N-Octane, n-Dodecane, and n-Hexadecane under High Pressures. Int. J. Thermophys. 1991, 12 (2), 245–264.

(22) Knapstad, B.; Skjoelsvik, P. A.; Oeye, H. A. Viscosity of Three Binary Hydrocarbon Mixtures. J. Chem. Eng. Data 1991, 36 (1), 84–88.

(23) VOGEL, H. Das Temperaturabhangigkeitsgesetz Der Viskositat von Flussigkeiten. Phys Z 1921, 22, 645–646.

(24) Fulcher, G. S. ANALYSIS OF RECENT MEASUREMENTS OF THE VISCOSITY OF GLASSES. J. Am. Ceram. Soc. 1925, 8 (6), 339–355.

(25) Tammann, G.; Hesse, W. Die Abhängigkeit Der Viscosität von Der Temperatur Bie Unterkühlten Flüssigkeiten. Z. Für Anorg. Allg. Chem. 1926, 156 (1), 245–257.

(26) Habrioux, M.; Bazile, J.-P.; Galliero, G.; Daridon, J. L. Viscosities of Fatty Acid Methyl and Ethyl Esters under High Pressure: Methyl Myristate and Ethyl Myristate. J. Chem. Eng. Data 2016, 61 (1), 398–403.

(27) Michailidou, E. K.; Assael, M. J.; Huber, M. L.; Perkins, R. A. Reference Correlation of the Viscosity of n -Hexane from the Triple Point to 600 K and up to 100 MPa. J. Phys. Chem. Ref. Data 2013, 42 (3), 033104.

Appendix C . Molecular Simulation Results of the Binary Mixtures of CO_2 + n-C_7.

Contents

C .1 Thermophysical Properties of MC Simulations of CO2 + n-C7 Mixtures. 178
C .2 Kirkwood Buff Integrals (KBIs) of CO2 + n-C7 Mixtures..... 182

Introduction

In this appendix, are provided molecular simulation data employed in the chapter 6. In section C.1, we present Monte Carlo simulation results of density, isothermal compressibility and Speed of sound. Section C.2 gives different Kirkwood Buff Integrals (KBIs) calculated by Molecular Dynamics.

C .1 Thermophysical Properties of MC Simulations of CO2 + n-C7 Mixtures.

Table.Appendix C.1 Density data of CO_2 + n-C_7 obtained from MC simulations

T (K)	P (MPa)	ρ + $\sigma(\rho)$									
X_{CO2}/mol%		0.00%		20.14%		40.00%		60.00%		83.26%	
303.35	10.12	691.8	0.5	708.4	0.8	729.2	0.6	756.0	0.5	790.4	2.0
303.35	20.14	701.1	0.4	719.2	0.4	742.5	0.8	774.4	1.0	826.0	1.4
303.35	30.18	709.7	0.8	728.8	0.6	753.7	0.4	788.8	0.2	851.2	1.0
303.35	40.25	717.8	1.0	737.3	0.3	763.8	0.2	802.2	0.6	872.4	0.7
303.35	50.35	724	0.7	745.8	0.5	773.4	0.7	814.1	0.7	891.0	0.6
303.35	60.47	731.3	0.6	752.9	0.4	781.7	0.5	824.7	0.5	906.8	0.5
303.35	70.62	737.6	0.5	759.6	0.8	789.9	0.2	834.1	0.5	920.4	0.5
313.25	10.11	683	0.5	698.7	0.4	717.5	0.7	739.7	1.1	757.7	2.6
313.25	20.13	693.1	1.0	710.2	0.6	732	0.4	759.9	1.1	799.3	1.7
313.25	30.16	701.9	0.4	720.1	0.4	743.8	0.4	776.1	0.9	831.0	1.8
313.25	40.23	709.8	0.7	729.4	1.0	754.5	1.0	790.6	0.6	854.3	1.4
313.25	50.31	717.5	0.3	737.6	0.8	764.4	0.6	802.3	0.8	873.4	0.7
313.25	60.41	724.1	0.8	745.7	0.3	773.4	1.0	813.5	0.7	890.9	0.6
313.25	70.54	730.5	0.6	752.6	0.3	781.4	0.7	823.9	0.1	905.3	0.8
X_{CO2}/mol%		88.49%		95.00%		99.00%		100%			
303.35	10.12	792.9	4.6	784	3.9	772.2	4.1	760.9	8.1		
303.35	20.14	839.7	3.4	858.3	2.4	868.8	1.6	873	6.4		
303.35	30.18	870.2	3.1	898.5	3.1	923.2	1.5	927.3	2		
303.35	40.25	896.2	1.9	930.6	0.8	957.0	2.1	965.9	1.5		
303.35	50.35	916.4	0.1	955.8	0.8	985.9	2.0	996.2	1.5		
303.35	60.47	933.9	0.7	978	0.5	1011.0	0.9	1020	0.6		
303.35	70.62	949.5	1.0	996.4	0.6	1033.0	0.4	1043	0.2		
313.25	10.11	750.9	2.3	716.1	6.8	647.5	6.6	606.9	21		
313.25	20.13	809.4	3.4	822.2	4.1	820.2	3.6	819.7	3.6		
313.25	30.16	844.9	2.2	868.9	2.9	884.2	3.5	888.6	4		
313.25	40.23	874.3	0.6	901.7	2.5	925.8	1.0	932.5	1.5		
313.25	50.31	895.8	1.3	931.7	1.3	958.4	1.2	965.4	1.3		
313.25	60.41	915.9	0.5	955.1	1.4	985.4	0.4	993.4	1.1		
313.25	70.54	932	0.8	975.4	0.4	1008.0	1.2	1017	1.5		

Table.Appendix C.2 Isothermal compressibility data of CO_2 + n-C_7 obtained from MC simulations

T (K)	P (MPa)	$\kappa_T + \sigma(\kappa_T)$									
X_{CO2}/mol%		0.00%		20.14%		40.00%		60.00%		83.26%	
303.35	10.12	1.485	0.101	1.583	0.069	1.945	0.167	2.550	0.184	5.048	1.137
303.35	20.14	1.249	0.029	1.380	0.066	1.635	0.131	2.176	0.111	3.699	0.471
303.35	30.18	1.199	0.074	1.211	0.053	1.386	0.094	1.722	0.104	2.381	0.192
303.35	40.25	1.108	0.079	1.061	0.088	1.230	0.073	1.471	0.078	2.109	0.568
303.35	50.35	0.980	0.058	1.025	0.052	1.115	0.052	1.340	0.087	1.834	0.098
303.35	60.47	0.851	0.059	0.876	0.039	1.005	0.031	1.202	0.069	1.711	0.114
303.35	70.62	0.780	0.048	0.891	0.038	0.929	0.040	1.071	0.024	1.399	0.083
313.25	10.11	1.439	0.090	1.762	0.044	2.053	0.142	2.994	0.167	7.204	0.472
313.25	20.13	1.365	0.070	1.447	0.045	1.742	0.077	2.328	0.088	4.335	0.515
313.25	30.16	1.187	0.053	1.282	0.093	1.514	0.041	1.972	0.124	3.136	0.338
313.25	40.23	1.108	0.066	1.149	0.039	1.442	0.047	1.631	0.106	2.159	0.255
313.25	50.31	1.049	0.061	1.083	0.031	1.237	0.045	1.365	0.061	1.978	0.066
313.25	60.41	0.949	0.020	0.960	0.046	1.100	0.040	1.272	0.057	1.752	0.082
313.25	70.54	0.882	0.041	0.890	0.072	0.992	0.025	1.130	0.078	1.549	0.087
X_{CO2}/mol%		88.49%		95.00%		99.00%		100%			
303.35	10.12	7.120	1.356	13.370	2.842	16.937	2.611	27.651	5.372		
303.35	20.14	4.192	0.322	5.824	0.592	7.168	0.631	7.578	1.132		
303.35	30.18	3.150	0.196	4.040	0.552	4.265	0.524	4.748	0.414		
303.35	40.25	2.536	0.397	2.868	0.190	3.122	0.100	3.309	0.126		
303.35	50.35	2.126	0.134	2.359	0.098	2.581	0.071	2.695	0.159		
303.35	60.47	1.781	0.103	1.966	0.061	2.089	0.150	2.266	0.056		
303.35	70.62	1.548	0.079	1.732	0.065	1.805	0.044	1.933	0.139		
313.25	10.11	11.473	3.313	25.939	7.663	74.370	19.951	116.3	13.5		
313.25	20.13	5.213	0.687	7.263	0.372	9.481	1.230	11.063	2.079		
313.25	30.16	3.915	0.421	4.461	0.280	5.575	0.788	5.567	0.442		
313.25	40.23	2.786	0.110	3.497	0.415	4.063	0.112	3.956	0.377		
313.25	50.31	2.352	0.158	2.733	0.093	2.959	0.106	3.191	0.169		
313.25	60.41	1.939	0.085	2.178	0.127	2.519	0.162	2.558	0.145		
313.25	70.54	1.676	0.100	1.816	0.063	2.088	0.034	2.153	0.097		

Table.Appendix C.3 Isentropic compressibility data of CO_2 + n-C_7 obtained from MC simulations

T (K)	P (MPa)	$\kappa_s + \sigma(\kappa_s)$									
X_{CO2}/mol%		0.00%		20.14%		40.00%		60.00%		83.26%	
303.35	10.12	1.144	0.001	1.199	0.001	1.394	0.001	1.676	0.001	2.647	0.007
303.35	20.14	0.981	0.001	1.056	0.001	1.193	0.001	1.432	0.002	1.963	0.004
303.35	30.18	0.929	0.001	0.939	0.001	1.023	0.001	1.181	0.000	1.426	0.002
303.35	40.25	0.864	0.001	0.838	0.000	0.923	0.000	1.032	0.001	1.256	0.001
303.35	50.35	0.776	0.001	0.798	0.000	0.843	0.001	0.939	0.001	1.097	0.001
303.35	60.47	0.688	0.001	0.700	0.000	0.764	0.000	0.854	0.000	1.017	0.001
303.35	70.62	0.638	0.000	0.696	0.001	0.712	0.000	0.772	0.000	0.871	0.000
313.25	10.11	1.142	0.001	1.322	0.001	1.504	0.001	1.950	0.003	3.580	0.012
313.25	20.13	1.062	0.002	1.117	0.001	1.279	0.001	1.566	0.002	2.314	0.005
313.25	30.16	0.945	0.001	0.997	0.001	1.126	0.001	1.348	0.002	1.750	0.004
313.25	40.23	0.878	0.001	0.904	0.001	1.056	0.001	1.136	0.001	1.328	0.002
313.25	50.31	0.829	0.000	0.844	0.001	0.923	0.001	0.982	0.001	1.198	0.001
313.25	60.41	0.761	0.001	0.764	0.000	0.834	0.001	0.904	0.001	1.063	0.001
313.25	70.54	0.707	0.001	0.707	0.000	0.763	0.001	0.821	0.000	0.950	0.001
X_{CO2}/mol%		88.49%		95.00%		99.00%		100%			
303.35	10.12	3.337	0.019	4.660	0.024	5.188	0.028	6.871	0.075		
303.35	20.14	2.110	0.008	2.514	0.007	2.759	0.005	2.802	0.021		
303.35	30.18	1.643	0.006	1.812	0.006	1.802	0.003	1.871	0.004		
303.35	40.25	1.371	0.003	1.400	0.001	1.409	0.003	1.418	0.002		
303.35	50.35	1.164	0.000	1.191	0.001	1.193	0.002	1.207	0.002		
303.35	60.47	1.012	0.001	1.025	0.001	1.004	0.001	1.035	0.001		
303.35	70.62	0.896	0.001	0.907	0.001	0.887	0.000	0.902	0.000		
313.25	10.11	4.529	0.016	8.227	0.080	13.546	0.150	17.990	0.622		
313.25	20.13	2.591	0.011	3.065	0.015	3.538	0.016	3.810	0.017		
313.25	30.16	2.008	0.005	2.056	0.007	2.270	0.009	2.246	0.010		
313.25	40.23	1.507	0.001	1.674	0.005	1.760	0.002	1.699	0.003		
313.25	50.31	1.300	0.002	1.351	0.002	1.353	0.002	1.400	0.002		
313.25	60.41	1.108	0.001	1.132	0.002	1.161	0.001	1.178	0.001		
313.25	70.54	0.977	0.001	0.970	0.000	1.000	0.001	1.003	0.002		

Table.Appendix C.4 Speed of sound data of CO_2 + n-C_7 calculated from MC simulations

T (K)	P (MPa)	$W + U_c$(w)									
X_{CO2}/mol%		0.00%		20.14%		40.00%		60.00%		83.26%	
303.35	10.12	1124.2	55.3	1084.9	34.5	992.0	71.6	888.4	59.4	691.3	193.7
303.35	20.14	1205.8	20.2	1147.6	42.2	1062.7	69.5	949.5	46.6	785.3	131.2
303.35	30.18	1231.9	58.0	1208.6	40.3	1139.0	62.6	1036.0	54.0	907.5	85.4
303.35	40.25	1270.1	66.9	1272.6	86.3	1191.2	54.4	1099.1	52.6	955.3	283.3
303.35	50.35	1334.5	55.8	1296.5	47.2	1238.1	45.5	1143.7	64.6	1011.3	59.8
303.35	60.47	1409.9	68.1	1377.5	44.7	1294.0	32.3	1191.4	59.8	1041.6	79.3
303.35	70.62	1457.3	62.2	1375.8	42.9	1333.7	46.6	1246.3	24.1	1116.9	71.9
313.25	10.11	1132.2	49.4	1040.5	20.6	962.6	51.9	832.5	43.7	607.2	51.8
313.25	20.13	1165.4	42.4	1122.9	26.0	1033.3	36.3	916.7	29.8	735.2	120.3
313.25	30.16	1228.0	37.8	1180.1	63.3	1092.6	21.2	977.6	54.4	829.2	114.8
313.25	40.23	1266.4	52.7	1231.2	30.6	1120.5	32.1	1055.3	61.5	938.8	109.1
313.25	50.31	1296.9	53.9	1267.1	26.9	1190.3	35.2	1126.5	41.1	977.4	33.9
313.25	60.41	1347.1	18.8	1325.2	44.7	1244.9	35.9	1166.3	45.0	1027.5	53.5
313.25	70.54	1391.8	44.8	1370.6	78.5	1295.1	26.4	1215.7	68.6	1078.1	65.4
X_{CO2}/mol%		88.49%		95.00%		99.00%		100%			
303.35	10.12	614.8	173.0	523.2	269.7	499.6	194.6	437.4	318.2		
303.35	20.14	751.2	86.9	680.7	124.9	645.9	113.2	639.4	205.3		
303.35	30.18	836.4	66.6	783.8	175.5	775.4	174.4	759.2	119.6		
303.35	40.25	902.2	177.0	876.3	86.9	861.1	44.9	854.3	69.5		
303.35	50.35	968.3	78.2	937.2	56.6	922.2	41.2	911.9	90.8		
303.35	60.47	1028.7	71.3	999.0	41.2	992.6	111.8	973.2	35.5		
303.35	70.62	1084.2	63.3	1051.8	53.2	1044.4	36.3	1030.9	115.9		
313.25	10.11	542.3	315.7	412.0	327.3	337.7	471.1	302.6	195.2		
313.25	20.13	690.5	136.3	629.9	50.1	587.0	160.5	565.9	251.8		
313.25	30.16	767.7	105.3	748.2	87.6	705.9	178.2	707.9	110.1		
313.25	40.23	871.1	40.2	813.9	146.3	783.5	50.5	794.6	130.4		
313.25	50.31	926.8	77.4	891.2	38.7	878.0	51.0	860.2	81.2		
313.25	60.41	992.5	53.9	961.5	75.6	934.9	101.1	924.3	85.8		
313.25	70.54	1047.9	70.4	1027.9	50.4	996.2	21.0	990.2	71.9		

C .2 Kirkwood Buff Integrals (KBIs) of CO2 + n-C7 Mixtures.

In this section, are reported the calculated KBIs. From these data we computed mixtures isothermal compressibilities and partial molar volumes of CO_2 and n-C_7 from equations (3.73) and (3.74).

Table.Appendix C.5 KBIs between CO_2 molecules

T (K)	P (MPa)	$KBI_{CO2-CO2} \pm \sigma$									
X_{CO2}/mol%		0.00%		20.14%		40.00%		60.00%		83.26%	
303.35	10.12	-	-	0.1237	0.0304	0.1607	0.0246	0.1869	0.0456	0.1131	0.0110
303.35	20.14	-	-	0.1681	0.0718	0.1363	0.0164	0.1935	0.0432	0.0981	0.0454
303.35	30.18	-	-	0.1228	0.0891	0.1203	0.0228	0.1733	0.0418	0.0790	0.0131
303.35	40.25	-	-	0.1227	0.0638	0.1427	0.0467	0.1564	0.0351	0.0855	0.0095
303.35	50.35	-	-	0.1222	0.0836	0.1270	0.0264	0.1712	0.0106	0.1099	0.0062
303.35	60.47	-	-	0.1142	0.0459	0.1353	0.0095	0.1614	0.0389	0.1078	0.0128
303.35	70.62	-	-	0.1420	0.0843	0.1354	0.0346	0.1806	0.0528	0.1083	0.0221
313.25	10.11	-	-	0.0818	0.0776	0.1480	0.0347	0.1552	0.0147	0.0941	0.0053
313.25	20.13	-	-	0.1682	0.0055	0.1513	0.0409	0.1493	0.0368	0.0869	0.0106
313.25	30.16	-	-	0.1311	0.0153	0.1333	0.0178	0.1353	0.0048	0.0696	0.0179
313.25	40.23	-	-	0.1589	0.0605	0.1116	0.0060	0.1343	0.0091	0.0647	0.0071
313.25	50.31	-	-	0.1143	0.0620	0.1072	0.0212	0.1520	0.0107	0.0821	0.0042
313.25	60.41	-	-	0.1367	0.0532	0.1138	0.0191	0.1400	0.0196	0.0883	0.0109
313.25	70.54	-	-	0.1096	0.0990	0.1706	0.0553	0.1419	0.0292	0.0854	0.0104
X_{CO2}/mol%		88.49%		95.00%		99.00%		Infinite dilution		100%	
303.35	10.12	0.0261	0.0053	-0.0209	0.0013	-0.0107	0.0010			0.0056	0.0016
303.35	20.14	0.0455	0.0104	-0.0260	0.0031	-0.0487	0.0005			-0.0529	0.0002
303.35	30.18	0.0471	0.0080	-0.0222	0.0015	-0.0554	0.0009			-0.0598	0.0002
303.35	40.25	0.0470	0.0195	-0.0292	0.0003	-0.0580	0.0001			-0.0626	0.0001
303.35	50.35	0.0382	0.0049	-0.0218	0.0046	-0.0578	0.0002			-0.0630	0.0001
303.35	60.47	0.0460	0.0233	-0.0247	0.0004	-0.0575	0.0005			-0.0628	0.0000
303.35	70.62	0.0547	0.0017	-0.0237	0.0054	-0.0565	0.0006			-0.0626	0.0001
313.25	10.11	0.0162	0.0090	-0.0041	0.0006	0.1380	0.0026	0.240	0.002	0.2438	0.0024
313.25	20.13	0.0467	0.0038	-0.0340	0.0012	-0.0446	0.0007			-0.0441	0.0002
313.25	30.16	0.0298	0.0044	-0.0319	0.0029	-0.0553	0.0002			-0.0567	0.0001
313.25	40.23	0.0326	0.0110	-0.0300	0.0041	-0.0575	0.0003			-0.0626	0.0002
313.25	50.31	0.0358	0.0070	-0.0330	0.0018	-0.0581	0.0006			-0.0634	0.0002
313.25	60.41	0.0297	0.0066	-0.0276	0.0029	-0.0586	0.0007			-0.0635	0.0001
313.25	70.54	0.0430	0.0063	-0.0301	0.0036	-0.0582	0.0003			-0.0632	0.0001

Table.Appendix C.6 KBIs between CO_2 and n-C_7 molecules.

T (K)	P (MPa)	KBI CO2-C7± σ									
X_{CO2}/mol%		0.00%		20.14%		40.00%		60.00%		83.26%	
303.35	10.12	-	-	-0.0913	0.0024	-0.1283	0.0057	-0.2132	0.0241	-0.4144	0.0211
303.35	20.14	-	-	-0.0922	0.0059	-0.1193	0.0042	-0.2080	0.0220	-0.3616	0.0772
303.35	30.18	-	-	-0.0866	0.0068	-0.1128	0.0049	-0.1915	0.0201	-0.3160	0.0226
303.35	40.25	-	-	-0.0840	0.0046	-0.1153	0.0098	-0.1792	0.0172	-0.3155	0.0149
303.35	50.35	-	-	-0.0834	0.0061	-0.1103	0.0044	-0.1817	0.0054	-0.3481	0.0108
303.35	60.47	-	-	-0.0814	0.0038	-0.1097	0.0023	-0.1751	0.0186	-0.3375	0.0195
303.35	70.62	-	-	-0.0816	0.0057	-0.1081	0.0067	-0.1816	0.0248	-0.3338	0.0339
313.25	10.11	-	-	-0.0902	0.0062	-0.1286	0.0080	-0.2039	0.0075	-0.4104	0.0112
313.25	20.13	-	-	-0.0941	0.0006	-0.1249	0.0085	-0.1914	0.0200	-0.3582	0.0214
313.25	30.16	-	-	-0.0895	0.0010	-0.1178	0.0049	-0.1769	0.0030	-0.3107	0.0308
313.25	40.23	-	-	-0.0897	0.0051	-0.1104	0.0014	-0.1727	0.0054	-0.2902	0.0115
313.25	50.31	-	-	-0.0849	0.0049	-0.1072	0.0050	-0.1770	0.0054	-0.3105	0.0061
313.25	60.41	-	-	-0.0840	0.0034	-0.1070	0.0035	-0.1677	0.0097	-0.3138	0.0173
313.25	70.54	-	-	-0.0813	0.0079	-0.1170	0.0118	0.1658	0.0139	-0.3039	0.0178
X_{CO2}/mol%		88.49%		95.00%		99.00%		Infinite dilution		100%	
303.35	10.12	-0.3349	0.0166	-0.2360	0.0124	-0.0837	0.0145			-	-
303.35	20.14	-0.3774	0.0286	-0.2977	0.0214	-0.2384	0.0065			-	-
303.35	30.18	-0.3635	0.0201	-0.3228	0.0047	-0.2086	0.0172			-	-
303.35	40.25	-0.3507	0.0487	-0.2823	0.0011	-0.2254	0.0071			-	-
303.35	50.35	-0.3214	0.0111	-0.3204	0.0302	-0.2302	0.0067			-	-
303.35	60.47	-0.3334	0.0559	-0.2966	0.0040	-0.2311	0.0138			-	-
303.35	70.62	-0.3496	0.0032	-0.2975	0.0326	-0.2505	0.0177			-	-
313.25	10.11	-0.3169	0.0284	-0.1305	0.0064	0.3118	0.0086	0.7559	0.2062	-	-
313.25	20.13	-0.3962	0.0079	-0.2513	0.0102	-0.1874	0.0166			-	-
313.25	30.16	-0.3344	0.0120	-0.2695	0.0168	-0.2102	0.0023			-	-
313.25	40.23	-0.3278	0.0299	-0.2891	0.0224	-0.2491	0.0203			-	-
313.25	50.31	-0.3232	0.0183	-0.2650	0.0120	-0.2494	0.0188			-	-
313.25	60.41	-0.3022	0.0155	-0.2887	0.0156	-0.2243	0.0235			-	-
313.25	70.54	-0.3272	0.0165	-0.2677	0.0230	-0.2240	0.0047		¤	-	-

Table.Appendix C.7 KBIs between n-C_7 molecules

T (K)	P (MPa)	KBI C7-C7± σ									
X_{CO2}/mol%		0.00%		20.14%		40.00%		60.00%		83.26%	
303.35	10.12	-0.2349	0.0000	-0.2464	0.0002	-0.2565	0.0013	-0.2362	0.0130	0.1990	0.0423
303.35	20.14	-0.2325	0.0000	-0.2435	0.0006	-0.2555	0.0010	-0.2383	0.0112	0.0320	0.1326
303.35	30.18	-0.2302	0.0001	-0.2414	0.0005	-0.2540	0.0012	-0.2443	0.0098	-0.0609	0.0391
303.35	40.25	-0.2281	0.0000	-0.2393	0.0003	-0.2510	0.0022	-0.2480	0.0085	-0.0702	0.0234
303.35	50.35	-0.2261	0.0000	-0.2371	0.0004	-0.2494	0.0008	-0.2448	0.0027	-0.0187	0.0189
303.35	60.47	-0.2243	0.0000	-0.2352	0.0004	-0.2473	0.0006	-0.2452	0.0090	-0.0379	0.0296
303.35	70.62	-0.2226	0.0000	-0.2334	0.0004	-0.2456	0.0013	-0.2397	0.0116	-0.0424	0.0527
313.25	10.11	-0.2375	0.0001	-0.2492	0.0005	-0.2596	0.0019	-0.2425	0.0038	0.2859	0.0213
313.25	20.13	-0.2348	0.0001	-0.2460	0.0001	-0.2573	0.0019	-0.2488	0.0109	0.0583	0.0424
313.25	30.16	-0.2323	0.0000	-0.2435	0.0001	-0.2558	0.0014	-0.2545	0.0019	-0.0635	0.0538
313.25	40.23	-0.2301	0.0001	-0.2411	0.0004	-0.2547	0.0004	-0.2537	0.0032	-0.1100	0.0197
313.25	50.31	-0.2281	0.0001	-0.2391	0.0004	-0.2528	0.0012	-0.2493	0.0026	-0.0793	0.0091
313.25	60.41	-0.2262	0.0001	-0.2372	0.0002	-0.2503	0.0006	-0.2515	0.0048	-0.0750	0.0274
313.25	70.54	-0.2244	0.0000	-0.2354	0.0006	-0.2461	0.0026	-0.2500	0.0065	-0.0900	0.0308
X_{CO2}/mol%		88.49%		95.00%		99.00%		Infinite dilution		100%	
303.35	10.12	0.2403	0.0552	0.6913	0.1098	1.5798	0.2817	-	-	-	-
303.35	20.14	0.2000	0.0799	0.4502	0.1461	1.5122	0.2525	-	-	-	-
303.35	30.18	0.1608	0.0502	0.4837	0.0156	-0.1740	0.3259	-	-	-	-
303.35	40.25	0.1061	0.1220	0.1689	0.0253	0.0796	0.2995	-	-	-	-
303.35	50.35	0.0273	0.0260	0.3880	0.1992	0.0526	0.2643	-	-	-	-
303.35	60.47	0.0521	0.1357	0.2316	0.0414	-0.0027	0.4551	-	-	-	-
303.35	70.62	0.0944	0.0062	0.2443	0.1990	0.6525	0.5629	-	-	-	-
313.25	10.11	0.4295	0.1079	1.5362	0.0661	1.2772	0.3912	-	-	-	-
313.25	20.13	0.3649	0.0147	0.4248	0.0780	1.3108	0.6896	-	-	-	-
313.25	30.16	0.1212	0.0335	0.2048	0.1164	0.3753	0.1931	-	-	-	-
313.25	40.23	0.0648	0.0787	0.2368	0.1280	0.7447	0.7961	-	-	-	-
313.25	50.31	0.0325	0.0466	0.0681	0.0831	0.7289	0.6541	-	-	-	-
313.25	60.41	-0.0210	0.0364	0.1889	0.0947	0.0134	0.8382	-	-	-	-
313.25	70.54	0.0376	0.0441	0.0632	0.1462	-0.1036	0.1872	-	-	-	-

ECOLE DOCTORALE :
École doctorale des sciences exactes et leurs applications

LABORATOIRE :
Laboratoire des Fluides Complexes et leurs Réservoirs,
UMR 5150 CNRS-TOTAL-UPPA

CONTACT

abdoul.saleyhamani@gmail.com
Université de Pau et des Pays de l'Adour
Avenue de l'Université
BP 576
64012 Pau Cedex